Photonuclear reactions - from basic research to applications

A. Zilges[1], D. L. Balabanski[2], J. Isaak[3], N. Pietralla[3]

[1] Institut für Kernphysik, University of Cologne, Cologne, Germany
[2] Extreme Light Infrastructure - Nuclear Physics / Horia Hulubei National Institute for R&D in Physics and Nuclear Engineering, Bucharest-Magurele, Romania
[3] Institut für Kernphysik, TU Darmstadt, Darmstadt, Germany

June 17, 2021

Abstract

Nuclear reactions induced by photons play a vital role for very different aspects of basic research and applications in physics. They are a key ingredient for the synthesis of nuclei in the Universe and provide, due to the selectivity and the model-independence of the reaction mechanism, an extremely valuable probe for researchers. The penetrability of photons in the MeV energy range makes them, in addition, an ideal tool for meeting various societal challenges. The last two decades saw a rapid development of advanced photon sources and detection methods for photonuclear reaction products. Bremsstrahlung and quasi-monoenergetic photon beams with unprecedented intensity and quality combined with state-of-the-art detector technology paved the way for new scientific discoveries and technological applications.

This review focuses on a comprehensive overview of the most important developments since the turn of the millenium restricted to the energy range between atomic and hadronic degrees of freedom. This includes a description of the formalism of photonuclear reactions below and above the particle-separation threshold. The most important techniques used to generate photon beams in the MeV energy range are presented along with selected facilities and instrumentation for diagnostics and for the analysis of photonuclear reactions. The power of photons to probe the atomic nucleus is exemplified in a number of selected examples from fundamental and applied science. New developments, facilities, and ideas promise a vivid future for photonuclear physics.

Contents

Glossary

Acronyms

2D	Two-dimensional
2E	Double Kinetic Energy
3D	Three-dimensional
3N	Three-nucleon
AIST	National Institute of Advanced Industrial Science and Technology
ALTO	Accélérateur Linéaire auprès du Tandem d'Orsay
ARIEL	Advanced Rare Isotope Laboratory
BBN	Big Bang nucleosynthesis
CCD	Charge-coupled device
CEN	Centre d'Etudes de Saclay
CERN	Conseil Européen pour la Recherche Nucléaire
CMOS	Complementary metal oxide semiconductor
CT	Computer tomography
CW	Continuous wave
DFC	Dual fission chamber
DHIPS	Darmstadt High Intensity Photon Setup
DNM	Direct neutron multiplicity
DNT	Direct neutron sorting technique
DSSSD	Double-sided silicon strip detectors
e-linac	Electron Linear Accelerator
ELI-NP	Extreme Light Infrastucture - Nuclear Physics, Magurele, Romania
EMPIRE	Nuclear Reaction Model Code System for Data Evaluation
ENDF	Evaluated nuclear data file
EPR	Electron paramagnetic resonance
FED	Flat-efficiency detector
FGIC	Frisch-gridded ionization chamber
FPY	Fission product yields
γELBE	Photon scattering facility at HZDR, Dresden-Rossendorf, Germany
GDH	Gerasimov-Drell-Hearn
GDR	Giant Dipole Resonance
GEANT4	Geometry and Tracking (code for Monte-Carlo simulations)
GEF	General Description of Fission Observables
GQR	Giant Quadrupole Resonance
HD	Hyperdeformed

HE	High Explosives
HF	Hauser-Feshbach
HIγS	High-Intensity γ-ray Source, Duke Free-Electron Laser Laboratory
IAEA	International Atomic Energy Agency, Vienna
IAEA CRP	IAEA Coordination Research Project
IAMI	Institute for Advanced Medical Isotopes, TRIUMF, Vancouver
INVS	Inventory sample counter
ISOL	Isotope separation on-line
IVGDR	Isovector Giant Dipole Resonance
JENDL	Japanese Evaluated Nuclear Data Library
LAL	Laboratoire de l'accélérateur linéaire, Orsay, France
LCB	Laser Compton backscattering
LEP	Large Electron–Positron Collider
LLNL	Lawrence Livermore National Laboratory
LOS	Light output signal
NDA	Non-destructive analysis
NewSUBARU	1.5 GeV electron storage ring at SPring-8 operated by the University of Hyogo
NLD	Nuclear level density
NN	Nucleon-nucleon
NRF	Nuclear Resonance Fluorescence
NSC KIPT	National Science Center Kharkov Institute of Physics and Technology
O-TPC	Optical time-projection chamber
PAF	Photonuclear Activation File
PDR	Pygmy Dipole Resonance
PES	Potential Energy Surface
PSD	Pulse Shape Discrimination
PSF	Photon Strength Function
QD	Quasi-deuteron
QPM	Quasi-particle Phonon Model
RIB	Radioactive Ion Beam
RIPL-3	Reference Input Parameter Library
ROSFOND	Russian national library of neutron data
RPIT	Resonant Photonuclear Isotope Transmutation
RSA	Relative Self absorption
S-DALINAC	Superconducting Darmstadt linear accelerator, TU Darmstadt, Germany
ScM	Scissors Mode
SD	Superdeformed

SNM	Special Nuclear Materials
SPECT	Single Photon Emission Computed Tomography
SPring-8	Super Photon Ring – 8 GeV
TALYS	Open source software package for the simulation of nuclear reactions
TKE	Total Kinetic Energy
ToF	Time of Flight
TPC	Time-projection chamber
TRIUMF	Tri-University Meson Facility, Vancouver, Canada
VEGA	Variable energy gamma system

Quantities

α_K	Resonance-absorption density, Eq. (33)
$\langle b_0 \rangle$	Average ground-state branching ratio: $\sigma_{\gamma\gamma}/\sigma_\gamma$, Sec. 2.3.6
$\langle b_i \rangle$	Average branching ratio to the i^{th} excited state relative to the ground-state, Eq. (60)
Δ	Doppler width, Eqs. (19,27)
ϵ	Polarization asymmetry, Eq. (45)
$\epsilon_n(\theta)$	Neutron polarization asymmetry, Eq. (86)
E_γ	Energy of the LCB photon beam
Φ_K	Normalized photon-flux density, Eq. (30)
$f_{\lambda L}$	Photon strength function of multipolarity L and transition character $\lambda = E, M$
Γ	Total width of a quasi-stationary quantum level
Γ_0	Partial decay width to the ground state, 'ground-state excitation width'
$\Gamma_{f,\Pi L}$	Monopolar partial decay width
I_a	Energy-integrated absorption cross section, Eq. (24)
I_n	Neutron yield
$I_{s,0}$	'Elastic' (NRF) cross section
$I_{s,f}$	Integrated (NRF) cross section, Eq. (35)
IR	Isomeric ratio, Eq. (87)
K	Resonance-absorption attenuation coefficient, Eq. (21)
$\dot{N}_\gamma$	(Spectral) Photon current, Eq. (36)
N_n	Neutron multiplicity
N_γ	(Spectral) Photon flux, Eq. (22)
N_γ^{tot}	Energy-integrated photon flux, Eq. (47)
N_μ	Normalized rate of photonuclear reactions
N_T	Total number of target nuclei, Eq. (47)
$\bar{n}$	Areal number density of target scattering centers, 'target thickness', Eq. (26)

n_γ	Spectral photon-current density, Subsections 2.2.2 and 2.2.3
$P_k^q(x)$	associated Legendre polynomials
P_γ	Degree of polarization of the incident photon beam, Eq. (37)
Q	Polarization sensitivity, Eq. (45)
$\rho(E)$	Nuclear level density at energy E
R	Self-absorption, Eq. (52)
R_{Alaga}	Alaga rules for the decay-branching ratio, Eq. (55)
R_{exp}	Decay-branching ratio, Eq. (54)
$\frac{d\sigma_\mu(\theta,\phi)}{d\Omega_\mu}$	Angular distribution of emitted particles, Sec. 2.4.4 and Eq. (78)
$\frac{d\sigma_\mu(E_\gamma)}{dE_\mu}$	Spectral distribution of emitted particles, Sec. 2.4.4
$\frac{d^2\sigma(E_\gamma)}{d\Omega_\mu dE_\mu}$	Double differential cross section, Sec. 2.4.4 and Eq. (81)
$\sigma(\gamma,\nu\text{n})$	Partial photoneutron cross section, Sec. 2.4.4, 2.5.2 and Eq. (106)
$\sigma(\gamma,\text{f})$	Photo-fission reaction cross section, Sec. 2.6
$\sigma[i^*(j,m)\mu]$	γ-particle cross section within the HF statistical theory, Eq. (68)
$\sigma_a^D(E)$	Doppler form of the effective photonuclear absorption cross section, Eq. (20)
σ_0	Photonuclear on-resonance absorption cross section, Eq. (14)
$\sigma_a(E)$	Photonuclear absorption cross section, Eq. (13)
$\sigma_{\gamma\gamma'}$	Average inelastic cross section, Eq. (48)
$\sigma_{\gamma\gamma}$	Average elastic cross section, Eq. (47)
σ_γ	Photoabsorption cross section
$\sigma_{exp}(\gamma,n)$	Total experimental photoneutron cross section, Eq. (75), Eq. (77)
$\sigma_{GDR}(E_\gamma)$	GDR cross section, Eq. (65)
$\sigma_{tot}(\gamma,\text{n})$	Total photoneutron cross section, Sec. 2.4.4 and Eq. (77)
$\sigma_{tot}(E_\gamma)$	Total photonuclear cross section, Eq. (64)
$\tilde{\sigma}_a^D(E)$	Effective photonuclear absorption cross section, Eq. (17)
S_n	Neutron separation energy
S_{2n}	Two-neutrons separation energy
Σ	Analyzing power, Eq. (42), Eq. (118)
Θ_D	Debye temperature
$T_\mu(E,J,\pi)$	Transmission coefficients within the HF statistical theory, Sec. 2.4.2
T_{eff}	Effective temperature, Eq. (28)
$W(\vartheta,\phi)$	Angular distribution function, Eq. (37)
$W_n(\theta,\phi)$	Angular distribution of emitted neutrons, Eq. (82), Eq. (**??**)
$Y(E_e)$	Yield of reaction products in bremsstrahlung experiments, Eq. (74)
Y_n	Normalized neutron yield
$\mathcal{Z}$	Target-penetration depth

1 Introduction

1.1 Photons and Nuclear Physics

All matter in our universe was and is permanently bombarded by photons from the lowest to the highest energies. The photons with high energies can lead to photoexcitation and photodisintegration of atomic nuclei. As soon as about one second after the Big Bang, photons dominated the energy of the universe. This era ended about 380,000 years later, when the temperature of the universe dropped to about 3000 K and photons decoupled from matter [1]. The universe became transparent for photons. Today, most of the photons have their origin in heated objects which emit a Planck photon bath with a continuous energy distribution around k_bT. Recently, lightning discharges have been found as another emitter of photons in the high-energy range [2, 3]. Typically, only photons in the energy regime of hundreds of keV to MeV corresponding to wavelengths smaller than about 10000 fm can induce nuclear reactions (including nuclear excitations). Such photons are, e.g., the reason for the elemental abundance peak in the iron region due to the nuclear statistical equilibrium and are a major player in the r and p processes of nucleosynthesis in explosive stellar environments.

The interaction of real photons (we use the notation "real" to distinguish those photons from virtual photons exchanged via the Coulomb force between charged systems) with atomic nuclei is very selective compared to other probes like, e.g., neutrons or energetic ions. Photons induce mainly dipole and to a much lesser extent quadrupole transitions. The interaction probability is directly correlated to the electromagnetic transition strength and can be deduced model independently from the measured data.

Photons in the MeV range are very penetrating. The distance which is passed by a photon beam with an energy of 5 MeV before the intensity is reduced by atomic absorption to 10% has values of about 9 cm in iron, 30 cm in aluminum and 76 cm in water. This characteristic becomes important for many diverse applications. Examples range from irradiations of cells in tumor therapy to the screening of cargo containers for homeland security measures or the identification of contraband.

The study of photonuclear reactions in the laboratory has seen a revival during the last decades partly triggered by the advent of new accelerator-based photon sources which create quasi-monoenergetic photon spectra with highest brilliance based on Laser Compton Backscattering (LCB). In addition, very efficient detection systems for the reaction products have been built. Both developments enable completely new experimental approaches for basic research and applications. The 20th century was denoted the "century of electrons" whereas the 21st century is now starting to be called frequently the "century of light". Laser beams in the eV energy range with unprecedented intensity and time structure made possible by new techniques like Chirped Pulse Amplification (CPA), an approach pioneered by Strickland and Mourou [4], opened new horizons for studies on atoms and molecules (and for certain applications like the acceleration of particles). Moreover, new photon beam facilities in the MeV energy range allow for the first time an extremely selective inspection and manipulation of nuclei. The area of Nuclear Photonics is quickly emerging.

With the present review article we make an attempt to serve the quickly growing community with an overview of the scientific and methodological progress achieved in the field of photonuclear reactions. We restrict ourselves to the reactions of atomic nuclei with real photons in the energy range between the energy scales of atomic and nuclear structure, i.e. between about 0.1 and 100 MeV. The wavelengths of photons of the discussed energies are in the range between 10000 fm to 10 fm. This means that the photon always interacts with the whole nucleus. In fact, the photonuclear cross section between the giant resonance region and the pion threshold is rather featureless, such that most experiments that are reviewed here had concentrated on energies below about 40 MeV. For higher energies we refer, e.g., to the review by Beck [5].

The study of photonuclear reactions is an enormously active research field since decades, see, e.g., the review articles [6–12]. However, a comprehensive review of the methodological achievements in this field since about the millenium year is missing. In our review, we will focus on experimental aspects and some recent developments which, we think, have pushed the field enormously in the last two decades. We apologize that we could not cover numerous additional very interesting research due to a lack of space. The results of photonuclear studies have led to numerous new theoretical insights. Again, we are unable to cover those in this review focusing on experimental aspects.

We start the review with a short voyage into the history of photonuclear reactions. The next section will give an introduction to the formalism for reactions below particle threshold (commonly denoted as photon scattering or Nuclear Resonance Fluorescence - NRF) and above particle threshold (commonly denoted as photodissociation and photofission). In the third section, the properties of various photon sources and some aspects of the instrumentation will be discussed. A few selected examples for the study of fundamental science using real photons will be described in section four. This will be followed by a discussion of some applications. Finally, we will summarize and try to give an outlook for this rapidly evolving field.

1.2 Historical milestones

In August 1934, Chadwick and Goldhaber published the first experimental paper on a photonuclear reaction [13]. They used photons with an energy of 2.615 MeV stemming from the γ decay of the first excited state of ^{208}Pb which had been populated in the ^{232}Th decay chain. They observed the photodissociation of deuterium (which they called "diplon" at this time) into a proton and a neutron and derived a better estimate for the neutron mass from their experiment. Shortly later, Szilard and Chalmers proved that neutrons are emitted from ^{9}Be after irradiation with photons with E_γ=1.765 MeV stemming from the radium decay chain [14]. The energies of these first photon sources were obviously fixed.

Three years later, Bothe and Gentner published their observation of nuclear transmutation - which was later understood as the photoneutron emission after the population of the Giant Dipole Resonance (GDR) - by the interaction of various isotopes with γ rays with energies of about 17 MeV stemming from the bombardment of ^{7}Li with protons with E_p=440 keV [15]. This production process, which in principle allows an adjustment of the γ-ray energy, had been discussed before by various authors, see, e.g. Ref. [16].

In 1947, Baldwin and Klaiber used for the first time a continuous γ-ray spectrum for a photonuclear study. This spectrum had been generated by bremsstrahlung from electrons accelerated by a betatron at the General Electric Laboratory. They investigated the energy dependence of the cross section of the GDR by varying the maximum electron energy between 10 and 100 MeV [17].

The idea to investigate bound states of nuclei by exciting them with bremsstrahlung and detecting the deexcitation via γ rays in photon detectors ("Nuclear Resonance Fluorescence - NRF" or "photon scattering") was proposed by Schiff in 1946 [18]. One decade later, it was put into practice by Hayward and Fuller [19] using a betatron with maximum electron energies from 4 to 40 MeV and a shielded NaI detector for the detection of the decay γ rays. A first review of the general ideas of the method was published by F.R. Metzger in 1959 [8]. Other review articles exhibiting the rapid development of the field followed [10, 11].

In August 1959, the famous Gordon Research Conference on photonuclear reactions took place for the first time, see Ref. [20]. Since then, the field developed very quickly. Numerous tools, scientific findings, and applications emerged and are still emerging.

F.R. Metzger pioneered the use of Van de Graaff accelerators with stable and intense beams of variable electron energy for the investigation of nuclei via bremsstrahlung [21]. A new sensitivity and quality of photon scattering data could be obtained in this way. This was further improved by the advent of dedicated high-current electron linear accelerators with high duty cycles to produce bremsstrahlung photons and the use of Ge semiconductor detectors with excellent energy resolution for the detection of

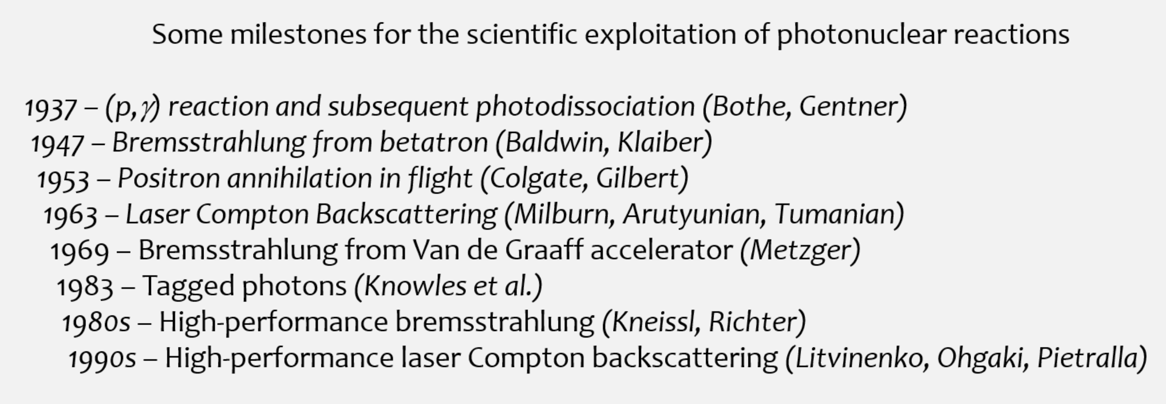

Some milestones for the scientific exploitation of photonuclear reactions

1937 – (p,γ) reaction and subsequent photodissociation (Bothe, Gentner)
1947 – Bremsstrahlung from betatron (Baldwin, Klaiber)
1953 – Positron annihilation in flight (Colgate, Gilbert)
1963 – Laser Compton Backscattering (Milburn, Arutyunian, Tumanian)
1969 – Bremsstrahlung from Van de Graaff accelerator *(Metzger)*
1983 – Tagged photons *(Knowles et al.)*
1980s – High-performance bremsstrahlung *(Kneissl, Richter)*
1990s – High-performance laser Compton backscattering *(Litvinenko, Ohgaki, Pietralla)*

Figure 1: A short list of major steps in scientific research with photonuclear reactions exploiting the development of different photon sources, see section 3 for details.

the scattered photons, see, e.g., Refs. [22–24]. Numerous photonuclear experiments were performed at the high-current cw electron beams of the Stuttgart Dynamitron [25] and the superconducting electron linear accelerator ("S-DALINAC") at the Technische Universität Darmstadt [26].

Bremsstrahlung facilities provide a continuous spectrum of the emitted photons with a steeply increasing intensity at low energies, see section 3.1. For dedicated tasks, in particular for detailed spectroscopy or the "manipulation" of specific nuclear excitations, the usage of energy-tunable (quasi-)monochromatic MeV-range photon beams can be advantageous as compared to bremsstrahlung which produces a high level of low-energy background. Therefore, the development of a quasi-monoenergetic photon-beam source with variable energy was advanced. In 1953, Colgate and Gilbert published first experiments showing the production of photons from positron annihilation in flight [27]. This method was later used, e.g., at the facilities in Saclay [28], Livermore [29] and Giessen [30] to study the photoresponse of atomic nuclei.

Another access to (quasi-)monochromatic excitation of nuclei are tagged photons, i.e., thin-target bremsstrahlung photons with a simultaneous detection of the corresponding decelerated electrons. Work at the photon tagger at the Illinois electron accelerator facility [31–33] has contributed significantly to study the dipole response of nuclei below the neutron binding energies for a broad mass region, see, e.g., Refs. [34–37].

The next major step forward was the idea and technical realization to generate MeV photons by Laser Compton Backscattering (LCB) [38, 39]. In this way, unprecedented intensities of quasi-monoenergetic and fully-polarized photon beams can be produced, see section 3.3. For a recent overview of such sources see Ref. [40]. For a short illustration of major steps in the history see Fig. 1.

2 Formalism of photonuclear reactions

This review article considers the reactions of atomic nuclei to impinging real photons in the energy range between the energy scales of atomic structure and of nuclear structure, i.e., roughly between about 0.1 and 100 MeV. In particular, on the low-energy side, the wavelength of the photon is significantly larger than the nucleus. Since the nucleus carries an electrical charge $+Ze$ it interacts with the photon. Figure 2 provides an overview of a variety of photonuclear reactions that will be discussed below.

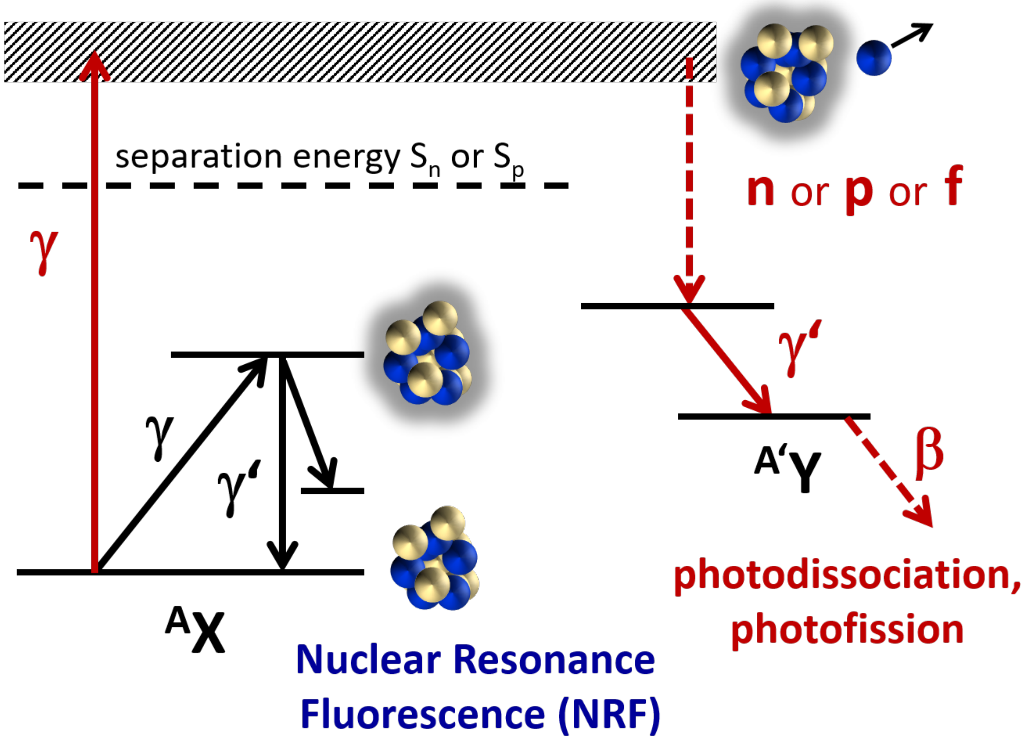

Figure 2: Sketch of typical photonuclear reactions around the particle separation threshold. Either particle-bound nuclear states, initially excited by photon absorption, decay by γ-ray emission representing the phenomenon of Nuclear Resonance Fluorescence, or particle-unbound states may decay by dissociation or fission causing photo-induced nuclear transmutation.

2.1 Elastic Scattering

The photon's elastic scattering off a nucleus can be considered as a relativistic elastic collision with a massive point charge, in analogy to the well-known Compton process for the scattering of a photon with an electron at rest, except that the nucleus has a significantly larger mass than the electron by the factor $A \cdot u/m_e$, where A is the nuclear mass number, $u = 931.5$ MeV/c^2 is the atomic mass unit, and $m_e = 0.511$ MeV/c^2 is the electron mass.

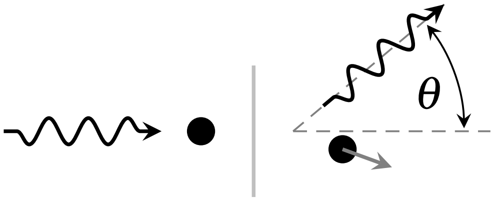

Figure 3: Sketch of an elastic scattering process of a photon off an (inert) nucleus.

Figure 3 shows a sketch of the elastic scattering process. In the elastic scattering at an angle θ, the photon with initial energy E_γ suffers from an energy loss due to the elastic recoil of the nucleus. The scattered photon energy amounts to

$$E_{\gamma'} = \frac{E_\gamma}{1 + \frac{E_\gamma}{Mc^2}(1 - \cos\theta)} = E_\gamma - \Delta E_\gamma(\theta) \tag{1}$$

with a relative energy loss of

$$\Delta E_\gamma / E_\gamma \approx \frac{E_\gamma}{Auc^2}\,(1 - \cos\theta)\,. \tag{2}$$

A typical situation of a photon energy of 5 MeV and a medium heavy nucleus with mass number $A = 50$, which we will consider for order-of-magnitude estimates repeatedly in this article, corresponds to the Thomson regime with $E_\gamma \ll Mc^2$ and $\lambda' \approx \lambda$. The maximum energy loss of the scattered photon amounts in this example to a fraction of 2×10^{-4}, i.e., to 1 keV on backward scattering, $\theta = 180°$.

The probability for such an elastic-scattering event to happen can be estimated in the same way as Klein and Nishina have calculated the cross section for Compton scattering except for that in the Klein-Nishina formula the classical electron radius $r_e = \alpha\hbar c/m_e c^2$ must be replaced by the corresponding expression for the (inert) atomic nucleus $r_A = Z\alpha\hbar c/Mc^2$ [41]. For a linearly-polarized photon scattered elastically off a free, point-like and inert nucleus at rest, the differential cross section is then estimated by

$$\frac{d\sigma}{d\Omega}(\theta,\phi) = \frac{1}{2} r_A^2 \left(\frac{\lambda}{\lambda'}\right)^2 \left[\frac{\lambda}{\lambda'} + \frac{\lambda'}{\lambda} - 2\sin^2\theta\cos^2\phi\right] \approx r_A^2\left[1 - \sin^2\theta\cos^2\phi\right]\ . \tag{3}$$

The approximation on the right hand side makes use of the fact that $\lambda' \approx \lambda$ as discussed above. For an unpolarized photon beam, an average over the azimuthal angle results in

$$\frac{d\sigma}{d\Omega}(\theta) = \frac{1}{2} r_A^2\left[1 + \cos^2\theta\right]\ . \tag{4}$$

This cross section is independent of the photon's energy, indicative for the Thomson regime, and amounts only to a few nanobarn (nb). This is about a billion times smaller than the probability for a Compton-scattering event to happen off any of the electrons in the electron cloud surrounding the nucleus. Therefore, elastic scattering of photons off nuclei is often considered sub-dominant or even negligible.

Up to this point, we have considered the nucleus as a point-like inert object, which of course, it is not. The situation changes dramatically when the internal structure of the nucleus is taken into account. The nucleus contains internal degrees of freedom, has an extended size, and can be polarized in the oscillating electromagnetic field of the passing photon. In particular, the nucleus may feature excited quantum states with lifetimes much longer than the order of 10^{-6} fs, the time scale it takes a photon wave packet of a few MeV to pass the nucleus. When the energy of the photon corresponds to the excitation energy E_x of a quasi-stationary quantum state of the atomic nucleus, the latter can be resonantly excited thereby absorbing the photon.

2.2 Nuclear photoabsorption

2.2.1 Kinematics

The absorption of an incident photon with wavelength λ and energy $E_{\gamma_{\text{in}}} = \hbar\omega = \hbar c/\lambda = cp_\gamma$ induces a recoil on the absorbing nucleus with mass M. The recoil energy $\Delta E_{\text{rec}} = E^2_{\gamma_{\text{in}}}/2Mc^2 + \mathcal{O}[(E_{\gamma_{\text{in}}}/Mc^2)^2]$ is transferred to the nucleus. For an incident photon to be capable of exciting a nucleus initially at rest to an excited quantum state at excitation energy E_x, it must have an energy of $E_{\gamma_{\text{in}}} = E_x + \Delta E_{\text{rec}} \approx E_x\,(1 + E_x/2Mc^2)$. For example, exciting a hypothetical nuclear state at an excitation energy of 5 MeV in a mass-50 nucleus by resonant absorption of an incident photon requires an excess energy of the incident photon of about 0.27 keV, an amount which is much larger than the typical widths of particle-bound nuclear levels.

This energy mismatch is the main reason why γ radiation from radioactive decays cannot easily be used for a re-excitation of other identical nuclei, a process which would be needed, for instance, for the straightforward establishment of a simple γ-ray laser. In his pioneering work on photoabsorption, Moon [42, 43] has overcome this energy mismatch by placing a γ-radiative source on an ultracentrifuge such that the radiation emitted in the direction of a target of identical nuclei has gained a sufficiently large Doppler boost to compensate for that energy mismatch with respect to resonant reabsorption of the γ radiation by identical nuclei in the irradiated target.

In a macroscopic ensemble, such as a target or a radioactive source, the nuclei are never entirely at rest. Thermal motion always leads to some Doppler shift which, averaged over the ensemble, results in Doppler broadening of resonance reactions as will be discussed below. For an order of magnitude estimate, one can consider the thermal energy $1/2\ k_BT$ per degree of freedom which, at room temperature, amounts to about 12 meV. This results in a root-mean-square velocity (in units of the speed of light c) in the direction of motion of the photon of $\beta_{\text{rms}} = \sqrt{<\beta_z^2>} = \sqrt{k_BT/Mc^2}$. This amounts to 7×10^{-7} for a mass-50 nucleus and, thus, leads to an average thermal Doppler-shift of 4 eV for a typical 5-MeV photon in the rest frame of the absorbing nucleus. Thermal motion is, therefore, insufficient to compensate for the photon recoil energy which is about two orders of magnitude larger than thermally induced Doppler shift in the laboratory. But the latter is of the order of or even larger than typical widths of particle-bound nuclear states that participate in nuclear photoabsorption reactions and must, therefore, be taken into account as we will discuss below.

2.2.2 Cross section

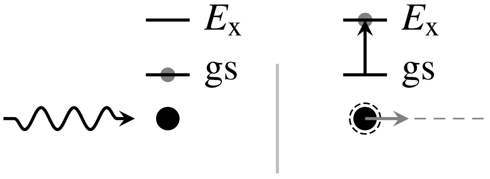

Figure 4: Sketch of a nuclear photoabsorption process of a nucleus initially at rest in its ground state to its excited state at excitation energy E_x.

For discussing the probability of a photoabsorption process to occur, we consider a photoabsorption reaction on a nuclear ground state to an isolated excited nuclear state J with excitation energy E_x as sketched in Fig. 4. At least due to its electromagnetic coupling to the ground state (and eventually due to other decay channels), the excited state must have a finite lifetime τ and a corresponding finite decay width

$$\Gamma = \hbar/\tau = 658.2/(\tau/\text{fs})\ \text{meV}\ . \tag{5}$$

Lifetimes of particle-bound excited nuclear states typically exceed hundreds of attoseconds corresponding to natural line widths in the eV and sub-eV regime. A particle-bound state's decay may be entirely dominated by electromagnetic decay transitions (neglecting weak decays) to lower-lying final states J_f, such that its width

$$\Gamma = \sum_{f,\Pi L} \Gamma_{f,\Pi L} \tag{6}$$

is the sum of all monopolar partial decay widths

$$\Gamma_{f,\Pi L} = 8\pi \frac{L+1}{L\left[(2L+1)!!\right]^2} \left(\frac{E_\gamma}{\hbar c}\right)^{2L+1} B(\Pi L; J^\pi \rightarrow J_f^{\pi_f}) \tag{7}$$

with polarities Π, either electric (E) or magnetic (M), and multipolarities L in agreement with the well-known selection rules for γ radiation

$$|J - J_f| \ \leq L \ \leq J + J_f \tag{8}$$

$$(-1)^L \pi\pi_f \quad = \quad \left\{ \begin{array}{c} +1 \\ -1 \end{array} \right. \text{for} \ \begin{array}{l} \Pi = \ E \\ \Pi = \ M \end{array} \tag{9}$$

to all possible final states J_f. $B(\Pi L; J^\pi \to J_f^{\pi_f}) = |\langle J_f \parallel T(\Pi L) \parallel J\rangle|^2/(2J+1)$ denotes the transition strength of multipolarity ΠL for the $J^\pi \to J_f^{\pi_f}$ γ-ray transition. The ratio of the sub-dominant monopolar partial decay width to the dominant one

$$\frac{\Gamma_{f,\Pi' L+1}}{\Gamma_{f,\Pi L}} = \delta^2_{(f)} \tag{10}$$

equals the square of the multipole mixing ratio

$$\delta_f = (\pm)_{\Pi'} \frac{\sqrt{L(L+2)}}{(L+1)(2L+3)} \frac{E_\gamma}{\hbar c} \frac{\langle J_f \parallel T(\Pi' L+1) \parallel J\rangle}{\langle J_f \parallel T(\Pi L) \parallel J\rangle} \ , \tag{11}$$

where $(\pm)_{\Pi'}$ is (+1) [(-1)] for electric [magnetic] sub-leading multipolarity Π'. Since, on resonance, the cross section scales as $\lambda\!\!\!^-{}^2$, which for a typical 5-MeV photon is of the order of 10 barn, the non-resonant scattering channel is much smaller and can be neglected such that Eq. (3F-13) from Ref. [44]

$$\frac{1}{(2s_1+1)(2I_1+1)} \sum_{h_1 M_1 h_2 M_2} \int_{\Omega_2} d\sigma(1 \to 2) = \frac{2I_r+1}{(2s_1+1)(2I_1+1)} \pi \lambda\!\!\!^-{}_1^2 \frac{\Gamma(1 \to r)\Gamma(r \to 2)}{(E-E_r)^2 + (\Gamma_r/2)^2} \tag{12}$$

from general resonance theory can be applied for obtaining the helicity-averaged and orientation-averaged total resonance-absorption cross section of an unpolarized photon beam impinging on an unpolarized target in its ground state with total angular momentum quantum number J_0 to an isolated excited resonance state. This yields [8]

$$\sigma_a(E) = \frac{2J+1}{2(2J_0+1)} \pi \lambda\!\!\!^-{}^2 \frac{\Gamma_0 \Gamma}{(E-E_r)^2 + (\Gamma/2)^2} = \frac{\sigma_0}{1 + \left(\frac{E-E_r}{\Gamma/2}\right)^2} \tag{13}$$

where it is considered [8] that the incident photon can have only two possible helicities and that the absorption cross section is equal to the sum of the cross sections to all possible final states, *cf.* Eq.(6). Γ_0 denotes the excitation width of the excited state from the ground state which, due to time-reversal symmetry, equals the partial decay width of the excited state to the ground state. The resonance energy E_r takes the nuclear recoil on photoabsorption into account. The on-resonance absorption cross section

$$\sigma_0 \equiv \sigma_a(E_r) = 2\pi g \lambda\!\!\!^-{}^2 \frac{\Gamma_0}{\Gamma} \tag{14}$$

with the commonly-used abbreviation $g = (2J+1)/(2J_0+1)$ for the statistical factor quantifies the maximum of the absorption cross section. For a typical 5-MeV photon and for exclusive decay to the ground state, $\Gamma_0 = \Gamma$, it amounts to hundreds of barns. This is much larger than the cross sections for most of all other possible nuclear reactions, apart from some low-energy neutron-capture or neutron-scattering reactions. The latter share with photon resonance absorption the absence of a Coulomb barrier, and hence possible low energies of the incident particles with large wavelengths and correspondingly large on-resonance cross sections.

At first glance, this large photonuclear absorption cross section may occur counter intuitive, in particular, since its size is independent of the multipolarity of the electromagnetic excitation, apart from the statistical factor which itself is of the order one. However, as indicated above, the width of the resonance is small, and in most cases even smaller than the Doppler shifts induced by thermal motion of nuclei in a sample. Therefore, a high spectral density of the incident photon beam at resonance energy is needed for inducing a substantial amount of photonuclear resonance absorption processes in a given sample and the thermal motion of nuclei in the absorbing material must be taken into account.

Let us first consider that a thin gas of atoms with nuclei of interest is placed as a photoabsorption sample in a photon beam along the z-axis. Equation (13) denotes the photonuclear resonance-absorption cross section in the nucleus' rest frame. However, at temperature T in the laboratory, the thermal velocity components of the nuclei with mass M along the beam direction are Maxwellian distributed according to

$$f(v_z)dv_z = \frac{1}{c}\sqrt{\frac{Mc^2}{2\pi k_B T}}\, e^{-\frac{M}{2}v_z^2/k_B T}\, dv_z \; . \tag{15}$$

Photons with energy E in the laboratory system that are incident on a nucleus moving at thermal velocity v_z in beam direction have a Doppler-shifted energy

$$E' = \left(1 - \frac{v_z}{c}\right)\gamma E \approx \left(1 - \frac{v_z}{c}\right) E \tag{16}$$

in the rest frame of this nucleus. If a nucleus, featuring in its rest frame a photoabsorption resonance at energy E_r, in the laboratory system is moving with velocity v_z in beam direction, it will exhibit in return a photoabsorption resonance at energy $E'_r \approx \left(1 + \frac{v_z}{c}\right) E_r$ which has to be considered in Eq. (13) with the probability given in Eq. (15) for an effective photonuclear resonance-absorption cross section

$$\tilde{\sigma}_a^D(E) = \int_{-\infty}^{\infty} \sigma_a(E)_{E'_r(v_z)} f(v_z) dv_z = \sigma_0 \psi(x,t) \tag{17}$$

on the given sample at temperature T. Besides Eq. (14), we have made use of the notation

$$\psi(x,t) = \frac{1}{2\sqrt{\pi t}} \int_{-\infty}^{\infty} \frac{e^{-\frac{(y-x)^2}{4t}}}{y^2+1} dy \tag{18}$$

with

$$x = \frac{E - E_r}{\Gamma/2}, \qquad y = \frac{E' - E_r}{\Gamma/2}, \qquad t = \left(\frac{\Delta}{\Gamma}\right)^2$$

and the Doppler width

$$\Delta = \sqrt{\frac{2k_B T}{Mc^2}} E_r \; . \tag{19}$$

In the long-lifetime limit $\Gamma \ll \Delta$, Eqs. (17,18) acquire the analytical Doppler form of the effective absorption cross section

$$\sigma_a^D(E) = K e^{-\left(\frac{E-E_r}{\Delta}\right)^2} \tag{20}$$

with the resonance-absorption attenuation coefficient

$$K = \sigma_a^D(E_r) = \frac{\sqrt{\pi}}{2}\sigma_0 \frac{\Gamma}{\Delta} \; . \tag{21}$$

Figure 5 provides a comparison between the resonance-absorption cross section in the nucleus' rest frame σ_a [Eq. (13)], the effective resonance absorption cross section in a target ensemble $\tilde{\sigma}_a^D$ [Eq. (17)], and its Doppler-form approximation σ_a^D [Eq. (20)] for the two situations $\Gamma = \Delta/10$, for which the Doppler cross section is a good approximation to the effective resonance-absorption cross section, and $\Gamma = \Delta$ for which this is not the case. Situations of $\Gamma \approx \Delta$ are rarely encountered, but nevertheless do occur, see e.g. [45–47].

The amount of radioactivity generated by photonuclear resonance absorption due to a given nuclear state in a thin sample exposed to a photon flux[1] $N_\gamma(E)$ is then proportional to the integral of the product of photon flux and absorption cross section over the energy

$$A \propto \int N_\gamma(E)\tilde{\sigma}_a^D(E)dE \ . \tag{22}$$

In many situations, the photon flux near resonance can be considered constant or at least linear, $N_\gamma(E) = N_\gamma(E_r) + dN_\gamma/dE(E_r)\cdot(E-E_r)$ to a good approximation over the effective width of a resonance. In such cases, it can be taken out of the integral with its value at resonance energy, $N_\gamma(E_r)$, because $\tilde{\sigma}_a^D(E)$ is an even function of the γ-ray energy around the resonance energy E_r, yielding

$$A \propto N_\gamma(E_r)\int \tilde{\sigma}_a^D(E)dE = N_\gamma(E_r)I_a \ . \tag{23}$$

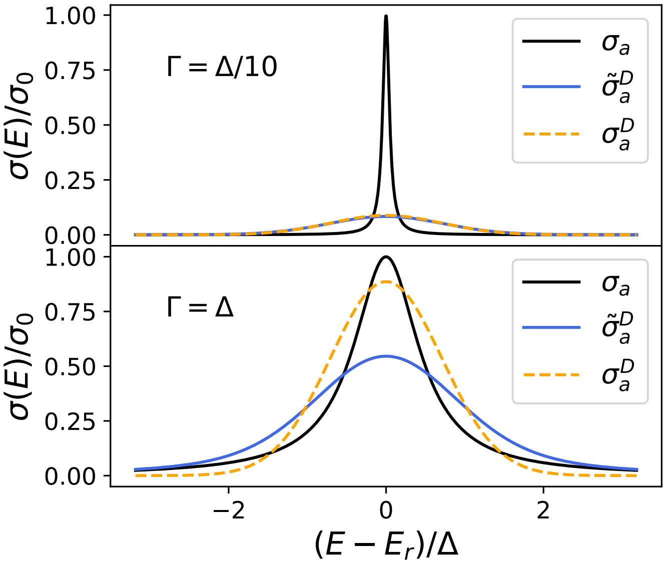

Figure 5: Photonuclear absorption cross sections $\sigma(E)/\sigma_0$ in the nuclear rest frame (black,solid), in its effective form for a target ensemble (blue, solid), and in its Doppler approximation (orange, dashed) in the energy interval around resonance energy in units of the Doppler width for two cases $\Gamma = \Delta/10$ (top) and $\Gamma = \Delta$ (bottom).

The integration of the cross section over the energy is independent of the details of the motion of the nuclei. It can be performed analytically on either form, Eq. (17) or Eq. (20), providing the energy-integrated absorption cross section

$$I_a = \int \tilde{\sigma}_a^D(E)dE = \int \sigma_a^D(E)dE = \frac{\pi}{2}\sigma_0\Gamma = g\pi^2\left(\frac{\hbar c}{E_r}\right)^2\Gamma_0 \ . \tag{24}$$

It is an experimentally well-accessible quantity when a photon beam with bandwith $\gg 10^{-5}$ is used on a thin target, i.e., when the curvature of the energy-dependence of the photon flux over the width of the resonance and when the decrease of photon flux around resonance energy due to previous absorption reactions in upstream layers of the target can be neglected to good approximation. The integrated cross section plays, thus, a central role in the phenomenon of Nuclear Resonance Fluorescence which will be discussed in the following subsection 2.3. Before we do this, let us first consider situations when the thin-target approximation is no longer valid and the formation of an absorption line needs to be taken into account which gradually reduces the photon flux at resonance energy along the path of the photon beam through the target.

---

[1] In the literature one encounters a variety of quantities that are addressed as 'photon flux'. In most cases, the energy-resolved, spectral photon-flux, $N_\gamma(E)$, incident on a target over the course of an experimental run in units of [#photons/(eV)] is meant. It represents the spectral density accumulated over the measurement time and over the surface of the target. For energy-resolved quantities we use the term 'spectral' while we reserve the term 'density' for spatial resolution. Some discussions require the consideration of the spectral photon-current density, $d^3N_\gamma/dE\,dA\,dt = n_\gamma(E,\sigma,t)$ in units of [#photons/(eV cm^2 s)], of the spectral photon-current, $d^2N_\gamma/dE\,dt = \dot{N}_\gamma(E,t)$ in units of [#photons/(eV s)], or of the spectral fluence density $d^2N_\gamma/dE\,dA$ in units of [#photons/(eV cm^2)]. All of them are occasionally addressed as 'photon flux'. The actual meaning is usually clear from the context and the units.

2.2.3 Self Absorption

The thin-target approximation requires that the absorption cross section at resonance, $\tilde{\sigma}_a^D(E_r)$, times the areal density of resonance-scattering centers in the target is negligible, i.e., when

$$\bar{n}\tilde{\sigma}_a^D(E_r) = \bar{n}\frac{\sqrt{\pi}}{2}\sigma_0\frac{\Gamma}{\Delta} \ll 1 \ . \tag{25}$$

The areal number density of target-scattering centers is given by

$$\bar{n} = \frac{\rho_t d}{\mu_{\mathrm{mol}}} N_A = \frac{M_t}{\mu_{\mathrm{mol}} A_t} N_A \tag{26}$$

with ρ_t, M_t, A_t, d, and μ_{mol} being the density, mass, area, thickness along the beam direction, and molar mass of the target, respectively. As an order of magnitude estimate, one obtains for a strongly absorbing resonance with $\Gamma_0 \approx \Gamma \approx \Delta$ and $E_r \approx 5$ MeV, that the thin-target approximation discussed above may no longer be valid anymore at areal densities of a few 10^{-2} scattering centers per barn. This corresponds to target thicknesses d exceeding already a few mm for solid targets with typical molar densities $\rho_t/\mu_{\mathrm{mol}} \approx 10^{-1}\ \mathrm{cm}^{-3}$. Such thicknesses of photonuclear reaction targets are not uncommon, and hence the experimentalists may need to check carefully for the validity of the thin-target approximation or, in turn, for the occurrence of self-absorption effects, in particular, for strongly absorbing resonances. Apart from the target thickness d and the value of the on-resonance absorption cross section σ_0, the thin-target criterion in Eq. (25) is proportional to the ratio of the level width Γ to the Doppler width Δ of the resonance which was introduced in Eq. (19) for a gaseous target. For solid targets, the probability distribution of nuclear thermal motion and its dependence on the temperature might be more complicated than that because of the binding of the target atoms in the lattice of the solid. The details depend on the precise structure of the target material and can be taken into account by solid-state theory [45].

Effective temperature In the discussion of photonuclear resonance absorption in solids, Metzger has pointed out that the formalism introduced previously by Lamb in the context of slow-neutron resonance scattering is applicable [8]. In particular, Lamb has shown that the absorption line in a solid at thermodynamical temperature T has the same form as in a gaseous target at a higher, effective temperature T_{eff} provided that the solid can be approximately described as a Debye continuum with Debye temperatur Θ_D and that the lattice binding is weak, thus fulfilling the condition $\Gamma + \Delta \gg 2k_B\Theta_D$ [48]. In this situation, the Doppler width to be considered in the effective absorption cross section $\tilde{\sigma}_a^D(E)$ is given by the expression

$$\Delta = \sqrt{\frac{2k_B T_{\mathrm{eff}}}{Mc^2}} E_r \tag{27}$$

with the effective temperature

$$T_{\mathrm{eff}} = 3\left(\frac{T}{\Theta_D}\right)^3 T \int_0^{\Theta_D/T} t^3 \left(\frac{1}{e^t - 1} + \frac{1}{2}\right) dt \ . \tag{28}$$

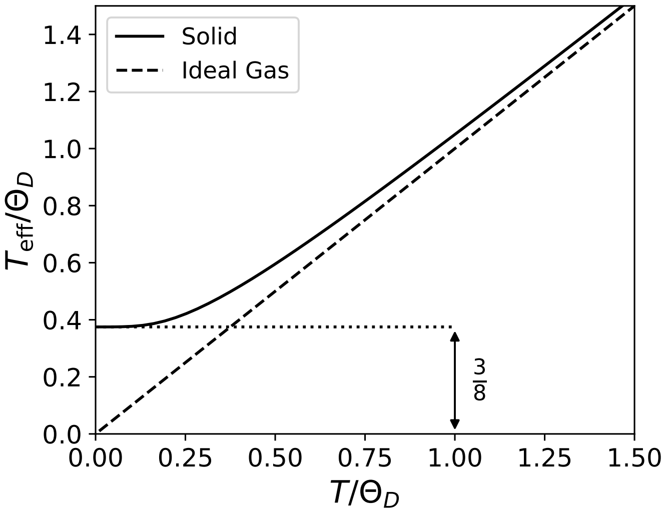

Figure 6: Effective temperature of the thermal motion of nuclei in a solid in units of its Debye temperature as a function of the thermal temperature in the same units according to Eq. (28).

It is a monotonically increasing function of the thermodynamical temperature T with the limits $T_{\text{eff}} = T$ for large thermodynamical temperatures $T \gg \Theta_D$ and $T_{\text{eff}} = 3/8\,\Theta_D$ for low temperatures $T \to 0$. The effective temperature is plotted versus the thermodynamical temperature, both in units of Θ_D, in Fig. 6.

For targets of typical metals with Debye temperatures of a few hundred K and at ambient temperatures, their effective temperatures range usually from 300 to 400 K. This results for a photonuclear absorption resonance at 5 MeV excitation energy in a typical $A = 50$ nucleus in a Doppler width of about 5 eV. Hence, the Doppler width, across which about 2/3 of the resonance-absorption strength is spread out due to thermal motion, is usually significantly larger than the level width Γ. This is the reason for the fact that even for an infinitely narrow bandwidth photon beam incident on a macroscopic solid target, which is even cooled down to low temperatures, the absorption process with high multipolarity and correspondingly small excitation width Γ_0 will be very small. At any energy, the effective absorption cross section [Eq. (20)] is proportional to the resonance-absorption attentuation coefficient $K \propto \Gamma_0/\Delta \ll 1$, despite the fact that the on-resonance absorption cross section σ_0 on a single nucleus does not depend on its multipolarity and is as large as hundreds of barns.

Local photon-flux density The photon beam incident on the target may be characterized by its spectral photon-current density $n_\gamma(E, \sigma, t)$, which most commonly is given in units of photons per $(\text{eV}\,\text{cm}^2\,\text{s})$, where σ denotes here the two-dimensional coordinate on the target surface perpendicular to the beam axis. On traversal through the target the beam is attenuated by several absorption processes. Only within a few Doppler widths around a nuclear resonance, i.e., typically within a few dozens of eV, nuclear absorption can compete with atomic absorption being dominated itself by Compton scattering and positron-electron pair production. Their variation as a function of energy over a few dozens of eV is very small and can be neglected to good approximation when the energy modulation due to self absorption near resonance is studied. Atomic attenuation therefore contributes a nearly constant attenuation as a function of energy of the incident photon beam with close-to-resonance energies. Nuclear resonance absorption adds a narrowly modulated attenuation on top of it. When we consider, for simplicity, spatially homogenous targets with homogenous values of the areal number density $\bar{n}(\sigma) \equiv \bar{n}$ over its surface along the beam axis and denote the local target penetration depth by $\mathcal{Z} \in [0, \bar{n}]$ in scattering centers per barn, then the spectral density at penetration depth $\mathcal{Z}$ has evolved into the form

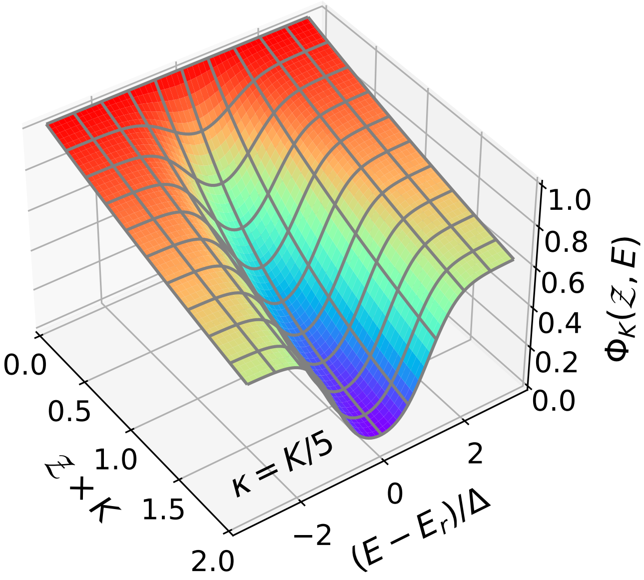

Figure 7: Normalized photon flux density at a nuclear resonance, Eq. (30), as a function of target-penetration depth $\mathcal{Z}$ times the resonance-absorption attenuation coefficient of the given resonance and as a function of the incident γ energy in units of the resonance's Doppler width.

$$N_\gamma(\mathcal{Z}, E) = N_\gamma(E) e^{-(\kappa + \tilde{\sigma}_a^D(E))\mathcal{Z}} dE \tag{29}$$

with the atomic attenuation cross section κ including, e.g., the Compton scattering and pair production cross sections. In cases of $\Gamma \ll \Delta$ when the resonance-absorption cross section can be well approximated by its Doppler from, then the normalized photon-flux density at penetration depth $\mathcal{Z}$ takes the analytical form

$$\Phi_K(\mathcal{Z},E) = \frac{N_\gamma(\mathcal{Z},E)}{N_\gamma(0,E_r)} = e^{-(\kappa+Ke^{-x^2})\mathcal{Z}} \ . \tag{30}$$

with $x = (E - E_r)/\Delta$ being here the incident γ energy around resonance in units of the Doppler width. As an example, the generic shape of the photon-flux density is plotted in Fig. 7 for an assumed ratio of the atomic absorption coefficient to the resonance-absorption attenuation coefficient of 1/5.

Resonance-absorption density Also at penetration depth $\mathcal{Z}$ the contribution to the radioactivity induced by resonance absorption in a target layer with thickness $d\mathcal{Z}$ is increased according to Eq. (22) where the energy dependence of the photon flux must now be considered. It amounts to

$$\begin{aligned} dA(\mathcal{Z}) \ &\propto \ \int N_\gamma(\mathcal{Z},E)\tilde{\sigma}_a^D(E)dE\, d\mathcal{Z} & (31)\\ &\approx \ N_\gamma(E_r)\int \alpha_K(\mathcal{Z},E)dE\, d\mathcal{Z} & (32)\end{aligned}$$

with the resonance-absorption density

$$\begin{aligned} \alpha_K(\mathcal{Z},E) \ &= \ \Phi_K(\mathcal{Z},E)\sigma_a^D(E) & (33)\\ &= \ Ke^{-(\kappa+Ke^{-x^2})\mathcal{Z}-x^2} \ , x = \frac{E-E_r}{\Delta} \end{aligned}$$

in the Doppler approximation. The generic shape of the resonance-absorption density is plotted in Fig. 8.

The phenomenon of the depletion of resonance absorption with increasing penetration depth into the target due to the development of the γ-ray absorption line is addressed as *self absorption*. Its evolution as a function of penetration depth depends strongly on the resonance-absorption coefficient K [Eq. (21)] and is strongest for resonances with large values of the ratio between the excitation width and the Doppler width Γ_0/Δ. A measurement of this depletion can, therefore, provide a direct measurement of the excitation width provided that the Doppler width is known, which itself depends on temperature via the atomic binding in the target material.

For experimental purposes, it can be useful to limit the amount of self absorption in a sample under study to a desired value. As a criterion, one may consider the *half-absorption penetration depth* $\mathcal{Z}_{1/2}$ where the resonance absorption has decreased by a factor of two compared to its value at the front of the sample. Neglecting atomic absorption, i.e., for $\kappa \ll K$ which is often the case, one finds

$$\mathcal{Z}_{1/2} \approx 1/K = \frac{1}{\sqrt{\pi^3}g}\left(\frac{E_r}{\hbar c}\right)^2 \frac{\Delta}{\Gamma_0} \ . \tag{34}$$

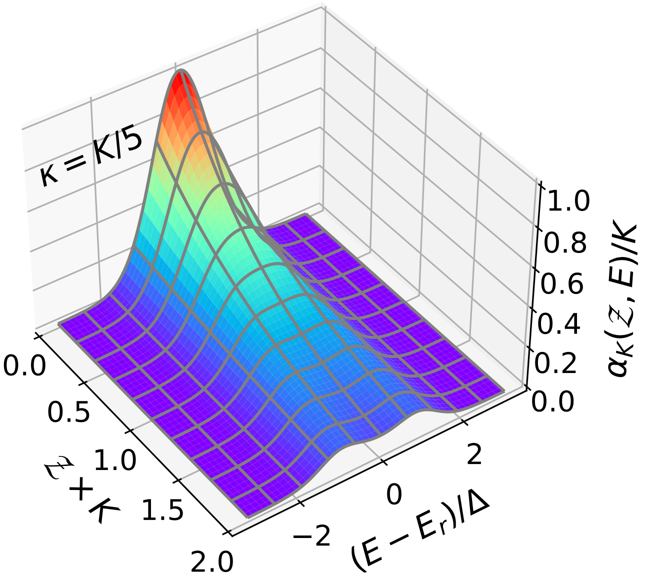

Figure 8: Normalized resonance-absorption density at a nuclear resonance, Eq. (33), as a function of target-penetration depth $\mathcal{Z}$ times the resonance-absorption attenuation coefficient of the given resonance and as a function of incident γ-energy in units of the resonance's Doppler width.

This half-absorption penetration depth depends, of course, strongly on the level's excitation width and on the actual target material, its isotopic enrichment etc. For a typical nuclear dipole excitation at 5 MeV in an even-even $A = 50$ nucleus in a metal target, it can amount in practical cases to about 0.1 nuclei per barn. This may correspond to geometric target thicknesses on the order of cm, however, with the above mentioned dependences.

2.3 Nuclear Resonance Fluorescence

The phenomenon of a photonuclear two-step process, consisting of the resonant absorption of an electromagnetic quantum by an atomic nucleus and the subsequent re-emission of γ radiation, represents a resonant photon-scattering reaction (γ, γ') on a nucleus, as illustrated to the lower left in Fig. 2. It is called Nuclear Resonance Fluorescence (NRF), in analogy to the well-known optical phenomenon of visible fluorescence shown by molecules. The wavelength and intensity of the nuclear fluorescence, its time delay, and angular distribution are governed by the properties of the nuclear quantum states involved in this process.

This subsection provides the formalism for a quantitative description of NRF after the first step, the photonuclear resonance absorption, discussed in the previous subsection 2.2, has happened. It includes the accessible nuclear observables and practical considerations for the performance of experiments applying the NRF method or exploiting possible applications.

The radioactivity induced by the resonance-absorption processes discussed above subsequently leads to decays into the accessible final states f according to the decay branching ratios Γ_f/Γ. The energy- and angle-integrated cross section for NRF of a level with angular momentum quantum number J into its exclusive decay channel to a specific final state J_f then amounts to

$$I_{s,f} = I_a \frac{\Gamma_f}{\Gamma} = \frac{\pi}{2}\sigma_0 \Gamma_f = g\pi^2 \left(\frac{\hbar c}{E_r}\right)^2 \frac{\Gamma_0 \Gamma_f}{\Gamma} \; . \tag{35}$$

It is customary in the literature to address this quantity in short as 'integrated cross section'. It is also customary, although not fully precise, to denominate the NRF process with a direct decay back to the initial state, i.e., $J_f = J_0$ and $\Gamma_f = \Gamma_0$ as 'elastic scattering' and the corresponding γ-ray transition with energy $E_{\gamma'} = E_r$, neglecting the small recoil energy, as the 'elastic transition', and $I_{s,0}$ as the 'elastic (NRF) cross section'. Consequently, NRF transitions to final excited states with γ-ray energies $E_{\gamma'} < E_r$ are in contrast often addressed as 'inelastic transitions'. The observable NRF intensity $\mathcal{I}_{s,f}$ depends on the luminosity of the resonance-absorption reaction and on the angular distribution. In the thin-target approximation, it is given by

$$\mathcal{I}_{s,f}(\theta, \phi) = \dot{N}_\gamma(E) \bar{n} I_{s,f} \frac{W(\theta, \phi)}{4\pi} \tag{36}$$

and can be detected with appropriate γ-ray detectors located at polar and azimuthal scattering angles, θ and ϕ, with respect to the incident photon beam axis and its polarization plane, respectively. W denotes the normalized angular distribution function.

2.3.1 Angular distribution

The angular distribution function $W(\theta, \phi)$ of the intensity of the photon scattering reaction about a linearly-polarized incident photon beam with degree of polarization P_γ is equivalent [11, 49] to a correlation function of a direction-polarization correlation and can be expanded in terms of Legendre polynomials. In the absence of parity violation and third order multipole contributions for the

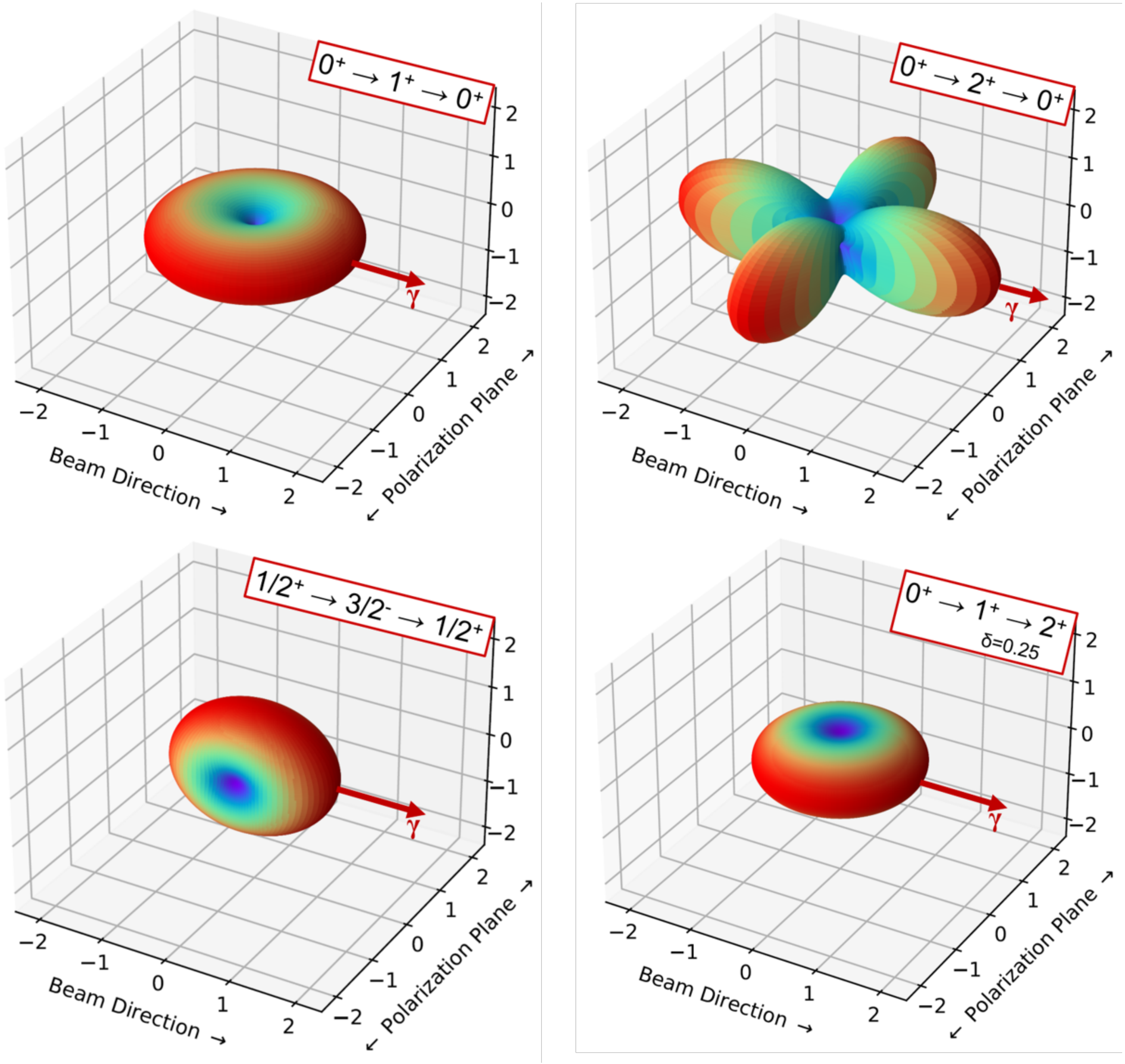

Figure 9: 3-D plots of the angular distribution of $(\vec{\gamma}, \gamma')$ NRF intensity about a fully linearly polarized photon beam ($P_\gamma = 1$) entering from the left for the spin-parity sequences $0^+ \rightarrow 1^+ \rightarrow 0^+$ (top left, both transitions pure $M1$), $0^+ \rightarrow 2^+ \rightarrow 0^+$ (top right, both transitions pure $E2$), $1/2^+ \rightarrow 3/2^- \rightarrow 1/2^+$ (bottom left, both transitions pure $E1$), and $0^+ \rightarrow 1^+ \rightarrow 2^+$ (bottom right, first transition pure $M1$ and second transition 94% $M1$ and 6% $E2$). The distinct shapes of the angular distributions as a function of the spin cascades and the multipolarities of the transitions typically allow for the unique assignment of spin and parity quantum numbers J^π and of multipole mixing ratios δ if the statistical uncertainties are small enough.

$J_0^{\pi_0}(L_1, L_1')J^{\pi_x}(L_2, L_2')J_f^{\pi_f}$ cascade, it can be written as

$$W(\theta, \phi) = \sum_{\nu=0}^{\text{even}} B_\nu(\vec{\gamma}_1) A_\nu(\gamma_2) P_\nu(\cos\theta) + (\pm)_{L_1} P_\gamma \cos(2\phi) \sum_{\nu=2}^{\text{even}} B'_\nu(\vec{\gamma}_1) A_\nu(\gamma_2) P_\nu^{(2)}(\cos\theta) \tag{37}$$

where P_ν and $P_\nu^{(2)}$ denote the ordinary and the unnormalized associated Legendre polynomial of νth order. Here, $(\pm)_{L_1}$ takes on the value +1 (-1) in case of electric (magnetic) character of the leading multipole L_1 of the first transition. Using the phase convention of Krane, Steffen, and Wheeler [50] for the multipole mixing ratios δ_1 and δ_2, the expansion coefficients A, B, and B' can be written in terms of tabulated F-coefficients [50] as derived in Ref. [51]

$$\begin{aligned} A_\nu(\gamma_2) &= \frac{1}{1+\delta_2^2}[F_\nu(L_2, L_2, J_f, J) + 2\delta_2 F_\nu(L_2, L_2', J_f, J) + \delta_2^2 F_\nu(L_2', L_2', J_f, J)] \quad (38) \\ B_\nu(\vec{\gamma}_1) &= \frac{1}{1+\delta_1^2}[F_\nu(L_1, L_1, J_0, J) - 2\delta_1 F_\nu(L_1, L_1', J_0, J) + \delta_1^2 F_\nu(L_1', L_1', J_0, J)] \quad (39) \end{aligned}$$

and

$$B_\nu'(\vec{\gamma}_1) = \frac{1}{1+\delta_1^2}[\kappa_\nu(L_1, L_1)F_\nu(L_1, L_1, J_0, J) + 2\delta_1\kappa_\nu(L_1, L_1')F_\nu(L_1, L_1', J_0, J) - \delta_1^2\kappa_\nu(L_1', L_1')F_\nu(L_1', L_1', J_0, J)] \quad (40)$$

where δ_1 and δ_2 are the multipole mixing ratios [Eq. (11)] of the exciting and the deexciting NRF transitions, respectively. The κ coefficients can be found in Ref. [52]. For the most important cases of dipole and quadrupole radiation, their values are $\kappa_2(1,1) = -1/2, \kappa_2(1,2) = -1/6, \kappa_2(2,2) = 1/2$, and $\kappa_4(2,2) = -1/12$ (see Ref. [52]).

The angular distribution function for NRF intensity for the ground-state decay of a dipole excitation to a $J = 1$ state with parity π_x in an even-even nucleus, i.e., with a $0^+ \xrightarrow{\vec{\gamma}} 1^{\pi_x} \xrightarrow{\gamma} 0^+$ spin cascade, about a linear-polarized incident photon beam with degree of polarization P_γ is given, for example, by the expression

$$\begin{aligned} W_{0-1-0}(\vartheta, \phi) &= 1 + \frac{1}{2}\left[P_2(\cos\vartheta) + \frac{1}{2}\pi_x P_\gamma \cos(2\phi) P_2^{(2)}(\cos\vartheta)\right] \\ &= \frac{3}{4}\left[1 + \cos^2(\vartheta) + \pi_x P_\gamma \cos(2\phi)\sin^2(\vartheta)\right] \ . \end{aligned} \quad (41)$$

Further analytical expressions for angular distribution functions of NRF intensities are provided in Appendix A for a comprehensive variety of spin sequences. Figure 9 provides plots of four relevant angular distributions as examples.

Up to now, we have discussed NRF angular distributions about linearly-polarized photon beams. The NRF angular distribution functions about circularly-polarized photon beams are, in absence of any parity violation, identical to those about unpolarized beams that have been discussed above. Situations where weak-interaction contributions to the nuclear Hamiltonian lead to parity-violation, e.g., due to the mixing of close-lying parity doublets, can result in forward-backward asymmetries of the NRF angular distribution [53]. Searches for forward-backward asymmetries of NRF intensities have, therefore, been proposed as a possible approach towards the detection of parity-violating contributions to the nuclear Hamiltonian [53, 54].

2.3.2 Polarimetry

The interpretation of nuclear structures generating pronounced NRF signals usually requires information on their polarity and, hence in most cases, on the parity quantum numbers of the excited nuclear states. Assignments of parity quantum numbers from NRF can be performed based on the polarization of at least one of the γ quanta involved. Either a polarized photon beam must be used in the entrance channel or polarization must be measured in the exit channel. The latter was frequently done, see, e.g. Refs. [11,55], using Compton polarimeters until the advent of intense polarized MeV-range photon beams from LCB processes. However, Compton polarimetry is difficult at γ-transition energies exceeding 4

MeV because the analyzing power of the Compton scattering process is energy dependent and becomes prohibitively small at these energies.

Using polarized photons in the entrance channel and measuring the intensity distribution with respect to the polarization plane of the beam is preferable for parity measurements in NRF experiments. In many important cases, such as ground-state decay transitions of $J = 1$ states of even-even nuclei, the analyzing power of this process is 100% and independent of the energy of the γ-ray transition. Therefore, already modest counting statistics can suffice to make parity assignments in these cases, and in addition the measurement of NRF intensity is comparatively simple. This method has mostly been applied for polarimetry in NRF measurements since about the turn of the century. We will, thus, restrict our discussion to this method. Off-axis bremsstrahlung can provide partially-polarized photon beams that have been and are still used at some facilities, e.g., γELBE at the Helmholtz-Zentrum Dresden-Rossendorf (HZDR). The following formulation is applicable also in those cases.

The analyzing power of a polarimetric reaction is in general defined as the normalized asymmetry of observables that is ideally sensitive to the quantity of interest, i.e.,

$$\Sigma = \frac{\mathcal{I}_{s,f}(\theta_1, \phi_1) - \mathcal{I}_{s,f}(\theta_2, \phi_2)}{\mathcal{I}_{s,f}(\theta_1, \phi_1) + \mathcal{I}_{s,f}(\theta_2, \phi_2)} \ . \tag{42}$$

The ideal asymmetry sensitive to the polarity $(\pm)_{L_1}$ of the leading multipole of the absorbed γ radiation, cf. Eq. (37), is achieved for a maximum polarized beam $P_\gamma = 1$, for the angles $\phi_1 = 0$ and $\phi_2 = 90^\circ$ because of the $\cos(2\phi)$-dependence of the NRF intensity, and in most cases for $\theta_1 = \theta_2 = 90^\circ$ because of its forward-backward symmetry when a linearly-polarized photon beam scatters off an unpolarized target. Thus, the analyzing power of the $J_0^{\pi_0} \xrightarrow{\vec{\gamma}} J^{\pi_x} \xrightarrow{\gamma} J_f^{\pi_f}$ NRF cascade in a fully polarized beam is given by

$$\Sigma = \frac{W(90^\circ, 0^\circ) - W(90^\circ, 90^\circ)}{W(90^\circ, 0^\circ) + W(90^\circ, 90^\circ)} = (\pm)_{L_1} \frac{\sum_{\nu=2}^{\text{even}} B'_\nu(\vec{\gamma}_1) A_\nu(\gamma_2) P_\nu^{(2)}(0)}{\sum_{\nu=0}^{\text{even}} B_\nu(\vec{\gamma}_1) A_\nu(\gamma_2) P_\nu(0)} \in [-1, 1] \ . \tag{43}$$

For the frequent case of a dipole-excited state of an even-even nucleus, this results in the maximum possible analyzing power

$$\Sigma = -(\pm)_{L_1} = \pi_x = \left\{ \begin{array}{c} +1 \\ -1 \end{array} \text{for} \begin{array}{c} J^\pi = 1^+ \\ J^\pi = 1^- \end{array} \right. \ . \tag{44}$$

For a partially polarized beam with $P_\gamma < 1$, as for instance provided by off-axis bremsstrahlung, the experimental asymmetry is reduced proportional to P_γ. An experimental setup with a finite polarization sensitivity $Q \leq 1$, e.g., due to finite opening angles of detectors, and with an intrinsic instrumental asymmetry a, is capable of detecting the polarization asymmetry

$$\epsilon = \frac{N(90^\circ, 0^\circ) - aN(90^\circ, 90^\circ)}{N(90^\circ, 0^\circ) + aN(90^\circ, 90^\circ)} = QP_\gamma \Sigma \in [-1, 1] \ . \tag{45}$$

Instrumental asymmetries a can be calibrated by using unpolarized or fully circularly-polarized photon beams for which the RHS of Eq. (45) vanishes. Then, the polarization sensitivity Q needs to be calibrated on a signal with a known analyzing power defined in Eq. (44). In contrast to Compton polarimeters, the polarization sensitivity of an intensity measurement about a fully polarized photon beam can be close to 100% independently of the γ-ray energy. NRF polarimetry about a fully-polarized photon beam can, therefore, be a very sensitive method for the assignment of the polarity of a given γ-ray transition and, hence, of parity quantum numbers of photoexcited nuclear levels of interest. Its figure-of-merit, usually defined as the absolute detection efficiency times the square of the polarization sensitivity of the setup, can be three orders of magnitude larger than the one for Compton polarimetry, reducing the necessary measurement time from factually a few weeks [11] to a few hours [51].

Besides the spin and parity quantum numbers of the involved nuclear states, the NRF angular distributions [Eq. (37)] and asymmetries [Eq. (45)] depend on the multipole mixing ratios δ_i defined in

Eq. (11). Consequently, they can be used to measure subdominant multipole components to the studied NRF γ-ray transitions [56].

2.3.3 Standard NRF experiments

A variety of NRF experiments that have been reported over the last few decades made use of intense artificial photon beams in the MeV range irradiating samples of interest and employed γ-ray spectrometers placed around the sample that detect the NRF signals with some energy resolution. The peak areas of the full-energy signals are given by

$$A_f = \epsilon_\gamma(E_{\gamma_f}) N_\gamma(E_r) I_{s,f} \frac{W(\vartheta,\phi)}{4\pi} \tag{46}$$

in the thin-target approximation, where ϵ_γ is the total full-energy detection efficiency of the γ-ray detector located at observation angles ϑ and ϕ. All other quantities were introduced above. Usage of thick targets can complicate the analysis because they might modify the detected peak areas with respect to Eq. (46) due to self-absorption effects and due to subsequent atomic absorption of NRF signals.

The primary observables comprise (*i*) energies, (*ii*) intensities, (*iii*) angular distributions, and since recently even (*iv*) $\gamma\gamma$-coincidence relations of NRF signals. The combination of these observables enables the experimentalists to deduce a suite of precious spectroscopic quantities, depending on the details of the chosen setup. They include

- γ-ray transition energies E_γ
- level energies E_x and placements of γ-ray transitions in the nuclear level scheme
- multipolarities ΠL of γ-ray transitions
- spin quantum numbers J of nuclear levels
- parity quantum numbers π of nuclear levels
- γ-decay branching ratios Γ_f/Γ_i
- K-quantum numbers of nuclear levels
- multipole-mixing ratios δ of γ-ray transitions
- integrated photonuclear resonance cross sections $I_{s(,f)}$
- partial decay widths $\Gamma_{f,\Pi L}$
- total level widths Γ
- level lifetimes τ
- reduced excitation strengths $B(\Pi L; \mathrm{gs} \rightarrow J^\pi)$
- decay transition strengths $B(\Pi L; J^\pi \rightarrow J_f^{\pi_f})$.

Usage of incident quasi-monochromatic beams can be very sensitive to spectroscopic information while precision measurements of cross sections and quantities deduced from them can be facilitated by wide band-width continuous-energy beams because their slowly-varying energy dependence can be easier to calibrate at the current state of the art. Some methodological examples for measurements of these quantities will be provided in subsection 2.3.6.

A combination of NRF experiments using polarized narrow band-width beams from LCB processes and continuous-energy bremsstrahlung can powerfully remove spectroscopic ambiguities such as adulterated NRF intensities due to unobserved feeding from simultaneously photo-excited higher-lying energy levels.

2.3.4 Average quantities

Usage of quasi-monochromatic beams can also provide valuable information in situations where NRF signals from individual quantum states cannot be resolved anymore due to too narrow level spacings because of too high level densities. Average decay properties from the narrow regions of excitation energies investigated with quasi-monoenergetic incident photon beams have been successfully considered in such situations.

For instance, photoabsorption cross sections $\sigma_\gamma = \sigma_{\gamma\gamma} + \sigma_{\gamma\gamma'}$ can be determined for different excitation energy bins defined by the narrow band-width of the impinging LCB photon beam. The method is illustrated in Fig. 10. Following resonant photoabsorption (black arrow), the observation of all ground-state decays including resolved and unresolved transitions [green arrows in Fig. 10.a)] is connected to the so-called elastic cross section

$$\begin{aligned}\sigma_{\gamma\gamma} &= \frac{\sum_x I_{0\to x\to 0}}{\Delta E} \\ &= \frac{1}{N_T N_\gamma^{tot}} \cdot \sum_x \frac{A_{0\to x\to 0}}{\int\limits_{\Delta\Omega} \mathrm{d}\Omega \; \varepsilon(E_x,\Omega) W_{0\to x\to 0}(\Omega)} \, ,\end{aligned} \tag{47}$$

with $N_\gamma^{tot} = \int N_\gamma(E)\,\mathrm{d}E$ being the energy-integrated total photon flux. The complete intensity is determined from the sum over ground-state transitions from all excited states x in a given excitation-energy window ΔE whether they are observed as resolved peaks or are located in the quasi-continuum.

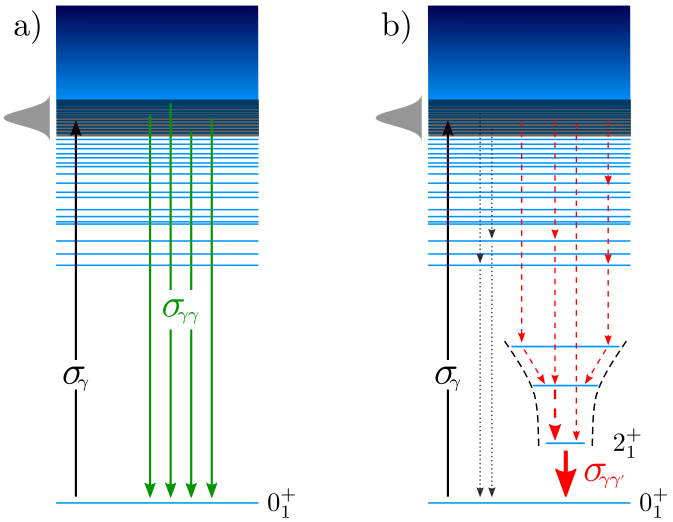

Figure 10: Experimental approach to extract photoabsorption cross sections ($\sigma_\gamma = \sigma_{\gamma\gamma} + \sigma_{\gamma\gamma'}$) with quasi-monochromatic photon beams. a) The elastic cross section $\sigma_{\gamma\gamma}$ is obtained by observation of all (including unresolved) ground-state transitions (green solid arrows). b) The inelastic cross section is estimated by the decay intensities of low-lying states (red solid arrow) collecting the majority of all cascades via intermediate levels (red dashed arrows). Transitions potentially bypassing the first few low-lying states are indicated (grey dotted arrows). Reprinted figure with permission from [57]. Copyright 2021 by the American Physical Society.

In analogy to the elastic decay channel, all cascades from excited states x decaying via intermediate levels i can be summarized in the inelastic cross section

$$
\begin{aligned}
\sigma_{\gamma\gamma'} &= \frac{\sum_x \sum_{i\neq 0} I_{0\to x\to i}}{\Delta E} \\
&= \frac{1}{N_T N_\gamma^{tot}} \cdot \sum_x \sum_{i\neq 0} \frac{A_{0\to x\to i}}{\int\limits_{\Delta\Omega} \mathrm{d}\Omega\ \varepsilon(E_x - E_i, \Omega) W_{0\to x\to i}(\Omega)} \\
&\approx \frac{1}{N_T N_\gamma^{tot}} \cdot \sum_j \frac{A_{2_j^+\to 0_1^+}}{\int\limits_{\Delta\Omega} \mathrm{d}\Omega\ \varepsilon(E_{2_j^+}, \Omega)\, W_{2_j^+\to 0_1^+}(\Omega)}\ .
\end{aligned}
\tag{48}
$$

In the last approximation, it is assumed that a large fraction of the cascades decay via low-lying levels, i.e., mainly 2_j^+ states [58]. This funnel-like effect is sketched in Fig. 10.b). Consequently, the inelastic cross section is estimated by the sum of the ground-state decay intensities of the respective 2_j^+ levels, which contain most of the cascading transition intensities directly related to $\sigma_{\gamma\gamma'}$. In principle, it is possible that a certain fraction of the cascades bypass the first few low-lying states [grey dashed arrows in Fig. 10.b)] and, thus, leading to an underestimation of $\sigma_{\gamma\gamma'}$. Statistical model simulations have been used to estimate the missing part, which depends on the nuclear level density and photon strength function of the specific nucleus. For instance, in the case of ^{128,130}Te, the fraction of bypassing transitions is in the order of 10 % in the vicinity of the neutron separation energy and decreases towards lower excitation energies [57]. Further average quantities that can be deduced are average branching ratios, which will be briefly discussed in subsection 2.3.6.

2.3.5 Self-Absorption Measurements

The extraction of integrated NRF cross sections requires information on the luminosity of the NRF reactions of interest, cf. Eq. (25), and on the incident photon flux at resonance energy, $N_\gamma(E_r)$. For smoothly-varying incident beams, such as those obtained from bremsstrahlung production, the photon flux can be calibrated at specific energies using certain photon-flux calibration standards, such as ^{6,7}Li, ^{11}B, ^{19}F, ^{27}Al, or others, with sufficiently well-known NRF cross sections (35), i.e., sufficiently well-known excitation width Γ_0 and branching ratios Γ_f/Γ. If several calibration points are available, then the photon-flux between them can be obtained by interpolation, provided that its energy dependence is sufficiently well known or can be simulated to the desired accuracy and precision. The latter can currently be done more satisfactorily for bremsstrahlung beams rather than for more rapidly varying spectral shapes of quasi-monochromatic beams from LCB processes. Therefore, photonuclear reactions on intense bremsstrahlung beams are still best suited for high-precision measurements of absolute NRF cross sections.

Establishment of the calibration standards or increase of their precision requires, however, an alternative method which is sensitive to the excitation width Γ_0 without relying on quantitative information on the photon flux. This option is offered by self-absorption measurements which occasionally is addressed also as 'transmission NRF'. Its underlying principle relies on the production of an absorption line at resonance energy on transmission of the incident photon beam through an initial absorber target, cf. Fig. 7, and on the quantitative determination of the resulting amount of resonance absorption with a subsequent scattering target. The fractional depletion of luminosity on the scatterer due to the absorption line induced by the absorber is called 'self absorption'. The self absorption is a function of the thickness of the absorber and it is sensitive to the resonance-absorption attenuation coefficient K and, thus, to the absolute value of the excitation width Γ_0 of the level of interest from the ground state. It is defined as the difference of the actual reaction luminosity on the resonance at the scatterer under the presence of an absorber $\mathcal{L}_{\mathrm{w}A}(E_r)$ to the (hypothetical) luminosity $\mathcal{L}'_{\mathrm{w}A}(E_r)$ if the absorption line is

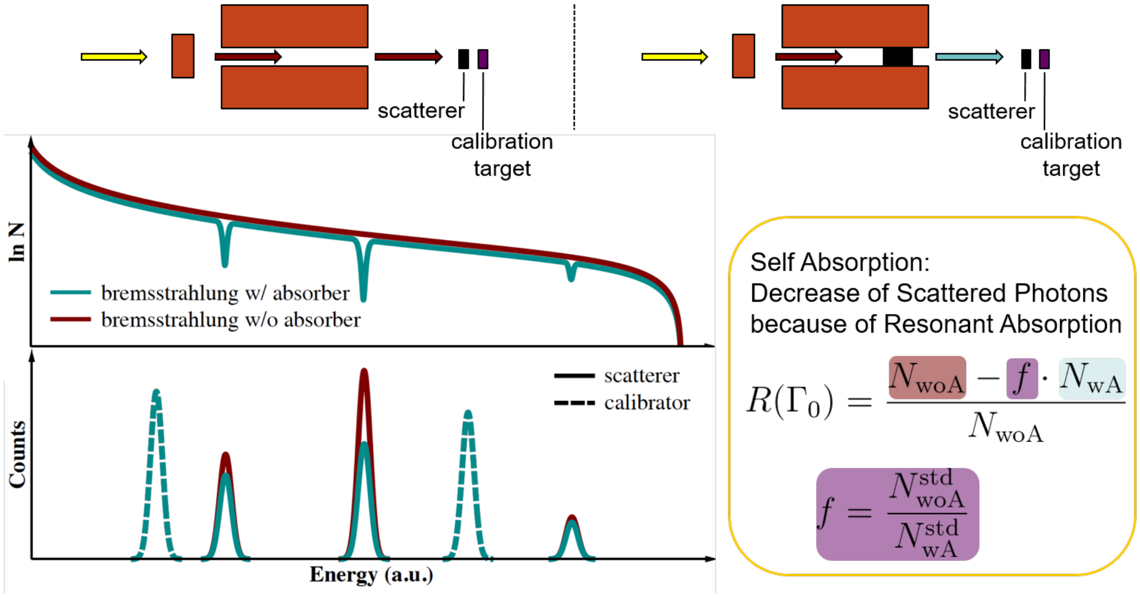

$$R(\Gamma_0) = \frac{N_{\mathrm{woA}} - f \cdot N_{\mathrm{wA}}}{N_{\mathrm{woA}}}$$

$$f = \frac{N^{\mathrm{std}}_{\mathrm{woA}}}{N^{\mathrm{std}}_{\mathrm{wA}}}$$

Figure 11: Sketch of the principle of a relative self-absorption (RSA) measurement. It consists of two parts (top panel left and right). NRF intensity of a photon-scattering target of interest with target thickness $\bar{n}_{sc}$ and of an arbitrary calibration target made out of atoms with nuclei differing from the nuclei of interest is measured with sufficient energy resolution for resolving the NRF lines from the nuclei of interest and from the calibration material. Then, the same measurement is repeated while a shielded absorber containing the nuclei of interest with the absorber thickness $\bar{n}_{abs}$ is placed into the incident beam. Due to atomic absorption varying smoothly with the γ-ray energy and the development of absorption lines at resonance energies originating from the absorber, the count rates in the second part of the measurement are reduced with respect to the first part. Normalizing the observed count rates to the NRF intensities from the calibration target ensures equal reaction luminosities at energies differing from the resonance energies of interest. The remaining reduction of this-way normalized NRF intensities of the NRF lines of interest is then, due to the depth of the absorption lines, originating from the absorber. It depends for a given combination of target thicknesses $\bar{n}_{sc(abs)}$ monotonically on the photo-excitation width Γ_0 from the ground state for the level of interest.

absent, i.e., for $\Gamma_0 = 0$ in the absorber, expressed by

$$R = \frac{\mathcal{L}'_{\mathrm{w}A}(E_r) - \mathcal{L}_{\mathrm{w}A}(E_r)}{\mathcal{L}'_{\mathrm{w}A}(E_r)} \tag{49}$$

$$= 1 - \frac{\int_{\bar{n}_{abs}}^{\bar{n}_{abs}+\bar{n}_{sc}} \int_0^\infty \tilde{\sigma}_a^D(E) e^{-[\kappa+\tilde{\sigma}_a^D(E)]\mathcal{Z}} dE\, d\mathcal{Z}}{e^{-\kappa \bar{n}_{\mathrm{abs}}} \int_0^{\bar{n}_{sc}} \int_0^\infty \tilde{\sigma}_a^D(E) e^{-[\kappa+\tilde{\sigma}_a^D(E)]\mathcal{Z}} dE\, d\mathcal{Z}} \tag{50}$$

$$\approx 1 - \frac{\int_{\bar{n}_{abs}}^{\bar{n}_{abs}+\bar{n}_{sc}} \int_{-\infty}^\infty e^{-(\kappa+Ke^{-x^2})\mathcal{Z}-x^2} dx\, d\mathcal{Z}}{e^{-\kappa \bar{n}_{\mathrm{abs}}} \int_0^{\bar{n}_{sc}} \int_{-\infty}^\infty e^{-(\kappa+Ke^{-x^2})\mathcal{Z}-x^2} dx\, d\mathcal{Z}} \,. \tag{51}$$

The approximation in (51) holds in the limit of $\Gamma \ll \Delta$ to the extent to which the Doppler cross section approximates the effective resonance-absorption cross section. Equations (50,51) depend on the knowledge of the target thicknesses of the absorber and the scatterer, on Γ_0, and on the Doppler width Δ. The two-dimensional integrals cannot be solved in closed form, but can easily be evaluated numerically to any desired precision, establishing thereby the monotonically increasing function $R(\Gamma_0)$ for a given combination of thermal motion in the absorber and scatterer targets and their thicknesses.

Its comparison to a measured amount of self absorption allows for the experimental determination of Γ_0.

Historically, the luminosity on the scatterer behind an absorber in absence of an absorption line had experimentally been approximated by using an absorber of a different material established in such a way that its atomic absorption at resonance energy matches the atomic absorption of the resonant absorber made out of the same material as the scatterer. This procedure is, however, prone to some systematical uncertainties that may limit the achievable accuracy.

Recently, the method of Relative Self-Absorption (RSA) measurements has been introduced [45, 59] which eliminates most of the systematical uncertainties of a self-absorption measurement due to the proper normalization of the observed NRF intensity from the scatterer to the actual luminosities by adding an appropriate calibration material to it. In this case, the self absorption is experimentally obtained as the double-normalized count-rate difference

$$R = \frac{N_{\mathrm{wo}A} - \frac{N_{\mathrm{wo}A}^{std}}{N_{\mathrm{w}A}^{std}} N_{\mathrm{w}A}}{N_{\mathrm{wo}A}} \tag{52}$$

with $N_{\mathrm{w}[o]A}^{(std)}$ being the NRF count rate of the transition of interest (of an NRF line in the normalization material) in the presence [absence] of an absorber. Note that information on the integrated cross section for the NRF line in the normalization material is not needed as long as it is thin enough such that its self absorption is not needed to be taken into account. The principle of an RSA measurement is sketched in Fig. 11. The achievable uncertainty of an RSA measurement on the ground-state excitation width Γ_0 of an NRF line of interest is mostly limited by counting statistics or, eventually, by the uncertainties on the knowledge of the thermal motion of the nuclei of interest in the target.

As a self-absorption measurement provides information on Γ_0 and NRF cross sections are proportional to $\Gamma_0\Gamma_f/\Gamma$, an RSA measurement which always includes a standard NRF measurement as well, is also sensitive to the total decay-branching ratio Γ_f/Γ. This feature can support the identification and quantification of significant decay branches that have escaped direct detection. In addition, self absorption can provide valuable spectroscopic information in cases where average decay quantities are considered because it has a different sensitivity to the level density as NRF, alone. Although the self-absorption technique has been introduced quite early [8], we consider it to be still at its infancy due to the absence of sufficiently intense beams up to now. It can be expected that with increasing availability of highly-intense photon beams, the application of self absorption will offer new opportunities for scientific research with potential for new discoveries.

2.3.6 Methodological examples

This subsection provides examples from the recent literature for observables from photonuclear reactions.

Placement of γ-ray transitions and establishment of the level scheme The recent advent of intense quasi-monochromatic LCB photon beams with bandwidths comparable to or even smaller than the excitation energy of the first excited state of a nucleus of interest provides access to unambigous placements of γ-ray transitions from NRF in its level scheme. Compact high-efficiency γ-ray spectrometer arrays even allow for measurements of $\gamma\gamma$-coincidence relations. Figure 12 shows a recent example which unambigously established aspects of the level scheme of dipole excitations of ^{164}Dy and their decays to intrinsic excitation modes [60].

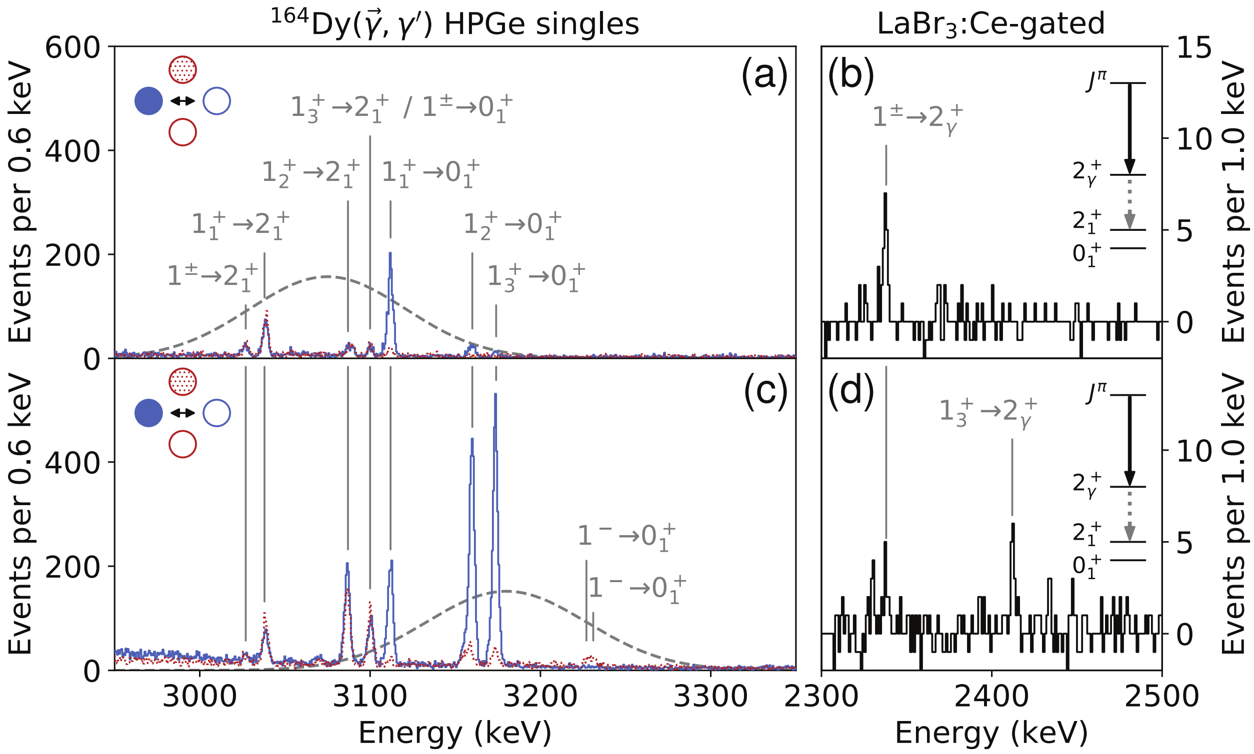

Figure 12: γ-ray spectra from the ^{164}Dy($\vec{\gamma}, \gamma'$) reaction taken at the HIγS facility with beam energies $E_{\text{beam}} = 3075(50)$ keV [panels (a) and (b)] and $E_{\text{beam}} = 3180(52)$ keV [panels (c) and (d)]. Detectors were placed at a polar angle of $\vartheta = 90°$ and azimuthally in the horizontal polarization plane (blue) of the incident photon beam or perpendicular to it (red). The luminosity profile of the incident $\vec{\gamma}$-ray beam in arbitrary units is indicated in gray by the dashed Gaussian curve. In the spectrum shown in panel (a), the $J^\pi = 1_3^+$ state is not excited. Hence, the peak observed at 3100 keV is the ground-state decay of hitherto unknown state(s). Their transitions to the 2_1^+ state are located at 3027 keV [cf. panels (a) and (c)] and decays to the 2_γ^+ state are visible in the spectrum gated on the $2_\gamma^+ \rightarrow 2_1^+$ transition [panel (b)]. The spectra shown in panel (c) are dominated by the $1_i \rightarrow 0_1^+$ ($i = 1$-3) transitions at 3111.0(4), 3159.1(4), and 3173.6(4) keV and the transitions to the 2_1^+ state at 3037.8(4), 3085.3(4), and 3100.1(4) keV, respectively. The peak stemming from the $1_3^+ \rightarrow 2_\gamma^+$ transition is visible in the gated spectrum shown in panel (d). Reprinted figure with permission from Ref. [60]. Copyright 2020 by the American Physical Society.

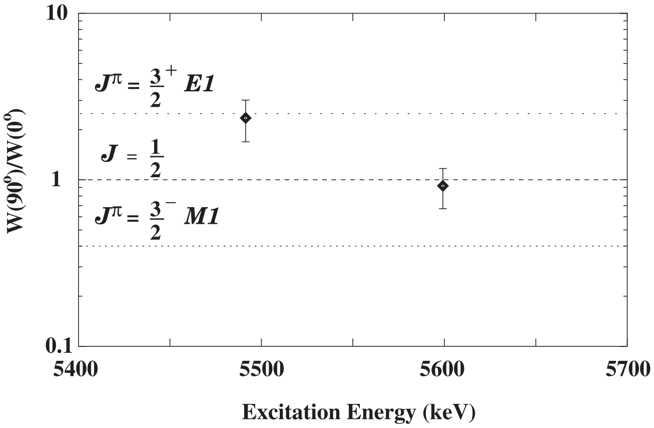

Figure 13: Spin assignments to states excited by dipole transitions of the odd-mass nucleus ^{207}Pb from azimuthal NRF intensity ratios about the linearly-polarized photon beam provided by the HIγS facility. The NRF intensities were measured at a polar angle of $\vartheta = 90°$ and azimuthal angles ϕ with respect to the polarization plane of the electrical field vector as indicated on the y axis. Reprinted figure with permission from Ref. [62]. Copyright 2009 by Elsevier.

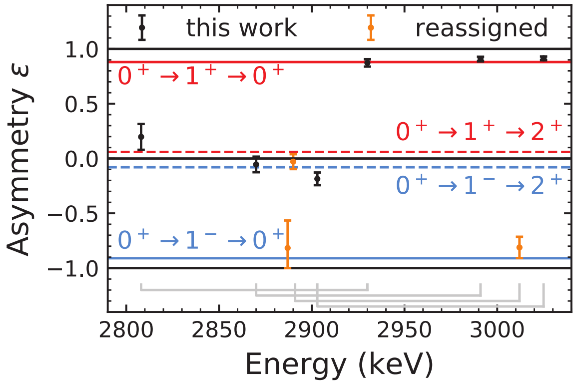

Figure 14: Parity assignments to $J = 1$ states of the transitionally deformed nucleus ^{152}Sm from azimuthal NRF intensity asymmetries about linearly-polarized LCB photon beams provided by the HIγS facility. Yellow labels are used in cases where the explicite polarization measurement required reassignments of parity quantum numbers with respect to previous literature. Reprinted figure with permission from Ref. [63]. Copyright 2021 by the American Physical Society.

Spin quantum numbers Spin-quantum numbers can be assigned in NRF measurements from the angular distribution of NRF intensities. The discrimination of $J = 1$ and $J = 2$ states of even-even nuclei is frequently obtained from the ratio of elastic NRF transition intensities at polar angles, where either a $0^+ \rightarrow (J = 1) \rightarrow 0^+$ or $0^+ \rightarrow (J = 2) \rightarrow 0^+$ have local extrema. This is the case for the ratio $W(\vartheta = 90°)/W(\vartheta = 127°)$ for NRF induced by an unpolarized incident photon beam. In this case, the ratios are 0.734 for $J = 1$ and 2.28 for $J = 2$ [11]. For odd-A nuclides with non-zero ground-state spin, the modulation of the angular distribution of NRF intensity is much less pronounced than for even-even nuclei. Usage of polarized beams can help to increase the sensitivity to the spin quantum number of photoexcited nuclear levels in such cases. An example from the literature for this approach is shown in Fig. 13.

Parity assignments Parity quantum numbers can be assigned to photonuclear excitations by measuring the multipolarity of the NRF γ-ray lines or of the excitation process. Compton polarimetry or NRF asymmetries in partially-polarized off-axis bremsstrahlung [11] have been used for this purpose until intense fully linearly-polarized MeV-range photon beams from LCB processes became available. As described in Section 2.3.2, fully linearly-polarized photon beams provide a superior sensitivity to the polarity of nuclear dipole excitations of even-even nuclei with a 0^+ ground state [51, 61]. Figure 14 displays a recent example from the literature.

Multipolarities and multipole-mixing ratios The assignment of the multipole character to NRF lines is trivial in even-even nuclei as long as the NRF transitions involve a $J^\pi = 0^+$ level, e.g., the ground state. In these cases, the multipole character is uniquely given by the γ-ray selection rules from Eqs. (8,9). If the spin quantum numbers of the initial and the final state in an NRF transition both differ from 0, then its multipole components must be measured explicitely. Either, the multipole character and possible multipole mixing can be obtained from $\gamma\gamma$-angular correlation measurements in other nuclear reactions [65, 66], or the sensitivity of the NRF angular distribution function on the multipole-mixing ratio must be exploited. The latter approach has only recently been demonstrated [56, 63].

Figure 15 shows the comparison of the measured intensity ratio of a $0_1^+ \xrightarrow{\vec{\gamma}} 1^+ \rightarrow 2_1^+$ NRF cascade at two different observation angles to the expectation from angular-momentum theory as a function of the multipole-mixing ratio of interest. In this particular case, a small but nonzero $E2/M1$ multipole-mixing ratio could be established revealing a small amount of 0.5(3)% of $E2$ contribution to the predominant $M1$-decay transition of a fragment of the scissors mode of the deformed nucleus ^{156}Gd to its 2_1^+ state of its ground-state rotational band.

Branching ratios and K-quantum numbers in axially-deformed nuclei NRF is an exclusive reaction, for which the observed NRF γ-ray line specifies the final state. Its integrated cross section $I_{s,f}$ is proportional to the quantity

$$\frac{\Gamma_0 \Gamma_f}{\Gamma} = \frac{\Gamma_f}{1 + \sum_{f>0} \frac{\Gamma_f}{\Gamma_0}} \ . \qquad (53)$$

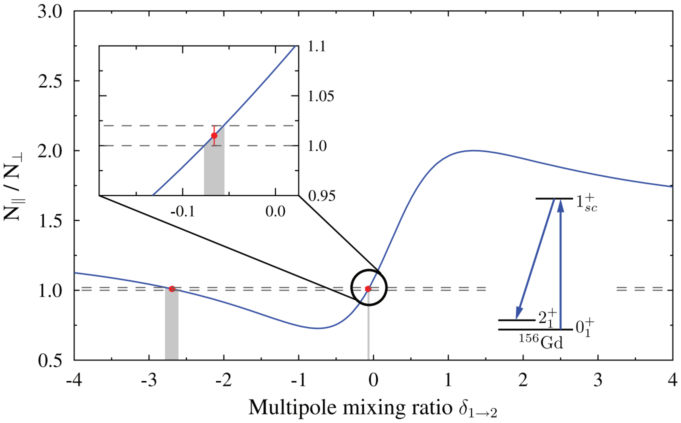

Figure 15: The intensity ratio of a $0_1^+ \xrightarrow{\vec{\gamma}} 1^+ \rightarrow 2_1^+$ NRF cascade observed at a polar angle of $\vartheta = 135°$ and azimuthal angles of $\phi = 0°$ ($N_\parallel$) and $\phi = 90°$ ($N_\perp$) with respect to the polarization plane of an incident linearly-polarized photon beam observed for the nucleus ^{156}Gd. The data are compared to the corresponding angular distribution ratio $W(135°, 0°; \delta_{1\rightarrow 2})/W(135°, 90°; \delta_{1\rightarrow 2})$ as a function of the $E2/M1$ multipole-mixing ratio $\delta_{1\rightarrow 2}$ indicated by the blue curve. The two possible solutions for the multipole-mixing ratio are indicated in red while the result $\delta_{1\rightarrow 2} = -0.07(1)_{stat}(2)_{syst}$, which is favored by comparison to the Alaga rule [64], is shown enlarged in the inlay. Reprinted figure with permission from Ref. [56]. Copyright 2017 by the American Physical Society.

The relative NRF cross section between two decay channels, f f', of a given nuclear state determines its decay intensity ratio $\Gamma_{f'}/\Gamma_f = I_{s,f'}/I_{s,f}$. The spectra shown on the LHS of Fig. 12 provide a good example for cases where decay intensities of $J = 1$ states into the 2_1^+ and 0_1^+ states of the ground-state rotational band of a deformed nucleus are observed. When corrected for detection efficiency and angular distribution, the observed NRF count rates are proportional to the integrated NRF cross sections for the various NRF lines. Gamma-decay intensity ratios can be measured to a few percent precision.

If multipole-mixing ratios are established along the lines discussed in the preceding paragraph, then the monopolar decay intensity ratios $\Gamma_{f',\Pi L}/\Gamma_{f,\Pi L}$ can be determined. It provides the ratio of transition strengths

$$R_{\text{exp}} = \frac{B(\Pi L; J \rightarrow J_{f'})}{B(\Pi L; J \rightarrow J_f)} = \left(\frac{E_{\gamma_f}}{E_{\gamma_{f'}}} \right)^{(2L+1)} \frac{\Gamma_{f',\Pi L}}{\Gamma_{f,\Pi L}} \qquad (54)$$

of multipolarity ΠL for the $J \rightarrow J_{f,(f')}$ transitions, which in NRF literature is often simply addressed as *branching ratio*. It differs from the decay-intensity ratio by the energy reduction factor $E_\gamma^{(2L+1)}$.

In axially-deformed nuclei, the branching ratio of transitions between two rotational bands can be used for assigning K-quantum numbers for the projection of the spin onto the intrinsic symmetry axis by comparison to the Alaga rules [64]

$$R_{\text{Alaga}} = \frac{B(\Pi L; J', K \rightarrow J_{f'}, K_f)}{B(\Pi L; J, K \rightarrow J_f, K_f)} = \left(\frac{C^{J_{f'}\,K_f}_{J'\,K\,L\,\Delta K}}{C^{J_f\,K_f}_{J\,K\,L\,\Delta K}} \right)^2 \qquad (55)$$

where the Cs denote the common Clebsch-Gordan coefficients for angular momentum coupling. Most importantly is certainly the application of the Alaga rules to the dipole branching ratios of $J_K = 1_K$ states of even-even deformed nuclei into the 0^+_1 ground state and the 2^+_1 state of the $K_f = 0$ ground-state rotational band. It takes the values

$$\frac{B(\Pi1; 1_K \to 2^+_{K_f=0})}{B(\Pi1; 1_K \to 0^+_{K_f=0})} = \left(\frac{C^{2\,0}_{1\,K\,1\,\Delta K}}{C^{0\,0}_{1\,K\,1\,\Delta K}}\right)^2 = \left\{\begin{array}{c} 2 \\ 1/2 \end{array}\right. \text{for} \quad \begin{array}{c} K = 0 \\ K = 1 \end{array} \quad . \tag{56}$$

Branching ratios that differ from these values are indicative for deviations from axially-symmetric deformation and for the occurrence of K mixing [60, 67]. The data displayed in Figs. 12 and 14 are good examples.

Photon-scattering cross sections and level widths NRF cross sections are frequently measured using a continuous-energy bremsstrahlung beam. Figure 16 provides a recent example for typical NRF spectra. The photon flux can be quantified by suitable calibration standards that feature several excited states in the energy-range of interest with sufficiently well-known NRF cross sections themselves. The photon flux at other energies is then obtained by interpolation with suitable functions, either using the Schiff formula (see Ref. [69] and Eq. (93) in Sec. 3.1) for single-interaction bremsstrahlung or by numerical simulations of the bremsstrahlung processes of relativistic electrons in thick radiator targets. Equation (46) then provides access to the integrated NRF cross sections $I_{s,f}$ for the identifiable NRF levels. Afterwards, their partial decay widths Γ_f can be extracted provided that information on their decay-intensity ratios Γ_f/Γ are known as discussed above. Examples for $E1$ excitation strength distributions, measured in this way, are given in Fig. 42.

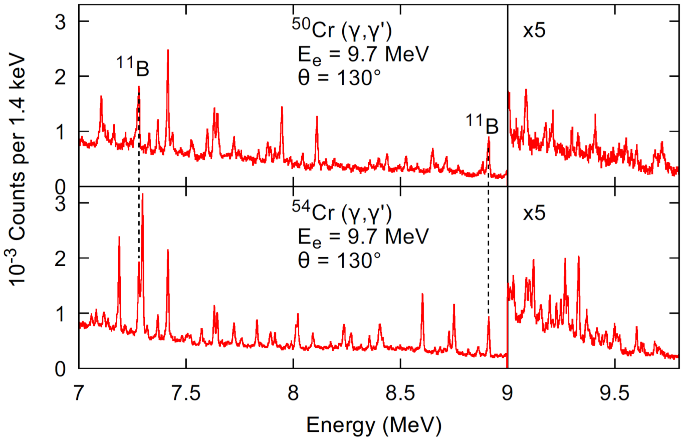

Figure 16: NRF spectra of ^{50,54}Cr for a measurement of NRF cross sections relative to the photon-flux calibration standard ^{11}B in a bremsstrahlung beam with end-point energy 9.7 MeV at the DHIPS facility at TU Darmstadt. Reprinted figure with permission from Ref. [68]. Copyright 2019 by the American Physical Society.

In cases where the polarities of dipole transitions or the spin quantum numbers of the NRF levels are unknown, the quantity

$$\begin{aligned} g\Gamma_0^{\text{red}} &\equiv \frac{2J+1}{2J_0+1}\frac{\Gamma_0}{E_r^3} \qquad (57)\\ &= \frac{1}{(\pi\hbar c)^2 E_r} I_{s,f}\frac{\Gamma}{\Gamma_f} \qquad (58)\\ &= \frac{16\pi}{9(\hbar c)^3} B(\Pi1)\!\uparrow \qquad (59) \end{aligned}$$

is frequently considered in the literature and is defined in Eq. (57). Its relation to the measured cross sections is provided by Eq. (58) and it can be interpreted in terms of dipole excitation strengths $B(\Pi1)\!\uparrow \equiv B(\Pi1; J_0 \to J)$ as given by Eq. (59). Here, the conversions $1\ e^2\text{fm}^2 = 1.44$ MeV fm^3 and $1\mu_N^2 = 0.016$ MeV fm^3 can be useful.

Average branching ratio In cases where the NLD is too high to resolve transitions from individual excited states, nuclear structure information can be still extracted from average decay properties measured in NRF experiments with quasi-monochromatic photon beams. The average ground-state branching ratio $\langle b_0 \rangle = \sigma_{\gamma\gamma}/\sigma_\gamma$ is deduced from single γ-ray spectroscopy discussed in Section 2.3.4. More detailed information about the decay behavior of photo-excited states below the neutron threshold can be determined from γ-γ coincidence experiments with LCB beams [57,70–72]. Figure 17 depicts average branching ratios[2]

$$\langle b_i \rangle = \frac{\langle \Gamma_0 \frac{\Gamma_i}{\Gamma} \rangle}{\langle \Gamma_0 \frac{\Gamma_0}{\Gamma} \rangle} \tag{60}$$

from excited states to the 2_1^+ ($i = 1$) and 2_2^+ ($i = 2$) state of ^{140}Ce, respectively, relative to the ground-state decay channel as a function of the excitation energy E_x in comparison to calculations from the QPM [70].

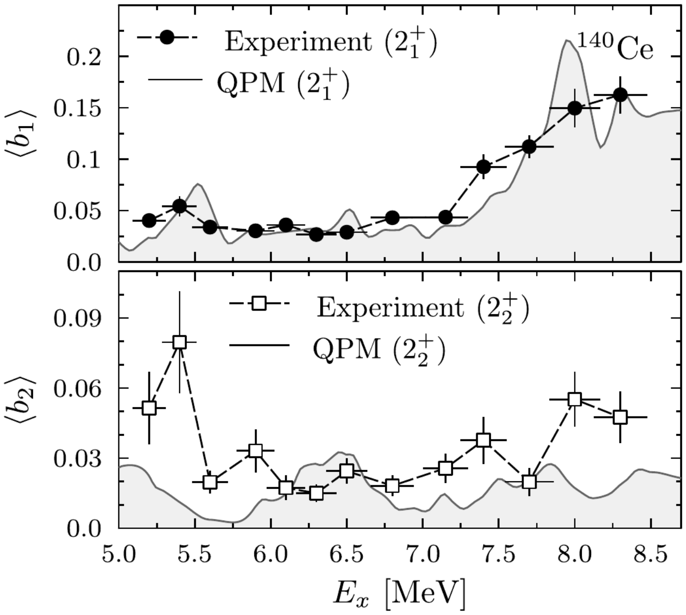

Figure 17: Average branching ratios to the 2_1^+ state (upper panel) and to the 2_2^+ state (lower panel) for ^{140}Ce. For details see text and Ref. [70]. Reprinted figure from [70]. Licensed under a Creative Commons Attribution 4.0 license.

Due to the narrow bandwidth of the LCB beam and its usage with a high-efficiency γ-γ coincidence setup, such as the γ^3 setup [71] at HIγS or ELI-ADE [73–75] at VEGA in the future (see Sec. 3.4.2), average branching ratios as small as a few percent can be determined with high precision as shown in Fig. 17 and Refs. [57,70].

2.4 Photonuclear reactions above particle thresholds

2.4.1 Excitation function, absolute cross section, and dipole sum rule

In photonuclear reactions, the incident particle is a photon and the emitted particles are γ rays, neutrons or charged particles, *e.g.*, protons, α particles, tritons, *etc*, see Fig. 2. As already mentioned, these studies can be traced back to the dawn of nuclear physics, when Chadwick and Goldhaber used the ^{2}H(γ,n)^{1}H reaction to investigate the proton-neutron mass difference [13,76]. Reactions with the emission of photons below the particle emission threshold were already discussed in the previous sections. Here we focus on photonuclear reactions with emission of neutrons or charged particles. Such reactions take place above a certain energy, which is specific for each isotope, the particle-emission treshold. They have two specific features. First, the reaction cross section, $\sigma_{abs}(E_\gamma)$, has a large hump in the region of the giant dipole resonance (GDR), and second, the sum of the photoabsorption cross section depends on the mass, A, proton, Z, and neutron, N, numbers of the target nucleus. The dipole sum rule [77]

$$\int_0^\infty \sigma_{abs}(E_\gamma) dE_\gamma = 60 \frac{NZ}{A} \text{ (MeV mb)} \tag{61}$$

is equivalent to the Thomas-Reiche-Kuhn sum rule, which was introduced in atomic physics to describe the physics of electric-dipole interactions with atoms [78–80].

---

[2] Note the difference to the definition of the average ground-state branching ratio $\langle b_0 \rangle$. The quantity $\langle b_i \rangle$ is defined relative to the ground-state decay channel, while $\langle b_0 \rangle$ denotes the ratio between the ground-state decay cross section following photoexcitation, $\sigma_{\gamma\gamma}$, and the total photoabsorption cross section, σ_γ.

The GDR has a peak energy at about 25 MeV for reactions on a ^{16}O target. The peak energy decreases slowly with the increase of the mass number of the target, taking a value of about 15 MeV for ^{238}U. For more details about recent GDR studies in photonuclear reactions see Sec. 4.1.

The reaction goes either to the ground state of the residual nucleus, described as a two-body process in the exit channel,

$$\gamma + A \to A^* \to (A-\mu)_0 + \mu, \tag{62}$$

or to an excited state, a three-body process in the exit channel

$$\gamma + A \to A^* \to (A-\mu)^* \to (A-\mu)_0 + \mu + \gamma' \tag{63}$$

where μ denotes the emitted particle, A^* an excited state of the target nucleus after the photon absorption, $(A-\mu)_0$ and $(A-\mu)^*$ the residual nucleus in ground and excited state.

The reaction is a two-step process, which goes through the formation of a compound nucleus. In the first stage of the reaction, the incident photon is absorbed by the target nucleus, setting it in an excited state. After reaching statistical equilibrium, the compound nucleus decays through a specific exit channel and its decay is independent of the formation of the compound nucleus, *i.e.*, in photonuclear reactions above the particle emission threshold the Bohr independence hypothesis applies [81].

2.4.2 Formalism of photonuclear reactions above the particle evaporation threshold

A model for photonuclear reactions should account for the photonuclear excitation process and the subsequent decay of the excited nucleus through different open exit channels. By neglecting the giant quadrupole resonance and the pygmy dipole resonance that may contribute only to the exotic nuclei, the photonuclear cross section can be given by a sum of two components, the GDR cross section, σ_{GDR}, and the quasideuteron cross section, σ_{QD},

$$\sigma_{tot}(E_\gamma) = \sigma_{GDR}(E_\gamma) + \sigma_{QD}(E_\gamma). \tag{64}$$

For photon energies below 30 MeV, $\sigma_{tot}(E_\gamma) \approx \sigma_{GDR}(E_\gamma)$ is a good approximation. The Pauli-blocking factor, which scales the QD cross section, tends to go to zero at energies $\sim$ 20 MeV, and at $\sim$ 140 MeV it tends to go to unity [82].

The GDR cross section is expressed by a Lorentzian function, whose parameters are defined by the shape of the GDR

$$\sigma_{GDR}(E_\gamma) = \sum_i \sigma_i \frac{E_\gamma \Gamma_\gamma}{(E_\gamma^2 - E_i^2)^2 + (E_\gamma \Gamma_\gamma)^2}, \tag{65}$$

where σ_i, E_i, and Γ_i are the GDR peak cross section, energy, and width, respectively. The summation is taking into account the splitting of the GDR in deformed nuclei.

For the description of the decay of compound nuclei, the Hauser-Feshbach (HF) statistical theory of compound nuclear reactions [83] or the more simplified Weisskopf-Ewing theory [84] is applied. The concept for the decay of the compound nucleus is based on Bohr's independence hypothesis [81], which says that the decay takes place after the nucleus has lost all information about its formation except for the energy, E, the angular momentum, J, and the parity, π, which are conserved. The difference between the two approaches is that the HF theory considers the conservation of the total angular momentum and parity. Within the Weisskopf-Ewing approach, it is neglected. The main assumption in the HF approach is that at high excitation energies the density of resonances and the variety of exit channels is large, which results in fluctuations in the energy dependence of the cross section.

In short, the probability that a specific reaction takes place is the product of the probability for formation of a compound nucleus, *i.e.*, the entrance channel, and the probability for its decay in a specific exit channel. Within the HF theory, these probabilities are expressed in terms of transmission coefficients, $T_\mu(E, J, \pi) = T_\mu(E, J, \pi; E_i^*, J_i^*, \pi_i^*; E_\mu, J_\mu, \pi_\mu; e_{i\mu})$, where E, J, and π are the excitation energy, the angular momentum, and the parity of the compound nucleus. The residual nucleus is labeled by i, and E_i^*, J_i^*, and π_i^* are the energy, the total angular momentum, and the parity for a given state, excited or ground state. The emitted particle μ is described by its excitation energy, E_μ, angular momentum, J_μ, and parity, π_μ. The kinetic energy of the emitted particle is $e_{i\mu}$ and the energy conservation implies that

$$E = E_i^* + E_\mu + e_{i\mu}. \tag{66}$$

Conservation of parity requires that the condition

$$\pi = (-1)^l \pi_i^* \pi_\mu \tag{67}$$

is fulfilled, where l is the angular momentum of the partial wave. Conservation of angular momentum involves different combinations of (J_i^*, J_μ, l) coupling to J. Only terms that fulfill the parity conservation condition are taken into account.

The same expression for the transmission coefficient can be written for an absorption reaction, where i labels the target nucleus and * its excited states. Thus, for a reaction in which a projectile j hits nucleus i and an ejectile μ is emitted leaving a residual nucleus m, the total cross section is

$$\sigma[i^*(j,m)\mu] = \frac{\pi}{k_{ij}^2(2J_i+1)(2J_j+1)} \sum_{J,\pi} (2J+1) T_j(E,J,\pi) \frac{T_m(E,J,\pi)}{T_{tot}(E,J,\pi)}, \tag{68}$$

where

$$T_m(E,J,\pi) = \sum_\nu T_m(E,J,\pi; E_\mu^\nu, J_\mu^\nu, \pi_m^\nu u; E_m, J_m, \pi_m; e_{\mu m}), \tag{69}$$

The wave number of the projectile, k_{ij}, in a photonuclear reaction is the wave number of the photon. The first transmission coefficient of Eq. (68), $T_j(E, J, \pi)$, defines the probability for formation of a compound nucleus. For photo-induced reactions $j = \gamma$. The second term of Eq. (68) describes the probability for compound-nucleus decay into the exit channel of interest, which is defined by the ratio of the transmission coefficient for this channel, $T_m(E, J, \pi)$, divided by the total transmission coefficient, $T_{tot}(E, J, \pi)$, which is the sum of the transmission coefficients of all possible exit channels. The sum ν runs over all excited states of the residue.

The transmission coefficients for the particle-emission channels are obtained from the S matrix for elastic scattering, which is calculated for a given optical model potential. In addition, the level density, $\rho(E_m, J_m, \pi_m)$, needs to be known, because the summation in Eq. (69) goes over a huge number of states. Above a certain excitation energy, the sum is replaced by an integral over the level density.

Within this approach, it is possible to obtain the energy spectrum and the angular distribution of the emitted particles. A detailed description of the theory can be found in Ref. [85].

2.4.3 Computer codes for photonuclear reaction calculations

Nowadays, the TALYS [86] and EMPIRE [87] nuclear reaction modeling codes are most often used for simulations of nuclear reactions. The TALYS code can be used to simulate reactions that involve neutrons, γ rays, protons, deuterons, tritons, ^{3}He, and α particles. The code considers different nuclear reaction models, i.e., the optical, compound nucleus, fission, γ-ray strength, level density, and pre-equilibrium models, and uses a database of nuclear structure parameters. The HF formalism for modeling the decay of compound nuclei is embedded in the code. As an output, the code provides a complete set of reaction data, *e.g.*, cross sections, spectral and angular distributions of the emitted particles, *etc.*, and can be used as a tool for the analysis of nuclear reaction experimental data.

The EMPIRE code is a modular system of nuclear reaction codes, comprising various nuclear models, and is designed for calculations over a broad range of energies and incident particles. Photons, nucleons, deuterons, tritons, ^{3}He, α particles, and light or heavy ions can be selected as projectiles. The energy range starts just above the resonance region in the case of a neutron projectile, and extends up to few hundred MeV for heavy ion induced reactions. Similar to TALYS, the code accounts for the major nuclear reaction models, including the full featured HF model. A database of input parameters covers nuclear masses, optical model parameters, ground-state deformations, discrete level and decay schemes, level densities, fission barriers, and γ-ray strength functions. It is based on the Reference Input Parameter Library (RIPL-3) [88] which provides validated nuclear-model input parameters.

2.4.4 Experimental studies above particle thresholds

Present day studies of photonuclear reactions are carried out with both, continuous beams of bremsstrahlung photons and quasimonochromatic photon beams. Accelerated electron beams are used for their production. Two basic techniques for studies of photonuclear reactions are used in experiments, the measurement of the residual activity, referred to as the activation method, and direct detection of the outgoing particles.

Most of the existing experimental data is related to studies of photo-neutron reaction cross sections, see Sec. 2.5.1, 2.5.2, and 2.5.3. Other experiments address measurements of isomeric ratios, see Sec. 2.5.5, studies of γ-ray strength functions, see Sec. 4.5, α-cluster excitations, see Sec. 4.8, or few-body problems, see Sec. 4.7.

Particle yields and sometimes particle spectra and angular distributions are measured in photonuclear experiments above the particle-evaporation threshold. From these data, the reaction cross section, $\sigma(E_\gamma)$, is extracted, as well as, spectral, $\frac{d\sigma(E_\gamma)}{dE_\mu}$, and angular, $\frac{d\sigma(E_\gamma)}{d\Omega_\mu}$, distributions of the emitted particles, μ. Since the emitted particles originate from the decay of a compound nucleus, their spectral and angular distributions are independent of each other. In the case, when the reaction goes through excited states in the daughter nucleus, a double differential cross section, $\frac{d^2\sigma(E_\gamma)}{dE_\mu d\Omega_\mu}$, can be obtained from the data. Cross sections for different photonuclear reactions are studied, e.g.,

$$\sigma(\gamma,\text{1n}),\ \sigma(\gamma,\text{2n}),\ \sigma(\gamma,\text{3n}),\ \sigma(\gamma,\text{p}),\cdots,\ \sigma(\gamma,\alpha),\cdots,\ \sigma(\gamma,\text{f}).$$

Some other studies, especially related to theoretical predictions, address the total photoneutron cross section

$$\sigma_{tot}(\gamma,n) = \sum_{\upsilon} \sigma(\gamma,\upsilon n) + \sigma(\gamma,np) + \sigma(\gamma,n2p) + \sigma(\gamma,2np) + \sigma(\gamma,n\alpha) + ... + \sigma(\gamma,f) \tag{70}$$

where

$$\sum_{\upsilon} \sigma(\gamma,\upsilon n) = \sigma(\gamma,n) + \sigma(\gamma,2n) + \sigma(\gamma,3n) + ... \tag{71}$$

and $\sigma(\gamma,\upsilon\text{n})$ are the partial photoneutron cross sections. The total photoabsorption cross section can be written as the sum of the total photoneutron cross section $\sigma_{tot}(\gamma,\text{n})$ and the cross sections of all the possible charged-particle emissions

$$\sigma(\gamma,abs) = \sigma_{tot}(\gamma,n) + \sigma(\gamma,p) + \sigma(\gamma,d) + \sigma(\gamma,\alpha) + ... + \sigma(\gamma,2p) + \sigma(\gamma,p\alpha) + ... \tag{72}$$

In heavy nuclei, the Coulomb force is strong and only small part of the total cross section is realized by charged-particle emission, and $\sigma(\gamma,\text{abs}) \approx \sigma_{tot}(\gamma,\text{n})$ is a good approximation. In light nuclei, charged-particle emission needs to be taken into consideration in the total cross section, *i.e.*, $\sigma(\gamma,\text{abs}) > \sigma_{tot}(\gamma,\text{n})$.

On the other hand, photoneutron experiments are the majority of measurements done worldwide. In such experiments, the neutron multiplicity for each involved reaction channels is measured, and from it the cross section of the inclusive photoneutron yield

$$\begin{aligned}\sigma_{inc}(\gamma,n) = \sigma(\gamma,n) + \sigma(\gamma,np) + \sigma(\gamma,n2p) + \sigma(\gamma,n\alpha) + ...\\ + 2\sigma(\gamma,2n) + 2\sigma(\gamma,2np) + 2\sigma(\gamma,2n\alpha) + ...\\ + 3\sigma(\gamma,3n) + 3\sigma(\gamma,3np) + ... + \kappa\sigma(\gamma,f)\end{aligned} \tag{73}$$

is extracted with κ the average multiplicity of photofission neutrons. Actually, this experimental deduced quantity is the photoneutron production cross section that is a weighted sum over all reaction channels with emission of neutrons. In many cases, *e.g.*, in medium and heavy nuclei, the contribution of charged-particle channels is neglected.

The neutron multiplicity is measured with arrays of proportional counters filled with ^{10}BF$_3$ or ^{3}He, embedded in a moderator, where the emitted neutrons are thermalized, see Sec. 3.4.3. This allows to determine partial reaction cross sections.

Experiments with bremsstrahlung beams: The use of a bremsstrahlung or wide-bandwidth photon spectrum means that the measured yield, $Y(E_e)$, is a convolution of the photonuclear cross section with the photon spectrum

$$Y(E_e) = N_0 \int_{E_{th}}^{E_{max}} \sigma(E_\gamma) f(E_e, E_\gamma) \frac{dE_\gamma}{E_\gamma}, \tag{74}$$

where E_e is the energy of the electron beam, E_γ is the photon energy, E_{th} is the threshold energy for the reaction, E_{max} is the end-point energy of the bremsstrahlung spectrum, $\sigma(E_\gamma)$ is the reaction cross section, N_0 denotes the number of target nuclei, and $f(E_e, E_\gamma)$ is the absolute intensity of the γ-ray spectrum function.

In experiments, the energy of the electron beam is varied in small increments. After unfolding the measured yield curve, the photonuclear cross section is obtained. Such an unfolding procedure requires solving an inverse problem. Different deconvolution techniques have been developed aiming at the correct treatment of the experimental data. The precision of this procedure depends on the correct knowledge of the γ-ray spectrum function and the accurate knowledge of the electron beam energy in the course of the measurement. It is worth noting that there are discrepancies in the results obtained in different laboratories under similar experimental conditions, which most probably is either due to insufficient knowledge of the experimental parameters, *e.g.*, the absolute normalization of the cross section and the calibration of the photon energy, or due to differences in the unfolding procedures. For more detailed discussions see Refs. [89, 90].

Experiments with LCB beams: In the last decades, the number of experimental studies, which are done using quasimonochromatic γ beams produced in LCB, is increasing and it becomes the preferred experimental technique (see Sec. 3.3).

Photonuclear reactions above the particle-evaporation threshold were studied for about 80 isotopes using LCB γ beams. They are listed in the table in Annex C, together with the energies or the energy range in which the measurement was done and the deduced experimental quantities. The physical quantities which are extracted from the experimental data are photodisintegration cross sections, nuclear level density (NLD) and photon strength functions (PSFs). The NLD is defined as the number of excited levels in a given energy bin. The concept dates back to the early days of nuclear physics [91]. For any applications of the statistical theory of nuclear reactions, it is very important to obtain the parameters of the NLD from reliable experimental data. One of the techniques, which is used, is to infer NLD parameters from the shape of evaporation spectra. The primary decay channels for the compound nucleus are neutrons, protons, and α particles. All of these have been used for NLD studies, although the Coulomb barrier suppresses proton and alpha decay substantially in medium and heavy mass nuclei.

The PSF describes the average response of a nucleus to a photon. The idea is that at high excitation energies the NLD is high enough such that the nuclear decay properties can be treated statistically. PSFs are related to photoabsorption cross sections in the GDR region, which is dominated by $E1$ radiation. Thus, photonuclear reactions are often used to deduce PSFs. A detailed description is provided in Sec. 4.5. For a recent review of the experimental data related to PSF see Ref. [92].

In cross-section measurements, discrepancies in the reported results, obtained by different groups, are observed. A possible explanation is that the LCB beams have low-energy tails, which, combined with the relatively large bandwidth, requires unfolding of the experimental data. In Fig. 18, an example of recent measurements of the photodisintegration of ^{9}Be is illustrated [90, 93–95]. The four measurements provide discrepant results for the observed resonances, *e.g.*, within the energy ranges where the cross section varies significantly, while for regions with slow energy variation, all three data sets are in relatively good agreement. Hence, it is unlikely that the beam flux monitoring, the neutron detection procedure or the target characterization causes the discrepancy. The most probable reason is the energy unfolding of the measured cross sections, which relies on the precise determination of the incident LCB photon beam spectral distributions [96].

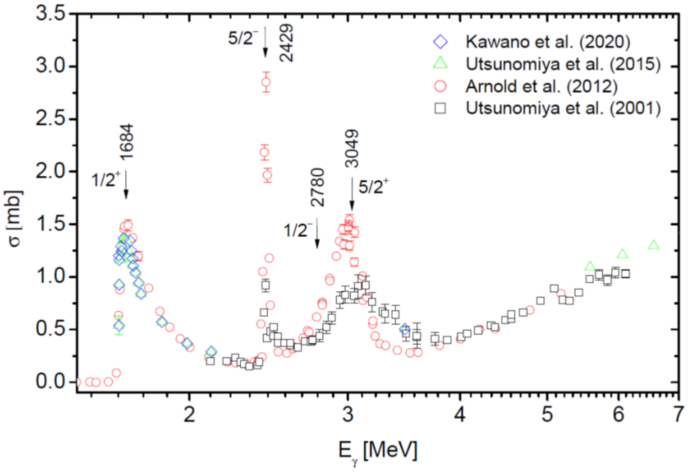

Figure 18: Comparison between various measured ^{9}Be photodisintegration cross-section data using LCB γ beams.

All these indicate the importance of developing precise beam-diagnostic tools at the existing and at next generation LCB facilities, such as ELI-NP [97] which is under construction at Magurele near Bucharest in Romania. The versatile γ-beam system (VEGA) at ELI-NP is expected to provide intense γ beams with a spectral density of 10^4 photons/(eV·s) and a narrow bandwidth of 0.5%, see also Sec. 6.1. The availability of such beams is expected to resolve some of the current discrepancies related to photonuclear cross-section data.

2.5 Methodological examples of photonuclear reaction studies above particle thresholds

In the experiments, the energy and angular distributions of the emitted particles or γ rays are measured. These provide information about the energies of excited states, neutron decays, and γ-ray transitions. The multipolarity of reaction neutrons, the mixing ratios of the γ-ray transitions, and the spins and parities of the excited states can be extracted. If neutrons and γ rays are measured simultaneously, neutron-to-γ decay branching ratios can be deduced. From neutron measurements partial cross sections, $\sigma(\gamma,\nu\mathrm{n})$, and absolute transition strength can be determined.

The quantities which are deduced most often in photonuclear experiments are reaction cross sections, *e.g.*, absolute or differential cross sections and isomeric ratios. In photofission reactions, next to cross-section measurements, mass-yield distributions, as well as kinetic energy, mass, charge, and angular momentum distributions of fission fragments are studied, see Sec. 2.6.

Photonuclear research above the particle threshold addresses a large variety of physical problems. In light nuclei, photonuclear reaction studies address few-body problems, role of 3N forces, polarization measurements, role of resonances, α-cluster excitations, Hoyle-state physics, and photodisintegration reactions related to the astrophysical Big Bang Nucleosynthesis (BBN) and helium burning. Other studies are related to (γ,n) cross-section measurements in medium and heavy mass nuclei. They address the understanding of the astrophysical s- and p-processes, cosmochronometry, the simultaneous understanding of photo-neutron and neutron capture reactions, and measurements of neutron asymmetries. Some of these physical cases will be discussed in Sec. 4.

2.5.1 (γ,particle) cross sections

Photonuclear reaction cross sections are measured by detecting the particles emitted in the reaction. In most of the cases, these are the emitted neutrons. The most common technique is by measuring the neutron multiplicity with arrays of ^{10}BF$_3$ or ^{3}He proportional counters, see Sec. 3.4.3. Measurements of neutron multiplicities in medium and heavy nuclei were carried out at the AIST [98–111], NewSUBARU [90, 95, 112–119], and HIγS [120–123] LCB facilities. As already discussed in Sec. 2.4.4, the total photoneutron cross section is a good approximation for the total photonuclear reaction cross section in medium and heavy nuclei.

Experimentally, the photoneutron cross section is given by

$$\sigma_{exp}(\gamma, n) = \frac{N_n}{f \epsilon_n N_\gamma N_T}, \tag{75}$$

where N_n is the total number of detected neutrons, N_γ denotes the number of photons monitored with the beam flux detectors, N_T the number of target nuclei per cm^2, ϵ_n the efficiency of the neutron detectors, and f is a correction factor, taking the attenuation of the γ beam in the target into account. The correction factor is given by

$$f = e^{\mu d} \cdot \frac{1 - e^{\mu d}}{\mu d}, \tag{76}$$

where μ denotes the γ-attenuation coefficient and d the target thickness. For the derivation of Eq. (75) see Ref. [102]. It is necessary to take also the energy distribution of the γ beam into account, since it has a finite bandwidth and might have a low energy tail [125]. This approach is described in Ref. [114].

In few cases, photoneutron reaction cross sections were measured by different teams in different laboratories, *e.g.*, for the ^{94}Mo [111, 123] and ^{152}Sm [103, 114] isotopes. The data for ^{152}Sm were measured at AIST and NewSUBARU using the same experimental technique and the data are in agreement with each other. Photoneutron cross sections ^{94}Mo were measured at AIST and HIγS using different neutron detectors, beam diagnostic devices and data-reduction techniques. The deduced reaction cross sections are presented in Fig. 19. The data of Ref. [124] were obtained using the annihilation in-flight technique. The data-reduction approach used by Banu *et al.* is described in Ref. [123] and by Utsunomiya *et al.* in Ref. [111].

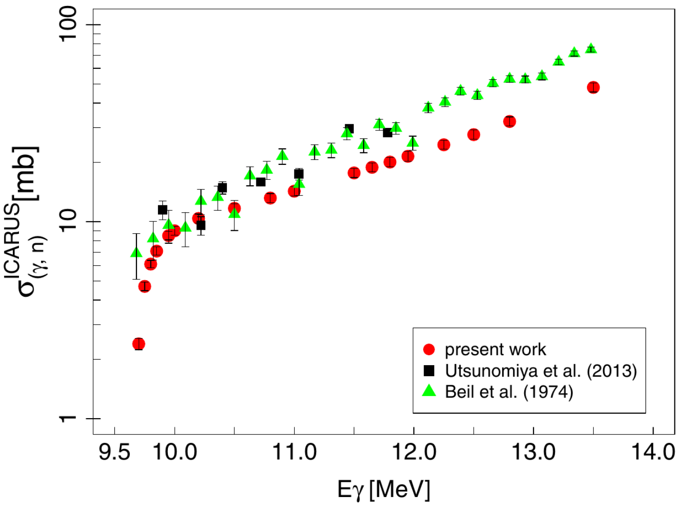

Figure 19: Excitation function for ^{94}Mo(γ,n) of Ref. [123] (red circles) compared with the previous measurements [111, 124]. Reprinted figure with permission from Ref. [123]. Copyright 2019 by the American Physical Society.

Photoneutron cross sections in light nuclei: In light nuclei, charged-particle emission starts to play a role and the total photoneutron cross section is no longer a good approximation for the total reaction cross section. Resonances are observed in the photoneutron cross section below the GDR region, see Fig. 18 for the case of ^{9}Be [90, 93–95]. From the data, the resonance parameters can be extracted, such as γ-decay widths for $E1$ and $M1$ transitions, or reduced transition probabilities $B(E1)$ and $B(M1)$. Similar studies were carried out for ^{26}Mg [126] and ^{48}Ca [127].

Considerable effort for understanding the photodisintegration of BBN nuclei has been carried out, *i.e.*, ^{2}H [128–132], ^{3}He [133–136], ^{4}He [137–139], ^{6}Li [140, 141], and ^{7}Li [142, 143]. Different techniques were utilized in these experiments, such as measurements of analyzing powers [128, 129, 131, 132], time projection chamber (TPC) experiments [137], and differential cross-section measurements [134–136, 140, 142, 143]. The TPC technique is described in Sec. 3.4.4 and the differential cross-section experiments in Sec. 2.5.3. In some of the measurements a polarized ^{3}He target was used [134–136].

The analyzing power, Σ, is defined by Eqs. (42 - 44) in Sec. 2.3.2. In the simplest version of the experiment, four neutron detectors are placed in a plane perpendicular to the γ beam, the ϕ plane, at angles $\phi = 0°, 90°, 180°, 270°$, see Sec.. 3.4.3. These experiments allow to deduce the $E1$ and $M1$ components of the total ^{2}H(γ,n) cross section [128] and to study the Gerasimov-Drell-Hearn (GDH) sum rule [144, 145] for the deuteron, see Sec. 4.7.

Photo-charged-particle reaction cross sections: Only a few measurements of photonuclear reaction cross sections with emission of charged particles were reported [137, 146–149]. Photodisintegration of ^{3}He [146], ^{4}He [137], ^{7}Li [149], ^{12}C [147], and ^{19}F [148] was measured. In the ^{7}Li experiment, an array of Si strip detectors was used [149]. For the ^{17}F experiment, a bubble chamber was utilized [148]. The other three measurements were done with TPCs. Details for these instruments and the experimental techniques can be found in Sec. 3.4.4.

In the ^{7}Li experiment, a low-energy resonance structure was observed, see Sec. 4.6. The ^{12}C measurement reports the 2^{+} resonance state built on the Hoyle state, see Sec. 4.8. In the ^{17}F case, the cross section obtained from the ^{19}F(γ,α)^{15}N reaction was converted to the scale of the time-inverse ^{15}N(α,γ)^{19}F reaction [148].

2.5.2 (γ,νn) partial cross sections

The method of direct neutron multiplicity sorting [150], see Sec. 3.4.3, in combination with LCB photon beams in the MeV range, allows complete mapping of the photoneutron reaction cross sections within the GDR energy range, *e.g.*, measurements of total, $\sigma(\gamma,\mathrm{n})$, and partial, $\sigma(\gamma,\nu\mathrm{n})$, cross sections. Within a IAEA coordinated research project (IAEA CRP) on updating the photonuclear data library, a series of measurements were carried out for ^{9}Be, ^{59}Co, ^{89}Y, ^{103}Rh, ^{139}La, ^{159}Tb, ^{165}Ho, ^{169}Tm, ^{181}Ta, and ^{209}Bi. Except for ^{209}Bi [116, 117], the data for all other isotopes were published in Ref. [90]. The measurements were performed with the flat-efficiency neutron detector (FED), which is described in Sec. 3.4.3. The following steps were taken in the data-reduction procedure to obtain the (γ,νn) partial cross sections:

- The experimental photoneutron cross section measured experimentally is expressed with Eq. (75). In this case, since neutron multiplicities are derived, N_n is the number of measured photoneutron reactions. Low reaction rates are required for avoiding that two reactions on two target nuclei happen simultaneously. A correction for the multiple-firing reaction effect is applied. The secondary γ rays produced in electromagnetic interaction of high-energy γ beam with the target material in the GDR region are also taken into account, since they produce extra neutrons, which should not be assigned to the (γ,n) channel. This correction is done with simulations within the GEANT4 toolkit [151].

- In a next step, the measured energy distribution of the γ beam is taken into account, *i.e.*, the experimental reaction cross section, $\sigma_{exp}(\gamma,\text{n})$, is a convolution of the normalized γ-beam spectral distribution, $W_\gamma(E)$, and reaction cross section, $\sigma_{tot}(\gamma,\text{n})$,

$$\sigma_{exp}(\gamma,n) = \int W_\gamma(E)\sigma_{tot}(\gamma,n)dE = \frac{1}{N_{\gamma,tot}}\int N_\gamma(E)\sigma_{tot}(\gamma,n)dE \qquad (77)$$

  The unfolding procedure of Ref. [114] was used.

- Finally, the photoneutron cross section was unfolded in partial $\sigma(\gamma,\nu\text{n})$ cross sections. A Lorentzian dependence was assumed below the two-neutron separation energy, S_{2n}, the Gaussian formula was used for the energy interval between S_{2n} and 18 MeV, and a simple Lorentzian function was assumed above 18 MeV. This trial cross section function is iteratively adjusted to obtain the best fit. The trial cross section functions required for unfolding the higher order partial cross sections, *e.g.*, for $\nu = 2, 3, 4$ were iteratively adjusted until the global deviation between Eq. (77) and $\sigma_{exp}(\gamma,\text{n})$ is minimized.

Unfolded partial photoneutron cross sections, obtained with this procedure, are shown in Fig. 20.

2.5.3 (γ,n) differential cross sections

In several experiments, differential photoneutron cross sections were measured [122,134–136,140,142,143]. Neutrons created in photodisintegration reactions were detected either with the Blowfish Neutron Detector Array [140, 142, 143], or with dedicated setups, using BC-501A-type neutron detectors positioned at angles which are sensitive to the neutron angular distribution [122, 134–136]. The Blowfish detector array [152] is described in Sec. 3.4.3.

In a series of experiments, the photodisintegration of ^{6,7}Li was studied, utilizing the Blowfish neutron array. Its detectors cover polar angles between 36° and 158° [142] and measure the energies of the neutrons and their angular distribution. In the experiments, the light output signal (LOS) of the scintillators, the time-of-flight (ToF) and the pulse-shape discrimination (PSD) spectra are recorded. The ToF and PSD are used to eliminate γ-ray and scattered neutron background. The LOS was used to distinguish between different open reaction channels, *e.g.*, the ground-state reaction channel,

$$^7\text{Li} + \gamma \rightarrow {}^6\text{Li} + \text{n}_0.$$

This is done by placing cuts in the data. However, at most energies, the competing reaction channels

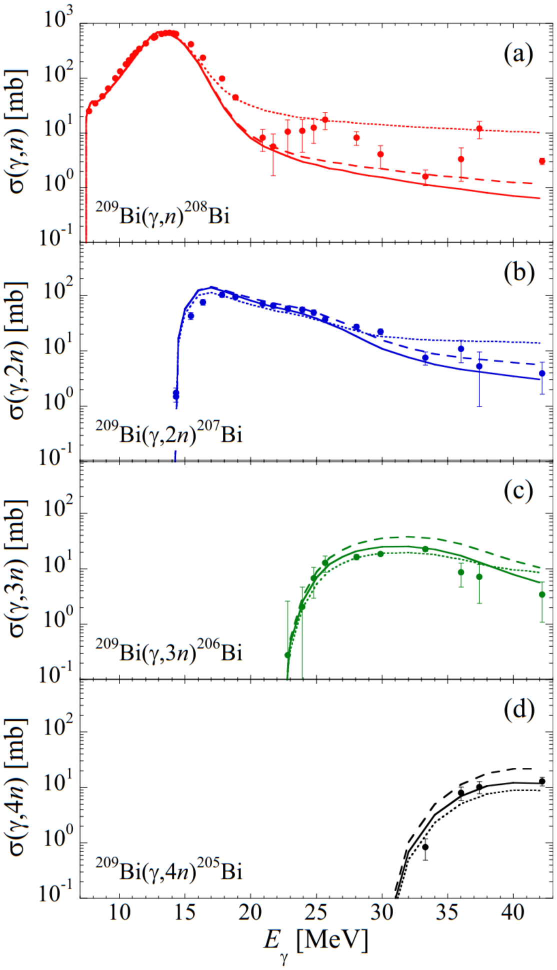

Figure 20: Comparison of the obtained partial cross sections, $\sigma(\gamma,\nu\text{n})$, ν = 1–4, in ^{209}Bi with the TALYS calculation obtained with the different parametrizations, for details see Ref. [117]. Reprinted figure with permission from Ref. [117]. Copyright 2019 by the American Physical Society.

had overlapping neutron kinetic energy spectra and it is difficult to separate them. An algorithm has been developed to overcome this limitation. The initial kinetic energy spectra of neutrons produced in the photodisintegration reaction are computed from relativistic kinematics for given initial photon energy and a specific reaction channel. The simulation is done within the GEANT4 toolkit [151]. The measured light-output response for the Blowfish detectors is used in the simulation. Neutrons, corresponding to different open channels, have specific angular distributions. The corresponding differential cross section is expressed in terms of expansion of Legendre functions [52, 140, 153]

$$\frac{d\sigma_n(\theta,\phi)}{d\Omega} = \frac{\sigma_{tot}(\gamma,n)}{4\pi}\left[1+\sum_{k=1}^{\infty} a_k P_k(\cos\theta) + \sum_{k=2}^{\infty} e_k P_k^{(2)}(\cos\theta)\cos(2\phi)\right], \tag{78}$$

where, again, $P_k^{(q)}$ are the associated Legendre polynomials (see appendix A) and a_k and e_k are their coefficients. The angle θ is the polar angle and ϕ is the angle from the polarization vector. The final result of the simulation is a computed neutron yield for each detector along with ToF and LOS spectra. The simulation is run for each reaction channel and each associated Legendre function coefficient. The next step is to fit the simulated ToF spectra to the measured ToF spectra. As a result, the associated Legendre function coefficients a_k and e_k are determined for the different reaction channels.

In another series of experiments, the photodisintegration of ^{3}He was studied utilizing a polarized target [134–136], see also Sec. 4.7. The neutrons from the three-body photodisintegration of ^{3}He were detected using 16 liquid scintillator detectors placed 1 m away from the center of the target at laboratory angles of 30°, 45°, 75°, 90°, 105°, 135°, 150°, and 165°. Neutron energy spectra were generated based on the extracted ToF for each incident photon energy and detector angle. The background was subtracted using a reference N_2 cell and normalization to the γ-beam flux. The background-subtracted yields, $Y_i^{P/A}$, i denotes the i^{th}-energy bin, were combined and the yields for parallel, P, and anti-parallel, A, spin-helicity states were extracted as

$$Y_i^P = \frac{1}{2}\left[Y_i^P\left(1+\frac{1}{P_tP_\gamma}\right) + Y_i^A\left(1-\frac{1}{P_tP_\gamma}\right)\right] \tag{79}$$

$$Y_i^A = \frac{1}{2}\left[Y_i^P\left(1-\frac{1}{P_tP_\gamma}\right) + Y_i^A\left(1+\frac{1}{P_tP_\gamma}\right)\right], \tag{80}$$

where P_γ and P_t are the beam and target polarization, respectively. The double differential cross section is defined as

$$\frac{d^2\sigma^{P/A}(\gamma,n)}{d\Omega dE_n} = \frac{Y_i^P}{\epsilon_i \Delta\Omega \Delta E_n N_T}, \tag{81}$$

where ϵ_i is the detector efficiency at the i^{th} energy bin, $\Delta\Omega$ is the acceptance from the 40-cm-long target to the corresponding neutron detector, ΔE_n is the width of the neutron energy bin, and N_T is the ^{3}He target thickness. Double differential cross sections obtained in these experiments are shown in Fig. 21.

2.5.4 Neutron angular distributions and neutron polarization asymmetries

Neutron energies are determined with the ToF technique, and $E1$ or $M1$ resonances are identified by measuring neutron angular distributions. The angular distribution of nucleons, consistent with the conservation principles of angular momentum and parity, was derived by Agodi [155]. For nucleons emitted from states excited via dipole transitions with linearly-polarized γ rays the neutron angular distribution, $W_n(\theta,\phi)$, is

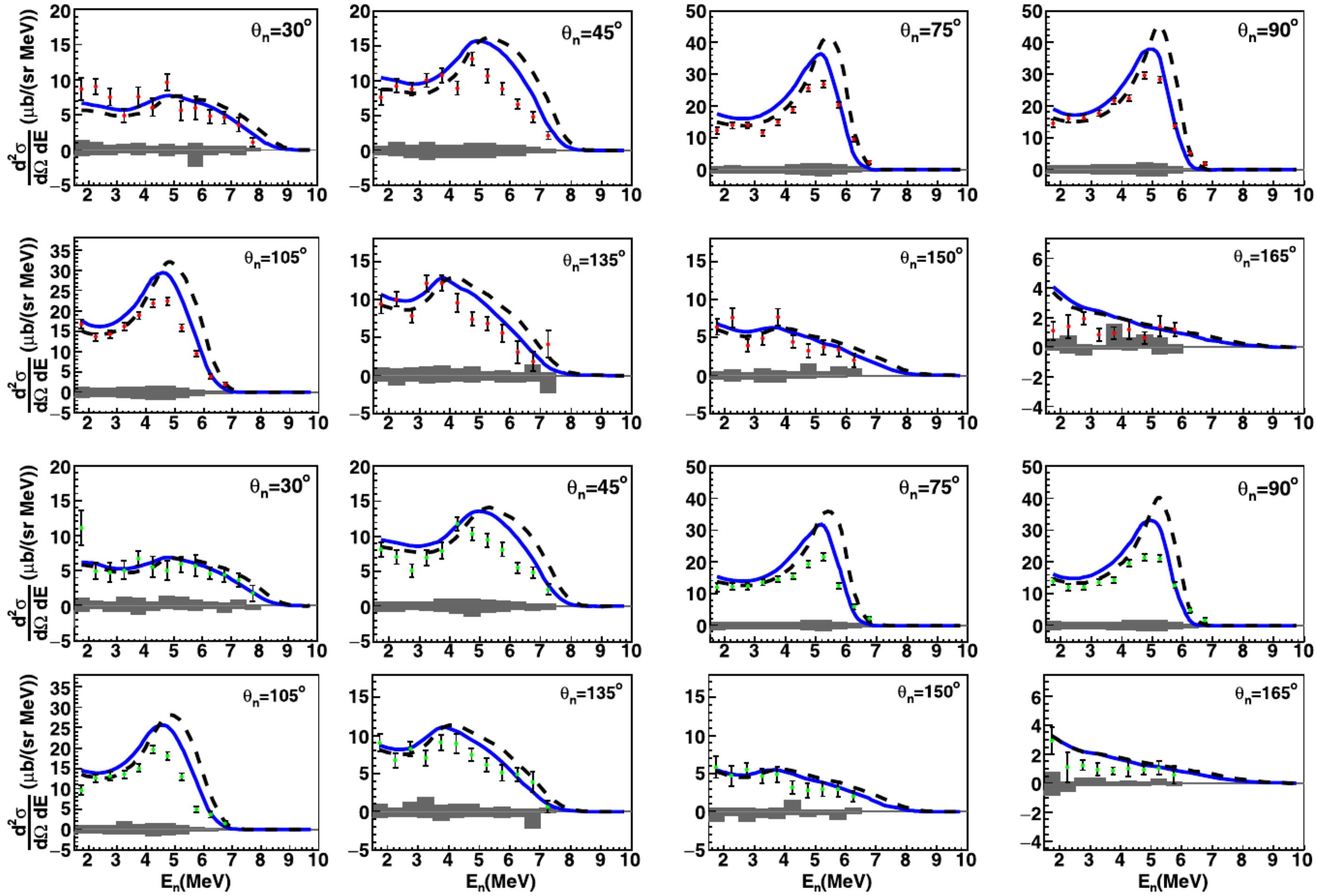

Figure 21: Spin-dependent double-differential cross sections for both parallel (two top rows) and anti-parallel (two bottom rows) spin states for eight neutron laboratory angles as a function of E_n, at $E_\gamma = 16.5$ MeV. The band at the bottom of each histogram shows the combined systematic uncertainties. See Ref. [136] for details related to the comparison with theory (solid and dashed lines). Reprinted figure from Ref. [136] with permission from Elsevier.

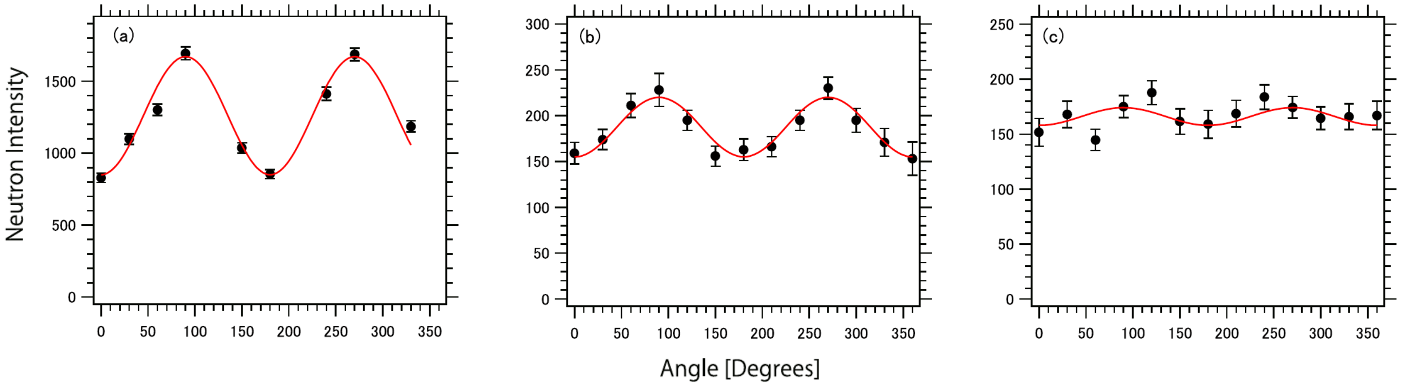

Figure 22: Angular distributions of neutrons of (γ,n) reactions on (a) Au, (b) NaI, and (c) natural Cu targets. The solid lines are obtained by χ^2-fitting with a function of $a + b \cdot cos(2\phi)$. Reprinted figure from Ref. [154] with permission from Elsevier.

$$W_n(\theta,\phi) = \frac{3}{8\pi}[\sin^2\theta(1+\cos 2\phi)]. \tag{82}$$

The angular distribution of nucleons emitted from states excited via dipole transitions with linearly-polarized γ rays at the polar angle of $\theta = 90°$ should follow a simple function: $a + b \cdot cos(2\phi)$, where ϕ is the azimuthal angle. Experiments at the NewSUBARU facility confirmed this distribution [154, 157]. Results from these measurements are presented in Fig. 22.

Generally assuming dipole and quadrupole transitions, the angular distribution of prompt neutron emission induced by linearly polarized photon beams is

$$\begin{aligned} W_n(\theta,\phi) &= a + b\sin^2(\theta) + c\sin^2(2\theta) \\ &\quad + P_\gamma\cos(2\phi)[b\sin^2(\theta) + c\sin^2(2\theta)]\,, \end{aligned} \tag{83}$$

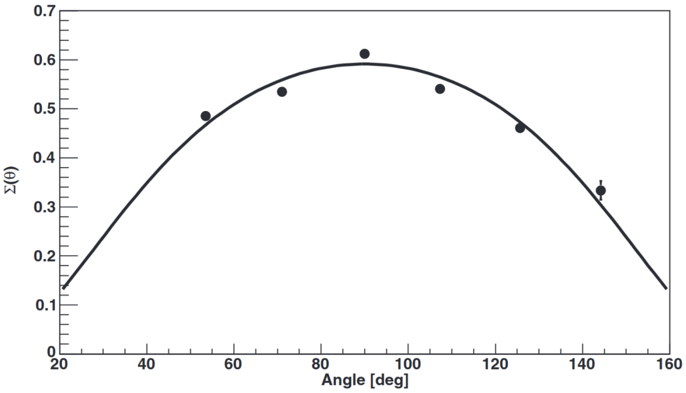

Figure 23: The measured polarization asymmetries $\epsilon_n(\theta)$ in the ^{9}Be(γ,n$_0$) reaction at a beam energy of 10.0 MeV are fit using Eq. (85). Reprinted figure with permission from Ref. [156]. Copyright 2013 by the American Physical Society.

where P_γ is the degree of beam polarization and the a and b coefficients are normalized to $a + b = 1$. The coefficient b is understood as equivalent of polarization asymmetry at scattering angle $\theta = 90°$. The corresponding analyzing power is defined as follows

$$\Sigma(\theta) = \frac{\sum_{\phi=0°}^{\phi=180°} W_n(\theta,\phi) - \sum_{\phi=90°}^{\phi=270°} W_n(\theta,\phi)}{\sum_{\phi=0°}^{\phi=180°} W_n(\theta,\phi) + \sum_{\phi=90°}^{\phi=270°} W_n(\theta,\phi)}\,. \tag{84}$$

Considering dipole transitions, only, hence $c = 0$, the normalization condition $a + b = 1$, and a fully polarized photon beam ($P_\gamma = 1$), the analyzing power simplifies to

$$\Sigma(\theta) = \frac{b\sin^2(\theta)}{1 - b + b\sin^2(\theta)}\,. \tag{85}$$

The prompt neutron polarization asymmetry, $\epsilon_n(\theta)$, is defined as

$$\epsilon_n(\theta) = \frac{\sum_{\phi=0°}^{\phi=180°} Y(\theta,\phi) - \sum_{\phi=90°}^{\phi=270°} Y(\theta,\phi)}{\sum_{\phi=0°}^{\phi=180°} Y(\theta,\phi) + \sum_{\phi=90°}^{\phi=270°} Y(\theta,\phi)}, \tag{86}$$

where $Y(\theta,\phi)$ denotes the normalized yield in a detector located at a scattering angle θ and azimuthal angle ϕ. At HIγS, the polarization asymmetry of prompt neutrons was measured in the ^{9}Be(γ,n$_0$) reaction [156] and in photofission [158, 159]. An example of the measured neutron polarization asymmetry from Ref. [156] is shown in Fig. 23. It has been suggested to use this technique for identification of special nuclear materials (SNM) [160], see also Sec. 5.2.

2.5.5 Excitations of isomers and isomeric ratios

From the first studies on isomeric states [161], the interest of investigating isomers and their decay continues, since they provide important information on nuclear structure. In the last two decades both, the excitations of isomers [162–164] and isomeric ratios [165–183] have been studied in photodisintegration experiments.

The decay of a compound nucleus obtained in a nuclear reaction proceeds through transitions of primary and intermediate states leading to the formation of the isomeric and ground states. The ratio of the probabilities for forming these states is called the isomeric ratio, *IR*. In *IR* experiments, nuclear structure problems related to the level density, namely the spin cut-off parameter and the level density parameter, as well as different aspects of the reaction mechanism are studied. The isomeric ratio depends on the target spin, the energy and the type of projectile, and on many other nuclear effects.

In photoneutron experiments, *IR* is defined as the ratio of the isomer production cross section, $\sigma_{i^*}(\gamma,n)$ over the total (γ,n), cross section, $\sigma_{tot}(\gamma,n)$,

$$IR = \frac{\sigma_{i^*}(\gamma,n)}{\sigma_{tot}(\gamma,n)}. \tag{87}$$

The statistical model of Huizenga and Vandenbosch [184,185] has been applied to describe *IR* in nuclear reactions induced by different projectiles.

These experiments were done with bremsstrahlung. In this case, the *IR* is defined as the yield of the isomeric state to that of the ground state, and is expressed as

$$IR = \frac{\int_{E^i_{th}}^{E^{max}_\gamma} \sigma_i(E_\gamma) f(E_e,E_\gamma) dE_\gamma}{\int_{E^g_{th}}^{E^{max}_\gamma} \sigma_g(E_\gamma) dE_\gamma}, \tag{88}$$

where E^{max}_γ is the bremsstrahlung end-point energy, E^g_{th} and E^i_{th} – the threshold energies for population of ground and isomeric states, respectively, $\sigma_g(E_\gamma)$ and $\sigma_i(E_\gamma)$ – the cross sections of ground and isomeric states, and $f(E_e,E_\gamma)$ – the bremsstrahlung photon flux.

The activation technique is used in these experiments, in which the target is irradiated for a certain period of time and, afterwards, the γ decay is measured. Almost all experiments for studies of isomeric ratios were carried out at the MT-25 microtron in Dubna, Russia, the M-30 microtron in Uzhgorod, Ukraine, the SB-50 microtron in Tashkent, Uzbekistan, and recently at the LUE-40 linac at NSC KIPT in Kharkov, Ukraine.

Several experiments were performed to measure halflives of isomers [162,164] or of the ground states of isotopes [163]. At the NewSUBARU facility, the halflife of the ^{184}Re ground state populated via the ^{185}Re(γ,n) reaction [163] and of an isomer in ^{164}Ho populated in the ^{165}Ho(γ,n) reaction [164] were measured. At the Idaho Accelerator, the halflive of an isomer in ^{24}Na was reported [162]. In another measurement, the yield for the excitation of ^{180g}Ta ($J^\pi = 1^+$) was deduced from measurements of γ rays emitted following the electron capture and β decays of the 8.15-h ground state [165]. As a result, the probability $\sigma_{i^*}/(\sigma_{i^*}+\sigma_g)$ for the production of the ^{180m}Ta isomer ($J^\pi = 9^-$) after photoabsorption was deduced in the energy region from 8 to 13 MeV.

2.5.6 (γ,n) *vs.* (n,γ) reactions

A series of experiments were performed aiming at the simultaneous understanding of (γ,n) and (n,γ) reactions. This was done by systematic measurements for the Zr [106], Mo [111], and Sn [105, 109] isotopes. In these experiments, photodisintegration was used to improve the prediction of the radiative neutron capture cross section by experimental constraining the PSF, which enters in the statistical model calculations. The goal is, by a systematic study of photoneutron and neutron capture reactions in an isotopic chain, to model the PSF for a given nucleus formed by neutron capture on the radioactive nucleus, which cannot be measured directly. The method determines the PSF which commonly quantifies radiative neutron capture and photoneutron cross sections by using the experimental data. The (n,γ) data is used to constrain on the PSF below the neutron evaporation threshold, S_n, while photoneutron cross sections provide an experimental constraint in absolute scale on the PSF around

S_n. This is done, relying on the Brink hypothesis [186], which simplifies the modeling of average photodeexcitation and photoabsorption probabilities, under the assumption that both depend on the energy of the involved γ-ray transition only.

For example, in the study of the molybdenum isotopes, photoneutron cross sections for two radioactive nuclei, ^{93}Mo and ^{99}Mo, are deduced with the γ-ray strength function method. The predicted neutron capture cross sections for ^{93}Mo and ^{99}Mo are displayed in Fig. 24. The resulting cross sections are also compared with the JENDL-4.0, ENDF/B-VII.1, and ROSFOND-2010 evaluated nuclear data files [187]. In this particular case, the resulting Maxwellian-averaged cross sections of astrophysical interest amount to 380 ± 200 mb for ^{93}Mo(n,γ)^{94}Mo and 410 ± 130 mb for ^{99}Mo(n,γ)^{100}Mo at 30 keV. The ^{99}Mo(n,γ)^{100}Mo estimate and, consequently, also the ENDF/B-VII.1 and JENDL-4.0 evaluations, are found to be significantly larger than the theoretical cross sections of 240 ± 40 mb recommended in Ref. [188].

2.6 Photofission

A specific type of a photonuclear reaction is the photofission process [189, 190], denoted as (γ,f), in which after the absorption of a photon, the nucleus splits in two or more fragments, see Fig. 2. This reaction proceeds through the formation of a compound nucleus. In the reaction, γ rays and neutrons are also emitted. The photofission cross section, $\sigma(\gamma,\mathrm{f})$, has a one- or two-humped peak in the region of the GDR.

Ever since its discovery, fission has been an active field of research both from theoretical point of view and with respect to practical applications. For recent reviews on theoretical and experimental advances in the field see Refs. [191, 192]. Photofission research is carried out with bremsstrahlung radiation, LCB quasimonoenergetic photon beams as well as with Coulomb excitation in peripheral heavy-ion collisions. Different problems have been addressed in photo-fission experiments in the last two decades, such as

- cross-section measurements, including sub-barrier photofission studies,
- studies of kinetic energy, mass, charge, and angular momentum distributions of fission fragments,
- measurements of isomeric ratios of fission fragments,
- comparison of fission yields induced by different probes,

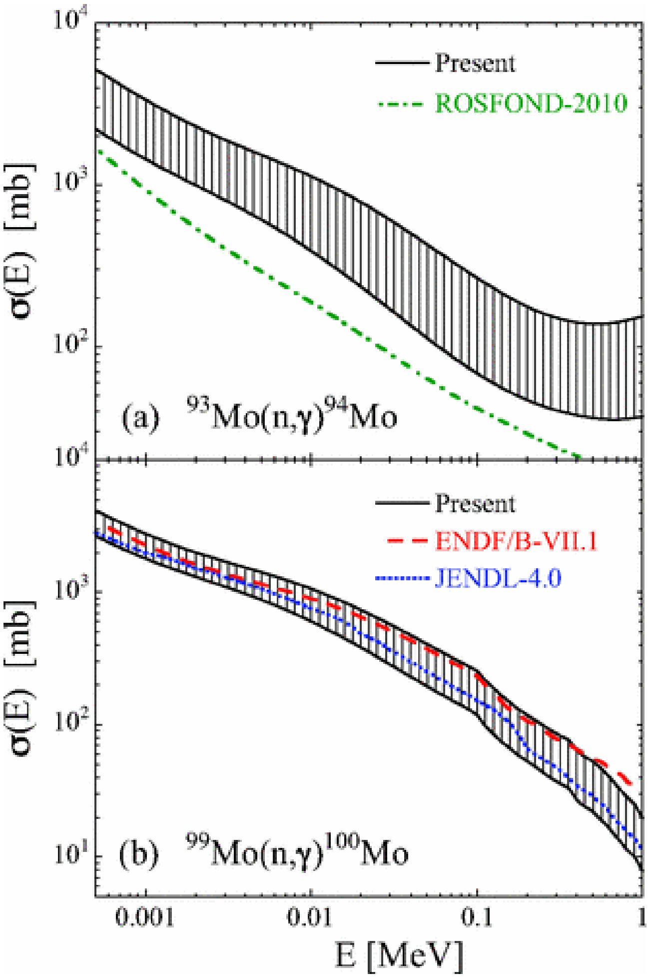

Figure 24: TALYS predictions for the radiative neutron capture cross sections (a) of ^{93}Mo(n,γ)^{94}Mo and (b) ^{99}Mo(n,γ)^{10}Mo. The error bands include uncertainties in the experimental PSF, as well as the theoretical nuclear level densities. The dotted, dashed, and dash-dot curves correspond to different evaluations, see text and Ref [111]. Reprinted figure with permission from Ref. [111]. Copyright 2013 by the American Physical Society.

- measurements of emitted prompt and delayed neutrons and γ rays.

Examples of such experiments are discussed in Sec. 2.6.2. Sub-barrier photo-fission experiments are discussed in Sec. 4.10.

2.6.1 Computer codes for photofission calculations

The modeling of the re-ordering of the nucleons from an excited nucleus into two or more fragments has been and is a challenge for nuclear theory. Nowadays, sophisticated models try to map the nuclear potential energy landscape in a multi-dimensional deformation space [193]. Fragment properties are calculated as a result of selection different fission modes, often together with a statistical population of states. The major problem is that a fissioning nucleus is described as an open system that evolves both, quasi-bound configurations and a continuum of possible configurations on the fission path, finally forming hundreds of different fragments with continuous distributions of different shapes, kinetic energies, excitation energies, and angular momenta. Estimates of the properties of the fission fragments still relies on empirical models. The excitation energy of the primary fragments is released by prompt-neutron and prompt-γ emission, which also need to be described.

The GEneral description of Fission observables (GEF) modeling code is the state-of-the-art tool for simulations of nuclear fission [194]. It describes the observables for spontaneous fission, neutron-induced fission, and, more generally, for fission of a compound nucleus from any other entrance channel, with given excitation energy and angular momentum. The results of the GEF model calculations are compared with fission barriers, fission probabilities, fission-fragment mass and isotope distributions, isomeric ratios, total kinetic energies, and prompt-neutron and prompt-γ yields.

2.6.2 Methodological examples of photofission experiments

Photofission product yields: In the last two decades photofission product yields (FPY) have been measured in both, bremsstrahlung [195–201] and LCB [202,203] γ-beam experiments. In bremsstrahlung experiments, the fissile target is irradiated with beams with different end-point energy. For measurements of the FPY, the activation technique is used. After a certain period of irradiation, the target was transported to a low-background Ge detector setup where the decay of the fission products is measured. A key component in obtaining accurate FPY data is the precise quantitative determination of the number of fission events which occur during the measurements. To accomplish this, a specially fabricated dual-fission ionization chamber (DFC) was usually used in an experiment at HIγS [203]. Two thin reference foils, ^{235}U in the first chamber and ^{239}Pu in the second chamber, were utilized. The ^{239}Pu thick activation target was placed at the center of the fission chamber. Pulse-height fission spectra produced by the DFC during the photon irradiation were measured. They are integrated to give the total number of fission events recorded in the individual chambers.

A program has been initiated at the Triangle Universities Nuclear Laboratory (TUNL) to carry out systematic comparisons of the FPY from neutron and photon induced fission on actinide nuclei, starting with ^{235,238}U and ^{239}Pu [202–205]. This study is intended to provide insight into the dependence of the FPY on the mechanism for inducing fission in the entrance channel. In particular, differences in the FPY for neutron and γ induced fission would indicate a connection between the FPY and the angular momentum of the fissioning compound nucleus.

Kinetic energy, mass, charge and angular momentum distributions of fission fragments: In experiments aiming at the detection of fission fragments, twin Frisch-gridded ionization chambers (FGIC) are used [206, 207], see also Sec. 3.4.5 for description of the FGIC. The fission-fragment mass distributions were measured at different bremsstrahlung end-point energies [206, 207]. A typical result of such a measurement is presented in Fig. 25. Pre-neutron mass distribution, mass distribution before the emission of neutrons, is shown in the the figure.

In these experiments, the fissile target is placed at the center of the common cathode of the FGIC. The setup allows detection of fission fragments in an almost 4π solid angle. At large emission angles multiple scattering of the fragments in the target material and energy straggling deteriorate the energy resolution.

The determination of fission fragment masses is based on the well established double kinetic-energy (2E) technique [208]. Momentum conservation, with the approximation that the sum of the masses of the two fission fragments is equal to the mass of the fissioning nucleus, results in an energy relation.

$$A_i = A_f \frac{E_i}{TKE}, \tag{89}$$

where $A_i, i = 1, 2$ are the mass numbers of the fission fragments, E_i - their kinetic energies, A_f the mass number of the fissioning nucleus, and $TKE = E_1 + E_2$ is the total kinetic energy. Since fission-fragment mass numbers and TKE are correlated, the fission-fragment yield as function of pre-neutron fragment-mass number and TKE can be extracted from the data, assuming some fission-model dependence. The emission angle is extracted from the drift time of ionization electrons, which is used for the determination of angular distributions. A detailed description of the procedure for determining the emission angles can be found in Ref. [209]. Fission fragment angular distributions, $W_f(\theta)$, can also be extracted from the data. They are described with the relation

$$W_f(\theta) = A + B\sin^2(\theta) + C\sin^2(2\theta). \tag{90}$$

Mass and TKE dependences of the angular distributions of the fission fragments were reported [207, 210], too.

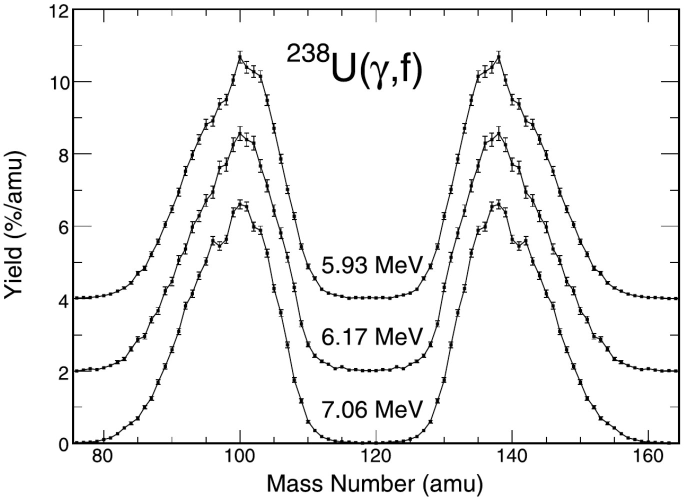

Figure 25: Pre-neutron mass distributions for photofission of ^{238}U with 6.5, 7.0, and 8.5 MeV bremsstrahlung. The curves are consecutively displaced by two percent units, and the average excitation energy is indicated above each distribution. Reprinted figure from Ref. [206] with permission from Elsevier.

3 Photon sources and instrumentation

3.1 Bremsstrahlung

A very straightforward way to generate an intense photon bath with continuous energy distribution is electron bremsstrahlung. The principle idea is depicted in the upper part of figure 26. An electron beam is decelerated (or - depending on the radiator thickness - stopped completely) in a radiator target. The energy and angle integrated photon flux scales quadratically with the charge Z of the radiator target nuclei. The generated bremsstrahlung spectrum for a thin radiator target (assuming one interaction only) can be approximated by the analytical formula of Schiff [69]. Schiff used the notations E_0 for the energy of incident electron, E for the energy of the scattered electron, k for the energy of the emitted photon, μ for the rest energy of the electron, θ for the angle between photon and electron, Z for the atomic number of the radiator target, and the screening constant $C = 111$. The approximation is true under the assumption that E_0, E, and k are large in comparison to μ. If θ is replaced by the reduced angle $x = E_0\theta/\mu$ one can derive the cross section for the energy-angle distribution:

$$\begin{aligned}\sigma\left(k,x\right)dkdx =&\frac{4Z^2}{137}\cdot\left(\frac{e^2}{mc^2}\right)\frac{dk}{k}xdx\left[\frac{16x^2E}{\left(x^2+1\right)^4E_0}-\frac{\left(E_0+E\right)^2}{\left(x^2+1\right)^2E_0^2}\right.\\ &\left.+\left(\frac{E_0^2+E^2}{\left(x+1\right)^2E_0^2}-\frac{4x^2E}{\left(x^2+1\right)^4E_0}\right)\ln\left(M(x)\right)\right],\end{aligned} \tag{91}$$

$$\frac{1}{M(x)}=\left(\frac{\mu k}{2E_0E}\right)^2+\left(\frac{Z^{1/3}}{C\left(x^2+1\right)}\right)^2 \tag{92}$$

To obtain the energy spectrum, this equation is integrated over x. The calculation is not valid for large angles but most of the radiation is directed under forward angles:

$$\begin{aligned}&dk\int_0^\infty\sigma\left(k,x\right)dx=\\ &\frac{2Z^2}{137}\left(\frac{e^2}{mc^2}\right)^2\frac{dk}{k}\left[\left(\frac{E_0^2+E^2}{E_0^2}-\frac{2E}{3E_0}\right)\right.\\ &\times\left(\ln\left(M(0)\right)+1-\frac{2}{b}\tan^{-1}(b)\right)\\ &\left.+\frac{E}{E_0}\left(\frac{2}{b^2}\ln\left(1+b^2\right)+\frac{4\left(2-b^2\right)}{3b^3}\tan^{-1}(b)-\frac{8}{3b^2}+\frac{9}{2}\right)\right]\end{aligned} \tag{93}$$

with $b = (2E_0EZ^{1/3}/C\mu k)$. Some more sophisticated versions of the Schiff formula have been published later, see, e.g. Refs, [211–213].

Nowadays, the energy spectrum of the bremsstrahlung photons is usually calculated by means of different Monte Carlo simulation codes [214–216]. The main challenge is to extract the bremsstrahlung flux close to the endpoint energy of the spectrum. This depends strongly on the energy of the electron beam and its fluctuations. A careful monitoring of this energy is, therefore, mandatory for many experiments.

The outer portion of the bremsstrahlung cone from a thin radiator ($< 10^{-3}$ radiation lengths) is partly polarized [217]. The optimum degree of polarization with an electron beam energy E_e can be reached at an off-axis angle $\theta = m_e c^2/E_e$. However, the degree of polarization decreases with the energy of the bremsstrahlung photons with a typical maximum value amounting to 10-20% only, see Refs. [24, 218]. In addition, the thin radiator leads to a lower photon intensity at similar electron current [10]. Nevertheless this technique has been used in a number of seminal experiments to determine the parity quantum number of excited states in nuclei.

In the following, a few selected examples for bremsstrahlung facilities are shortly described. Please note that most bremsstrahlung setups worldwide are used for medical and industrial applications and will not be discussed here.

The Darmstadt High Intensity Photon Setup (DHIPS) at TU Darmstadt uses a continuous wave (cw) electron beam with currents of up to 60 μA and a maximum energy of 10 MeV stemming from the injector of the superconducting electron accelerator S-DALINAC to produce a bremsstrahlung beam. The beam is stopped completely in a 14 mm thick Cu disk which rotates to prevent heat damage. The

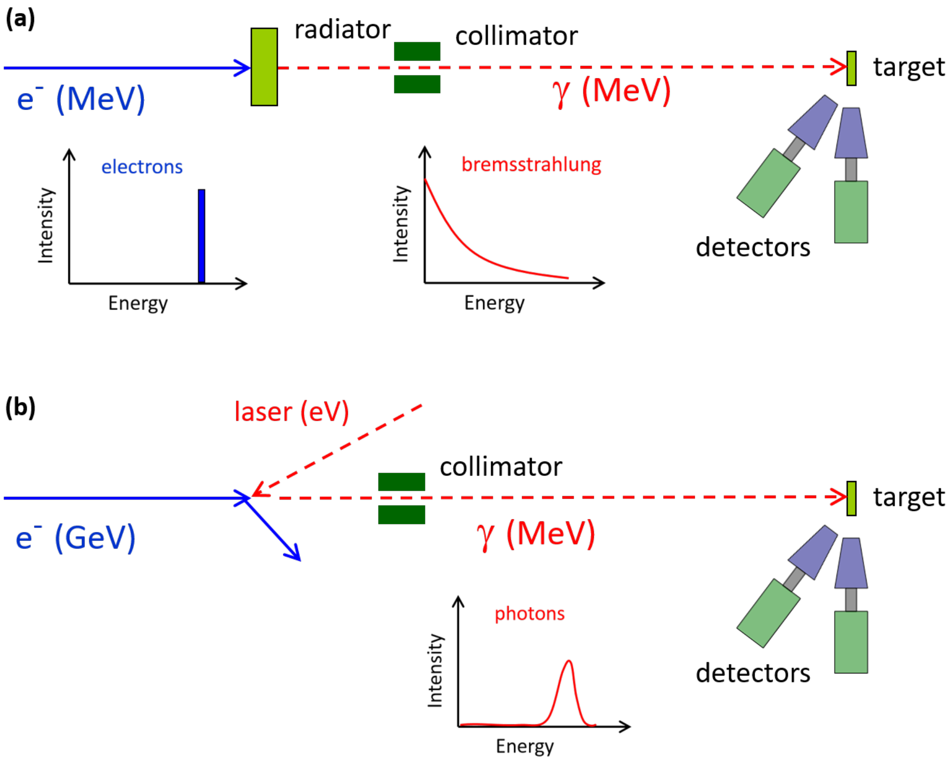

Figure 26: Principle of generating a photon beam by (a) bremsstrahlung or by (b) laser Compton backscattering.

photon beam is collimated by a conical Cu collimator with a length of 95.5 cm and an exit diameter of 20 mm. A previously used Ta bremsstrahlung target and a Pb collimator [219] were replaced by Cu because of the rather high neutron binding energies of the stable Cu isotopes [220] which avoids neutron induced background in the γ detectors. At target position, the spectral photon flux rate (commonly denoted as "photon flux") amounts to around 10^3 photons/(eV $\cdot$ cm^2 $\cdot$ s) at an energy of $E_\gamma=0.7\cdot E_e$. The target is usually surrounded by three well-shielded HP(Ge) detectors, see Ref. [221] for a detailed description.

The γELBE facility at the Helmholtz-Zentrum Dresden-Rossendorf in Germany uses a superconducting cw electron linear accelerator (e-linac) to generate photon beams with maximum energies of up to 13 MeV typically (which is the neutron separation energy of ^{27}Al in the Aluminum collimator) and currents up to 1 mA [215]. The electron beam is decelerated in a Niobium radiator with variable thickness between 1.5 and 11 mg/cm^2. The main fraction of the electrons passes the radiator without interaction and is deflected by a dipole magnet. Off-axis bremsstrahlung can be used to generate partly polarized beams. The experimental area is separated from the bremsstrahlung-generation area by a heavy concrete wall. The photon beam is transported to the scattering target in an evacuated beam pipe to avoid scattering with air molecules. The scattering target is usually surrounded by four standard HPGe detectors with 100% efficiency each (relative to a 7.68 cm × 7.68 cm NaI detector) and one HPGe Euroball Cluster detector. All detectors are actively shielded by BGO scintillation shields.

The bremsstrahlung facility at the MT-25 microtron at the Flerov Laboratory of the JINR in Dubna, Russia operates with an electron energy between 10 and 25 MeV with a current of up to 20 μA [222]. Tungsten with a thickness of 30 mm is used as a converter material. The energy integrated total flux of bremsstrahlung photons is given as 10^{14} photons/s [223–225]. A very similar setup (where the bremsstrahlung is mainly used to produce neutrons) is installed at the Nuclear Physics Institute of the Czech Academy of Sciences in Prague, Czech Republic [226].

	γELBE/HZDR	S-DALINAC/TUD	MT-25/JINR	PRISM/LLNL
E_{max}	13 MeV	10 MeV	25 MeV	25 MeV
$I_{max}(e^-)$	1000 μA	10 μA	20 μA	30 μA
radiator material:	Nb (Z=41)	Cu (Z=29)	W (Z=72)	W (Z=72)
radiator thickness:	10-100 μm	14000 μm	30000 μm	15000 μm
photon flux:	$10^2\ \gamma/(\mathrm{eV}\cdot\mathrm{cm}^2\cdot\mathrm{s})$	$10^3\ \gamma/(\mathrm{eV}\cdot\mathrm{cm}^2\cdot\mathrm{s})$	$10^{12}\ \gamma/\mathrm{s}$	$10^{14}\ \gamma/\mathrm{s}$

Table 1: Parameters of four selected bremsstrahlung facilities. Note that either the differential photon flux at target position (ELBE, S-DALINAC) or energy and angle integrated photon fluxes (MT-25, PRISM) are given. The radiator material and thickness can be varied at all facilities, given are the standard values.

At the Lawrence Livermore Laboratory in Livermore, CA, USA the recently installed S band accelerator PRISM (which stands for "Photonuclear Reactions for Isotopic Signature Measurements") delivers presently an electron beam in the energy range from 15 to 25 MeV with an average electron current of up to 30 μA [227]. The maximum design energy is 55 MeV. Bremsstrahlung with an integrated intensity of about 10^{14} photons/s is generated in a tungsten radiator. First experiments investigating the photoactivation of ^{169}Tm have recently been performed [228]. A comparison of some parameters of the four aforementioned facilities is given in Table 1.

The High Voltage Research Laboratory (HVRL) at the Massachusetts Institute of Technology (MIT) operates an electron accelerator which can be used for Nuclear Resonance Fluorescence experiments in the energy range up to about 3.5 MeV with currents in the 100 μA range [229]. The electrons impinge on a 100 μm thick Au radiator target backed by 1 cm Cu for cooling purposes. In experiments on the actinides ^{235}U, ^{239}Pu and ^{240}Pu a number of resonances has been detected in the energy range between 2 and 3 MeV which are interesting not only from a nuclear structure point of view but as well for non-intrusive, unique detection of these isotopes [230, 231].

At the NSC KIPT in Kharkov, Ukraine [232], an S-band e-linac (LUE-40) with an energy range between about 35 and 95 MeV is utilized to generate the bremsstrahlung beam. The maximum pulsed electron current is 70 mA with a repetition rate of 50 Hz. The typical average electron current amounts to 6 μA. The photon beam has been used in a number of photoactivation experiments, e.g. to study (γ,xn) cross sections [233].

The Idaho Accelerator Center (IAC) at Idaho State University, USA [234] operates four e-linacs with maximum electron energies up to 40 MeV and average maximum currents between 85 and 240 μA. Bremsstrahlung is produced by means of tungsten or tantalum radiators with variable thicknesses [235]. Examples for experiments performed at the IAC are photon activation analysis studies in the photon energy range between 10 and 30 MeV [236]. In addition, they run a program for medical isotope production, see section 5.5.

A new high intensity bremsstrahlung source using electrons from a superconducting e-linac with energies between 15 and 40 MeV and currents up to 1.5 mA is presently set up at the Turkish Accelerator and Radiation Facility (TARLA) in Ankara, Turkey. The facility is planned to become operational in 2022 [237–239].

Bremsstrahlung beams are still a workhorse for many photonuclear studies.

3.2 Tagged photons

Bremsstrahlung beams with an 'energy tagging' of their γ quanta have been used in photonuclear science since the 1970s [240]. The principle of photon tagging is depicted in Fig. 27. If the bremsstrahlung beam is produced in a sufficiently thin radiator, it can be ensured that the vast majority of the photons originate from electrons that interacted with the radiator material only once. Therefore, the momentum of an incoming electron $\vec{p}_0$

$$\vec{p}_0 = \vec{p}_e + \vec{p}_\gamma + \vec{p}_{recoil} \tag{94}$$

is shared between the momenta of the scattered electron, the emitted photon, and the recoil of the nucleus given by $\vec{p}_e$, $\vec{p}_\gamma$, and $\vec{p}_{recoil}$, respectively. The scattered electron then exits the radiator with decreased kinetic energy E_e which is related to the energy of the produced bremsstrahlung photon

$$E_\gamma = E_0 - E_e \tag{95}$$

neglecting the recoil energy transferred to the involved nucleus. The electrons and the produced photons enter a dipole magnet, where the electrons are bend and their momentum is analyzed, while the photons pass straight through and hit the target and a beam dump, respectively. Measuring the energies E_e of the scattered electrons by usage of a magnetic spectrograph then provides the energies E_γ event by event when the observation of subsequent reactions induced by the produced bremsstrahlung beam is performed in coincidence with the signals from the spectrograph. Thus, despite the broad bandwidth of the continuous-energy bremsstrahlung distribution, photonuclear reactions induced by bremsstrahlung photons with measured 'energy tags' enable the determination of energy-resolved reaction cross sections.

One example facility is the low-energy photon tagger NEPTUN [241] at the S-DALINAC [242] at the TU Darmstadt which covers photon energies from 5 to 15 MeV with excellent energy resolution. Due to the combination of continuous-energy bremsstrahlung with the photon tagging technique, several γ-ray detection systems were characterized at NEPTUN exploiting quasi-monochromatic photon beams with variable energy [243, 244]. Recently, NEPTUN was upgraded to provide tagged photons in the range of 5 to 35 MeV for photon scattering and total photoabsorption experiments to determine the complete dipole strength from energies below particle thresholds to above the region of the IVGDR [242].

Tagged-photon beams are actively used in hadron physics and the interested reader is referred to Refs. [245–253] and references therein for further reading, since the scope of the present review article is on research activities in the energy range of nuclear structure.

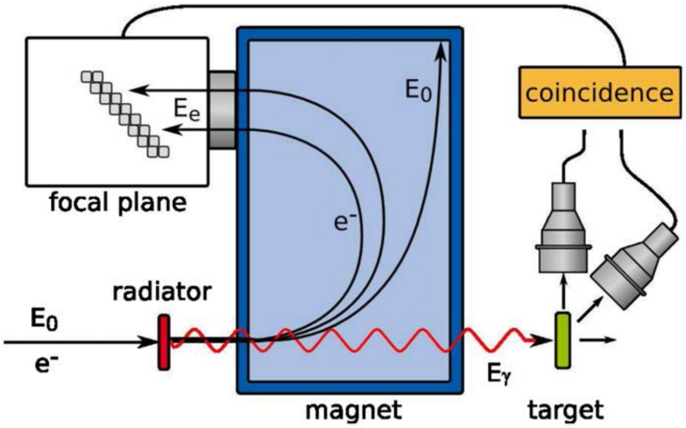

Figure 27: Principle of photon tagging. The energy of the produced bremsstrahlung photon E_γ is determined from the energy difference between the incident and scattered electron energy E_0 and E_e, respectively. Reprinted figure with permission from [241]. Copyright 2010 from Elsevier.

3.3 Laser Compton Backscattering

The technique of tagged photons discussed in the previous section provides information on the energy of the produced bremsstrahlung photons. However, this information requires a coincidence to the tagging system while the beam energy profile itself remains that of a continuous-energy bremsstrahlung spectrum. In contrast to that, the method of Laser Compton Backscattering (LCB) provides a real (almost) monochromatic beam without the need to tag the produced photons. While this provides superior conditions for some experiments, the continuous character of (tagged) bremsstrahlung yields advantages in others. Both methods should therefore be seen as complementary.

Nuclear physics experiments usually require high-brilliance and intense LCB photon beams. The influence of electron and laser beam properties on the bandwidth of the generated high-energy photon beam will be discussed in the following section, while conditions for optimal photon flux intensities will be elaborated afterwards. At the end of this section, a short summary of the parameters of current and future LCB facilities is given in Table 2.

3.3.1 Electron-photon interaction

In this paragraph, the energy of the Compton-scattered laser photon off an ultrarelativistic electron is briefly derived for the general case illustrated in Fig. 28. The incident laser photon with a momentum $\vec{p}_L = \hbar\vec{k}$ impinges the electron with a momentum $\vec{p}_e$ at an angle θ_i. The angle of the Compton-scattered photon with a momentum $\vec{p}_\gamma = \hbar\vec{k}'$ with respect to the incident electron and photon is expressed by θ_f and θ_p, respectively. The conservation of energy and momentum in collisions of relativistic particles is conveniently described by four-momentum conservation

$$p + k = p' + k' \tag{96}$$

where the four-momentum of the electron before and after the collision is $p = (E_e/c, \vec{p}_e)$ and $p' = (E'_e/c, \vec{p}'_e)$, respectively. Analogously, the four-momenta for the incident and scattered photon are denoted as $k = (E_L/c, \vec{p}_L)$ and $k' = (E_\gamma/c, \vec{p}_\gamma)$, respectively. The reaction is defined by the kinematics of the incoming electron and the incident and scattered photon. Therefore, Eq. (96) is converted to p' and squared to derive the general expression for the energy of the Compton-scattered photon

$$E_\gamma = \frac{(1-\beta\,\cos\theta_i)\,E_L}{(1-\beta\,\cos\theta_f) + (1-\cos\theta_p)\,E_L/E_e}\,, \tag{97}$$

with the electron velocity β relative to the speed of light c. Considering head-on collisions ($\theta_i = \pi$ and $\theta_p = \pi - \theta_f$), Eq. (97) can be simplified to

$$E_\gamma = \frac{(1+\beta)\,E_L}{(1-\beta\,\cos\theta_f) + (1+\cos\theta_f)\,E_L/E_e}\,. \tag{98}$$

It becomes clear that for given energies E_L and E_e, the energy of the scattered photon depends on the scattering angle θ_f only. Photons that are scattered at $\theta_f = 0$ have the highest energies, while the energy drops quickly for increasing scattering angles. With the focus on small scattering angles ($\theta_f \ll 1$) and ultrarelativistic electrons with a Lorentz factor $\gamma = 1/\sqrt{1-\beta^2} \gg 1$, Eq. (98) can be approximated to

$$E_\gamma \approx \frac{4\gamma^2\,E_L}{1 + (\gamma\theta_f)^2 + 4\gamma^2\,E_L/E_e}\,. \tag{99}$$

Neglecting the recoil term ($4\gamma^2\,E_L/E_e \ll 1$), the maximum photon energy is achieved for backscattering ($\theta_f = 0$):

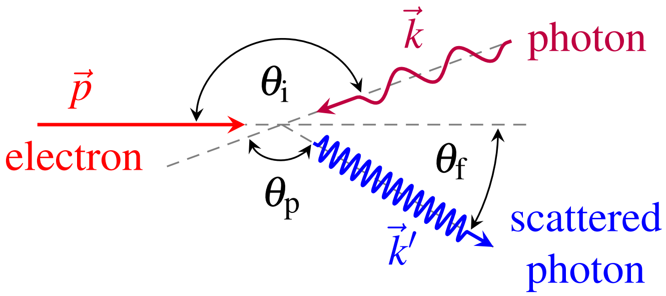

Figure 28: Schematic drawing of Compton scattering between an electron and a photon with a momentum of $\vec{p}$ and $\vec{k}$, respectively, at a collision angle of θ_i. The direction of the Compton-scattered photon (with momentum $\vec{k}'$) is defined by the angles θ_f and θ_p with respect to the incoming electron and initial photon.

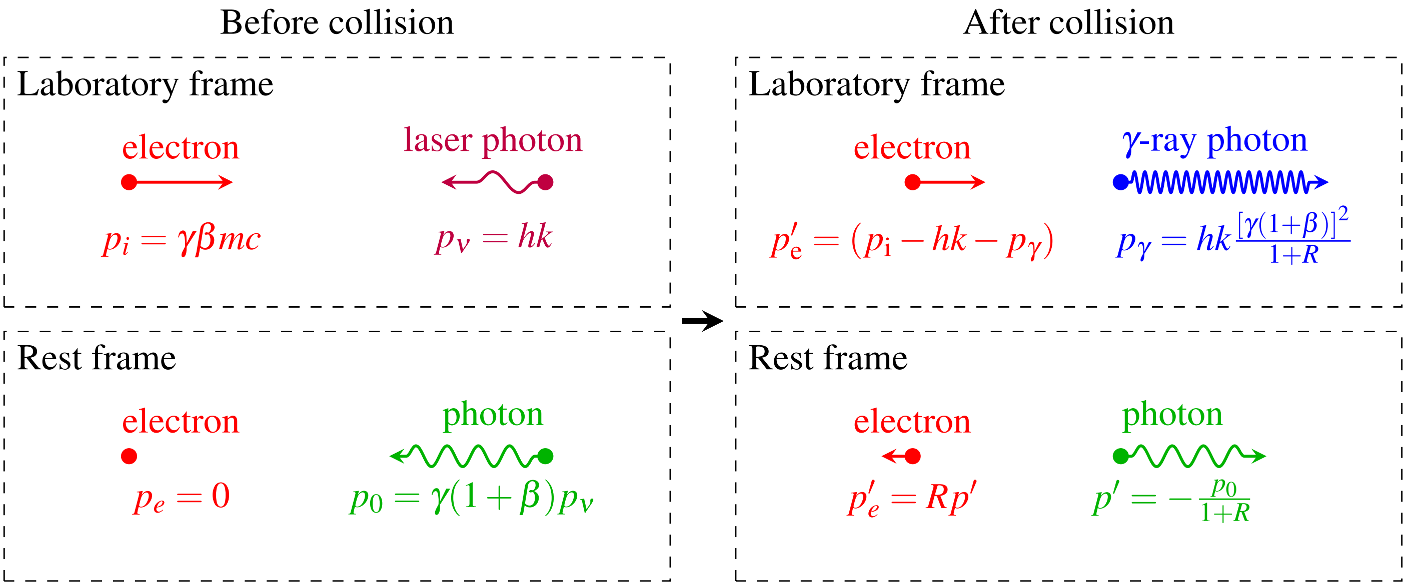

Figure 29: Scheme of the head-on collision of an electron and a low-energy optical photon. Before collision, the transformation from the laboratory frame to the rest frame of the electron induces an energy boost of the photon by a factor of $\gamma(1+\beta)$. After the collision in the rest frame of the electron, the Compton-backscattered photon gains an additional boost by a factor of $\gamma(1+\beta)$ in the transformation back to the laboratory frame. The recoil factor is given by $R = 2\gamma(1+\beta)(hk/mc)$.

$$E_\gamma^{max} \approx \frac{4\gamma^2 E_L}{1 + 4\gamma^2 E_L/E_e} \approx 4\gamma^2\, E_L\,. \qquad (100)$$

The generation of high-energy photons from LCB can also be understood in a more illustrative way depicted in Fig. 29. Assume a head-on collision ($\theta_i = \pi$) of an electron and a laser photon in the laboratory frame shown in the upper left panel of Fig. 29. A transformation to the rest frame of the electron results in a Lorentz boost of the photon of $\gamma(1+\beta)$ before the collision (lower left panel). After the head-on collision in the rest frame, the photon experiences a maximum momentum change when Compton backscattered (lower right panel). Consequently, the transformation back to the laboratory frame (upper right panel) induces an additional Lorentz boost of $\gamma(1+\beta)$ to the photon. Neglecting the recoil factor $R = 2\gamma(1+\beta)(hk/mc)$, this results in a final maximum energy of $E_\gamma^{max} = \gamma^2(1+\beta)^2 E_L$, which simplifies to Eq. (100) for ultrarelativistic electrons ($\beta \approx 1$).

Conclusively, laser photons are boosted by a factor of roughly $4\gamma^2$ into the MeV regime, which is the interesting range for nuclear physics experiments, when scattered off ultrarelativistic electrons with energies of several hundreds of MeV. By a proper collimation system, the scattered photons at very backward angles can be selected resulting in an almost monoenergetic photon beam, that can be tuned by varying the electron or laser photon energy. In addition, because the Compton effect preserves the polarization of the incoming photons, the resulting photon beam shows the same polarization character as the laser. Thus, the method of LCB provides a (nearly) monochromatic polarized beam of high-energy photons.

Uncertainty of scattered photon energy The energy distribution of the scattered photons depends in general on uncertainties of the variables in Eq. (97), namely E_e, E_L, θ_f, and θ_i. Under the assumption $\theta_i \approx \pi$ and $\theta_f \approx 0$, the relative uncertainty of the scattered photon energy $\Delta E_\gamma/E_\gamma$ is approximated by the contribution of each variable (see, e.g., Ref. [254])

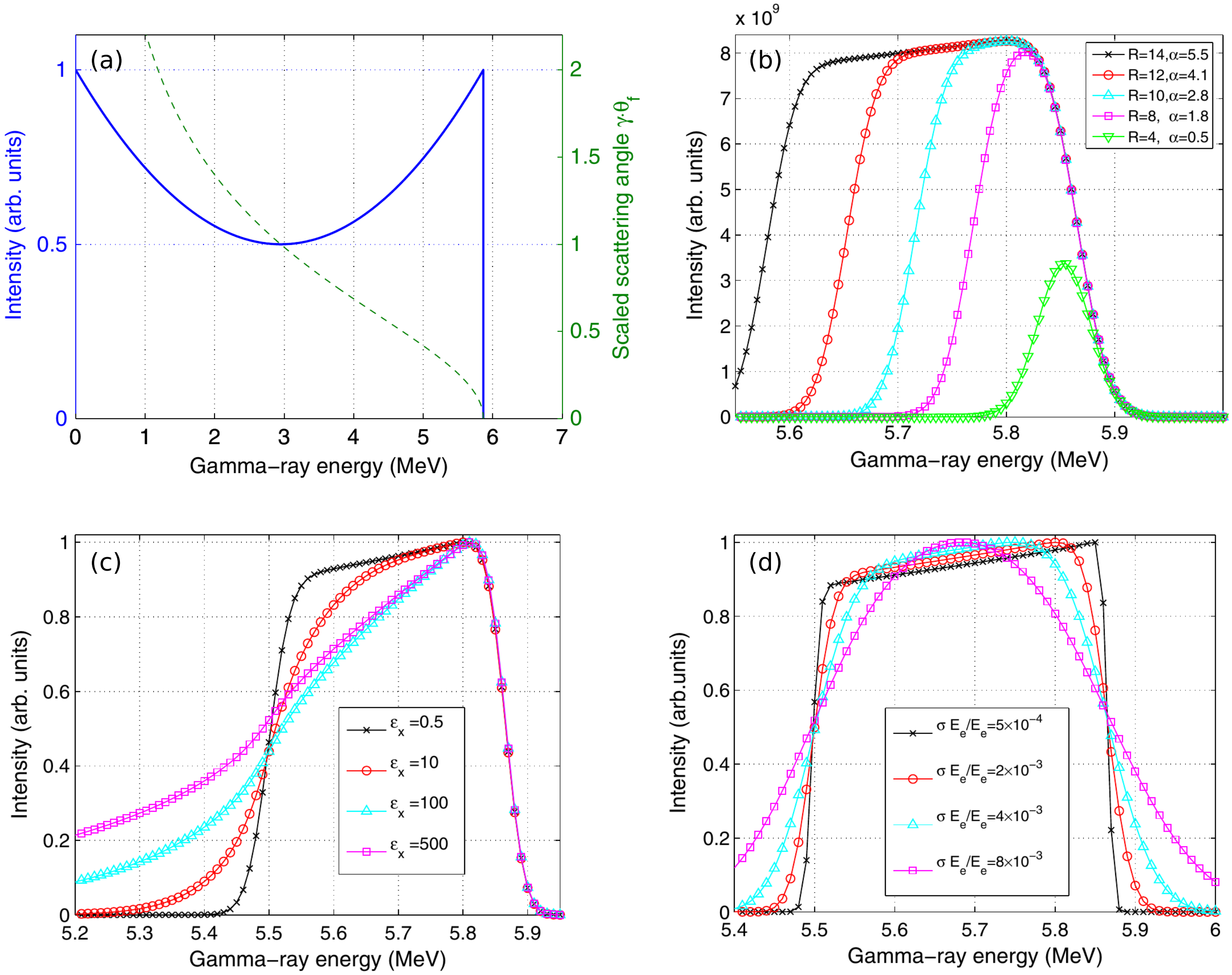

Figure 30: Calculated energy spectra of photons scattered off relativistic electrons. The relative energy distribution of Compton-scattered photons (blue solid line) and the relation between the γ-ray energy and the scaled scattering angle $\gamma\theta_f$ are shown in (a). Panel (b) illustrates the effect of collimation with an aperture radius R (and relative collimation factor α) of the LCB beam to the spectral distribution and beam intensity. The impact of the horizontal emittance ε_x and the relative energy spread σ_{E_e}/E_e of the electron beam are compared in panels (c) and (d). For details see text and Refs. [254, 255]. Reprinted figures from [254, 255]. Licensed under a Creative Commons Attribution 3.0 License.

$$\frac{\Delta E_\gamma}{E_\gamma} \approx \sqrt{\left(2\frac{\Delta E_e}{E_e}\right)^2 + \left(\frac{\Delta E_L}{E_L}\right)^2 + \left(-\gamma^2\Delta\theta_f^2\right)^2 + \left(-\frac{1}{4}\Delta\theta_i^2\right)^2}\,. \tag{101}$$

The limit to the energy spread of the LCB beam is defined by the interplay of the laser bandwidth $\Delta E_L/E_L$, the energy spread of the electron beam $\Delta E_e/E_e$, and the angular spread induced by $\Delta\theta_f$ and $\Delta\theta_i$.

3.3.2 Energy distribution of scattered photons

In photonuclear reactions with LCB beams, it is often necessary to know its spectral distribution to extract, for instance, reaction cross sections. The energy-differential cross section for the production of a single LCB photon by a head-on collision of a monoenergetic pointlike electron and laser beam is approximately described by [255]

$$\frac{d\sigma}{dE_\gamma} \approx \frac{4\pi r_e^2}{E_\gamma^{max}} \left[1 - 2\frac{E_\gamma}{E_\gamma^{max}} + 2\left(\frac{E_\gamma}{E_\gamma^{max}}\right)^2 \right] \quad \text{for} \;\; E_\gamma \leq E_\gamma^{max} \tag{102}$$

with the classical electron radius r_e and the maximum energy E_γ^{max} given in Eq. (100). The energy distribution computed from Eq. (102) is depicted as blue solid line in Fig. 30 (a) [254]. For illustration of the correlation between the spectral intensity and the scattering angle θ_f of the Compton-scattered photon, the product of θ_f and the Lorentz factor γ of the electron is deduced as a function of the γ-ray energy from Eq. (99) and displayed on the second ordinate (green dashed line). The maximum spectral intensity is observed at $\theta_f = 0$, while the minimum at $\theta_f = 1/\gamma$ is a factor of two smaller. From the scattering angle dependence follows that the energy width of the LCB beam can be narrowed down by a geometrical collimator.

To illustrate the effect of the aperture of the collimation system on the spectral distribution of the produced LCB beam, a very small horizontal electron beam emittance value of $\varepsilon_x = 0.05$ nm rad and an energy spread of the electron beam of $\sigma_{E_e}/E_e = 2 \times 10^{-3}$ are used in the calculations. As an example, Fig. 30 (b) shows the calculated energy distribution of the photon beam for the case of the High Intensity γ-ray Source (HIγS) for different collimator apertures located about 60 m downstream from the collision point. The radius R of the collimator is varied between 4 and 14 mm and leads to a narrower energy spread until a point, where the effects of the electron beam properties start to play a dominant role. Beyond that point, further collimation only reduced the intensity and shifts the centroid of the distribution to higher energies, but the width is basically constant.

The electron beam is not monoenergetic, but has a certain energy spread and a finite emittance resulting in a smoothening of the low- and high-energy cutoffs of the LCB beam distribution. The effect of the divergence and the energy spread of the electron beam on the brilliance of the produced high-energy photon beam is discussed in detail in Ref. [255]. The calculated impact of the horizontal electron beam emittance ε_x (in nm rad) and the energy spread σ_{E_e}/E_e is compared in Fig. 30 (c) and Fig. 30 (d), respectively. While the high-energy cutoff is not changed, a low-energy tail emerges when the emittance is increased. A larger energy spread and divergence of the electron beam directly translates into a larger spread of the LCB beam.

Therefore, it should be emphasized that one must usually balance between the spectral width and intensity of the LCB beam for matching the required experimental conditions. From the presented systematics in Fig. 30, it is obvious that for a high-brilliant LCB beam not only the collimator aperture has to be well defined, but also the properties and quality of the electron beam are of high importance. For a comprehensive discussion of the underlying effects and a detailed derivation of the presented relations see Refs. [254–256] and references therein.

3.3.3 Luminosity

A common measure of the intensity of LCB beams is the photon flux

$$\frac{dN_\gamma}{dt} = \mathcal{L}\sigma\,, \tag{103}$$

i.e., the number of scattered photons per unit time, which is the product of the total Compton-scattering cross section σ and the luminosity of the electron-laser collisions

$$\mathcal{L} = \frac{N_e N_L}{A_{\text{eff}}} \cdot f\,. \tag{104}$$

The luminosity depends on the number of electrons per bunch, N_e, and photons per laser pulse, N_L, as well as on the collision rate, f. The effective overlap area in the collision of an electron bunch and a laser pulse, A_{eff}, is determined by specific characteristics of their phase space intensity functions and the collision time. Assuming Gaussian distributions of the phase space intensity functions for both, electron and laser beam [256], the luminosity in the beam-beam collision

$$\mathcal{L} = \frac{N_e N_L}{2\pi\sqrt{\frac{\lambda\beta_0}{4\pi} + \beta_x\varepsilon_x}\sqrt{\frac{\lambda\beta_0}{4\pi} + \beta_y\varepsilon_y}} \cdot f \tag{105}$$

depends on the $\beta_{x,y}$ values of the β function, the transverse emittance $\varepsilon_{x,y}$ of the electron beam, and on the Rayleigh length β_0 and wavelength λ of the laser photons.

Table 2: Parameters of LCB facilities with focus on nuclear structure studies. Tabulated are the electron energy E_e, the average electron beam current $\langle I\rangle$, the repetition rate f_{rep}, the laser wavelength λ_L as well as the energy E_γ and bandwidth $\Delta E_\gamma/E_\gamma$ of the generated LCB beam. Furthermore, the available polarization modes, the total photon flux $N_{\gamma,total}$ and the (collimated) photon flux on target $N_{\gamma,on-target}$ are given.

	HIγS [12, 257]	UVSOR-III [258]	SLEGS [259]	XGLS [260]	VEGA [261]
Location	Durham USA	Okazaki Japan	Shanghai China	Xi'an China	Magurele Romania
E_e (MeV)	240 - 1200	750	3500	120 - 360	234 - 742
λ_L (nm)	190 - 1060	1940 / 10600	10640	800	515 / 1030
$\langle I\rangle$ (mA)	10 - 120	300	100 - 300	N/A	non-disclosed
E_γ (MeV)	1 - 100	1 - 5.4	0.4 - 20	0.1 - 3	1 - 19.5
$\Delta E_\gamma/E_\gamma$ (FWHM)	0.8 % - 10 %	2.9 % (ϕ = 2 mm)	$<$ 5 % (ϕ = 2 mm)	1.2 % - 10 %	$<$ 0.5 %
f_{rep} (MHz)	5.58	90	347	pulsed, 10 Hz	71.4
polarization	lin, circ	lin, circ	lin, circ	lin, circ	lin
$N_{\gamma,total}$ (γ/s)	10^6 - $3 \cdot 10^{10}$	10^7	10^6 - 10^8	10^8 - 10^9	10^{11}
$N_{\gamma,on-target}$ (γ/s)	10^3 - $3 \cdot 10^9$	$4 \cdot 10^5$	10^5 - 10^7	10^6 - 10^8	$\sim 10^8$

3.4 Instrumentation

3.4.1 Beam diagnostics

Photon beams are characterized by different parameters, such as the position relative to the target or to a defined reference trajectory, the photon yield, the γ-ray spectral distribution, the beam intensity, the beam polarization, and the time structure. A variety of instruments have been developed to monitor the beam parameters.

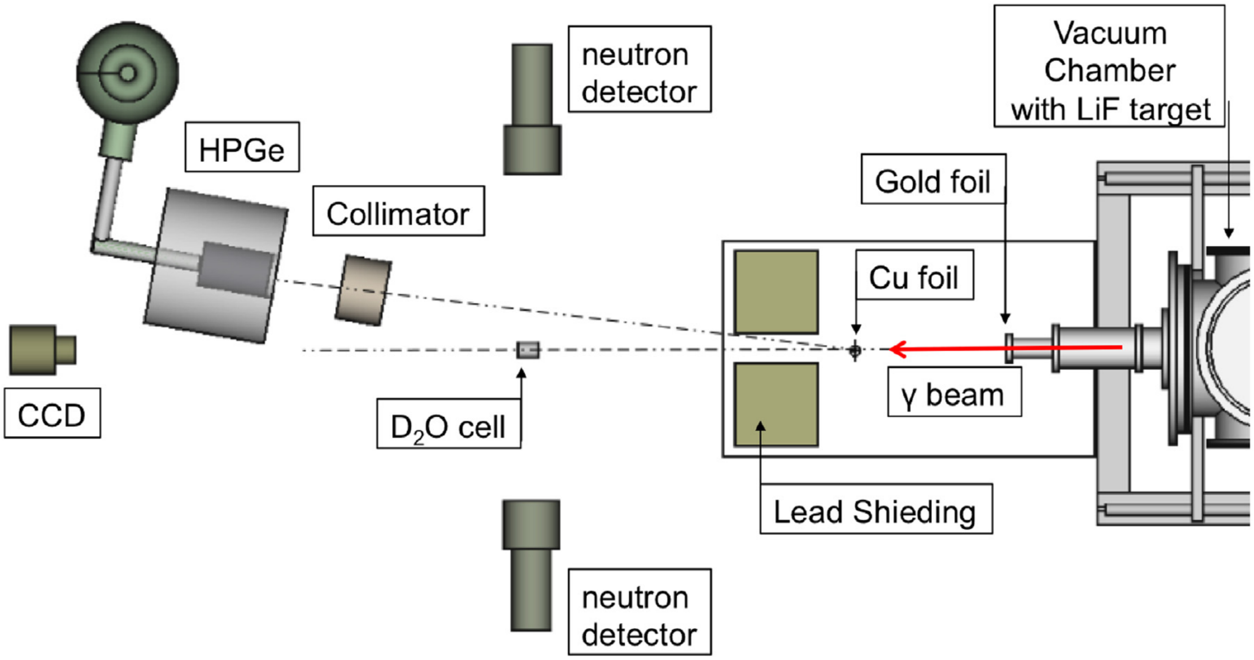

Figure 31: The layout of the experimental arrangement of the beam-diagnostic devices at the HIγS facility (drawing not to scale). The vacuum chamber is housing the experimental setup. The other experimental setups in the figure were used for the characterization of the photon beam. Reprinted figure from Ref. [262] with permission from Elsevier.

Table 3: Diagnostic devices which are used at the HIγS facility

Type	Detection method	Beam parameter
Paddle detector	e^-/e^+ tracking	γ-beam intensity
Compton spectrometer	γ-ray detection	γ-beam intensity
^{2}H photodisintegration	neutron detection	γ-beam intensity
Zero-degree detector	γ-ray detection	γ-beam energy
Au activation foils	γ-ray detection	γ-beam intensity
CCD system	scintillation light monitoring	γ-beam position

Beam diagnostics at HIγS: The diagnostic devices which are used, *e.g.*, at the HIγS facility are listed in Table 3. In a recent experiment at the HIγS facility, several different diagnostic detectors were utilized [262], as shown in Fig. 31.

Paddle detector: A beam flux monitor, called paddle detector, is used to measure the γ beam-intensity within a systematic uncertainty of 2% [263]. It consists of five scintillator paddles and an Al converter. Each paddle is comprised of a 2 mm thick piece of solid plastic organic scintillator, BC-400, joined to a light guide and a photomultiplier tube (PMT). The five paddles are held in place by a custom made aluminum frame. Two paddles are upstream of a 2 mm Al converter and three paddles are downstream from it. The paddles and the converter are placed equidistantly from each other. The aluminum converter produces electrons and positrons when hit by the incoming γ rays. The signal from the flux monitor is defined by a triple coincidence between the three downstream paddles in anticoincidence with the up-stream paddle, which serves as veto. The triple-coincidence requirement ensures that the detected event is only due to the recoiling electrons or positrons. Thus, signals from radioactivity in the room are effectively rejected.

Compton spectrometer: The γ-beam intensity is measured also with a Compton spectrometer monitoring scattered γ rays. A Cu plate is mounted downstream the experimental target. It scatters the beam. Collimated Compton-scattered γ rays under a certain angle are measured with a large-volume HPGe detector with an anti-Compton shield. The well-known Klein-Nishina differential cross section of scattered photons [264] is used to determine the γ-beam intensity.

^{2}H photodisintegration: Two BC501A-based liquid scintillation neutron detectors mounted at a reaction angle of 90° are used to detect the neutrons from deuteron photodisintegration. They monitor a 4.5-cm-long, 3.7-cm-diameter heavy water cell. The on-target intensity of the beam is determined using the well-known ^{2}H(γ,n) cross section.

Zero-degree detector: A large-volume high-efficiency detector can be placed at $\theta = 0°$ downstream for measurements of the photon-beam energies and their spectral distributions. In experiments, either a large-volume NaI(Tl) or the HPGe detector with an anti-Compton shield, which is also used for the Compton spectrometer, are positioned as a zero-degree detectors. Since the measurement is done in-beam and the HPGe detector is positioned at $\theta = 0°$ with respect to the beam axis, the beam should be attenuated before reaching the detector, keeping the count rate in the 2–4 kcps range. Measurements with the HPGe detector are taken before and after each experimental run.

Au activation foils: A gold foil is mounted for measurements of the γ-beam intensity above the particle-evaporation threshold. As a result of the ^{197}Au(γ,n)^{196}Au reaction, activity is built in the foil. After a certain irradiation time, the foil is taken out of the beam and transferred to a low-background detection station, where the intensity of decay γ rays is measured. By taking into consideration the known photodisintegration cross section of ^{197}Au, the γ-beam fluence is determined.

CCD system: An assembly, consisting of a scintillation screen and a CCD camera, placed in the beam line, is used for finer target alignment and spatial characterization of the beam. The beam interacts with the scintillation material of the screen, which is constantly monitored by a CCD camera.

Beam diagnostics at NewSUBARU: The flux and the spectral distribution of the LCB γ beams at the NewSUBARU beamline were monitored with γ-ray detectors. A HPGe detector or a LaBr$_3$(Ce) scintillator was used for measurements of the γ-beam energies and γ-ray spectral distribution, and a large-volume NaI(Tl) detector was utilized for γ-beam intensity measurements.

Energy monitoring: The absolute value for the maximum energy of the LCB beams at NewSUBARU was obtained by relying on the precise knowledge of the laser photon and electron-beam energies at the interaction point. The electron-beam energy has been calibrated between 0.5 and 1.5 GeV with an accuracy of the order of 10^{-5} and the spread of the electron beam was found to be 0.4% [265]. In recent experiments, monitoring of LCB photon spectral distribution was performed with a $3.5'' \times 4''$ LaBr$_3$(Ce) detector for each photon-beam energy before and after each target irradiation. In these measurements, the laser operated in the continuous-wave mode at a reduced power in order to avoid pile-up effects. The detector was used as a zero-degree detector. For obtaining the energy of the LCB beam the inverse problem was solved, *e.g.*, a full-scale Monte Carlo simulation within the GEANT4 toolkit [151] was performed for the laser-electron interaction and the γ-beam interaction within the collimators. The laser beam was considered as a continuous Gaussian beam with the spatial parameters of Ref. [266]. The values for the electron-beam emittance and spot size at the focal point were iteratively adjusted starting from the values published in Ref. [265], until the experimental $LaBr_3(Ce)$ detector response was reproduced by the GEANT4 simulation.

Flux monitoring: An 8.0″ × 12.0″ NaI(Tl) detector with 100% detection efficiency was used as a flux monitor of the LCB beam. Multi-photon spectra are measured, which are used to deduce the number of photons incident on a target. The idea is that, since the product of the numbers of laser photons and electrons involved in each laser pulse is very large and the collision probability is very small, the probability distribution of the number of scattered photons has a Poisson distribution. It was shown that energy spectra of pulsed LCB photon beams measured with a BGO detector are characterized by a Poisson distribution [267]. An algorithm was established for deducing the flux of LCB photons for the experimental determination of the average number of scattered photons per laser pulse [268].

3.4.2 γ-ray detection

Information on quantum numbers, excitation strengths, and the intrinsic structure of nuclear levels can be obtained from a detailed γ-ray spectroscopy of the decay of photo-excited states as discussed in Section 2. Depending on the specific application, γ-ray detection systems should meet different requirements. Nowadays, the most commonly used detectors in low-energy photonuclear physics are build from semiconductor diodes and scintillator materials. Semiconductors such as high-purity germanium (HPGe) detectors stand out for their excellent energy resolution of about 0.2 % at 1332 keV enabling a detailed spectroscopy of γ-ray decays. In contrast, scintillators exhibit energy resolutions of > 2 %, but their detection signals have typically much shorter decay times ranging from about 16 ns for cerium-doped lanthanum bromide [$LaBr_3(Ce)$] to about 250 ns for thallium-doped sodium iodide [NaI(Tl)] scintillators compared to tens of μs for HPGe detectors. Therefore, scintillators provide high-rate capabilities and a superior time resolution ($\lesssim$ 500 ps) allowing efficient background suppression in coincidence experiments.

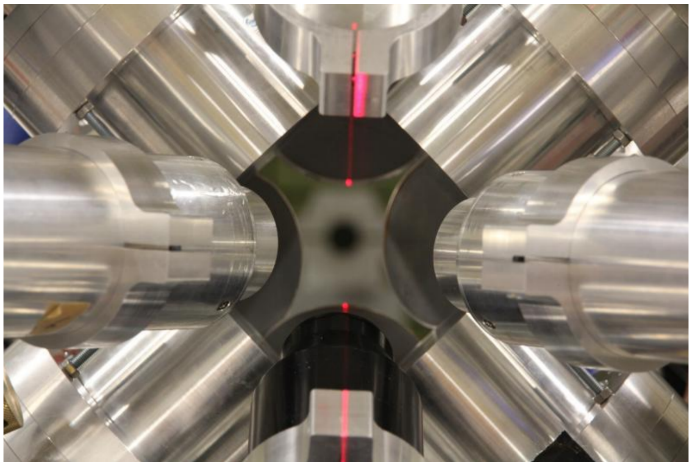
Figure 32: Photograph of the γ^3 setup in photon-beam direction. Courtesy of Bastian Löher.

In the following, examples of current and future γ-ray spectrometers that are and will be extensively used in photonuclear reactions will be briefly summarized. For detailed descriptions, we refer to the corresponding technical publications.

γELBE and DHIPS: Several (typically three to four) large-volume HPGe detectors are used in NRF measurements at γELBE [215] and at DHIPS [221] , respectively, to perform high-resolution γ-ray spectroscopy. The HPGe detectors can be equipped with a BGO scintillator for active Compton-background suppression. They are usually placed at polar angles of $\vartheta = 90°$ and $\vartheta = 127° - 130°$ with respect to the impinging continuous-energy bremsstrahlung photon beam for angular distribution measurements of γ rays emitted in the NRF reaction. This geometry allows to distinguish between $J = 1$ and $J = 2$ states in even-even nuclei and to measure energy-integrated cross sections of individual excited states (see Sec. 2.3.6 and Refs. [11, 55]).

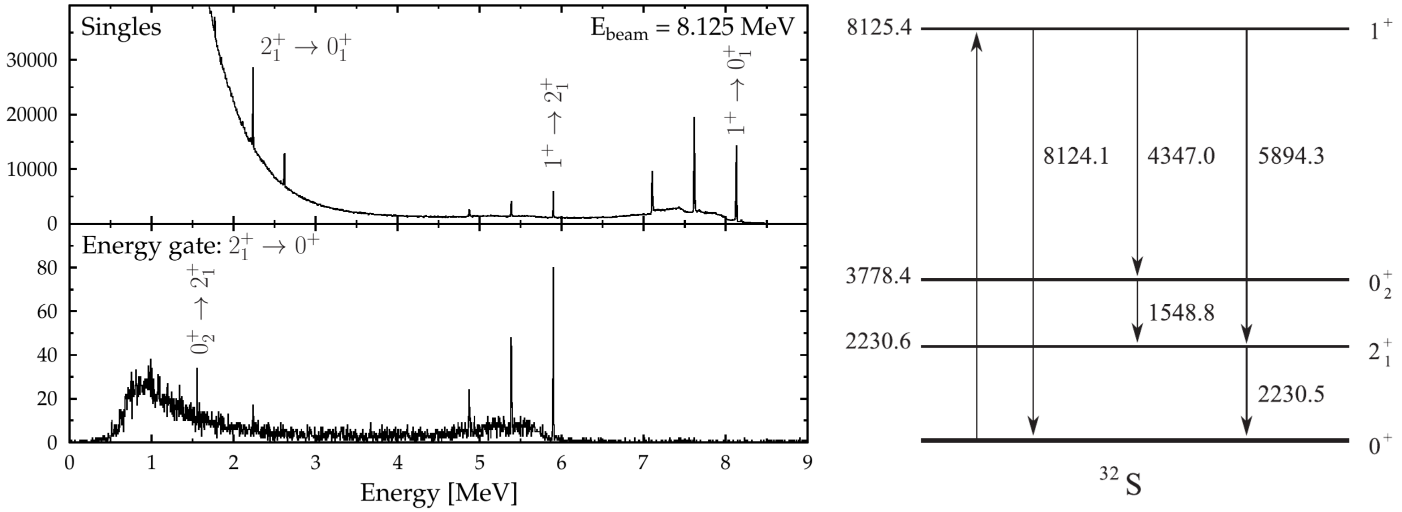

Figure 33: Coincidence experiment with an LCB beam energy of 8.125 MeV exciting the well-known 1^+ state at 8.125 MeV in ^{32}S. Left: Singles spectra obtained with HPGe detectors (upper panel) and HPGe spectra gated on the $2_1^+ \rightarrow 0_1^+$ transition with $E_\gamma = 2.23$ MeV in the LaBr$_3$(Ce) detectors (lower panel) [269]. Right: Decay scheme of the 1^+ state at 8.125 MeV. Reprinted figure with permission from [269].

γ^3 setup: The γ^3 setup at HIγS [71] is composed of four HPGe detectors with a relative efficiency of 60 % and four $3'' \times 3''$ LaBr$_3$(Ce) scintillators (see Fig. 32). The setup has a typical total full energy peak efficiency of about 6 %. It exploits the advantages of both detector types, namely the excellent energy resolution of HPGe semiconductors and the high detection efficiency and timing resolution of the LaBr$_3$(Ce) scintillators. Combining experiments with quasi-monochromatic LCB beams and the γ-γ coincidence technique, studies of (average) branching ratios [60, 70] and primary γ-ray transitions [72] are feasible for varying excitation energies. Figure 33 depicts an illustrative example for studying the decay branches of the well-known 1^+ state at 8.125 MeV of ^{32}S (see level scheme on the right-hand side). The HPGe γ-ray spectrum recorded under the condition that the $2_1^+ \rightarrow 0_1^+$ transition ($E_\gamma = 2.23$ MeV) has coincidently been detected by one LaBr$_3$(Ce) detector is displayed in the lower panel on the left-hand side. The $1^+ \rightarrow 2_1^+$ transition (and the corresponding detector response) is clearly visible at 5.894 MeV. For comparison, the single γ-ray spectrum is shown in the upper panel, where the transitions of the 1^+ state to the ground state and the 2_1^+ state are apparent at 8.125 MeV and 5.894 MeV, respectively. Due to the improved peak-to-background ratio in the gated spectrum, weak branching ratios smaller than a few percent of individual transitions, but also average decay properties for groups of excited states in a given excitation-energy window can be determined [57, 70, 71].

ELIADE: The ELI-NP Array of Germanium Detectors (ELIADE) [73–75] to be used at ELI-NP is dedicated for NRF experiments with linearly-polarized quasi-monoenergetic photon beams. It is composed of eight segmented HPGe clover detectors (total full energy peak efficiency of about 6 %) with the option to add large-volume LaBr$_3$(Ce) scintillators. For reduction of background radiation, each clover will be equipped with a BGO detector for active Compton suppression. It will enable very sensitive studies of γ-ray angular correlations, parity-quantum numbers as well as γ-decay branches to the ground state and to excited states.

3.4.3 Neutron detection

Neutron-detection systems aim at measurements of intensities, yields, multiplicities, spectra, and angular distributions of neutrons emitted in photonuclear reactions.

Photoneutron cross section measurements are carried out with neutron detectors based on the slowing down, *i.e.*, thermalization of neutrons, followed by conversion reactions of neutrons into charged particles. The conversion reaction can be ^{10}B(n,α)^{7}Li, ^{6}Li(n,α)^{3}H or ^{3}He(n,p)^{3}H. In experiments, the neutron multiplicity of slow neutrons is measured. In the experimental setup, proportional counters filled with ^{10}BF$_3$ or ^{3}He are embedded in moderators, paraffin or polyethylene, where the emitted neutrons of the reaction are thermalized. Two different techniques are used for estimating the number of measured neutrons, *i.e.*, the neutron multiplicity, the ring-ratio [270] and the flat-efficiency technique [271].

Ring-ratio technique: In this case, the proportional counters are arranged geometrically in three or more concentric rings with respect to the direction of the γ beam. The outermost ring is relatively more sensitive to high-energy neutrons than is the innermost, since there is much more moderating material between it and the target. Hence, the ratio of the number of neutrons detected in the outermost to that in the innermost ring, *e.g.*, the ring ratio, varies with the average neutron energy [270]. The efficiency calibration of the detector array and of each ring as a function of neutron energy is done with various radioactive sources, such as Sb-Be (γ,n) [272], Pu-Be (α,n), or ^{252}Cf spontaneous-fission sources. During the calibration, ring ratios are measured, too. As different ring ratios depend in a different way on the original neutron energy, they are used to determine the average neutron energy, which allows to measure total or partial cross sections, see Sec. 2.5.1 and 2.5.2.

At HIγS, neutrons are detected in an Inventory Sample Model IV detector (INVS) [273], which is an array of eighteen ^{3}He proportional counters arranged in two concentric rings and embedded in a cylindrical shell of polyethylene moderator. In recent experiments, the INVS was modified to read out each proportional counter separately in order to observe asymmetries in the photofission neutron azimuthal angular distribution relative to the polarization plane of the γ-ray beam, which makes possible the determination of neutron multiplicities [274]. A similar detector was utilized at the AIST and NewSUBARU facilities [275].

Flat-efficiency technique: The flat-efficiency technique aims at direct neutron multiplicity determination. The idea is that the neutron counters are placed in such a way in the moderator that the detection efficiency does not depend on the neutron kinetic energy for energies up to 5 MeV. It is not only needed to have a flat efficiency over a wide range of energies, but it is necessary to achieve high-detection efficiency for the reaction neutrons. High-efficient detectors with flat efficiency were developed for measurements of delayed neutrons [276] and for photoneutron measurements [150]. The flat-efficiency neutron detector (FED) [150], which was developed at the NewSUBARU laboratory, consists of three concentric rings of four, nine, and 18 ^{3}He counters embedded in a 46 cm × 46 cm × 50 cm polyethylene moderator at the distances of 5.5, 13.0, and 16.0 cm from the photon-beam axis, respectively, the largest dimension being along the beam axis. The total efficiency of the FED changes from 37.8% at 10 keV to 32.9% at 5.0 MeV for evaporation neutrons.

The direct neutron sorting (DNT) technique was developed for the extraction of the neutron multiplicity. The partial photoneutron cross section $\sigma(\gamma,\nu\text{n})$ is related to the number of (γ,νn) reactions, N_ν as

$$N_\nu = N_\gamma N_T \sigma(\gamma, \mu n), \tag{106}$$

where N_γ is the number of incident γ rays and N_T is the number of target nuclei. However, N_ν is not a direct experimental observable. Under the consideration that a FED measures neutron multiplicity events with $\nu = 1, 2, 3$, which are relevant for the energy range, which is considered in this review, the detected single, N_s, double, N_d, and triple, N_t, neutron events can be expressed as [150]

$$N_s = \epsilon N_1 + \epsilon N_2 (1-\epsilon) + \epsilon N_3 (1-\epsilon)^2, \tag{107}$$

$$N_d = \epsilon^2 N_2 + \epsilon^2 N_3 (1-\epsilon), \tag{108}$$

$$N_t = \epsilon^3 N_3. \tag{109}$$

In case only one neutron is detected, all possible (γ,νn) reactions contribute to the event. The first term in Eq. (107) considers the detection of a neutron emitted in a (γ,1n) reaction, the second term takes into account that only one neutron is detected from a (γ,2n) reaction, and the third term that a single neutron is detected from a (γ,3n) reaction. In a similar way, the first term in Eq. (108) considers the detection of two neutrons emitted in a (γ,2n) reaction, while the second term accounts for the detection of only two neutrons from a (γ,3n) reaction. Finally, Eq. (109) considers that all the three neutrons emitted in a (γ,3n) reaction are detected. The efficiency of the FED is denoted as ϵ. The idea of the DNT is by solving this system of equations to determine the partial neutron cross sections with Eq. (106).

Another flat-efficiency detector was developed at ELI-NP, called ELIGANT-TN [277]. The ^{3}He proportional counters are placed equally spaced in three concentric rings, of 118, 260, and 310 mm diameter, respectively. The inner contains four detectors, while the two outer rings contain eight and sixteen detectors each. The neutron moderator is a cube of 46 × 46 × 64 cm^3 made of polyethylene, the largest dimension being along the beam axis. The moderator cube is covered by additional 10-cm-thick polyethylene plates with 1-mm-thick cadmium metal for background neutron suppression. The detector is designed such that it has a flat efficiency of about 38% below $E_n \approx 3$ MeV, dropping to about 35% at higher energies up to 5 MeV [75].

Neutron energy measurements: Neutron energies are measured with the time-of-flight (ToF) method. The start signal is provided by the LCB γ-beam burst and the stop signal by a neutron detector placed at a certain distance from the target.

At HIγS, the Blowfish neutron detector, shown in Fig. 34, is operational [132]. It is composed of an array of 88 detector cells, which covers a solid angle of about 25% of 4π steradian. The detector cells are arranged on eight uniformly spaced arms, which can rotate about the conventional beam axis in the ϕ direction. Each arm contains eleven uniformly spaced cells on the surface of a 16 inch radius sphere covering polar angles from $\theta = 22.5°$ to $\theta = 157.5°$. The large solid angle coverage of the array makes it possible to measure neutron-energy spectra with a high efficiency and the angular distribution of reaction neutrons. The fact that the array can be rotated about the beam axis allows for accurate determination of any systematic effects in the detector efficiency.

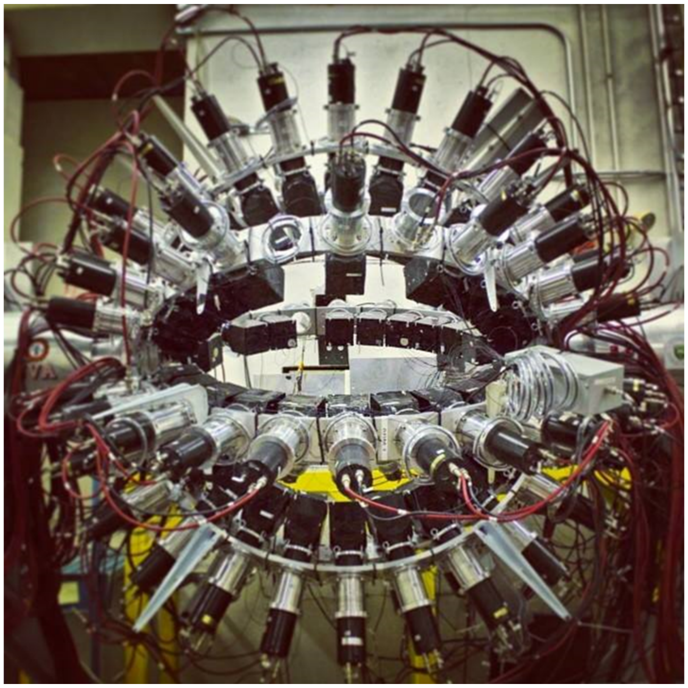

Figure 34: The Blowfish neutron detector. Picture taken from Facebook.

The detector cells of the Blowfish detector are made of three main components: a liquid organic scintillator, a light guide, and a PMT. The scintillator cell is a 8.2 cm × 8.2 cm × 7.1 cm rectangular box with 0.3-cm-thick walls, filled with a BC-505 liquid scintillator. Each cell is optically coupled to a Phillips XP2262B PMT through a 4.5 cm light guide. The BC-505 scintillator allows the discrimination between energy deposited by electrons, produced by *e.g.*, photoeffect, or by heavier charged particles, produced in interactions with neutrons [152]. The pulse-shape discrimination (PSD) technique is utilized. The method allows to distinguish between different types of incident particles by examining the shape of the light pulses from scintillation detectors.

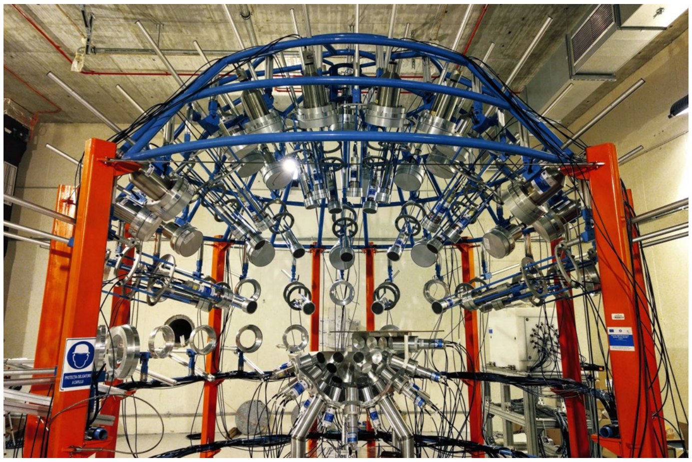

Figure 35: The ELIGANT-GN neutron detector in one of the experimental halls of ELI-NP.

At ELI-NP, the ELI Gamma Above Neutron Threshold - Gamma Neutron (ELIGANT-GN) 35 detector array was constructed [277,278] for recording γ rays and neutrons emitted during deexcitation of PDR/GDR states. The array provides the possibility for measurements of single and coincidence γ-ray events, single-neutron events, and coincidence γ–n events in the γ and neutron detectors. The array is designed to be made up of two hemispheres, an inner one, placed 30 cm from the target, and an outer placed at 1.5 m, as shown in Fig. 35. The inner array is used for γ-ray detection, and consists of 19 $CeBr_3$ scintillators coupled with Hamamatsu R233-100 PMTs and 15 $LaBr_3(Ce)$ scintillators coupled with Hamamatsu R11973 PMTs. All detectors have cylindrical crystals with a diameter of 3″ and length of a 3″. The outer array is used for fast neutron detection utilizing the ToF technique. It consists of 37 EJ-309 liquid scintillators and 25 GS20 ^{6}Li glass detectors. The inner hemisphere is placed downwards with respect to the beam axis and the detectors are at backward angles. The outer hemisphere is placed upwards with respect to the beam and detectors cover the whole of hemisphere. The neutron detectors are mounted on movable mechanical structures, allowing a maximum distance of 1.5 m from the target, which is sufficient for the ToF measurements. The high-energy response of the large-volume $LaBr_3(Ce)$ detectors of ELIGANT-GN was studied [279] with an emphasis on the selection of unfolding methods to resolve small structures in γ-ray spectra with high energies.

Figure 36: A schematic view of the half-meter flight-path detector array for measurements of neutron polarization asymmetries at HIγS. Reprinted figure with permission from Ref. [158]. Copyright 2012 by the American Physical Society.

The neutron kinetic energy is usually measured using the ToF technique. For that purpose, the liquid scintillator EJ-309 is utilized. The neutron identification efficiency [280, 281] of a EJ-309 detector strongly decreases for low-energy neutrons. Therefore, for energies $E_n < 1$ MeV, GS20 ^{6}Li glass detectors are used. Their detection principle is based on the ^{6}Li(n,α)^{3}H reaction, which has a high cross section for low-energy neutrons. In order to predict the performance of the ELIGANT-GN array, a dedicated GEANT4 simulation code was developed [278].

Neutron angular distribution and polarization asymmetry measurements: In experiments at the NewSUBARU facility, neutron angular distributions were measured [154, 157], see also Sec. 2.5.4. The detector was a plastic scintillator of a diameter of $\Phi = 100$ mm and 100 mm length, coupled to an ET enterprises 9305KB PMT. The detector was located at the polar angle of $\theta = 90°$ outside of the irradiation room with a concrete shield with a thickness of 540 mm. For measurements of the angular distribution of neutrons, the linear polarization plane angle of the LCB photons was tuned by changing the linear polarization plane of the incident laser.

In experiments at HIγS, the polarization asymmetry of prompt neutrons was measured [156,158,159], see also Sec. 2.5.4 and 5.2. An array of twelve to eighteen detectors was used to count neutrons generated by photofission. The active volume in each detector was filled with a BC-501A liquid scintillator and was 12.7 cm in diameter and 5.1 cm thick. Twelve detectors were placed at polar angles $\theta = 55°$, $90°$, and $125°$ and at azimuthal angles $\phi = 0°$, $90°$, $180°$, and $270°$, and the remaining six detectors were placed at $\theta = 72°$, $107°$, and $142°$, and at $\phi = 0°$ and $90°$, as schematically shown in Fig. 36.

3.4.4 Charged-particle detection

Charged particles emitted in photonuclear reactions can be detected with Si strip detectors. In a recent experiment at HIγS, the photodisintegration of ^{7}Li was studied [149]. Triton-α coincidences were measured with the large-area annular silicon detector array (SIDAR) [282]. SIDAR was arranged in a lamp shade configuration with twelve YY1-type detectors [283], where each detector is tilted at 42° from the plane perpendicular to the beam axis. YY1-type detectors, which are segmented into 5-mm-wide annular strips, covered an active area with an inner radius of 5 cm and an outer radius of 13 cm. 300-, 500-, and 1000-μm-thick detectors were used in the experiment. The 300- and 500-μm-thick detectors have an energy resolution of approximately 30 keV (FWHM) for 5.8 MeV α particles, while the 1000 μm detectors have a resolution around 70 keV (FWHM).

A 4π array of Si strip detectors devoted to charged-particle detection is presently been built at ELI-NP [284], called the ELI Silicon Strip Array (ELISSA). It consists of 36 X3-type double-sided Si strip detectors (DSSSDs) [283] which form the barrel and eight QQQ3-type DSSSDs [283] which cover the end caps. The total angular coverage is 80%. The energies of detected protons are in the range of $E_p = 100$ keV $-$ 10 MeV and for α particles in the range of $E_\alpha = 100$ keV $-$ 30 MeV. The average energy resolution of the detector batch was measured with a standard two-peak open ^{241}Am/^{239}Pu α source as $\Delta E_\alpha \approx 40$ keV for the front strips and 80 keV for the back strips [285].

In recent years, a number of active targets implemented in time projection chambers (TPCs) were developed for different low-energy nuclear physics experiments with ion beams. For a review see Ref. [286]. In an active-target experiment, the target material is at the same time the detector medium. The vertex of the reaction products is determined for each event. The implementation of active targets in TPCs allows a large solid-angle coverage of the emitted reaction products, which further contributes to the increase in detection rate. This experimental technique is suggested to be used in photonuclear experiments, too [287]. The motivation for such measurements is related to the need of performing accurate measurements of cross sections of nuclear reactions that are essential for the stellar evolution theory. Due to extremely small, picobarn cross sections, such reaction rates remain uncertain for energies in the Gamow window. A possibility to achieve a considerable improvement is the measurement of the time-reversed reactions, *i.e.*, (γ,p) or (γ,α).

An optical TPC (O-TPC) was constructed [287, 288] and was used in experiments at HIγS. Before that, in nuclear physics the O-TPC technique was used in dosimetry [289] and two-proton decay studies [290]. The O-TPC concept consists of optical recording of track images formed within large gas volumes. The detection is based on capturing light emitted from avalanches induced by ionization electrons drifting into the detector. The three-dimensional (3D) images are reconstructed from projected 2D track images in CCD cameras and the third dimension from the projected time structure recorded by PMTs. So far, results related to the Hoyle-state physics were reported from these experiments [147,291], see Sec. 4.8.

A natural next step is the development of a TPC with electronic readout, aiming at an increase of the track-reconstruction resolution. Such a project was initiated at ELI-NP by a group from Warsaw University [284], the ELITPC detector, which is under construction at present. It utilizes a 1024-channel electronic readout in the horizontal plane perpendicular to the drifting electrons, consisting of three lines oriented at 120° to each other placed on a multilayer PC board, referred to as a *u*-*v*-*w* readout. The electron multiplication is achieved with three 35×20 cm^2 Gas Electron Multipliers (GEMs) [292, 293]. A smaller version, the mini-TPC detector, has been constructed already at the University of Warsaw [294]. It was used to perform feasibility tests of the 3D-track reconstruction. It has a 10.6×10.6 cm^2 readout surface and a drift length of 20 cm. Its 256-channel readout strips are analyzed by the Generic Electronics for TPCs (GET) [295], which was developed for low-energy nuclear physics imaging experiments. Event reconstruction for data taking relies on the creation of 3D-data structure of the deposited charges corresponding to the TPC active volume. A reconstructed event from a neutron-induced reaction in the mini-TPC is presented in Fig. 37.

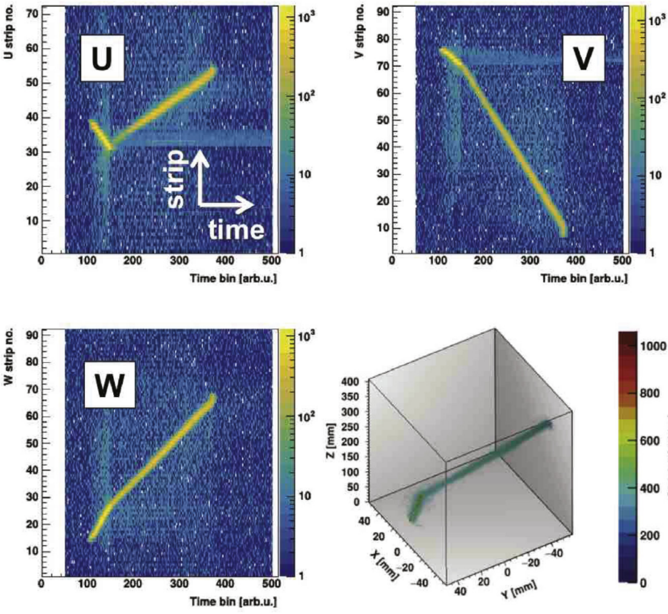

Figure 37: Raw signals collected on *u*-*v*-*w* coordinates represented as 2D histograms, charge *vs.* time and a 3D reconstruction of the reaction products of neutron interaction with the CO_2 gas at 100 mbar. Reprinted figure from Ref. [288] with permission from Elsevier.

A different TPC has been developed at AIST [296]. It consists of a drift region with a uniform electric field with an active area of 60×60 mm^2 and a length of 250 mm, and a multiwire proportional counter (MWPC) region with one anode and two cathode planes. The anode plane is sandwiched by the cathode planes with a spacing of 2 mm. The cathode wires in front of and behind the anode plane are stretched along the x and y axes to obtain 2D track information of a charged fragment. The z axis is parallel to the LCB photon-beam direction. The TPC was filled with a mixed gas of 80% ^{3}He (99.7% enrichment) as a target for the photodisintegration reactions and 20% CH_4 as an operational gas. The TPC was used for studies of ^{3}He [146] and ^{4}He [137] photodisintegration.

In a proof-of-principle experiment at HIγS, a bubble chamber was utilized [297]. It makes use of the instability of super-heated liquids against bubble formation for the detection of charged particles from a nuclear reaction, which takes place in the volume of the chamber. In this case, C_4F_{10} serves as a liquid active target. The operating temperature was near 30°C and the super heat pressure was in the range of 1–4 bar. For the experiments relevant to nuclear astrophysics, the energies of the reaction products are small and they are stopped in the liquid after a few microns, which means that no direct kinematic information can be obtained, but a bubble is formed in the active volume of the chamber. The active-target fluid was contained within a cylindrical glass vessel with a length of 102 mm and an inner diameter of 30 mm. The thickness of the glass cylinder was 3 mm. The vessel was continuously monitored by two 100-Hz CMOS cameras, placed at ±45° with respect to the incident γ beam. Continuously, each new frame was subtracted from the previous one, and the difference was evaluated. The analysis took about 5 ms, which allows to take full advantage of the speed of the cameras. If a certain threshold of difference was exceeded, a signal would be send to the control system to repressurize the chamber. The bubble chamber was used to study the $^{19}F(\gamma,\alpha)^{15}N$ reaction [148].

3.4.5 Detection of fission fragments

In photofission experiments, double-sided Frisch-gridded ionization chambers (FGIC) [298] are commonly used for the study of fission-fragment energy, charge, mass, and angular distributions. These instruments cover almost 4π in solid angle and have a good energy resolution. These are, in principle, two coupled ionization chambers with a common cathode. At the center of the cathode, the target is mounted. Each of the fragments generated in a fission event enters a different region of the detector and both fragments are detected in coincidence. Each fragment drifts toward its respective grid in the longitudinal electric field. Charge is released as the fragment interacts with the fill gas. Upon passing the grid, a step change in electric field strength is experienced and the charge is rapidly collected by the anode. The full height of the anode signal is proportional to the energy deposited by the fission fragment and its derivative to the stopping power of the fragments. FGICs are usually filled with P-10 gas, 90% Ar and 10% CH_4. There has been attempts to use P-30 gas, 70% Ar and 30% methane, for which the electron drift velocity is faster [299]. A photograph of a FGIC is presented in Fig. 38.

In the last years, a lot of effort was put into the improvement of the performance of twin FGICs, *e.g.*, by making the chambers more compact [299], by increasing the position sensitivity [300], and by introducing digital signal processing [301]. A compact twin FGIC can be used in conjunction with an array of Ge detectors in order to study delayed γ rays of fission fragments. A higher position sensitivity is achieved by replacing each anode plate in the ionization chamber by a wire plane and a strip anode [300]. This provides information about the fission axis orientation, which is necessary for the reconstruction of the neutron-emission process. In this case, the FGIC can be used in coincidence with a neutron detector array.

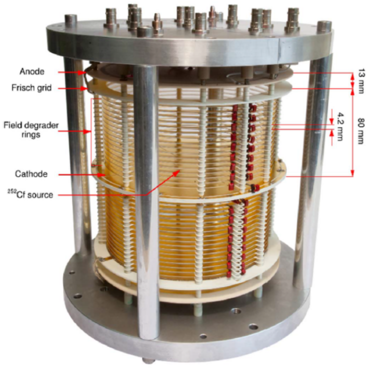

Figure 38: Photograph of a Frisch-grid ionization chamber. Reprinted figure from Ref. [299] with permission from Elsevier.

4 Examples of fundamental science with photonuclear reactions

This section will discuss a few selected examples of research on nuclear structure and nuclear astrophysics using photon beams.

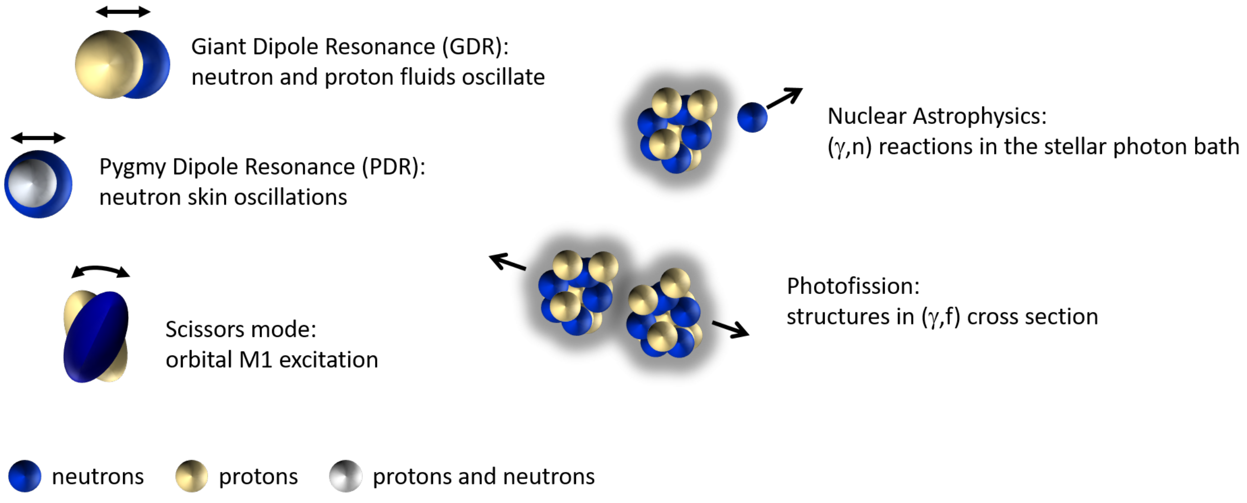

Figure 39: Schematic view of some phenomena in nuclei induced by photons.

4.1 Giant Dipole and Quadrupole Resonances

Due to parity conservation an atomic nucleus cannot possess a static electric dipole (E1) moment. However, the electromagnetic interaction between a photon and a nucleus can induce dynamic E1 moments. The most famous example is the isovector Giant Dipole Resonance (GDR or IVGDR) which was discovered by Bothe and Gentner [15] in a photonuclear reaction and later described by Migdal as an out-of-phase oscillation of the proton fluid against the neutron fluid [302]. The total photoresponse of an atomic nucleus is dominated by this excitation mode which can be found in the energy region between around 25 MeV for lighter and around 13 MeV for heavier nuclei. Its peak energy E_{GDR} deduced from a Lorentzian fit to the cross section can be estimated by:

$$E_{GDR} = 31.2\,\mathrm{MeV} \cdot A^{-1/3} + 20.6\,\mathrm{MeV} \cdot A^{-1/6}. \tag{110}$$

An overview of the GDR and other giant resonances can be found in the seminal books by Harakeh and van der Woude [303] and Bortignon, Bracco, and Broglia [304].

In the 1970's, most of the systematic photonuclear studies of the IVGDR were carried out at the laboratories in Saclay and Livermore using positron annihilation in flight as photon source. An excellent overview of the experiments at these two places has been given in the review article by Berman and Fultz [305]. There is a serious systematic disagreement between the results from the two labs for the (γ,xn) cross sections, especially above the 2n cross section, which has been discussed since many years. For a recent update, see Ref. [306].

A new quality for photonuclear experiments on the fine structure of the GDR became possible by the advent of intense quasi-monoenergetic photon beams from Laser Compton backscattering. As an example we mention one of the pioneering experiments by Harada et al. at the electron storage ring TERAS at ETL in Tsukuba, Japan to measure the photabsorption cross section of ^{18}O in the energy range from about 9 to 13 MeV [307]. Later, Utsunomiya and coworkers performed numerous

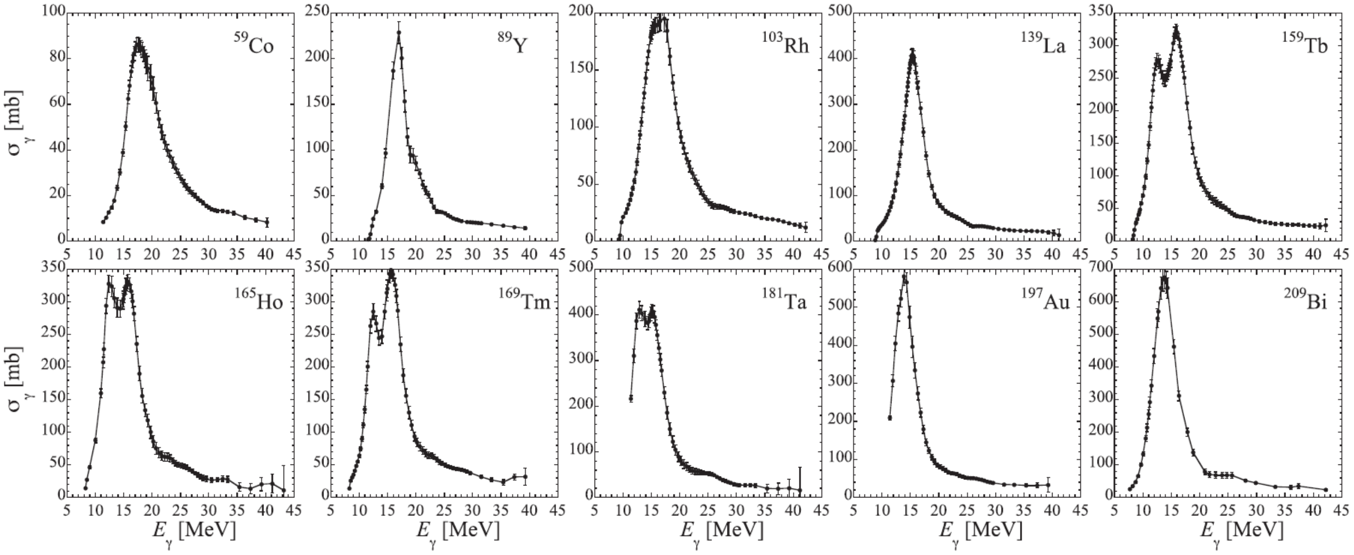

Figure 40: E1 photoneutron cross sections as a function of the photon energy. Reprinted figure with permission from [92]. Copyright 2020 by the American Physical Society.

experiments at the same facility focusing on the photoneutron cross section in the low energy tail of the GDR, see, e.g., Ref. [106, 112].

Another recent example is a systematic study on the photoneutron cross section up to 40 MeV in ten odd-even nuclei performed at the LCB facility NewSUBARU in Japan [92]. To give an idea about the quality of these measurements we show the measured cross sections in Fig. 40. The integrated cross sections, the centroid energies, and the polarizabilities extracted from these experiments could be reproduced in most cases with state-of-the-art theoretical calculations. For the most recent update on ground-state photoabsorption in the region of the GDR we refer to the data collections by Plujko et al. [309] and by Kawano et al. [90] which include a list of all relevant references.

Due to its high energy, its large width and the dominance of the IVGDR in its low-energy region, the study of the isovector Giant Quadrupole Resonance (IVGQR) has always been a challenge. Most data still stem from a series of electron scattering experiments performed by Pitthahn et al. in the 1970's, see, e.g., [310]. The derived parameters of the IVGQR usually show large statistical uncertainties and additional systematic errors have to be added. An estimate of the excitation energy E_{IVGQR} of the IVGQR is given by:

$$E_{IVGQR} = (125\ \text{MeV} - 135\ \text{MeV}) \cdot A^{-1/3} \quad (111)$$

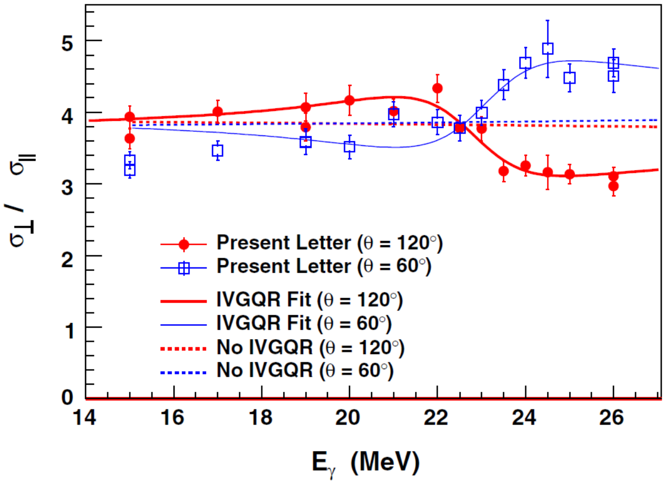

Figure 41: Polarization ratios from Compton scattering off a ^{209}Bi target in the region of the IVGQR. The dotted curves ("No IVGQR") show the expected ratios if only the isovector dipole and no isovector quadrupole strength is present. Reprinted figure with permission from [308]. Copyright 2020 by the American Physical Society.

Dale et al. used the off-axis polarization of a tagged bremsstrahlung beam at the University of Illinois to investigate the properties of the IVGQR in ^{208}Pb [311]. Photons in the entrance channel select dominantly E1, M1, and E2 resonances. The E2 contribution can be observed in the relevant energy region by its interference with the GDR. The polarization ratio of the Compton scattered beam, that is the ratio of cross sections perpendicular and parallel to the plane of polarization of the incident beam, allowed to extract reliable parameters for the IVGQR, however, with rather large uncertainties.

This method has been refined recently using the nearly 100% polarized, quasi-monoenergetic photon beam from the HIγS facility to investigate the IVGQR in ^{209}Bi [308] and ^{89}Y [312]. The pulse structure of the beam allowed to reduce the non-beam-related background. Figure 41 shows the measured polarization ratios for 13 different incident photon beam energies between 15 and 26 MeV. The bandwidth of the beam was about 2.5%. From the measurement of the energy, width, and strength of the IVGQR in ^{209}Bi were deduced with statistical and systematic errors each smaller than 1%, 20%, and 10%, respectively.

4.2 Pygmy Dipole Resonances

At energies well below the peak energy of the IVGDR various phenomena have been discussed as a possible source of electric dipole excitations, such as, e.g. two-phonon excitations involving an octupole vibration (see Sec. 4.3), α clustering [313,314] or - in light exotic neutron rich system - the appearance of a neutron halo [315].

In a series of experiments in the 1950s and 1960s a group around Bartholomew observed in thermal neutron capture experiments an enhancement of emitted γ rays around 5-7 MeV [316]. The notation "Pygmy Dipole Resonance (PDR)" introduced by Brzosko in the 60s [317] has been established for such an increased E1 strength at energies well below the GDR. Frequently, the PDR is considered as $1\,\hbar\omega$ E1 strength which has not been shifted to GDR energies by the isovector residual interactions. The observation by Bartholomew was confirmed later by Laszewski and Axel using tagged photons to excite the PDR [318]. Review articles on experimental studies of the PDR have been published by Bracco et al. [319] and Savran et al. [320]. In a simplified geometrical interpretation, these excitations are described as an oscillation of neutrons at the surface against an isospin-saturated core (this picture was first given by Mohan [321]). Some state-of-the-art theoretical calculations support this picture. For a recent overview about theoretical calculations see the special issue of European Physical Journal A [322].

In the last two decades, improved photon sources and γdetector arrays led to a new quality of the data on E1 distributions up to the particle thresholds. The pionieering high-sensitivity NRF experiments at these energies by Herzberg et al. [323] at the bremsstrahlung facility of the Darmstadt S-DALINAC were the kickoff of a series of experiments to investigate the PDR via photon scattering. The results on the semi-magic N=82 isotonic chain [324] triggered numerous experimental and theoretical efforts. Figure 42 shows the distribution of E1 strength measured in NRF experiments on various nuclei with a closed neutron and/or proton shell. In all cases, a considerable enhancement of E1 strength is observed below the neutron separation threshold indicated by S$_n$.

The use of monoenergetic photon beams allows to scan the photoresponse of a nucleus directly below and directly above particle threshold if the PDR is expected in this energy region. As one example, we show the result of a study by Shizuma et al. [325] using the LCB beam from NewSUBARU for (γ,γ') experiments below threshold and the LCB beam from TERAS for (γ,n) experiments above threshold in Fig. 43 . The measured cross sections are compared with different theoretical calculations.

Another advantage of monoenergetic photon beams comes into play if high level densities are present in the relevant energy range. The analysis of the data allows to identify not only discrete levels but as well strength in the quasi-continuum and weaker branchings into lower-lying states. For examples of recent publications see Refs. [57,70,72,326].

As discussed above, experiments with photons yield very robust data on the E1 (and M1) strength

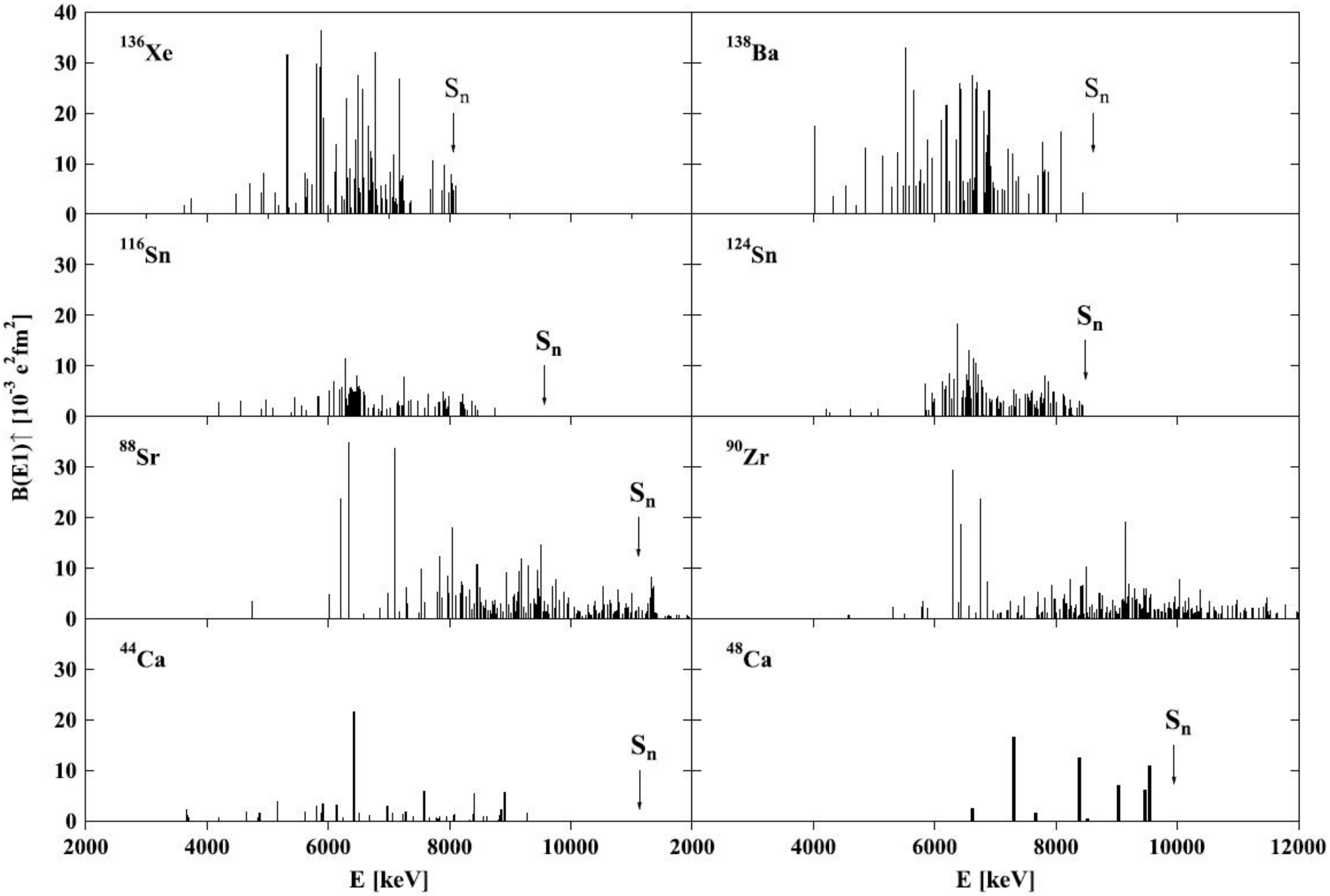

Figure 42: E1 strength distribution in various semi-magic or doubly-magic nuclei measured in photon scattering experiments. Reprinted Figure with permission from [320]. Copyright 2013 by Elsevier.

distribution. However, to understand the underlying structure, complementary experiments are mandatory. Today, the structure of the PDR has been investigated by the combination of different experimental probes, see, e.g., Refs. [319, 327, 328]. Proton, α and ^{17}O scattering experiments at particle spectrometers combined with high-resolution γ detectors at the KVI Groningen [329], the LNL INFN Lab, and recently at the RCNP Osaka and at iThembaLABS, have shown that the E1 strength below particle threshold seems to split into two parts in many nuclei. One part (which is concentrated at lower energies in heavy nuclei) seems to show a dominating isoscalar excitation pattern with charge transition densities dominated by neutrons at the surface of the nucleus. The other, higher-lying part seems to be dominated by isovector E1 excitations, i.e., resembles more the pattern associated with the GDR. Very recently, the microscopic structure of the E1 excitations below particle threshold has been studied in the doubly-magic nucleus ^{208}Pb in a particle transfer reaction and the results have been compared to large-scale shell model (LSSM) and energy-density functional plus quasiparticle-phonon model theoretical approaches [330].

The photon scattering experiments on stable nuclei have been complemented by virtual photon scattering experiments on neutron rich, unstable nuclei. Here, the expected enhancement of the PDR strength due to the increased neutron skin has been verified, see, e.g. [331, 332]. It has been shown that for a systematic comparison of the E1 strength in different isotopes in a wide mass range the Coulomb-corrected Fermi energy is an adequate parameter [320]. For a recent overview of the PDR in unstable nuclei we refer to the review article by Aumann [333].

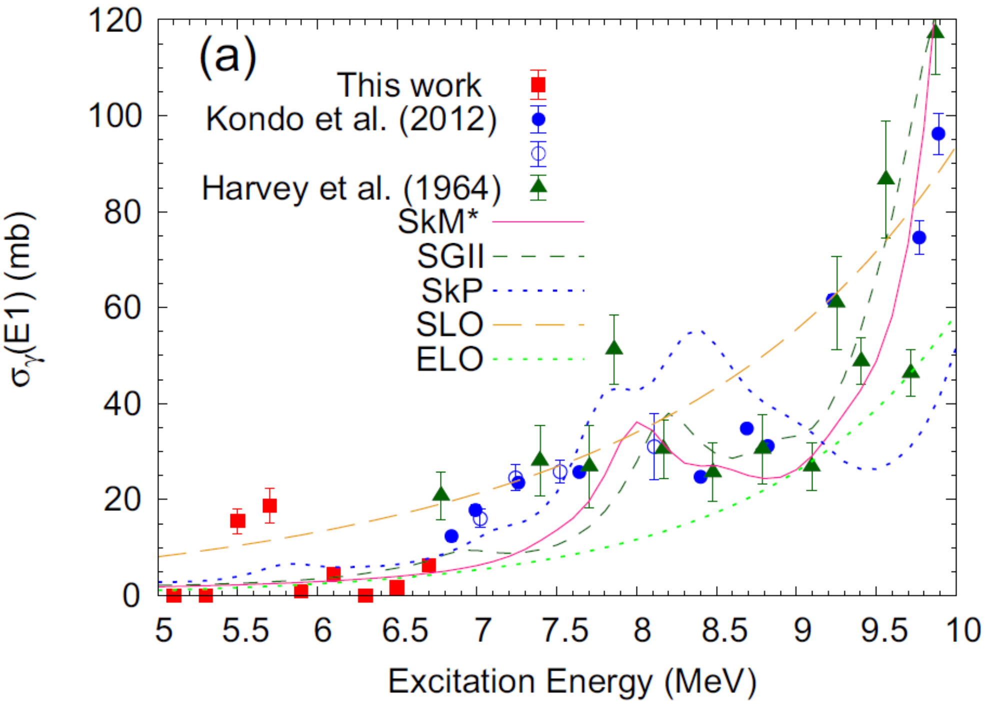

Figure 43: E1 photoabsorption cross sections of ^{207}Pb in the energy range 5 to 10 MeV obtained from (γ,γ') and (γ,n) experiments. Reprinted Figure with permission from [325]. Copyright 2021 by the American Physical Society.

Despite the intensive effort in the last decades, many questions about properties of the PDR are still unsolved. This concerns, e.g., the region of the onset of the PDR, the evolution of the PDR with neutron excess and deformation, the branching of the PDR into lower-lying states, the validity of the Brink-Axel hypothesis, and the underlying single-particle structure.

4.3 Two-phonon excitations

The low-energy excitation pattern of nearly all atomic nuclei shows phenomena of a coherent superposition of many single-particle excitations which are described as "collective". Two prime examples are relatively low-lying 2^+ and 3^- states in even-even nuclei which are characterized as quadrupole and octupole vibrations, respectively. A common alternative denomination is quadrupole or octupole "phonon" in analogy to the quantized vibrations of a crystal lattice. In a geometrical model, these phonons are visualized as isoscalar oscillations of the neutron-proton fluid around the ground-state shape. The E2 (or E3) transition strength from these phonon excitations at typical energies around 1-2 MeV to the ground state is enhanced with respect to the single-particle scale. In a simplified harmonic phonon-coupling picture, one would expect the existence of two-phonon excitations forming a multiplet of states with the structures $2^+ \otimes 2^+$, $3^- \otimes 3^-$, and $2^+ \otimes 3^-$ in the same nuclei. The energy of these two-phonon excitations is expected around the sum energy of the phonon constituents. The decay to the one-phonon state should be correlated to the strength of the decay from the one-phonon state to the 0^+ ground state:

$$
\begin{aligned}
B(E2, 2^+ \otimes 2^+ \to 2^+) &= 2 \times B(E2, 2^+ \to 0^+) && (112)\\
B(E3, 3^- \otimes 3^- \to 3^-) &= 2 \times B(E3, 3^- \to 0^+) && (113)\\
B(E2, 2^+ \otimes 3^- \to 3^-) &= B(E2, 2^+ \to 0^+) && (114)
\end{aligned}
$$

The factor of two in the coupling of identical phonons stems from the fact that the two constituents are indistinguishable. The coupling of a quadrupole phonon with an octupole phonon leads in even-even nuclei to a quintuplet of states with spin and parity quantum numbers $J^\pi=1^-$, 2^-, 3^-, 4^-, and 5^-. Because of the different single-particle structure of the two constituents, one (partly) avoids Pauli blocking. Pauli blocking can lead to strong anharmonicities if one couples identical phonons based on the same single-particle excitations. The 1^- state of the quintuplet is an ideal candidate to be studied in photonuclear reactions.

Already in the 1970s the group around Metzger and Swann have discussed their results on 1^- states investigated in NRF experiments in various lanthanide nuclei in this context, see, e.g., Ref. [334]. The picture can be extended to deformed nuclei where the octupole phonon couples to the quadrupole-deformed core creating $J^\pi=1^-$ band heads of rotational bands. A systematic survey of results from

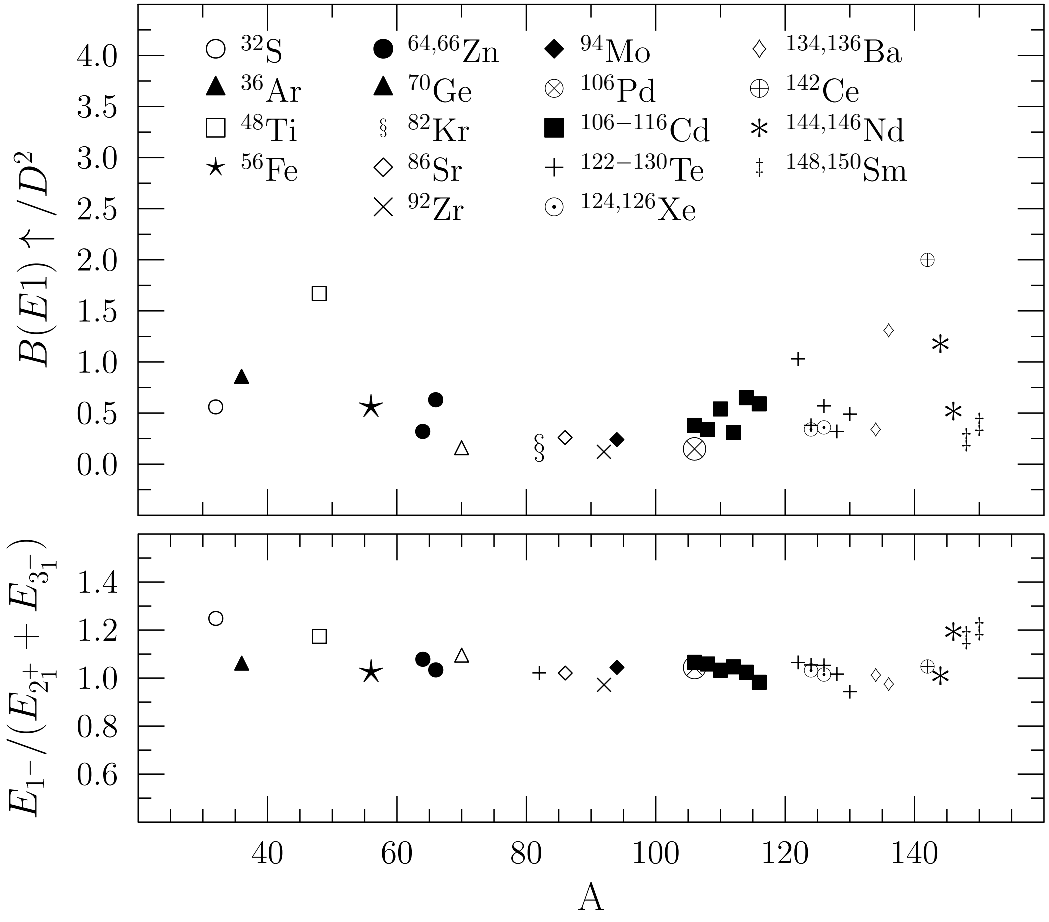

Figure 44: Two-phonon excitations in vibrational nuclei. The lower part shows the energy of the first 1^- excitation relative to the sum energy of the first 2^+ and 3^- states. The upper part illustrates the respective B(E1↑) ground-state transition strength relative to the squared dipole moment (see equation 115) derived from experimental data. (Semi)-magic nuclei are not included, they show a strong enhancement of the B(E1↑) /D^2 ratio.

bremsstrahlung experiments on vibrational nuclei in the mass range A≃30-150 is given in the article by Babilon et al. [335]. Here, the measured B(E1) strength from the octupole-coupled levels in non-magic nuclei to the ground state is compared to the squared dynamic dipole moment D estimated by:

$$\text{D in e·fm} = 5.376 \times 10^{-4} \cdot A \cdot Z \cdot \beta_2 \cdot \beta_3 \tag{115}$$

where β_2 and β_3 are the quadrupole and octupole deformations, respectively which have been derived from the B(E2) and B(E3) strength of the single-phonon levels [313, 336]. An updated plot is shown in Figure 44. The lower part depicts the ratio between the energy of the two-phonon 1^- state and the sum energy of the 2^+ and 3^- single phonon levels. The upper part shows the ratio of the B(E1↑) strength from the ground state to the 1^- two-phonon state normalized to the square of the product of the quadrupole and octupole deformations (see Equation 115).

A more detailed study of the properties of two-phonon states is possible by a combination of a monoenergetic γ beam for the excitation and a high-efficient array for the detection of the decay photons. Derya et al. [337] recently studied the $2^+ \otimes 3^-$ E1 excitation in doubly-magic ^{40}Ca and in neutron-magic ^{140}Ce utilizing the γ^3 setup [71] at HIγS. In this way, not only the ground-state decays but inelastic decays to the one-phonon 3^- level in ^{40}Ca and decays to the 2^+ state and to the 0_2^+ state could be observed as well. These new results together with theoretical calculations supported the two-phonon picture for the 1^- excitation.

We note that various complementary probes have been used to investigate the quadrupole-octupole excitation in even-even nuclei. As examples, we mention the seminal neutron scattering studies by the Kentucky group around Yates [338] and inelastic proton scattering [339].

The picture of quadrupole-octupole excitations has been broadened, e.g., by the additional coupling of an unpaired neutron or proton in odd-A nuclei [340–343], by involving other off-yrast phonons like the "gamma" vibration [344], and by the coupling of proton-neutron symmetric with mixed symmetric phonons [345]. All these phenomena have been studied in NRF experiments. Low-lying dipole modes in vibrational nuclei studied by photon scattering have been discussed in a review by Kneissl et al. [55].

4.4 Scissors Mode

The scissors mode (ScM) is a collective orbital $M1$ excitation of deformed, coupled, two-fluid quantum systems, in which the two deformed sub-systems can exhibit counter-rotational out-of-phase oscillations against each other in a scissors-like fashion. It can occur in a variety of quantum systems [346, and references therein]. In even-even nuclei it is characterized by a comparably strong $M1$ excitation from the ground state to excited $J^\pi = 1^+$ states with intrinsic-projection quantum number $K = 1$. The ScM has first been observed experimentally in deformed nuclei in the mid-1980s using inelastic electron-scattering reactions on the nuclide ^{156}Gd [347]. An accumulation of more-or-less fragmented $M1$ excitation strength was associated with the nuclear ScM. Its discovery has historically led to a renaissance of experimental activities employing photonuclear reactions on bound nuclear states at comparatively low-excitation energies of about 2 - 5 MeV because the NRF technique quickly turned out as being in many respects superior to other experimental approaches to the nuclear scissors mode in terms of energy resolution, sensitivity, and access to decay properties [348].

Extensive reviews have been published [10, 11, 55, 346, 349] on the nuclear ScM until about a decade ago. The investigation of the ScM using NRF has recently advanced, in particular by employing the opportunities offered by the advent of intense, quasi-monochromatic, fully polarized photon beams from LCB sources. These developments along with recent more classical studies using intense bremssstrahlung have not been covered in the review literature so far. We, thus, provide in this subsection a brief compilation of recent photonuclear studies of the nuclear ScM.

Identification and strength systematics The experimental identification of candidate fragments of the nuclear ScM relies on the measurement of their character of a strong $M1$ excitation of the nuclear ground state in combination with the collective features expected from the ScM, such as proportionality of the total excitation strength to the square of the nuclear quadrupole deformation [346, 350] or agreement with the specific $M1$ and $E2$ decay strengths or selection rules. As the ScM occurs at excitation energies where also $E1$ excitations can occur, it is mandatory for a clear identification of the ScM that the polarity of the dipole excitation is established as being of magnetic character.

The superior sensitivity of fully polarized photon beams to the polarity of nuclear dipole excitations of even-even nuclei with a 0^+ ground state [49, 61] has facilitated the identification of the ScM, tremendously. Figure 14 displays a recent example. The quasi-monochromacy of the incident LCB beam from the HIγS facility and its complete polarization have uncovered misassignments in previous literature where, due to the lack of sensitivity to the polarity of the NRF transition, parity quantum number assignments had been partly based on branching ratio systematics or enhanced transversal character in electron scattering. For example, the $J^\pi = 1^-$ states of ^{152}Sm at excitation energies of 2887 keV and 3012 keV had erroneously been misinterpreted as fragments of the $M1$ ScM in the earlier literature [350, 351]. In a recent NRF measurement at HIγS, Ide *et al.* [63] unambigously established the decay scheme of some strong dipole excitations of ^{152}Sm near 3 MeV excitation energy and the parity quantum numbers of the corresponding nuclear levels. A part of the data is shown above in Fig. 14.

In recent years, the $M1$ excitation strength of the ScM and its systematics had been investigated in photonuclear reactions on even-even isotopes of the Cr [352], Mo [353, 354], Ru [355], Cd [356, 357], Xe [358], Sm [63], Gd [66], Hf [359], Pt [360], U [361], and Pu [231] isotopic chains. Spin quantum numbers $J = 1$ and parity quantum numbers $\pi = +$ had in most cases been obtained from angular NRF intensity distributions. The corresponding dipole excitation strength had been determined from the total NRF intensities. Notably, Garrel et al. [358] have succeeded in tracking the scissors mode over a spherical-to-softly triaxially-deformed shape transition in the sequence of Xe isotopes thereby probing the dependence of the $M1$ excitation strength of the ScM on the nuclear deformation.

In odd-mass nuclei, the ScM is subject to an even stronger fragmentation into a multitude of nuclear states in the energy range of the ScM of neighboring even-even nuclei. This results typically in rather weak NRF intensities from the individual fragments. This fact, together with the rather small modulation of angular distribution about isotropy as compared to even-even nuclei makes the assignment of spin and parity quantum numbers in odd-mass nuclei usually very difficult. Hence, the data frequently suffer from missing spin and parity quantum number assignments.

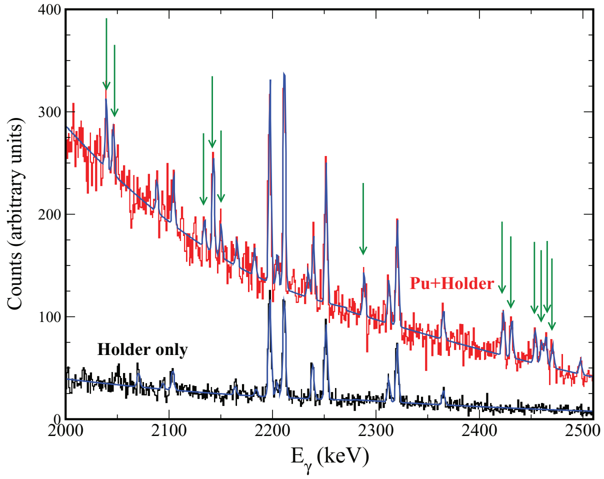

Figure 45: Dipole excitations of ^{239}Pu. Reprinted figure with permission from Ref. [230]. Copyright 2008 by the American Physical Society.

For example, Bertozzi *et al.* [230] have studied NRF of gram-sized samples of highly enriched ^{235}U and ^{239}Pu using unpolarized bremsstrahlung beams with endpoints at 2.2 MeV and 2.8 MeV, respectively. Integrated cross sections have been measured using photon flux calibration standards made out of aluminum and manganese. Nine NRF lines in ^{235}U and 12 in ^{239}Pu have been observed at energies between 1.6 and 2.5 MeV. The close proximity of the observed NRF lines to the energy of the ScM of ^{238}U may indicate that they are part of the ScM in the neighboring odd-mass isotopes. The ScM was studied by the NRF technique in odd-mass isotopes of the Rh [362], Ba [342], Eu [363], Dy [363], Ho [363], Ta [364, 365], U [366], and Np [367] isotopic chains. The odd-odd nuclide ^{176}Lu was investigated with NRF as well in a search for fragments of the ScM [368].

Decay features A comprehensive investigation of the nuclear ScM should combine high accuracy for the NRF cross sections with high sensitivity to its various decay channels. This can be achieved by particular combinations of experimental techniques. Broad-band intense bremsstrahlung offers sensitivity to the overall distribution of elastic NRF intensity and high accuracy for the necessary cross section calibration. Usage of polarized quasi-monochromatic photon beams or $\gamma\gamma$-coincidence spectroscopy following β-decay provide superior sensitivity to parity quantum numbers and to the details of the decay properties of the ScM. As an example for the latter, Beller *et al.* have studied $M1$ excitations of the transitional nucleus ^{154}Gd close to 3 MeV excitation energy by NRF using intense unpolarized bremsstrahlung at the DHIPS facility at the S-DALINAC injector TU Darmstadt on one hand and by $\gamma\gamma$-coincidence spectroscopy on the other hand. The latter were obtained following electron-capture reactions of the 0^+ isomer of $^{154}\mathrm{Tb}^m$ with a decay Q-value of 3.6 MeV which was previously populated by ^{154}Gd(p,n) reactions at the TANDEM accelerator at the University of Cologne. The 1^+ state of ^{154}Gd at 2934-keV excitation energy with an $M1$ excitation strength of $B(M1;0^+_1 \rightarrow 1^+) = 1.6(2)\ \mu_N^2$ [66] belongs to the fragments of the ScM with the largest $M1$ transition strength in the entire nuclear chart. The detailed decay pattern obtained from $\gamma\gamma$-coincidences provided information on its $M1$ decay to excited 0^+ states of ^{154}Gd. This made refined estimates possible for the $0\nu\beta\beta$ neutrinoless double-beta decays of its isobar ^{154}Sm and its isotone ^{150}Nd [66]. Further observations of $M1$ decays from ScM fragments to the 0^+_1 ground state and to the first excited 0^+_2 state of ^{98,100}Mo enabled Rusev *et al.* to determine the mixing of coexisting shapes of these isotopes [369].

Recently, Beck *et al.* [56] measured the $E2$ decay strength of the ScM of ^{156}Gd by a detailed study of the angular distribution of its NRF decay intensity into the 2^+_1 state of the ground-state rotational band. Its sensitivity to the $E2/M1$ multipole mixing ratio of the $1^+ \rightarrow 2^+_1$ transition has been discussed in subsection 2.3.6 where a part of the data are shown in Fig. 15. The corresponding isovector $E2$ strength was found to be quite small, on the order of a few percent of the single-particle strength, only. The observations are in semi-quantitative agreement with various theoretical predictions.

The characteristic quantum number $K = 1$ for the projection of the ScM's angular momentum onto the intrinsic symmetry axis of an axially-deformed nucleus can be assigned by comparison of the $M1$ branching ratio of the ScM into the ground state band to the Alaga rules. Savran *et al.* [67] have studied the distribution of decay branching ratios of the ScM in deformed even-even rare-earth nuclei. Data deviating from the Alaga rules require some amount of K mixing. From a K-mixing analysis of the strongest fragments of the ScM of ^{164}Dy, Beck *et al.* have recently quantified the K-mixing involving a ScM state [60]. A comparatively small K-mixing matrix element of 6.9 keV was found. The analysis revealed, in addition, a K-conserving $M1$ transition strength about two orders of magnitude smaller than the $M1$ decay strength of the ScM with $\Delta K = 1$. The corresponding data have been presented above in Fig. 12.

Related isovector valence-shell modes With decreasing nuclear deformation the character of the ScM gradually changes from a one-phonon mode excited from the deformed ground state by the isovector orbital part of the $M1$ transition operator to a quadrupole-collective two-phonon state formed by the coupling of the isoscalar and the isovector $E2$ phonon excitations of the valence shell. The latter is often addressed as the mixed-symmetry $2^+_{1,\mathrm{ms}}$ state. First firm evidence for this two-phonon character of the 1^+ state has been obtained from a combination of NRF studies with $\gamma\gamma$-coincidence spectroscopy [370].

The $2^+_{1,\mathrm{ms}}$ state represents the building block of mixed-symmetry structures of vibrational nuclei. It exhibits a weakly-collective $E2$ excitation strength from the ground state and, hence, can be studied well with NRF [370, 371]. Mixed-symmetry structures of vibrational nuclei have been reviewed some time ago [372]. Recent examples for NRF studies of mixed-symmetry one-phonon and two-phonon modes of vibrational nuclei were obtained for nuclides of the Zr [373], Ru [355], Cd [357], and Sm [374] isotopic chains.

4.5 Photon strength function

Photon strength functions (PSFs) characterize the average γ-ray transition probability of atomic nuclei [375]. Their concept is based on the assumption, that at sufficiently large nuclear level densities (NLDs) the excitation as well as decay properties of a nuclear state ensemble can be treated statistically, i.e. it can be described by mean values and a given statistical distribution. The PSF (and the NLD) are important ingredients to Hauser-Feshbach calculations [83] and for the modeling of nuclear reactions [376]. In addition to their impact on our understanding of the nucleosynthesis in astrophysical objects like supernovae or neutron-star mergers, PSFs are used in applied research areas such as the transmutation of nuclear waste [377] and reactor safety [378]. Experimental and theoretical studies often make the simplification, that the average electromagnetic excitation and decay probability merely depends on the photon energy and neither on the excitation energies of the initial or final states nor on the specific structure of the nuclear levels involved. These assumption are known as the Brink-Axel (BA) hypothesis [186, 379] and allow large-scale reaction network calculations for nuclear astrophysics (see, e.g., Refs. [380, 381]).

The photon strength function

$$f_{\lambda L}(E_\gamma) = \frac{\langle \Gamma^{ij}_{\lambda L} \rangle \, \rho(E_i)}{E_\gamma^{2L+1}} \tag{116}$$

is expressed in terms of the average reduced transition width $\langle \Gamma^{ij}_{\lambda L} \rangle$ between nuclear levels at excitation energy E_i to levels at E_j for a given electromagnetic transition character λL. It further depends on the NLD $\rho(E_i)$ and the γ-ray transition energy $E_\gamma = E_i - E_j$. Applying the principle of detailed balance, i.e. the photo-deexcitation can be directly linked to the photoexcitation, the PSF for photon emission and photoabsorption are considered to be equal. The PSF can therefore be derived from photoabsorption cross sections $\sigma_{\gamma,\lambda L}$

$$f_{\lambda L}(E_\gamma) = \frac{\sigma_{\gamma,\lambda L}}{(\pi \hbar c)^2 g E_\gamma^{2L-1}} \tag{117}$$

with the spin-dependent factor $g = (2J_i + 1)/(2J_0 + 1)$ and the spin of the excited state and the ground state J_i and J_0, respectively. Since dipole transitions are usually the dominant component of PSFs, the suffix λL is omitted in the following and we refer to the explicit transition character ($E1$ and $M1$) in the text.

Photonuclear reactions have been extensively used in the past to measure photoabsorption cross sections, which are directly linked to the PSF built on the ground state. Decades of research were dedicated to systematically study nuclei throughout the nuclear chart in the energy regime of the isovector giant dipole resonance [303, 304] as well as below particle threshold [11, 320]. Recent reviews on existing experimental data on PSFs and experimental methods can be found in Refs. [382, 383].

In this section, we show a few selected examples of current research activities with respect to the measurement of PSFs in photonuclear reactions.

Below particle threshold Experiments with continuous-energy bremsstrahlung have produced numerous data on stable nuclei. The extraction of photoabsorption cross sections in such measurements is challenging, because the spectroscopy of all decay channels is indispensable. Strong (ground-state) transitions are observed as prominent and resolved peaks in the corresponding γ-ray spectra. Weaker transitions usually cannot be directly distinguished from the existing background radiation which is why they are often denoted as unresolved transitions or quasi-continuum.

One approach to determine photoabsorption cross sections from NRF experiments with bremsstrahlung is based on the inclusion of the quasi-continuum in the analysis and the application of statistical methods. It was first described in the analysis of ^{88}Sr [218] and subsequently applied to many other isotopes; see for instance Refs. [326,384–398]. Exemplarily, photoabsorption cross sections for ^{54}Fe are shown in Fig. 46. Results from two NRF measurements with bremsstrahlung with endpoint energies of 7.5 MeV (blue triangles) and 13.9 MeV (red dots) are presented [384] in comparison to (γ, n) data (green squares) above the neutron separation threshold S_n [399]. The depicted data are compared to parametrizations of the IVGDR using a Triple Lorentzian (TLO; black dashed line) [400, 401] and to calculations from the TALYS-based evaluated nuclear data library (TENDL-2019) [402], which takes all reaction channels into account (black solid line). Since the (γ, p) cross sections dominate the photoabsorption cross section from 12 to 25 MeV, the TENDL-2019 results overestimate the experimental cross sections.

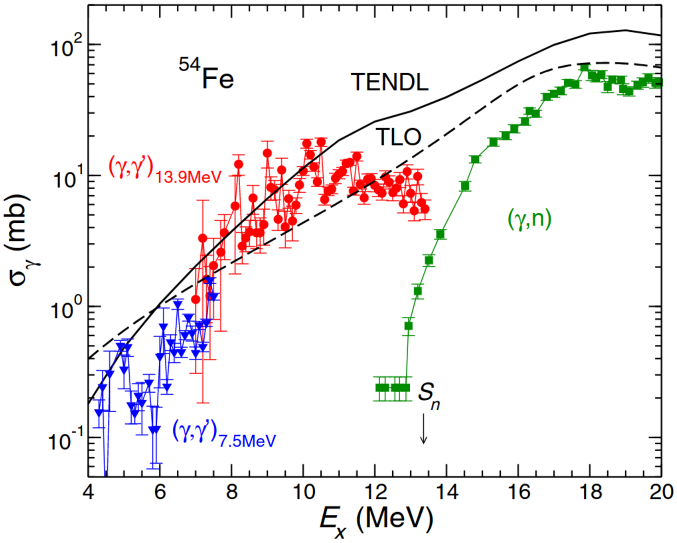

Figure 46: Photoabsorption cross sections for ^{54}Fe [384]. Reprinted figure with permission from [384]. Copyright 2020 by the American Physical Society.

A complementary and model-independent approach to extract photoabsorption cross sections in NRF measurements was introduced by Tonchev *et al.* [58] and is briefly discussed above in Sec. 2.3.4. The photoabsorption cross section ($\sigma_\gamma = \sigma_{\gamma\gamma} + \sigma_{\gamma\gamma'}$) can be devided into a so-called "elastic" component ($\sigma_{\gamma\gamma}$) referring to ground-state transitions after photoexcitation and into an "inelastic" component ($\sigma_{\gamma\gamma'}$) accounting for events decaying via intermediate states. Exploiting the narrow bandwidth of LCB photon beams, the inelastic part is approximated by the depopulation intensity of low-lying excited states, which collect most of the cascading events. The resulting PSF values from the measured photoabsorption cross sections between 4 and 8.6 MeV for ^{138}Ba, considering only resolved ground-state transitions, are displayed in panel (b) of Fig. 47 as blue squares. In the past decade, further nuclei have been studied with this method [57, 72, 326, 403–406], which was further developed to include also unresolved ground-state transitions [57, 72, 326, 403, 404] to allow a complete determination of the photoabsorption cross sections and PSF values, respectively.

In most experimental methods, the determination of PSFs is limited either to the excitation channel or the deexcitation channel. Very recently, a novel approach was presented allowing to extract PSFs from photoabsorption and photon emission measurements simultaneously in a single experiment [72] using the combination of LCB beams at HIγS [12] and the γ-γ coincidence setup γ^3 (see Ref. [71] and Sec. 3.4.2). The photoabsorption cross sections are obtained in the same way as discussed in the preceding paragraph. In addition, γ-γ coincidence measurements are used to determine the direct feeding (primary γ-ray transitions) of low-lying levels from excited states in a narrow excitation-energy window defined by the quasi-monochromatic LCB photon beam at HIγS. The beam energy is varied and for each measurement a set of primary γ-ray transition intensities as a function of the γ-ray transition energy is extracted. Scaling all individual data sets to each other allows to extract the shape of the underlying PSF, while it is not possible to determine absolute values of the PSF. The comparison between the two obtained PSFs for ^{128}Te reveals a discrepancy that hints towards a violation of the Brink-Axel hypothesis in this nucleus below the neutron separation energy. For a detailed discussion see [72, 407].

Above particle threshold Above the particle thresholds, photoabsorption cross sections and the resulting PSFs were determined using, e.g., total photoabsorption [409, 410] measurements mainly applied to light isotopes or in γ-particle reactions. The existing data bases on photoabsorption cross sections in the energy region of the IVGDR were compiled by extensive (γ, xn) measurements using quasi-monochromatic photon beams from positron annihilation in-flight during the 1960s and 1970s [305, 411]. However, data obtained from different facilities disagreed by 10-40 %. Thus, systematic investigations of photoabsorption cross sections in photoneutron reactions below the two-neutron separation thresholds were conducted, for instance at LCB facilities such as TERAS [100, 104, 412, 413], NewSUBARU [95, 114, 414, 415], and HIγS [12, 94, 123]. Figure 47 shows experimental photoneutron data (red circles) for (a) ^{137}Ba and (b) ^{138}Ba together with previous measurements (black circles and open diamonds) [408]. Below the neutron threshold, data from NRF experiments are shown for ^{138}Ba separated into their respective $E1$ (blue squares) and $M1$ (green circles) contributions [58]. For each dipole radiation character two different PSF models are depicted, namely a global parametrization denoted using SMLO models (solid lines) [416] and PSFs calculated within the so-called D1M + QRPA approach (dotted lines) [417–419]. Both $E1$ models describe the photoneutron data reasonably well up to the maximum of the IVGDR at $\sim$ 15 MeV even though the SMLO underestimates the experimental results between 9 and 11 MeV. Large deviations are observed in the case of ^{138}Ba below the neutron threshold, where the $E1$ PSF exhibits a pronounced double-humped structure, which cannot be described by either of the two monotonically decreasing PSF models. The additional concentration of $E1$ strength in the vicinity of the particle threshold is often associated with the so-called pygmy dipole resonance (PDR) [320] discussed in Sec. 4.2. Discrepancies to different parametrizations for the $E1$ PSF have been observed in several other cases. For a recent review on existing PSF data and the comparison to different models see [383].

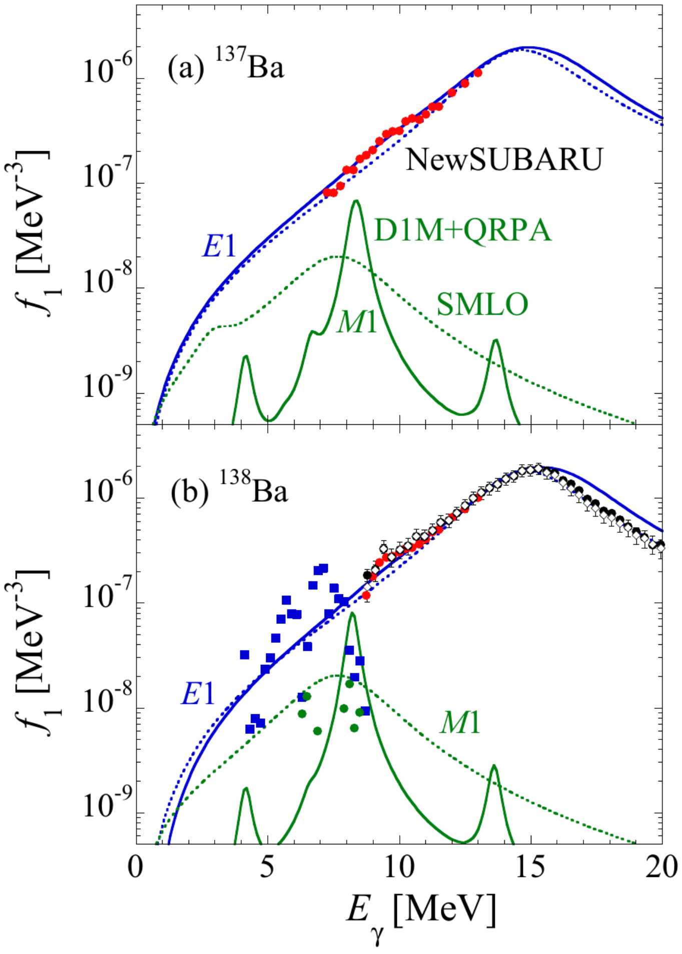

Figure 47: Photon strength function from photoneutron reactions for (a) ^{137}Ba and (b) ^{138}Ba [408]. Reprinted figure with permission from [408]. Copyright 2019 by the American Physical Society.

In recent years, a new method based on direct neutron-multiplicity sorting with a flat-efficiency ^{3}He counter was developed [150] allowing to measure complete (γ, xn) photoneutron reaction cross sections [116, 117, 420]. For a detailed discussion of the formalism of photoneutron reactions and neutron detection techniques see Sections 2.4 and 3.4.3, respectively.

4.6 Nuclear astrophysics

Nuclear reactions induced by photons play a dominant role in the synthesis of many atomic nuclei [421]. The high energy part of the Planck distribution emitted by heated objects can photodissociate nuclei. This becomes especially relevant in hot burning phases or explosive stellar scenarios. One example is silicon burning in the late stage of massive stars where fast photodisintegration reactions create free protons, neutrons and α particles. The subsequent capture of these particles produce the nuclei up to the broad abundance peak around iron. Finally, a so-called nuclear statistical equilibrium (NSE) is reached. Another example is the synthesis of heavier nuclei above iron. Here, the equilibrium between (n,γ) and (γ,n) reactions defines the path of the rapid neutron capture process (”*r* process”) on the neutron rich side of the valley of stability [382, 422]. On the other hand, for the synthesis of proton rich nuclei via the *p* process, photodissociations of heavy seed nuclei via (γ,n), (γ,p), and (γ,α) reactions are the driving force, see, e.g. [102, 423].

Due to their selectivity and the possibility to derive, e.g., total and partial γ decay width in a straightforward and model-independent way, photon scattering experiments can be a valuable tool to measure certain observables which are important in nuclear astrophysics. As an example, we refer to the NRF measurement of the level structure of ^{26}Mg close to the neutron threshold using photons from laser Compton backscattering (LCB). This level structure is important to understand the neutron production for the *s* process in the ^{22}Ne(α,n)^{25}Mg reaction during the pulsing period of AGB stars [424].

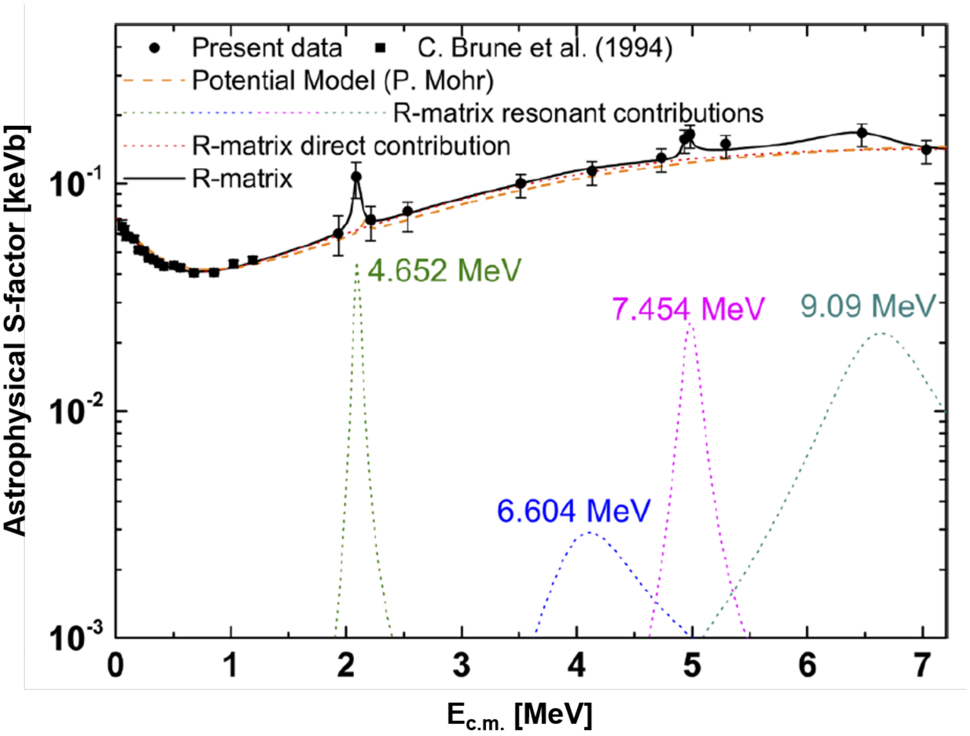

Figure 48: Astrophysical S factor derived from the results of a ^{7}Li(γ,t) experiment at HIγS together with a R matrix fit. Direct contribution and individual resonance contributions (dotted lines) and total contribution (solid line) are shown. Reprinted figure with permission from [149]. Copyright 2020 by the American Physical Society.

A measurement of the cross section of the (γ,t) reaction on ^{7}Li recently helped to constrain the rate of the inverse ^{3}H(α,γ)^{7}Li reaction which is important to understand Big Bang nucleosynthesis. For this purpose, monoenergetic photons at HIγS in the energy range 4.4 to 10 MeV have been used, where tritons and α particles were detected in coincidence by segmented silicon detectors [149]. The S factor of the inverse (α,γ) reaction on ^{3}H could be derived from the data and was compared with R matrix calculation, see Fig. 48. An interesting approach to investigate the interaction of a Planck photon bath with a nucleus has been followed by Mohr et al. [426]: A superposition of electron bremsstrahlung spectra with different endpoint energies creates a spectrum of photons which looks very similar to the distribution of photons from a Planck spectrum (see Fig. 49) in the relevant energy range. The temperature of the Planck spectrum to be reproduced can be adjusted by adequate superposition factors. Photodissociation (γ,n) cross sections are then derived from activation experiments where the irradiation with the "Planck" photon bath leads to a radioactive nucleus whose γ decay is detected off-beam. This technique has been used, e.g., to investigate the γ process of explosive nucleosynthesis in Pt, Hg, and Pb isotopes [427, 428].

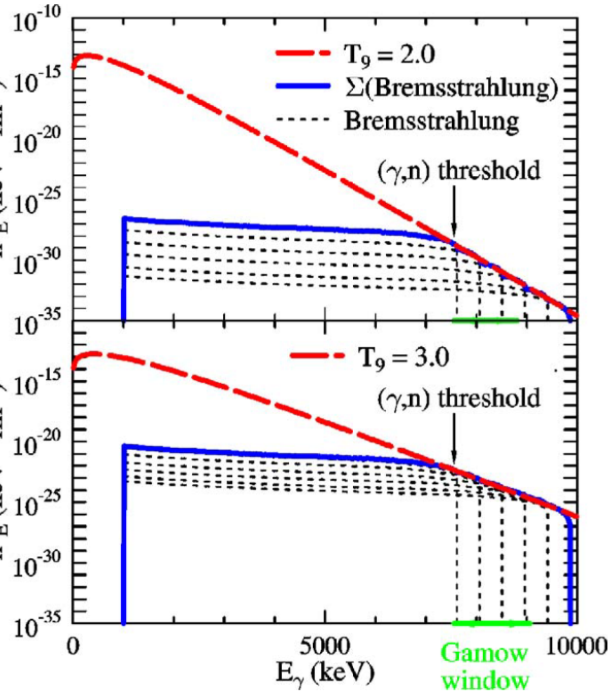

Figure 49: A superposition of bremsstrahlung spectra (dotted line) creates a photon spectrum (full line) which can be compared with a Planck spectrum at a certain temperature (dashed line). Reprinted figure with permission from [425]. Copyright 2006 by Elsevier.

Furthermore, the knowledge of the photodissociation cross section can help to estimate the neutron capture rate on radioactive nuclei. For instance, the s-process branching in ^{185}W was studied by the photodissociation of ^{186}W via bremsstrahlung [429]. Here, the detailed balance theorem was used to derive the reverse (n,γ) rate on the β unstable nucleus ^{185}W. Another approach is to measure the energy dependence of the (γ,n) cross section with LCB photons. Examples are the studies to investigate the *s*-process branching nuclei ^{79}Se [430] and ^{85}Kr [120]. It was shown that a combination of this technique with other experimental results allows to estimate the neutron-capture cross section on various radioactive nuclei [111], see Sec. 2.5.6.

A further open question in nuclear astrophysics which had been investigated by means of photons is the occurence of the rarest isotope on earth, ^{180}Ta. There is a long-standing debate on the isomeric state (with an half-life limit of 4.5×10^{16} years) and how it can be depopulated by photons via intermediate states to the ground state which has a half life of only $T_{1/2}$=8.15 h. Such a scenario would exclude certain temperatures for the astrophyical scenarios where ^{180}Ta has been synthesized. Various experiments have been performed looking for a possible depopulation of the isomer by photons from bremsstrahlung [431, 432] and from LCB [101, 433]. Recently, an overview of different experimental studies concluded that the isotope is likely synthesized in the astrophysical *p* process [434]. A compilation of experiments to depopulate isomers by photons has been published by Kneissl [435].

In cosmochronology the γ-ray strength function derived from photoneutron cross sections has recently been used to investigate the ^{205}Pb-^{205}Tl- and ^{187}Re-^{187}Os-chronometers [100, 408].

Finally, we would like to guide the reader to a recent overview article discussing possible future photodisintegration reactions with monoenergetic photon beams, see Ref. [436].

4.7 Few-body systems

This subsection addresses photonuclear approaches to the relicts of sub-nucleonic degrees of freedom in observables for light nuclei. The largest amount of corresponding research in the last years have addressed the verification of the Gerasimov-Drell-Hearn (GDH) sum-rule [144, 145]. It relates the total cross section for the absorption of a circularly polarized photon by a polarized target with its spin parallel, $\sigma^P(E_\gamma)$, or antiparallel, $\sigma^A(E_\gamma)$, to the photon spin to the anomalous magnetic moment as

$$\int_{E_{th}}^{\inf} (\sigma^P(E_\gamma) - \sigma^A(E_\gamma)) \frac{dE_\gamma}{E_\gamma} = \frac{4\pi^2 e^2}{A^2} \kappa^2 I, \tag{118}$$

where E_γ is the photon energy, E_{th} is the two-body photodisintegration threshold, κ is the anomalous magnetic dipole moment, A is the mass, and I is the spin of the nucleus. The relation was first written for polarized protons, but it can be extended to polarized nuclei.

In first experiments, the GDH sum rule for the deuteron was studied. The experiments covered a range of γ-ray energies between 2.39 and 16 MeV [128,129,131,132]. The analyzing power of the reaction was measured, utilizing linearly polarized γ rays and non-polarized targets. The photodisintegration cross section for linearly polarized beam and unpolarized target is written in terms of an $M1$ and an $E1$ components of the total ^{2}H(γ, p) cross section. Under certain assumptions, see *e.g.*, Ref. [131] for details, an indirect determination of the GDH sum rule for the deuteron was obtained.

With the development of polarized ^{3}He targets, an experimental check of the GDH sum rule became feasible. The photodisintegration of spin-polarized ^{3}He was studied at HIγS [134–136]. In the first experiment, a longitudinally polarized ^{3}He target and a nearly monoenergetic, $\sim 100\%$ circularly polarized photon beam were used. The beam was pulsed at a rate of 5.5 MHz with intensities of $(1 - 2) \times 10^8$ γ/s, having an bandwidth of $\Delta E_\gamma / E_\gamma = 3\%$ at 12.8 MeV and 5% at 14.7 MeV [134, 135]. A follow-up experiment was performed at the incident photon energy of 16.5 MeV with on-target intensity of (7.3–9.5) $\times 10^7$ γ/s and bandwidth $\leq 5\%$. The photon flux was monitored utilizing the ^{2}H photodisintegration setup, see also Sec. 3.4.1.

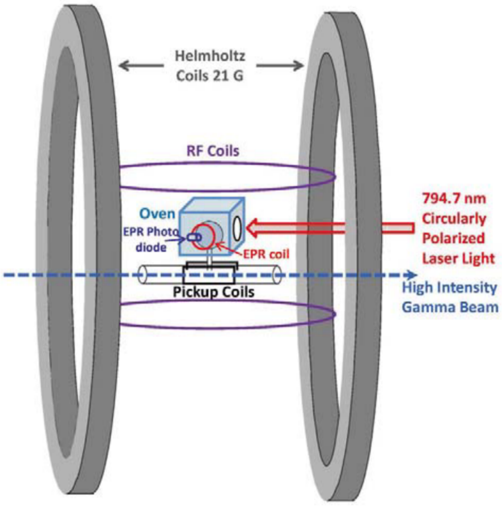

Figure 50: Schematic presentation of the polarized ^{3}He target set-up. Reprinted figure from Ref. [437] with permission from Springer.

The main experimental challenge, which was addressed in these experiments, was the construction of a polarized ^{3}He target [437, 438]. A target polarization of the order of 33–46% has been achieved. The target cell is a pyrex glass cell coated with aluminosilicate and contains a mixture of Rb-K. The paramagnetic-free aluminosilicate glass-coated surface reduces the probability of ^{3}He depolarization from the walls. The target set-up is shown schematically in Fig 50. It consists of a pair of Helmholtz coils with a diameter of 173 cm to provide a magnetic holding field with a typical value of 21 G. The gas cell consists of a spherical pumping chamber with a radius of 4.3 cm and a target chamber with a length and a diameter of 38.7 cm and 3.1 cm, respectively. The chambers are connected by a tube that is 9 cm long with a diameter of 1.3 cm. The pumping chamber is placed in a oven. The whole gas cell system is installed in the center of the Helmholtz coils. The RF coils and the electron paramagnetic resonance (EPR) photo diode, which are shown in the Fig. 50

are used for measurements of the polarization of ^{3}He, for details see Ref. [437].

Angular distributions and energies of neutrons emitted in the three-body break-up were detected in the experiment. Spin-dependent double-differential cross sections, see Sec. 2.5.3, and the GDH integrand from three-body breakup were deduced from these measurements.

In a recent experiment, the GDH sum rule for the ^{3}He(γ,p)^{2}H reaction, the two-body breakup channel, was measured [439]. The results related to the GDH sum rule are presented in Fig. 51.

At AIST, the photodisintegration cross sections of the ^{3}He three-body system was used to investigate the nucleon-nucleon (NN) potential and the role of three-nucleon (3N) forces in nuclear reactions. The data were used to compare to theoretical calculations based on the AV18+Urbana IX nuclear force model [146].

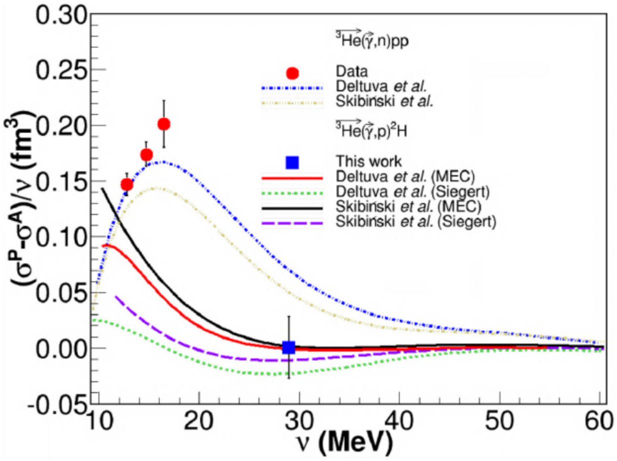

Figure 51: (Color online) The GDH-sum-rule results for the ^{3}He(γ,p)^{2}H reaction (blue square), and the ^{3}He(γ,n)pp reaction (red circles) with theoretical predictions, for details see Ref. [136, 439]. Reprinted figure with permission from Ref. [439]. Copyright 2021 by the American Physical Society.

4.8 The 2^{+} excited state built on the Hoyle state

The isotope ^{12}C is synthesized in the helium burning phase of star evolution. Its synthesis is understood as a two-step process, first two α-particles fuse to resonantly form ^{8}Be. In a second step ^{8}Be captures an α-particle to form ^{12}C. Hoyle recognized the need for a $J^{\pi} = 0^{+}$ state with an energy of about 7.5 MeV, called the Hoyle state, in order to account for the absolute abundance of ^{12}C and the abundance ratio of ^{12}C and ^{16}O [440]. The idea is that the capture of an α-particle by ^{8}Be proceeds by tunneling through a potential barrier. Despite its short lifetime, there is a statistical equilibrium of some concentration of ^{8}Be in the stellar plasma which enables the process. In the case of an s-wave capture the probability of ^{12}C synthesis is highest. In addition, the presence of the Hoyle state boosts the capture process by a factor of 10^{7}–10^{8}. Hoyle predicted the existence of a state at 7.68 MeV [440]. Simultaneously at Caltech the ^{14}N(d,α)^{12}C reaction was measured and a state at 7.68 ± 0.03 MeV was observed [441]. Subsequent measurements refined the energy of the state to 7.653 ± 0.008 MeV and indicated the most probable spin and parity to be $J^{\pi} = 0^{+}$ [442]. In the years to follow, there has been significant effort to understand the structure of the Hoyle state. For a recent review see Ref. [443].

Morinaga described the Hoyle state in terms of three weekly interacting α-particle [444], which means that the Hoyle state might be highly deformed, in case the α-particles are configured in a chain or in a bent arc [445]. In such a case, excited states built on top of the Hoyle state should form a rotational band. The existence of a $J^{\pi} = 2^{+}$ was long sought for. Excitation energy spectra in ^{12}C were populated in proton and α-particle inelastic scattering experiments [446]. The data provide evidence for the existence of a 2^{+} state at $E_{ex} = 9.75 \pm 0.15$ MeV with a width of 750 ± 150 keV. This state was suggested to corresponds to the 2^{+} excitation of the 7.65 MeV Hoyle state [446]. In an experiment with the O-TPC [287] (see Sec. 3.4.4) at HIγS, exploring the ^{12}C(γ,3α) reaction, the nature of this state was unambiguously identified [147], because real-photon beams excite either $J = 1$ or $J^{\pi} = 2^{+}$ state out of a $J^{\pi} = 0^{+}$ ground state of an even-even nucleus. Thus, 0^{+} states (the 3 MeV broad 10.3 MeV resonance) are not populated and the 9.64 MeV 3^{-} state will be populated with very small probability.

The excitation energy of the 2^+ resonance state was measured as $E_{ex} = 10.03 \pm 0.11$ MeV, with a total width of 800 ± 130 keV. Angular distributions were measured in the experiment, which demonstrate the 2^+ character of the observed resonance state.

Almost all (98%) of the ^{12}C dissociation events were reported to proceed via the ^{12}C(γ,α_0)^{8}Be reaction leading to the ground state of ^{8}Be, and the subsequent immediate decay to two nearly collinear α particles as shown in Fig. 52.

Another possible decay path is by emitting simultaneously three α particles. Theoretical predictions provide a limit of $< 1\%$ for such a direct decay [447]. This prediction was tested experimentally [448–450] and upper limit for the direct rare decay branching ratio was set to 0.019% [450], *e.g.* $\approx 2 \times 10^{-4}$.

Recently, Smith et al. re-examined the O-TPC data from the HIγS experiment [291] and observed a second class of events with large opening angles between the three α particles. In this case the α particles share the breakup energy more evenly and the decays do not go through the ^{8}Be ground state, as shown in Fig. 52. These events were identified as direct three-α decays or decays to excited states in ^{8}Be. A limit on the direct three-α branching ratio was deduced as $\frac{\Gamma_{3\alpha}}{\Gamma} < 5.7 \times 10^{-6}$. This is approximately two orders of magnitude lower than the previously reported experimental limit [450].

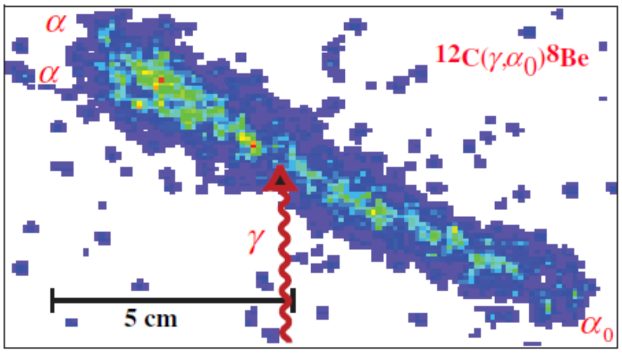

Figure 52: Typical image recorded by the CCD camera of the O-TPC. Three alpha particles from the reaction ^{12}C(γ,α_0)^{8}Be, followed by the subsequent decay to 2α particles are displayed. Reprinted figure with permission from Ref. [147]. Copyright 2013 by Americal Physical Society.

4.9 Parity mixing

Fundamental symmetries play a paramount role in our understanding of the building blocks of nature. The weak interaction violates symmetry under space reflection. While the strong force conserves parity, the effective nuclear force violates parity due to contributions of the weak interaction to the effective nucleon–nucleon interaction. Observable consequences of the latter can be enhanced in peculiar situations where two nuclear energy levels with opposite predominant parity and otherwise identical quantum numbers are located very close to each other in a parity doublet. Parity-mixing due to the weak interaction then results in the inheritance of some unnatural-parity decay mode by the predominantly natural-parity state and vice versa. The so-called '*nuclear enhancement factor*' $\mathcal{F}_E$, defined as the ratio of the unnatural-parity versus natural-parity decay matrix element divided by the energy separation of the parity doublet, quantifies the potential of the parity doublet to exhibit observable parity violation.

The $J^\pi = 1^+/1^-$ parity doublet in ^{20}Ne at 11.26 MeV excitation energy has been suggested as one of the best cases for the study of parity violation in isolated nuclear eigenstates [53]. The energy-ordering with corresponding excitation energies $E(1^-) = 11255.4(\pm 0.7)_{\mathrm{stat}}(^{+1.2}_{-0.6})_{\mathrm{syst}}$ keV and $E(1^+) = 11258.6(2)$ keV and the nuclear enhancement factor $\mathcal{F}_E = 1.4(\pm 0.3)_{\mathrm{stat}}(\pm 0.2)_{\mathrm{syst}}$ keV^{-1} have recently been measured by Beller *et al.* [54] using a pioneering combination of linearly-polarized and circularly-polarized photon beams from the HIγS facility.

While the energies of the $1^-/1^+$ levels are too close for their γ-decays being resolvable with any state-of-the-art γ-ray spectrometer, Beller *et al.* studied the variation of the centroid of this γ-ray doublet in NRF as a function of observation angle and polarization of the incident photon beam. At polar angle

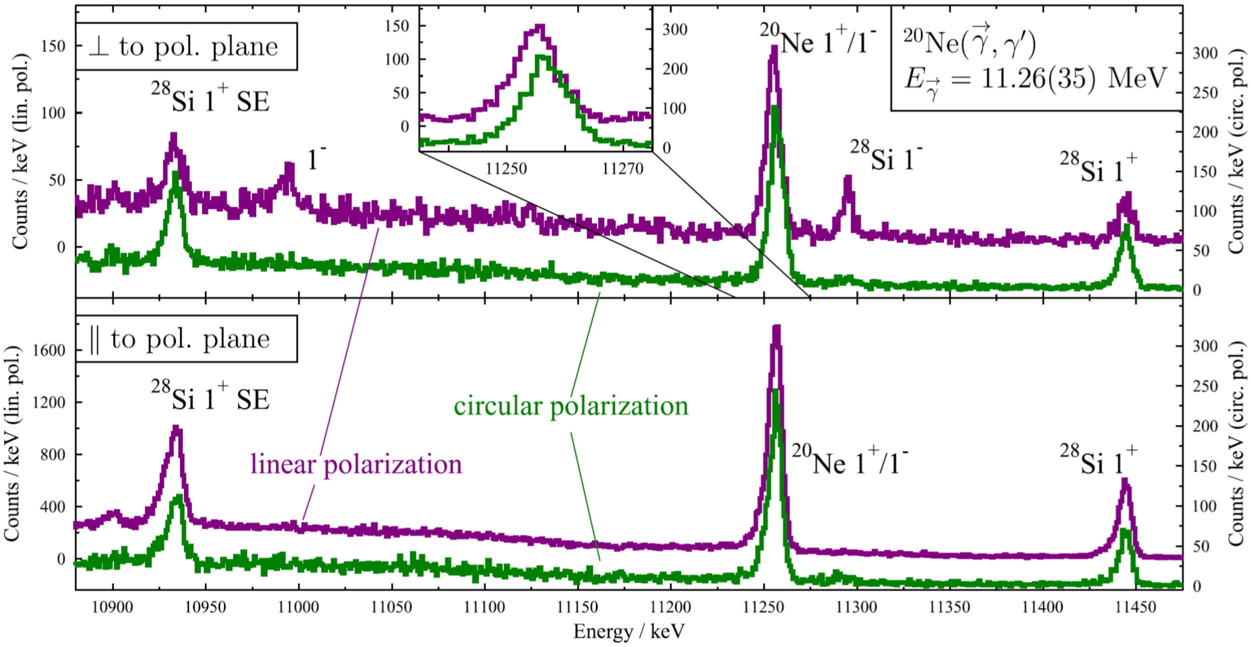

Figure 53: NRF spectra of ^{20}Ne detected vertically (top) and horizontally (bottom) around the target irradiated with a horizontally linearly-polarized (purple) and a circularly-polarized (green) LCB photon beam at HIγS. The spectra obtained with an incoming linearly-polarized beam (purple) use the left axis, while the spectra obtained with an incoming circularly-polarized beam (green) use the right axis. The visible energy shift of the 11.26-MeV NRF-doublet from ^{20}Ne between the NRF spectra obtained with linear and circular polarization in the vertical detectors demonstrates that the 1^- level must be located at a lower excitation energy than the 1^+ level. This shift is enlarged in the inlay. Reprinted figure with permission from Ref. [54]. Copyright 2015 by Elsevier.

$\vartheta = 90^\circ$ the contribution of the 1^- (1^+) level to this doublet is enhanced in directions perpendicular to (within) the polarization plane of an incident linearly-polarized photon beam as compared to the usage of unpolarized or circularly-polarized photon beams. From the measured energy shifts and count rates for various combinations of azimuthal observational directions and incident photon-beam polarizations shown in Fig. 53, Beller *et al.* were able to demonstrate that in this way it is possible to determine the level ordering, their excitation energies, and their individual excitation strengths. This parity doublet in ^{20}Ne features the largest nuclear enhancement factor [53, 54] of any parity doublet known in the literature. Parity violation in either one of these $J = 1$ states will result in a forward/backward-asymmetry of NRF intensity from each of these states when excited with a circularly polarized beam. Such an experiment has been proposed [53] and analyzed with respect to the necessary luminosity [54]. Its successful execution is still pending.

4.10 Photofission transmission resonances

In the actinide nuclei, the superdeformed (SD) second minimum in the potential energy surface (PES) was discovered experimentally [451] and explained theoretically [452] in the 1960s and is rather well understood. The existence of a third minimum at hyperdeformed (HD) nuclear shapes has been suggested theoretically [453–455]. However, there are other models that do not predict any third minimum of the PES [456, 457]. In the light actinides, the assumption of a double-humped barrier fails to explain the experimental results. This discrepancy was suggested to be related to the existence of a third HD minimum in the PES [458].

Highly excited states in the second or third well could be studied by measuring the fission probability as a function of excitation energy. The states in the second minimum are expected to be predominantly of β-vibrational type, *i.e.*, the stretching mode, which leads to fission. States in the third minimum are expected to be of mixed octupole-quadrupole origin. If excited states in the first well are populated, *e.g.*, by (d,p) reactions, one will observe an enhanced fission probability (transmission resonances) for those excitation energies, because states in the first well will couple to coinciding vibrational states in the second or third well. Hence, measurements of transmission resonances in the fission cross section enable selective investigation of extremely deformed nuclear states in light actinides and can be utilized to better understand the landscape of multiple-humped PES in these nuclei [458].

Studies of transmission resonances were mostly carried out using transfer reactions and photofission. The advantage of the transfer reactions is the very good (≤ 5 keV) energy resolution, which gives better than 0.1% resolution in excitation energy, which is provided by the magnetic spectrometers. Observing transmission resonances as a function of excitation energy caused by resonant tunneling through excited states in the second and third minimum of the potential barrier, allows us to identify the excitation energies of the SD and HD states, see *e.g.* Ref. [459–461] and references therein. Moreover, the observed states can be ordered into rotational bands, with moments of inertia, proving that the underlying nuclear shape of these states is indeed of SD or HD configuration. For the identification of rotational bands, the information on spin can be obtained by measuring the angular distribution of the fission fragments [459]. Furthermore, the PES of the actinides can be parametrized very precisely by analysing the overall structure of the fission cross-section and by fitting it with the nuclear reaction code (EMPIRE [87] and TALYS [86]) calculations.

Experimentally, evidence for HD structures was provided by measurements of subbarrier resonances of the fission probability [460, 462]. For ^{230,231,232}Th the microstructure of the resonances was described as being HD rotational bands. A high-resolution study of the transmission resonances in a (d,p) reaction was reported in ^{236}U, and the results were interpreted as consequence of the hyperdeformed states lying in the third well of the fission barrier [461].

In photofission experiments, the selectivity of these measurements originates from the low and reasonably well-defined amount of angular momentum transferred during the photoabsorption process. Photofission studies were carried out with bremsstrahlung photons measuring integrated fission yields [463]. Better resolution was achieved with measurements using bremsstrahlung monochromator [464] and tagged photons [33]. However, high-resolution measurements of transmission resonances with much better statistics are needed for the study of extremely deformed nuclear shapes in the light actinides.

An experiment with LCB photons exploring the multiple-humped fission barrier via sub-barrier photofission was performed at HIγS, and indicated the existence of three minima in ^{238}U, because the measured sub-barrier cross section in the 4.7 – 6.0 MeV energy range was described best by a model assuming a deep HD minimum [465]. The LCB beam bandwidth of typically about 3 % was not narrow enough to resolve possible transmission resonances (see Fig. 54). In a follow-up experiment, the prompt photofission neutron polarization asymmetries, neutron multiplicities, and the photofission cross sections were measured in the near-barrier energy range of 4.3 to 6.0 MeV in ^{232}Th and ^{238}U [274]. Large polarization asymmetries are observed in both nuclei, consistent with the $E1$ excitation. The ^{238}U(γ,f) reaction-cross-section data are consistent with the data of Csige et al. [465] above $E_\gamma \approx 5.3$ MeV, as shown in Fig. 54. There is increasing disagreement between the data sets below this energy, with a factor of ~ 3 discrepancy at 4.8 MeV. The data of Ref. [465] were also obtained at the HIγS facility by using nominally the same photon beams. The low-energy enhancement can be explained by a bremsstrahlung beam contamination present at the HIγS facility [467].

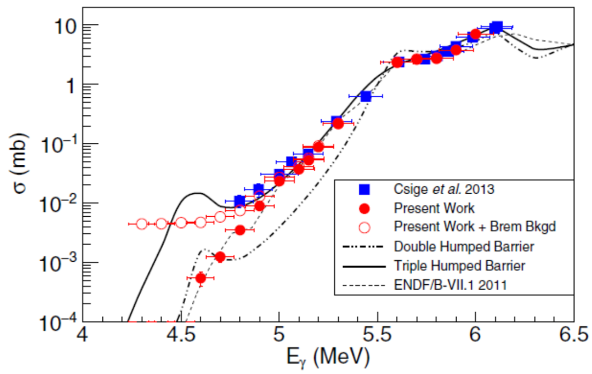

Figure 54: Photofission-cross-section results of ^{238}U with and without the HIγS photon beam bremsstrahlung background subtracted, compared with the data of Csige et al. [465] and the ENDF/B-VIII.0 evaluation [466]. Photofission-cross-section calculations from Ref. [465] for double- and triple-humped fission barrier fits to their data are also shown. Reprinted figure from Ref. [274] with permission. Copyright 2018 by the American Physical Society.

The calculations from Ref. [465] were performed with the EMPIRE code [87], assuming a double- or triple-humped barrier. Neither calculation is in good agreement with the reported results in Ref [274].

While the resonance structure in ^{238}U is questionable, a plateau in the photo-fission reaction cross section for ^{232}Th in the energy range of 5.4 to 5.7 MeV was confirmed [274]. This asks for further studies with intense quasi-monochromatic photons with bandwidth of about 1 % which is comparable to the reported resonance bandwidth [33]. The capabilities of the next-generation LCB facilities, such as ELI-NP, will allow one to aim at identifying the sub-barrier transmission resonances in the fission decay channel.

5 Applications

In this section examples of various applications of photonuclear physics are discussed. The increased brilliance of γ-ray sources opens new perspectives for their use in various fields of technology, *e.g.* finding new routes for production of medical radioisotopes or nuclear transmutation. The spectral density of the next generation LCB γ beams increases to 10^4 photons/(s·eV), compared to 10^3 photons/(s·eV) which are available at present. This enables a new quality for γ-beam based computer tomography (CT) and 3D radiography. The perspectives in the field were highlighted in Ref. [468]. We will focus on the ongoing research in the field.

5.1 Databases for (γ,n) reactions

The detailed knowledge of photo-induced reaction cross-section data are of importance for a variety of current or emerging applications, such as radiation-shielding design and radiation-transport analyses, calculations of absorbed dose in the human body during radiotherapy, physics and technology of fission reactors (the influence of photonuclear reactions on the neutron balance), and fusion reactors (plasma diagnostics and shielding-activation analyses), safeguards and inspection technologies, nuclear-waste transmutation, medical-isotope production and astrophysical applications.

Starting in the 1960s till the 1980s, a systematic effort has been undertaken to measure partial (γ,νn) reaction cross sections using quasimonochromatic annihilation photons, produced in positron annihilation in-flight. The experiments were done at LLNL in USA and at CEN Saclay, France. The results of these measurements were published as data compilations [305, 411]. However, there are differences in the two data bases. Facing this problem, the Nuclear Data Section at the International Atomic Energy Agency organized in 1996 a coordinated research project (IAEA CRP) to evaluate the partial and total (γ,n) reaction cross sections. As a result, the 1999 Photonuclear Data Library was produced [89]. Within this activity, the cross sections for 164 isotopes were evaluated, which fall in the following categories: (i) structural, shielding and bremsstrahlung target materials, (ii) biological materials, (iii) fissionable materials, and (iv) others.

Soon after the appearance of the 1999 database, a method for evaluating the consistency of the reported cross sections was suggested [469]. As a result of this study, it was recommended that the total photoneutron $\sigma_{tot}(\gamma,\mathrm{n})$ and partial $\sigma(\gamma,1\mathrm{n})$ and $\sigma(\gamma,2\mathrm{n})$ cross-sections resulting from measurements at LLNL must be multiplied by a factor. The total photoneutron cross sections, which were measured at Saclay, were suggested to be used as they are, while values of the partial Saclay cross sections had to be recalculated, using a complex procedure [469].

In parallel, in 2006, the photonuclear activation file (PAF) has been developed [470]. It includes the photoactivation cross sections for more than 600 isotopes in the energy range of photons up to 25 MeV. In the case of the actinide isotopes, PAF contains also isotopic photofission fragment distributions and delayed-neutron tables. This database was built by using the experimental data from the 1999 IAEA evaluations for 164 isotopes and calculations with different reaction codes (for more than 500 isotopes).

In 2016, a follow-up IAEA CRP was organized and as a result the 2019 IAEA Photonuclear Data Library was released [90]. It contains data for 219 isotopes. Several reaction cross sections were remeasured with LCB beams at the NewSUBARU facility and the data for 188 isotopes were reevaluated. Out of these, 20 evaluations were retained from the previous 1999 IAEA Photonuclear Data Library [89].

5.2 Nuclear safeguards

Contact-free analysis of the chemical composition of a material occupying a region of space, *e.g.*, hidden in a container, greatly enhances the identification of threats such as explosives, fissile or toxic materials and weapons of mass destruction. Screening systems need to be designed to involve minimal operator intervention, to minimize dose to the sample, and to provide high throughput at commercial seaports, airports and other entry points.

Nuclear resonance fluorescence can be used to non-intrusively interrogate a region of space and measure the isotopic content of the material in that space for any element heavier than helium. The promise of NRF as a non-destructive analysis (NDA) technique in safeguards applications lies in its potential to directly quantify a specific isotope in an assay target. The technique involves exposing the material to an intense photon beam and detecting the scattered photons that have a discrete energy distribution unique to an isotope. The interrogating photons, which range from 2 to 8 MeV, are the most penetrating probes and are effective in cases where the isotopes of interest are shielded by steel or other materials.

NDA utilizing bremsstrahlung radiation was first suggested by Bertozzi and Ledoux [472]. NRF analysis with quasimonochromatic photon beam generated through LCB on relativistic electron beams has been proposed as an alternative [473]. Actually, the utilization of LCB beams is advantageous, provided correct estimation of the background is done. The point is that safeguard applications need to go beyond mere detection and precisely quantify the elemental or isotopic content.

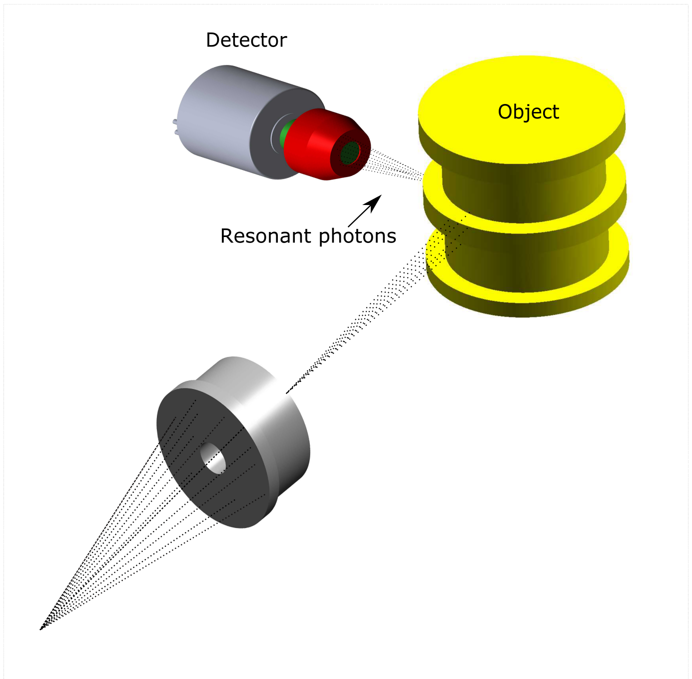

Figure 55: Schematic view of a scattering NRF experimental set-up. Reprinted figure from Ref. [471] with permission. Copyright (2016) by the Publishing House of the Romanian Academy.

The topics related to nuclear safeguards that were identified, are mostly related to special nuclear materials (SNM) like uranium enrichment confirmation of UF_6 canisters, geo-sourcing of material, weapons dismantlement verification, direct measurement of Pu in spent fuel, analysis of gas samples, characterization of suspect material, and verification of SNM in a cargo container [474].

Two detection schemes are used for NRF-based investigations, the scattering and the transmission method. In both cases interrogating photons are used to induce the resonant absorption while the de-excitation photons are detected either directly in a backscattering geometry or indirectly in a forward, self-absorption (transmission) geometry. In scattering experiments, the investigated object is placed in the beam and the resonant photons are detected in a backscattered geometry by a detector located off-beam, see Fig. 55.

The NRF transmission method, known also as NRF notch detection method, has been proposed for NDA measurements of the isotopes of interest [472]. The absorption of γ rays by nuclear resonance is occurring only in the nuclide of interest, because nuclear resonance widths are considerably narrower than the energy width of an incident LCB photon beam, see Sec. 2.2. Schematically a transmission NRF experimental set-up is presented in Fig. 56. When an isotope of interest is already present in the measured sample, the spectral flux of the transmitted photons at the resonant energy decreases due to the absorption in the target, leading to a narrow and sharp dip, called a notch, in the transmitted γ-ray energy spectrum, see Sec. 2.2.3. Further downstream the witness target is placed. When the transmitted γ rays irradiate the witness target that includes the same isotope of interest, γ rays are emitted via the NRF process, but their intensity is smaller, because the first target has already reduced the flux at the relevant energies. The detection of resonant photons scattered by the witness foil is done with an off-beam detector in a back-scattering geometry, often referred to as the notch detector in Fig. 56.

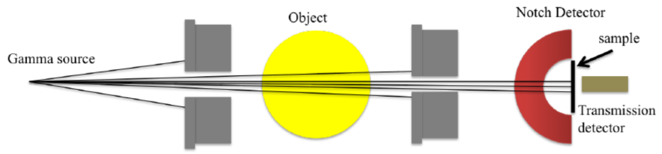

Figure 56: Schematic view of a transmission NRF experimental set-up. Reprinted figure from Ref. [471] with permission. Copyright (2016) by the Publishing House of the Romanian Academy.

In a proof-of-principle experiment utilizing LCB photons, one-dimensional mapping of a lead block hidden behind 1.5-cm-thick iron plates was done [475]. The results from this measurement are shown in Fig. 57.

Hagmann *et al.* demonstrated that transmission-based, isotopic detection works and can distinguish different materials from each other, even if they have the same areal density [476]. In a further experiment, it was demonstrated that the NRF transmission method is unaffected by the shielding material [477]. Warren *et al.* validated experimentally a method assaying the uranium enrichment inside a UF_6 container [478]. Another pilot study presents an interactive proof system that can validate the structure and composition of a nuclear warhead to arbitrary precision [479]. All these techniques rely on the knowledge of resonant states in SNM. Therefore, a lot of effort has been undertaken to perform NRF studies in the actinides [230, 231, 361, 366, 367, 480, 481].

The ultimate goal of these studies is the construction of an active-interrogation systems for nuclear security. Such a system needs to detect the presence of special nuclear material inside an object by detecting the emitted radiation when the object has been exposed to known sources of external radiation. Because of the cost, complexity, and the need to avoid irradiating occupants, active-interrogation systems are intended as secondary screening for cargo applications where shielding can prevent standard detection by, *e.g.*, X-ray scanning systems. The requirements and the expected performance of an active system have been summarized in Ref. [482, 483].

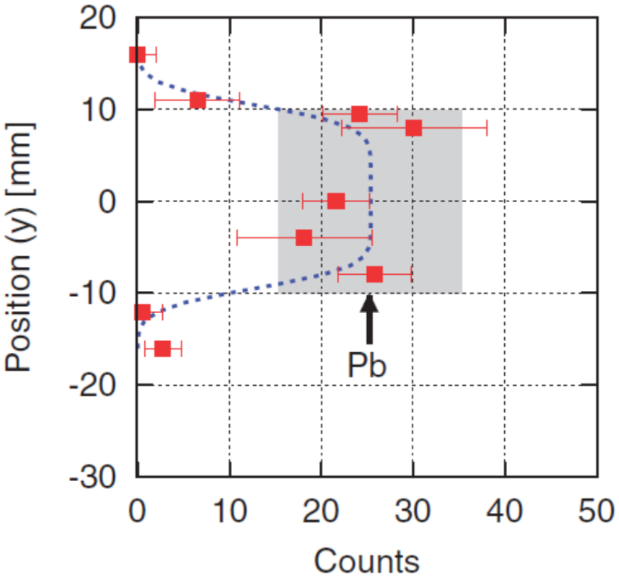

Figure 57: Isotope mapping with vertical scanning of target using photon beams. The number of photons accumulated within the NRF peak is plotted as a function of irradiation position. The number of photons is normalized by the flux of the incident photon beam. The gray box indicates the position of the lead block. Reprinted figure from Ref. [475] with permission. Copyright (2009) by IOP Publishing.

A natural way for continuation of these studies is the development of methods for γ-ray computer tomography (CT) and three-dimensional (3D) radiography, which will be used in the active-interrogation systems for nuclear safeguards. The advance in this field is described in the follow-up Sec. 5.4.

Another aspect of this research is the investigation of spent fuel and of nuclear waste management. Hayakawa *et al.* suggested a conceptual design of a system for nondestructive assay of ^{235}U, ^{239}Pu, and minor actinides in spent nuclear fuel assembly in a water pool with the NRF technique [484], while Hajima *et al.* discussed a nondestructive analysis of radionuclides in nuclear waste [485].

Recently, a new technique has been proposed to identify odd-A or even-even mass samples of fissionable SNM [160]. The prompt neutron polarization asymmetries, defined in Eq. (86) as the difference in the prompt neutron yields parallel and perpendicular to the plane of beam polarization divided by their sum, differ significantly depending on the sample. Prompt neutrons from photo-fission of even–even targets (which have a low thermal fission cross section) have significant polarization asymmetries, $\sim$ 0.2 to 0.5, while those from odd-A targets (which have a large thermal fission cross section) have polarization asymmetries close to zero. This difference in the polarization asymmetries is suggested to be utilized for measurements of the even-even *vs.* odd-A content of SNM.

5.3 Interrogation of hazardous materials

The detection of hazardous materials can be enhanced by the identification of multiple elemental concentrations and total mass in each volume element. Many hazardous materials, such as high explosives (HE), drugs, poisons, are characterized by high concentrations and defined composition of oxygen, nitrogen and carbon. Poisonous gases and toxic agents contain specific quantities of other characteristic elements such as arsenic, fluorine, chlorine, sulfur and phosphorus. Hence, any dangerous material is labeled by its elemental content. It is the correlation of key elements, along with the measurement of the mass of each element that needs to be determined in a NRF NDA measurement. For the interrogation of hazardous materials the technique, which was described in Sec. 5.2 can be applied.

The feasibility of identifying HE using NRF techniques was demonstrated in Ref. [487, 488]. In a further experiment, Hayakawa *et al.* demonstrated a nondestructive assay method for measuring molecules or chemical compounds hidden by heavy shields such as iron of thickness of several centimeters [489].

By combining NRF spectroscopy and the isotope ratio approach, Lan *et al.* demonstrated with Monte Carlo simulations that widely abused drugs, such as methamphetamine, cocaine, heroin, ketamine and morphine, can be identified with high significance of 7 to 24 σ ($\sigma \equiv$ standard deviation) considering a LCB beam with a flux of 10^{11} photons/s [486]. The ratio of the NRF peaks from ^{12}C, ^{14}N and ^{12}O provide a sensitive identification tool. The results of this study are presented in Fig. 58.

It is worth mentioning that the NRF NDA technique can be used for a wide variety of other applications where isotope identification is needed. For example, it was suggested to apply the technique for cultural heritage studies [490]. The penetrability of γ rays will enable studies of bulk objects, complex archeological artefacts and works of art non-intrusively.

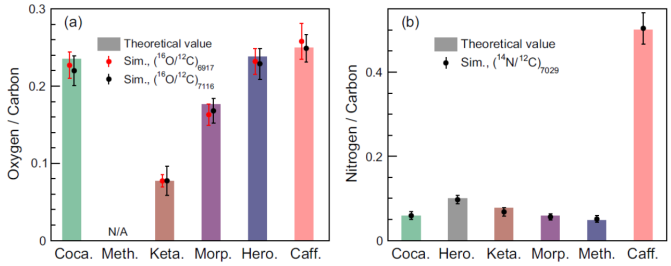

Figure 58: Element ratios of oxygen to carbon (a) and nitrogen to carbon (b). Coca., Meth., Keta., Hero. and Caff. are abbreviations for the drugs cocaine, methamphetamine, ketamine, heroin and caffeine, respectively. The values of the 6917 and 7116 keV ^{16}O lines and the 7029 keV ^{14}N line are indicated in the figure. Ratios are taken with the 4438 keV ^{12}C line. Reprinted figure from Ref. [486] with permission. Copyright (2021) by Springer Nature.

These NDA methods will be further developed with the availability of the high-brilliance γ beams. In a transmission experiment at HIγS, the γ beam was fired at a 1.3 cm thick slab of depleted uranium (DU), shielded by a 1.3 cm slab of tungsten [476]. The conclusion was reached that a six-hour measurement would be required for a 6-σ level detection of a sensitive material in the object when using the 100 photons/(eV·s) which were available. At ELI-NP, using a conservative value for the spectral density of $2.8 \cdot 10^4$ photons/(eV·s), the same statistics could be reached in less than two minutes.

5.4 γ-ray imaging techniques

After the demonstration of one-dimensional mapping [475] (see Fig. 57), the obvious step was to demonstrate two-dimensional (2D) imaging [491]. This opened the avenue for the development of γ-ray imaging techniques. The idea is to combine the NRF spectroscopy with computer tomography (CT). CT is an imaging technique used to reconstruct the cross-sectional image of a sample from several projections acquired at different projection angles. The single-photon computed tomography (SPECT) technique is widely used in medicine [492] and for non-destructive industrial inspections [493].

Experimentally, Zen *et al.* obtained an image of ^{208}Pb in natural lead [494]. The experiment was carried out at the UVSOR-III electron storage ring. The CT target consisted of an 8-mm diameter natural lead rod, a 10-mm iron rod, and a 10-mm cylindrical air hole embedded in a 30-mm aluminum cylinder wrapped by an iron cylinder with a thickness of 2.5 mm, and was placed on a rotating table in the plane of the beam axis. The LCB photon beam had a flux of approximately 2 photons/(eV·s). In total, γ-ray spectra were measured for 43 different positions of the cylinder with respect to the beam. The exposition time was 60 hours. The NRF image was obtained using the NRF notch technique. In a follow up experiment [495], the 2D image of two enriched lead isotope rods (^{206}Pb and ^{208}Pb) embedded in an aluminium cylinder was obtained. Since these two rods show the same γ-rays attenuation in atomic processes, it is impossible to differentiate between them using a standard γCT technique based on atomic attenuation of γ rays. The unique feature of NRF-CT, which was used in the analysis, is that the isotope of interest can be selectively identified from a sample containing several isotopes. This measurement traces the route to 3D radiography.

For achieving high-resolution CT imaging, it is necessary to correctly take into account the background, which is caused by elastic photon scattering. Four processes need to be taken into consideration, *e.g.*, Rayleigh scattering, nuclear Thompson scattering, Delbrück scattering, and scattering from excited nuclear states [496]. However, particle transport codes, such as GEANT4 [151], consider only Rayleigh scattering. Therefore, some effort was undertaken to implement the remaining processes [497, 498].

Turturica *et al.* explored two analysis methods for Z_{eff} evaluation using both, experimental and simulated γ-ray attenuation data [499]. In this study, particle-capture reactions on composite targets were used for the generation of multi-monoenergetic γ rays between 1 and 12 MeV. Neural networks were used in the analysis.

The availability high-brilliance LCB γ beams at ELI-NP will provide the next step in establishing the CT and 3D radiography technique as tool for different industrial applications. A case computer simulation study for CT imaging with quasi-monoenergetic photon beams for ELI-NP was done, which demonstrates the feasibility of such studies [500].

5.5 New production routes for medical radioisotopes

An important challenge of modern nuclear medicine is to find new techniques capable to provide effective cancer diagnostics and treatment at the very early stages of the disease. The aim is to develop theranostic approaches which combine diagnostic and therapy. To achieve this goal, new highly-selective radio-pharmaceuticals are under development. These are radionuclides which possess identical chemical properties, such that they can be linked to the same molecule and be used simultaneously for diagnostic and therapy. Isotopes of interest are the following pairs ^{44}Sc/^{47}Sc, ^{64}Cu/^{67}Cu, ^{152,155}Tb/^{149,161}Tb, or pairs with similar chemical properties, *e.g.* ^{99m}Tc/^{188}Re. Another approach is to use a single radionuclide for both imaging and therapy, such as ^{117m}Sn or ^{223}Ra. Modern medical imaging and therapy explore different radioisotope decays, *i.e.* α, β^-, β^-, and IT decays emitting Auger electrons. Some of the medical radioisotopes are still not available commercially and research related to establishing efficient production schemes is going on.

Currently thermal neutron-induced fission and charged-particle reactions with protons are the main production routes for medical radioisotopes. Production of medical radioisotopes with bremsstrahlung beams is also been considered. This is one of the activities at the NSC KIPT in Kharkov, Ukraine. This experimental program includes simulations [501–503], production of medical isotopess [504–507] and the corresponding radiochemistry [504, 508].

At Canada's particle accelerator center TRIUMF a new high-intensity (up to 10 mA) superconducting electron accelerator (e-linac) with a maximum energy of 30 MeV was commissioned within the

Advanced Rare Isotope Laboratory (ARIEL) project [509] (see also Sec. 5.6). The research program addresses isotope production via photo-production and photo-fission, including production of medical isotopes for the imaging and treatment of diseases. A dedicated institute, the Institute for Advanced Medical Isotopes (IAMI), has been established, which will address research on radiotracers, radiopharmaceuticals, and radiotherapeutics. These laboratories are designed to accept targets and isotopes from any of TRIUMF isotope production sites. Research will address a broad range of novel radioisotopes that could find use in medical imaging or radiotherapeutics of the future. Radionuclides of interest are ^{225,224}Ra, ^{225}Ac, ^{213,212}Bi, ^{212}Pb, ^{211}Rn, ^{211}At, ^{119}Sb, ^{90}Nb, ^{44}Ti [509].

Habs and Köster published a survey of the medical radioisotopes that can be produced with high specific activity in photonuclear reactions with γ beams of high intensity and large brilliance [510]. In a pilot experiment at NewSUBARU, the feasibility for production of ^{99}Mo/^{99m}Tc and ^{196}Au medical radioisotopes with LCB γ beams was demonstrated. They were produced by the resonant photonuclear isotope transmutation (RPIT) technique on ^{100}Mo and ^{197}Au targets [511]. Other studies, which exploit numerical simulations, conclude that γ beams with a spectral density of about 10^2 photons/(eV·s) are needed to explore new production schemes for medical radioisotopes [512].

Research in the field of production of medical radioisotopes at ELI-NP would focus on detailed cross-section calculations and evaluation of specific activity yields for medical radioisotopes produced in different photonuclear reactions, *e.g.*, the ^{117m}Sn(11/2$^-$), ^{123m}Te(11/2$^-$), ^{135m}Ba(11/2$^-$) and ^{195m}Pt(13/2$^-$) isomers produced in (γ,γ') reactions, ^{44}Sc, ^{47}Ca, ^{64}Cu, ^{99}Mo, ^{103}Pd, ^{165,169}Er, ^{186}Re and ^{225}Ra produced in (γ,n) reactions, and ^{47}Sc and ^{67}Cu produced in (γ,p) reactions. Experimental studies are planned for the investigation of new production routes of medical radioisotopes, *e.g.*, search for doorway states for population of isomers in the medical radioisotopes of interest, measurements of (γ,n) and (γ,p) reaction cross sections of the medical radioisotopes of interest, and measurements of specific activities of medical radioisotopes produced in photonuclear reactions.

5.6 Production of rare isotopes in photo-fission

The idea of producing a beam of neutron-rich isotopes that are formed in the fission of uranium and thorium nuclei have existed for many years. One option to realize it is to utilize photo-fission of ^{238}U. In the interaction between electrons having an energy E_e and converter material bremsstrahlung radiation is produced with end-point energy $E_\gamma^{max} = E_e$, see Sec. 3.1. Fission of heavy nuclei induced by γ rays with different energies is determined by the region of the GDR. The yield of γ-quanta in the GDR region, $E_\gamma = 10$–17 MeV depends on the energy of electrons and defines the fission fragment yield. It sharply grows with the increase of the electron energy up to $E_e = 30$ MeV and then continues to grow smoothly up to $E_e = 50$ MeV and higher [513].

Ibrahim *at al.* studied the production of neutron-rich isotopes of nobel gases, Kr and Xe, in photo-fission [514]. The conclusion of this study was that photo-fission of ^{238}U was suggested as an interesting alternative to rapid neutron-induced fission for the production of radioactive nuclear beams. This marked the beginning of the ALTO (Accélérateur Linéaire auprès du Tandem d'Orsay) project for production of radioactive ion beams (RIB) at Orsay, France.

There are two laboratories, which utilize high-energy intense photon sources for production of RIBs, the ALTO laboratory in Orsay, France [515], which is operational, and the ARIEL facility in Vancouver, Canada [516], where the electron linac is under commissioning.

At Orsay, the main components of the electron accelerator were recovered from the decommissioned LEP injector (CERN) and LAL test station. Irradiating a uranium carbide target (^{238}UC$_x$) heated up to 2,000°C with bremsstrahlung produced by a 10 μA electron beam at 50 MeV allows to deliver a large variety of neutron-rich isotope beams. The isotopes of interest are extracted using the ISOL technique. The new ARIEL facility [516], expected to be completed in 2023, will transform TRIUMF into one of the most powerful multiuser beam facilities in the world for production of rare isotopes. At the heart of ARIEL is an e-linac. The first stage of the e-linac is designed to achieve maximal energy of 30 MeV and up to 10 mA beam intensity, and the final stage performance aims at maximal energy of 50 MeV and 500 kW power on target.

6 Outlook and Summary

We tried to show in this review that nuclear reactions with photons were, are, and will be a precious tool to inspect, or even manipulate, atomic nuclei. Since photons, unlike any other particles, can excite an absorbing nucleus to a pre-selected quantum state, they potentially offer the opportunity for a sort of 'quantum manipulation' at the nuclear level in a similar way as we know it for decades from the field of atomic physics. This emerging field of '*Nuclear Photonics*' is clearly still at its infancy and it is facing enormous technological challenges, partly because of the lack of efficient lenses and mirrors for γ-radiation as compared to laser science and atomic physics. Yet, photonuclear science is presently undergoing a dramatic transformation, triggered by the advent of new facilities with unprecedented beam parameters and by new scientific or technological visions providing unparalleled prospects for scientific research and applications. If this pace of development will continue, then we will witness a strong growth of the field of Nuclear Photonics. The following subsections provide a short sketch of the technology of next-generation photon sources, being under discussion already now, and a list of crucial parameters and their potential for advancing photonuclear science and technology.

6.1 Next generation photon sources

The last decades saw a steady development of γ-photon beams with optimized beam properties for research and application. Fig. 59 categorizes the past and possible future developments of photon sources into five generations. The first generation of photon sources made use of artificially induced γ-radioactivity of various excited nuclei. Such sources barely provided any energy-tunability. The second generation of MeV-range photon sources either provide broad-band bremsstrahlung or low-intensity beams with some energy resolution or energy-tagging. These sources have enormously boosted the field of photonuclear science in the past as described above. At present, the most sophisticated sources use the principle of laser Compton backscattering on electrons in synchrotrons or storage rings. The HIγS facility has been the most productive example in the past [12].

Some new LCB facilities with further improved parameters as compared to existing ones are already announced to become operational within the next few years. As an example we will shortly describe the Variable Energy Gamma-Ray System (VEGA) currently being assembled at the international research centre Extreme Light Infrastructure - Nuclear Physics (ELI-NP) in Magurele, Romania. VEGA, a development by Lyncean Technologies, uses a warm electron LINAC with a maximum energy of 750

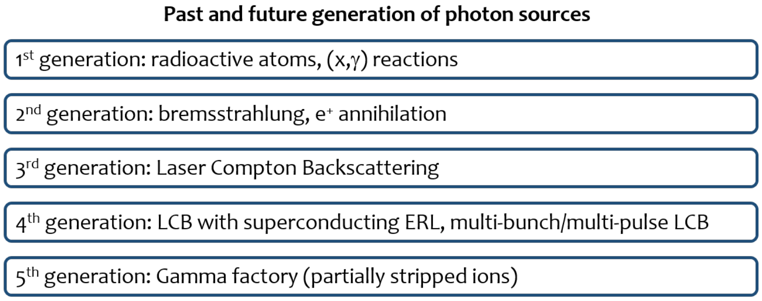
Past and future generation of photon sources

1st generation: radioactive atoms, (x,γ) reactions

2nd generation: bremsstrahlung, e^+ annihilation

3rd generation: Laser Compton Backscattering

4th generation: LCB with superconducting ERL, multi-bunch/multi-pulse LCB

5th generation: Gamma factory (partially stripped ions)

Figure 59: Past and possible future generation of photon sources.

MeV as an injector for a high-frequency storage ring, see Fig. 60. The storage ring will operate in the so called top-off mode which means that electrons are continuously injected into the ring to keep the current in the storage ring at a near-constant level. The collision frequency between electrons and laser photons will be around 35 MHz. This continuous wave (cw) beam will minimize deadtime losses in most typically used detectors with ns-ranged time resolutions. Two kinds of lasers will be used, one in the infrared (IR) and the other in the green wavelength regime. The energy range of the generated photon beams can then be varied continuously between 1 and 20 MeV by selecting one of these two interaction lasers and by accordingly tuning the electrons' energy in the storage ring. A small electron beam emittance gives rise to a small bandwidth of about or even below 0.5% for the Compton backscattered laser photons. The total photon flux will be larger than 10^{11} photons/s, the collimated, time averaged spectral intensity at peak position will be larger than 5×10^3 photons per second and eV. VEGA is scheduled to become fully operational in 2023.

VEGA is expected to represent the state-of-the-art of photon beam production for at least the 2020s. Another approach to reach even higher intensities is based on the multi-bunch multi-pulse concept proposed by Chris Barty and coworkers [517]. In this concept the laser beam collides with electron microbunches with small temporal spacing.

The achievable bandwith of an LCB beam from collisions with electrons in a storage ring is ultimately limited by the finite emittance inevitably caused by stochastic synchrotron radiation. This limits the focal diameter of the electron beam and, hence, the luminosity of the Compton collision with an external laser, and it limits the resulting bandwidth of the LCB beam. The next step would require a limitation of the number of beam bends while keeping the high repetition rate of laser-on-electron-bunch collisions and the large effective electron current. The first condition calls for the deployment of a linear accelerator. High-repetition rate requires cw acceleration and, thus, a superconducting radio-frequency (SRF) linac. Its operation at high current in the 1-GeV range for laser-Compton collisions is only economically useful if the external RF-power consumption of the SRF-linac is limited by energy recovery capabilities [518–520]. Indeed, a corresponding conceptional design report for a superconducting multi-turn energy-recovery linac (ERL) has been published, recently, by the international ERL community [521]. Such an SRF-ERL would produce a cw electron beam with extremely low emittance and very high current being capable of generating LCB photon beams with further reduced bandwith (going down to the per mille range) and yet higher intensity. Research on the design of multi-turn SRF-ERLs is consequently

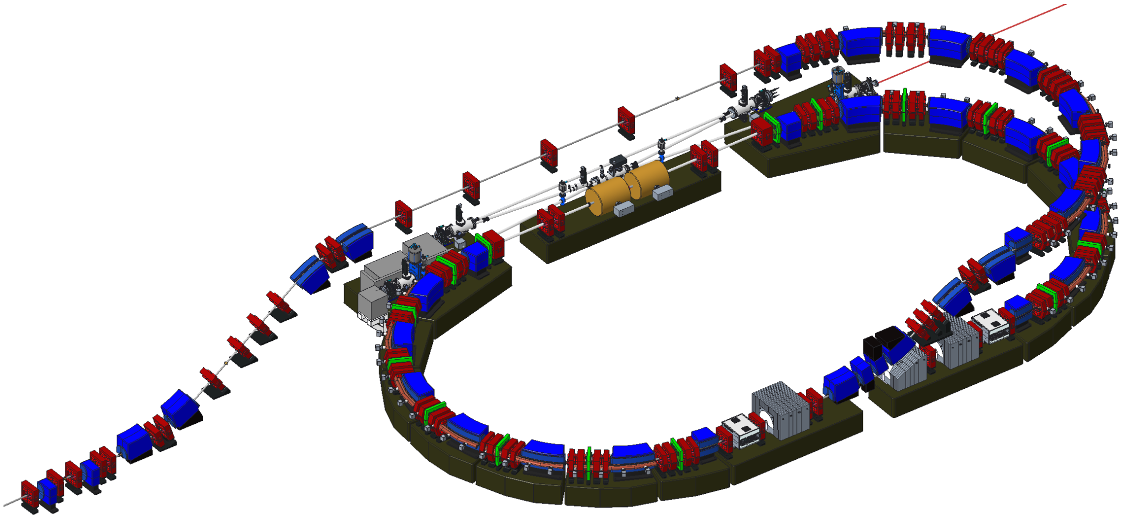

Figure 60: The VEGA laser Compton backscattering facility planned at ELI-NP. Figure courtesy of Lyncean Technologies, Fremont,USA.

ongoing also at the centers for photonuclear research [376].

The rather small cross section for Compton scattering in the range of barns defines one restriction for the maximum photon flux which can be obtained from laser Compton backscattering facilities. A principle which overcomes this limitation was brought up a few years ago and is presently discussed as the "Gamma Factory at CERN" [522,523]. The idea is to use a partially stripped ion beam from the SPS or LHC. A resonant absorption of laser photons from this ultra-relativistic ion beam is followed by an atomic transition. The emitted photon energy is boosted by a factor up to four times the squared Lorentz factor of the particle beam. At LHC this would mean a tunable photon beam energy range from about 1-400 MeV. Due to the massively larger cross section for the laser photon absorption (which is in the Gbarn range) as compared to the laser-Compton scattering on the point-like electron, unprecedented γ beam intensities could be reached. The idea was recently endorsed by the CERN management by creating the Gamma Factory study group, embedded within the Physics Beyond Colliders studies framework. Up to now, the study group has demonstrated that an efficient production, acceleration, and storage of bunches of atomic beams of high Z, partially stripped ions is possible in the CERN accelerator complex. A number of possible applications have already been discussed, see, e.g., Refs. [524, 525].

6.2 The future of photonuclear reactions

The scientific and technological reach of photonuclear reactions will crucially depend on the advances of photon beam parameters. Below we have listed four aspects that need to be addressed by future facilities to further develop the field into the next decade:

- Photon flux
  Due to the typically rather low photonuclear cross sections the photon flux is a crucial parameter for all experiments. The advent of new high-power photon beams in the next years will allow to reduce the typical sample weight by orders of magnitude. This enables for the first time precision studies on very rare stable isotopes or on certain radioactive targets with half lives down to the range of 10^4 years. Other measurements will become possible due to significantly increased statistics of recorded events compared to what is possible today. For the same reason, the scanning of objects for applications can be accelerated enormously. However, the inspection of radioactive ion beams is still beyond reach due to the limited luminosity. If one could increase the photon flux even further (as proposed, e.g., by the Gamma factory described in Sec. 6.1) one can think about overcoming this limitation, too.

- Photon beam diameter
  Typical photon beam diameters of todays facilities at target position are in the range of cm. A reduction of this diameter to the mm size (as planned, e.g., for the upcoming VEGA beam at ELI-NP) or even smaller can have several advantages. First, the concentration of the same number of photons in a smaller beam spot means that the target sample weight can be reduced while keeping the target thickness $\bar{n}$ constant with the effects discussed above. Secondly, the photonuclear reaction in a certain probe gets a much improved spatial resolution which is interesting for a number of isotope-sensitive applications.

- Bandwidth
  A dramatic step forward for basic research and applications has become possible by the advent of LCB facilities. Bandwidths in the range of a few percents allowed completely new approaches. The implementation of the next generation of photon beams in the upcoming years with bandwidth in the sub-percent range will not only provide a higher energy resolution for measurements of average quantities as discussed in Sec. 2.3.4 and 2.3.6, but will also open the window to a state-sensitive

excitation in many more nuclei. This selective manipulation of nuclear levels by photon beams has great potential for scientific discoveries and technological applications.

The next step could be a further reduction of the bandwidth from the keV range to the range of the typical Doppler width of NRF lines including thermal motion, i.e. to the eV range. A double-crystal monochromator like the GAMS5 at the ILL in Grenoble [526, 527] can reach a resolution of $\Delta E/\mathrm{E}$ in the 10^{-6} range. Certainly, the pay-off is a significant reduction in photon flux due to the very low angular acceptance of the crystal monochromators. A completely different way to tailor photon spectra in the eV range is the self absorption technique [328]. This technique could benefit from the Mößbauer-like idea of rapidly moving absorbers or/and targets to scan energies in a certain energy range.

- Compact photon sources
  Typical present-day photon beam infrastructures in the MeV range need floor spaces from 100 m^2 for bremsstrahlung setups to several 100 m^2 for LCB facilities. This limits the prospects for applications in many fields, examples have been given in Sec. 5. Therefore, the development of new compact photon sources would boost further usage. Laser wakefield acceleration of electrons with low energy spread and low emittance may in principle provide a way to reduce the size of the electron accelerators to produce bremsstrahlung or acting as scattering partners in LCB [528]. As one example of the numerous research centers working in this field, we mention the BELLA center at Berkeley Lab which works on such sources for applications, e.g., in national security [529]. Recently electron beams with quasi-monoenergetic energies up to 7.8 GeV could be generated using this principle [530].

Photonuclear reactions have revealed a lot of secrets of the atomic nucleus in the past and at present. We are sure that photon beams have an enormous potential for further advances and that photonuclear reactions will have a bright future for basic research as well as for applications!

Acknowledgments

This review is dedicated to Peter von Brentano who was one of the driving forces in the field of photonuclear physics at the end of the 20th century.

Such a review would not have been possible without the outstanding support by many colleagues in experiment and theory.

First, we would like to thank D. Savran who was involved from the first ideas to the final realization of this manuscript. In addition we thank our long-standing close collaborators T. Beck, A. Bracco, C. Fransen, U. Friman-Gayer, M.N. Harakeh, U. Kneissl, M. Müscher, R.V.F. Janssens, A. Richter, M. Scheck, R. Schwengner, A. Tonchev, W. Tornow, C.A. Ur, H. Utsunomiya, H.R. Weller, V.Werner, J. Wilhelmy, and N.V. Zamfir.

We are particularly grateful to U. Friman-Gayer and O. Papst for calculations of the NRF angular distribution functions and for support with figures for the NRF formalism and the LCB process, to J. Sieber for help on the references to recent NRF publications, and to K. Ide for the proper formatting of reference citations.

We thank M. Müscher, F. Heim, U. Friman-Gayer, and J. Wilhelmy for carefully proofreading the manuscript.

This work was supported by the German Federal Ministry of Education and Research (BMBF) under grant Nos. 05P18PKEN9 and 05P18RDEN9, by the Deutsche Forschungsgemeinschaft (DFG, German Research Foundation) under grants No. SFB 1245 (Project-ID 279384907) and No. 510/7-1, and by the State of Hesse through the research project "Nuclear Photonics" within the LOEWE excellence program and the Cluster Project "ELEMENTS". DLB acknowledges support by Extreme Light Infrastructure-Nuclear Physics (ELI-NP) Phase II, a project co-financed by the Romanian Government and by the European Regional Development Fund the Competitiveness Operational Programme (1/07.07.2016, COP, ID 1334).

Appendices

A Angular distribution functions of NRF intensity

The angular distribution, Eq. (37), of NRF intensity for a general $\vec{\gamma}\gamma$-cascade $J_0^{\pi_0} \overset{\vec{\gamma},\delta_1}{\rightarrow} J^{\pi} \overset{\delta_2}{\rightarrow} J_f^{\pi_f}$ about an incident γ-ray beam with a degree of polarization P_γ assumes the functional form

$$W(\vartheta,\phi) = 1 + \frac{1}{(1+\delta_1^2)(1+\delta_2^2)} \Big\{ \Big[p_2 P_2(\cos\vartheta) + p_4 P_4(\cos\vartheta) \Big] \\ (\pm) P_\gamma \cos(2\phi) \frac{1}{2} \Big[p_2' P_2^{(2)}(\cos\vartheta) + p_4' P_4^{(2)}(\cos\vartheta) \Big] \Big\} \tag{119}$$

as function of the polar angle ϑ with respect to the incident beam axis and of the azimuthal angle ϕ with respect to the polarization plane of the electric field vector of the incident beam when only dipole or quadrupole multipolarities are assumed. $P_{2(4)}^{[(2)]}$ denote normalized [and associated unnormalized] Legendre polynomials

$$P_2(\cos\vartheta) = \frac{1}{2}(3\cos^2\vartheta - 1) \qquad P_2^{(2)}(\cos\vartheta) = 3(1-\cos^2\vartheta) \tag{120}$$

$$P_4(\cos\vartheta) = \frac{1}{8}(35\cos^4\vartheta - 30\cos^2\vartheta + 3) \qquad P_4^{(2)}(\cos\vartheta) = -\frac{15}{2}(1 - 8\cos^2\vartheta + 7\cos^4\vartheta) \tag{121}$$

The NRF intensity distribution is insensitive to the polarity of the second transition. Therefore, it does not depend on the parity quantum number π_f of the final state. In the following table we provide the coefficients $p_{2(4)}^{(\prime)}$ of Eq. (119) for a variety of spin/parity sequences. Since a simultaneous change of the parity quantum numbers $\pi_0 \to -\pi_0$ and $\pi \to -\pi$ does not change the polarity of the initial transition, it features the identical angular distribution as the original one. If instead the polarity of the initial transition is changed, i.e., $\pi_0 \to -\pi_0$, then the angular distribution is azimuthally rotated by 90° being identical to a replacement of the symbol (±) by (∓). Therefore, Table covers all possible combinations of parity quantum numbers to all levels in the indicated NRF cacsades.

Table 4: Angular distribution functions of NRF intensity about a linearly-polarized γ-ray beam with a degree of polarization P_γ as functions of the polar angle ϑ with respect to the beam axis and of the azimuthal angle ϕ with respect to the polarization plane of the electric field vector of the incident beam for NRF cascades $J_0^{\pi_0} \overset{\vec{\gamma},\delta_1}{\rightarrow} J^{\pi} \overset{\delta_2}{\rightarrow} J_f$.

$J_0^{\pi_0} \overset{\vec{\gamma},\delta_1}{\rightarrow} J^{\pi} \overset{\delta_2}{\rightarrow} J_f$	Coefficients			
	p_2	p_2'	p_4	p_4'
$0^+ \to 1^\pm \to 0$	$\frac{1}{2}$	$\frac{1}{2}$	0	0
$0^+ \to 1^\pm \to 1$	$-\frac{1}{4} - \frac{3}{2}\delta_2 - \frac{1}{4}\delta_2^2$	$-\frac{1}{4} - \frac{3}{2}\delta_2 - \frac{1}{4}\delta_2^2$	0	0
$0^+ \to 1^\pm \to 2$	$\frac{1}{20} + \frac{3}{2\sqrt{5}}\delta_2 + \frac{1}{4}\delta_2^2$	$\frac{1}{20} + \frac{3}{2\sqrt{5}}\delta_2 + \frac{1}{4}\delta_2^2$	0	0

Continued on next page

Table 4 – *Continued from previous page*

$J_0^{\pi_0} \overset{\vec{\gamma},\delta_1}{\to} J^{\pi} \overset{\delta_2}{\to} J_f$	Coefficients			
	p_2	p_2'	p_4	p_4'
$0^+ \to 2^\pm \to 0$	$\frac{5}{14}$	$\frac{5}{14}$	$\frac{8}{7}$	$-\frac{4}{21}$
$0^+ \to 2^\pm \to 1$	$-\frac{1}{4} + \frac{\sqrt{5}}{2}\delta_2 + \frac{5}{28}\delta_2^2$	$-\frac{1}{4} + \frac{\sqrt{5}}{2}\delta_2 + \frac{5}{28}\delta_2^2$	$-\frac{16}{21}\delta_2^2$	$\frac{8}{63}\delta_2^2$
$0^+ \to 2^\pm \to 2$	$\frac{1}{4} + \frac{1}{2}\sqrt{\frac{15}{7}}\delta_2 - \frac{15}{196}\delta_2^2$	$\frac{1}{4} + \frac{1}{2}\sqrt{\frac{15}{7}}\delta_2 - \frac{15}{196}\delta_2^2$	$\frac{16}{49}\delta_2^2$	$-\frac{8}{147}\delta_2^2$
$0^+ \to 2^\pm \to 3$	$-\frac{1}{14} - \frac{\sqrt{30}}{7}\delta_2 - \frac{10}{49}\delta_2^2$	$-\frac{1}{14} - \frac{\sqrt{30}}{7}\delta_2 - \frac{10}{49}\delta_2^2$	$-\frac{4}{49}\delta_2^2$	$\frac{2}{147}\delta_2^2$
$0^+ \to 3^\pm \to 0$	$\frac{3}{4}$	$-\frac{1}{2}$	$\frac{1}{22}$	$-\frac{1}{33}$
$0^+ \to 3^\pm \to 2$	$-\frac{3}{10} + 3\sqrt{\frac{3}{10}}\delta_2 + \frac{3}{28}\delta_2^2$	$-\frac{2}{3}p_2$	$\frac{1}{7}\delta_2^2$	$-\frac{2}{21}\delta_2^2$
$J_0^{\pi_0} \to \frac{1}{2}^\pm \to J_f$	0	0	0	0
$\frac{1}{2}^+ \to \frac{3}{2}^\pm \to \frac{1}{2}$	$\sqrt{\frac{3}{4}}(\delta_1 - \delta_2)(1 + \delta_1\delta_2)$ $+\frac{1}{4}(\delta_1^2 - 1)(\delta_2^2 - 1) - 3\delta_1\delta_2$	$p_2 - \frac{2}{\sqrt{3}}\delta_1$ $+4\delta_1\delta_2 + \frac{2}{\sqrt{3}}\delta_1\delta_2^2$	0	0
$\frac{1}{2}^+ \to \frac{5}{2}^\pm \to \frac{1}{2}$	$\frac{2}{7}$	$\frac{2}{7}$	$\frac{8}{21}$	$-\frac{4}{63}$
$\frac{3}{2}^+ \to \frac{3}{2}^\pm \to \frac{3}{2}$	$\frac{4}{5}\Big[\frac{1}{5} - 3\delta_1\delta_2$ $+\sqrt{\frac{3}{5}}(\delta_2 - \delta_1)\Big]$	$\frac{4}{5}\Big(\frac{1}{5} + \frac{1}{\sqrt{15}}\delta_1$ $+\sqrt{\frac{3}{5}}\delta_2 + \delta_1\delta_2\Big)$	0	0
$\frac{3}{2}^+ \to \frac{5}{2}^\pm \to \frac{3}{2}$	$\frac{7}{50} + \frac{3}{5}\sqrt{\frac{7}{5}}(\delta_1 - \delta_2)$ $-\frac{1}{14}(\delta_1^2 + \delta_2^2)$ $+\frac{3}{7}\sqrt{\frac{5}{7}}(\delta_1^2\delta_2 - \delta_1\delta_2^2)$ $-\frac{18}{5}\delta_1\delta_2 + \frac{25}{686}\delta_1^2\delta_2^2$	$p_2 - \frac{4}{5}\sqrt{\frac{7}{5}}\delta_1$ $+\frac{24}{5}\delta_1\delta_2 + \frac{4}{7}\sqrt{\frac{5}{7}}\delta_1\delta_2^2$	$\frac{512}{1029}\delta_1^2\delta_2^2$	$-\frac{256}{3087}\delta_1^2\delta_2^2$
$\frac{3}{2}^+ \to \frac{7}{2}^\pm \to \frac{3}{2}$	$\frac{75}{343}$	$\frac{75}{343}$	$\frac{44}{343}$	$-\frac{22}{1029}$
$\frac{1}{2}^+ \to \frac{3}{2}^\pm \to \frac{3}{2}$	$-\frac{1}{5} - \frac{\sqrt{12}}{5}\delta_1$	$p_2 + \frac{8}{5\sqrt{3}}\delta_1 + \frac{8}{\sqrt{5}}\delta_1\delta_2$	0	0

Continued on next page

Table 4 – *Continued from previous page*

$J_0^{\pi_0} \xrightarrow{\vec{\gamma},\delta_1} J^{\pi} \xrightarrow{\delta_2} J_f$	Coefficients			
	p_2	p_2'	p_4	p_4'
	$+\frac{1}{5}\delta_1^2 - \sqrt{\frac{3}{5}}\delta_2$ $-\frac{6}{\sqrt{5}}\delta_1\delta_2 + \sqrt{\frac{3}{5}}\delta_1^2\delta_2$			
$\frac{1}{2}^+ \rightarrow \frac{3}{2}^\pm \rightarrow \frac{5}{2}$	$\frac{1}{20} + \frac{\sqrt{3}}{10}\delta_1 - \frac{1}{20}\delta_1^2$ $+\sqrt{\frac{7}{20}}\delta_2 + \sqrt{\frac{21}{5}}\delta_1\delta_2$ $-\sqrt{\frac{7}{20}}\delta_1^2\delta_2 + \frac{5}{28}\delta_2^2$ $+\frac{5\sqrt{3}}{14}\delta_1\delta_2^2 - \frac{5}{28}\delta_1^2\delta_2^2$	$p_2 - \frac{2}{5\sqrt{3}}\delta_1$ $-4\sqrt{\frac{7}{15}}\delta_1\delta_2 - \frac{10}{7\sqrt{3}}\delta_1\delta_2^2$	0	0
$\frac{5}{2}^+ \rightarrow \frac{3}{2}^\pm \rightarrow \frac{5}{2}$	$\frac{1}{100} + \frac{1}{10}\sqrt{\frac{7}{5}}(\delta_2 - \delta_1)$ $+\frac{1}{28}(\delta_1^2 + \delta_2^2) - \frac{7}{5}\delta_1\delta_2$ $+\frac{1}{2}\sqrt{\frac{5}{7}}(\delta_1^2\delta_2 - \delta_1\delta_2^2) + \frac{25}{196}\delta_1^2\delta_2^2$	$p_2 + \frac{2}{15}\sqrt{\frac{7}{5}}\delta_1$ $+\frac{28}{15}\delta_1\delta_2 + \frac{2}{3}\sqrt{\frac{5}{7}}\delta_1\delta_2^2$	0	0
$\frac{5}{2}^+ \rightarrow \frac{5}{2}^\pm \rightarrow \frac{5}{2}$	$\frac{32}{175} + \frac{24}{35}\sqrt{\frac{2}{5}}(\delta_2 - \delta_1)$ $-\frac{4}{49}(\delta_1^2 + \delta_2^2) - \frac{36}{35}\delta_1\delta_2$ $+\frac{3\sqrt{10}}{49}(\delta_1\delta_2^2 - \delta_1^2\delta_2) + \frac{25}{686}\delta_1^2\delta_2^2$	$p_2 + \frac{32}{35}\sqrt{\frac{2}{5}}\delta_1$ $+\frac{48}{35}\delta_1\delta_2 - \frac{4\sqrt{10}}{49}\delta_1\delta_2^2$	$\frac{54}{343}\delta_1^2\delta_2^2$	$-\frac{9}{343}\delta_1^2\delta_2^2$
$\frac{5}{2}^+ \rightarrow \frac{7}{2}^\pm \rightarrow \frac{5}{2}$	$\frac{3}{28} + \frac{5\sqrt{3}}{14}(\delta_1 - \delta_2)$ $-\frac{5}{196}(\delta_1^2 + \delta_2^2) - \frac{25}{7}\delta_1\delta_2$ $+\frac{25}{98\sqrt{3}}(\delta_1^2\delta_2 - \delta_1\delta_2^2) + \frac{25}{4116}\delta_1^2\delta_2^2$	$p_2 - \frac{10}{7\sqrt{3}}\delta_1$ $+\frac{100}{21}\delta_1\delta_2 + \frac{50}{147\sqrt{3}}\delta_1\delta_2^2$	$\frac{11264}{27783}\delta_1^2\delta_2^2$	$-\frac{5632}{83349}\delta_1^2\delta_2^2$
$\frac{5}{2}^+ \rightarrow \frac{9}{2}^\pm \rightarrow \frac{5}{2}$	$\frac{55}{294}$	$\frac{55}{294}$	$\frac{286}{3969}$	$-\frac{143}{11907}$

B Recent studies of Nuclear Resonance Fluorescence

A compacted overview on literature reporting on NRF measurements is provided in Table 5. It indicates the nuclides that have been studied by NRF, the experimental facility where this was done, the γ-ray energy range covered in the experiment, the major quantities deduced from the data, and the literature references. NRF data on isotopes of the same chemical element are concatenated in one line. Then the indicated energy range and deduced quantities may apply to a subset of the isotopes, only. The provided literature must then be consulted for details.

In situations where several articles have been published by the same group of authors on different aspects of certain NRF measurement campaigns we have restricted ourselves to the most recent reference citations, for brevity, as the preceding articles can then easily be found in the references of those publications. Due to the restriction of the present review discussed in the Introduction we consider literature published since the year 2000. A multitude of conference proceedings, presentations made available on the internet, or internal laboratory reports with unclear review procedures have not been considered.

Table 5: Overview on recent NRF studies and their bibliographic references. The studied nuclides are given in the first column. The second column indicates the facility where the NRF experiments were performed using the notation: a: Dynamitron, Univ. Stuttgart, unpolarized bremsstrahlung, b: Van De Graaff, MIT, unpolarized bremsstrahlung, c: DHIPS, S-DALINAC, TU Darmstadt, unpolarized bremsstrahlung, d: γELBE, HZDR Dresden, (un)polarized bremsstrahlung, e: HIγS, Duke Univ., LCB, f: TERAS, Tsukuba, LCB. Studied energy-ranges and deduced quantities are provided in columns three and four. If more than one isotope is given in the first column than the following columns indicates the combined information which may not apply to every isotope. The literature from column five should be consulted for details.

Isotope	Facility	Energy range (MeV)	Deduced quantity	Ref.
^{6}Li	c	< 7.1	Γ_0	[45]
^{11}B	e	2.1 - 8.9	E_γ, $I_{s,f}$, δ	[51, 387]
^{15}N	d	< 12.6	$I_{s,0}$	[531]
^{20}Ne	e	11.3	E_r, $I_{s,0}$, $\mathcal{F}_E$	[54]
^{26}Mg	d, e	< 13	E_γ, Γ_f, Γ	[424, 532, 533]
^{27}Al	e	2.2, 2.9 - 3.1	E_γ, J, $I_{s,0}$, R	[477, 534]
^{28,30}Si	e	9.3 - 11.4	E_γ, J^π	[54, 535]
^{32}S	e	< 9.9	E_γ, J^π, Γ_f/Γ	[51, 70, 335, 536]
^{40}Ar	e	4.3 - 11	E_γ, $I_{s,0}$, $\sigma_{\gamma\gamma'}$	[537, 538]
^{40,44,48}Ca	c, e	< 9.9	E_γ, J^π, $I_{s,0}$	[337, 539–541]
^{50,52,54}Cr	c, e	< 9.9	E_γ, J^π, $I_{s,0}$	[68, 352, 542–544]
^{54,56}Fe	d, e, f	< 13.9	E_γ, J^π, $I_{s,0}$	[384, 545]
^{58,60}Ni	c, e	< 9.9	E_γ, J^π, $I_{s,0}$, $\sigma_{\gamma\gamma'}$	[405, 546]
^{66}Zn	d, e	< 13.4	E_γ, J^π, $I_{s,0}$	[398]
^{74,76}Ge	c, d, e	< 11	E_γ, J^π, $I_{s,0}$	[394, 547]
^{76,78,80}Se	c, d, e	< 11.5	E_γ, J^π, $I_{s,0}$, $\sigma_{\gamma\gamma'}$	[391, 406, 548, 549]
^{86}Kr	d, e	< 11.2	E_γ, J^π, $I_{s,0}$	[550]
^{87}Rb	a, d, e	< 13.2	E_γ, $I_{s,0}$, $\sigma_{\gamma\gamma'}$	[326, 551]
^{88}Sr	c, d, e	< 16	E_γ, J^π, $I_{s,0}$, Γ_f/Γ_0	[49, 218, 552]
^{89}Y	d, e	< 13.2, 23 - 36	E_γ, $I_{s,0}$, ΠL	[312, 553]
^{90,92}Zr	a, d, e	< 13.2	E_γ, J^π, $I_{s,0}$	[373, 385, 554, 555]
^{93}Nb	a	< 2.5	E_γ, $I_{s,0}$	[556]
^{92,94,96,98,100}Mo	a, c, d, e	< 13.9	E_γ, J^π, $I_{s,0}$, $\sigma_{\gamma\gamma'}$	[353, 369, 387, 388, 404, 554]
^{96}Ru	a	< 3.8	E_γ, J, $I_{s,0}$, Γ_f/Γ_0	[355]
^{103}Rh	a	< 4.1	E_γ, J, $I_{s,0}$, Γ_f/Γ_0	[362]
$^{106-116}$Cd	d	< 10	E_γ, J^π, $I_{s,0}$, Γ_f/Γ_0, $\sigma_{\gamma\gamma}$	[356, 357, 395, 557]
^{112,120}Sn	a, c, d	< 9.5	E_γ, J, $I_{s,0}$	[397, 558, 559]

Continued on next page

Table 5 – *Continued from previous page*

Isotope	Facility	Energy range (MeV)	Deduced quantity	Ref.
^{121,123}Sb	a	< 4	E_γ, $g\Gamma_0^{\rm red}$	[341]
^{128,130}Te	c, e	< 10	E_γ, J^π, $I_{s,0}$, $\sigma_{\gamma\gamma'}$	[57, 72]
$^{124-136}$Xe	a, d	< 12	E_γ, J^π, $I_{s,0}$, $\sigma_{\gamma\gamma'}$	[358, 393, 560]
$^{134-138}$Ba	a, c, d, e	< 11.4	E_γ, J^π, $I_{s,0}$, $\sigma_{\gamma\gamma'}$	[61, 324, 342, 390, 561]
^{139}La	a, d	< 9	E_γ, $I_{s,0}$, Γ_f/Γ_0	[343, 389]
^{140,142}Ce	a, c, e	< 8.3	E_γ, J^π, $I_{s,0}$, $\sigma_{\gamma\gamma'}$	[59, 70, 324, 337, 562]
^{141}Pr	a	< 4.1	E_γ, $I_{s,0}$, Γ_f/Γ_0	[343]
^{142}Nd	e	4.2 - 9.7	$\sigma_{\gamma\gamma'}$	[563]
^{144,148,152}Sm	a, c, e	< 9.9	E_γ, J^π, $I_{s,0}$, δ, Γ_f/Γ_0	[63, 324, 374]
^{151,153}Eu	a	< 4	E_γ, J, $I_{s,0}$, Γ_f/Γ_0	[363]
^{154,156}Gd	c, e	< 6.2	E_γ, J^π, $I_{s,0}$, δ, Γ_f/Γ_0	[56, 66, 564]
^{163,164}Dy	a, c, e	< 7.7	E_γ, J^π, $I_{s,0}$, δ, Γ_f/Γ_0, $\sigma_{\gamma\gamma'}$	[60, 363, 565]
^{165}Ho	a	< 4	E_γ, J, $I_{s,0}$, Γ_f/Γ_0	[363]
^{172,174}Yb	e	2.9 - 3.6	E_γ, J^π, $R_{\rm exp}$	[67]
^{176}Lu	a	< 3	E_γ, J, $I_{s,0}$, $R_{\rm exp}$	[368]
^{176,178,180}Hf	a	< 4.1	E_γ, J, $I_{s,0}$, Γ_f/Γ_0	[359]
^{180m,181}Ta	a, d, e	< 9.6	$\sigma_{\gamma\gamma}$	[364, 365, 432]
^{194,196}Pt	c, d	< 4.5	E_γ, J, $I_{s,0}$, Γ_f/Γ_0, $\sigma_{\gamma\gamma}$	[360, 392]
^{203,205}Tl	c, e	< 7.5	E_γ, J, $I_{s,0}$, Γ_f/Γ_0	[566]
^{204,206,207,208}Pb	c, d, e, f	< 10.5	E_γ, J^π, $I_{s,0}$, Γ_f/Γ_0, $\sigma_{\gamma\gamma}$	[62, 396, 567–572]
^{209}Bi	e	14 - 26	ΠL	[312]
^{232}Th	b	2 - 4	E_γ, $I_{s,0}$, $R_{\rm exp}$	[480]
^{235,238}U	b, e	< 6.2	E_γ, J^π, $I_{s,0}$, $R_{\rm exp}$	[230, 361, 366, 481]
^{237}Np	e	< 2.8	E_γ, $I_{s,0}$	[367]
^{239,240}Pu	b	< 2.8	E_γ, J, $I_{s,0}$, $R_{\rm exp}$	[230, 231]

C Recent studies of photonuclear reactions above the particle evaporation threshold with LCB photon beams

An overview on the literature reporting on photonuclear reaction studies above the particle evaporation threshold with LCB photon beams is presented in Table 6. It indicates the isotopes which were studied, the facility where the experiments were done, the photonuclear reaction which was utilized, the γ-ray energy range of the measurement, the deduced experimental quantities, and the bibliographic references. Conference proceedings or laboratory reports have not been considered. The cut-off end date of the literature survey is February 2021.

Table 6: Photonuclear reactions above the particle evaporation threshold measured with LCB photon beams. The studied isotopes are provided in the first column. The facility, where the experiment was carried out is given in the second column. For the NewSUBARU facility the abbreviation NS is used. The studied photonuclear reaction, the energy range and the deduced quantity are given in columns three to five. The bibliographic references are provided in the last column. E_γ and N_γ denote the energy and the flux of the photon beam, Σ – the analyzing power, n-ToF, I_n, N_n, Y_n, $W_n(\theta,\phi)$, $\epsilon_n(\theta)$ – the neutron time-of-flight, yield, multiplicity, normalized yield, angular distribution and polarization asymmetry, N_μ – the normalized number of reactions, PSD are pulse-shape discrimination spectra, and FPY – fission product yields.

Isotope	Facility	Reaction	Energy range (MeV)	Deduced quantity	Ref.
^{2}H	HIγS	(γ,n)	3.58	n-ToF, PSD, I_n, Σ, E_γ, N_γ	[128]
	HIγS		2.39 - 4.05	n-ToF, PSD, I_n, Σ, E_γ, N_γ	[129]
	AIST		2.33 - 4.58	N_n, E_γ, N_γ	[130]
	HIγS		14.0, 16.0	n-ToF, PSD, I_n, Σ, E_γ, N_γ	[132]
	HIγS		2,44, 2.60, 2.72	n-ToF, PSD, I_n, Σ, E_γ, N_γ	[131]
^{3}He	HIγS	(γ,n)	12.8, 14.7	n-ToF, PSD, Y_n, E_γ, N_γ	[134]
			12.8, 14.7	n-ToF, PSD, Y_n, E_γ, N_γ	[135]
			16.5	n-ToF, PSD, Y_n, E_γ, N_γ	[136]
		(γ, p)	7.0 - 16.0		[133]
^{4}He	AIST	(γ,n),(γ,p)	21.8 - 29.8	N_μ, E_γ, N_γ	[137]
	HIγS	(γ,n)	27.0, 27.5, 28.0	N_μ, E_γ, N_γ	[138]
		(γ,p)	22.0 - 23.0		[139]
^{6}Li	HIγS	(γ,n$_0$)	8 - 35	n-ToF, PSD, I_n, E_γ, N_γ	[140]
	NS	(γ,νn)	4.9 - 53.6	N_n, E_γ, N_γ	[141]
^{7}Li	HIγS	(γ,n$_0$)	10 - 35	n-ToF, PSD, I_n, E_γ, N_γ	[142]
		(γ,n$_i$), (γ,d$_1$)	13.0, 15.0	n-ToF, PSD, I_n, E_γ, N_γ	[143]
		(γ, α)	4.4 - 10.0	α-^{3}H coincidences, E_γ, N_γ	[149]
^{9}Be	AIST	(γ,n)	1.78 - 6.11	N_n, E_γ, N_γ	[93]
	AIST	(γ,n)	1.5 - 4.5	N_n, E_γ, N_γ	[573]
	HIγS	(γ,n)	1.5 - 5.2	N_n, E_γ, N_γ	[94]
	NS	(γ,n)	1.67 - 2.11	N_n, E_γ, N_γ	[574]
	HIγS	(γ,n)	5.5 - 15.5	n-ToF, PSD I_n, $\epsilon_n(\theta)$, E_γ, N_γ	[156]
	NS	(γ,n), (γ,νn)	1.6 - 32.0	N_n, E_γ, N_γ	[90]
^{12}C	HIγS	(γ,α)	9.1 - 10.7	N_μ, E_γ, N_γ	[147]
		(γ,2α)	9.1 - 10.7	N_μ, E_γ, N_γ	[291]
^{17}F	HIγS	(γ,α)	5.0 - 6.0	N_μ, E_γ, N_γ	[148]
^{26}Mg	HIγS	(γ,n)	10.80 - 12.05	N_n, n-ToF, E_γ, N_γ	[126]
^{48}Ca	HIγS	(γ,n)	9.5 - 15.3	N_n, E_γ, N_γ	[127]
^{56}Fe	NS	(γ,n)	14.0 - 16.7	n-ToF, $W_n(\theta,\phi)$, E_γ, N_γ	[157]
^{59}Co	NS	(γ,n), (γ,νn)	11.0 - 40.0	N_n, E_γ, N_γ	[90]
^{58}Ni	NS	(γ,n)	8.00 - 22.02	N_n, E_γ, N_γ	[95]
^{60}Ni	NS	(γ,n)	8.00 - 22.02	N_n, E_γ, N_γ	[95]
^{61}Ni	NS	(γ,n)	8.00 - 22.02	N_n, E_γ, N_γ	[95]
^{64}Ni	NS	(γ,n)	8.00 - 22.02	N_n, E_γ, N_γ	[95]
^{nat}Cu	NS	(γ,n)	16.7	n-ToF, $W_n(\theta,\phi)$, E_γ, N_γ	[154]
^{76}Se	AIST	(γ,n)	11.2 - 14.1	N_n, E_γ, N_γ	[110]
^{78}Se	AIST	(γ,n)	10.6 - 14.0	N_n, E_γ, N_γ	[110]

Continued on next page

Table 6 – *Continued from previous page*

Isotope	Facility	Reaction	Energy range (MeV)	Deduced quantity	Ref.
^{80}Se	AIST	(γ,n)	9.91 - 12.7	N_n, E_γ, N_γ	[389]
	AIST	(γ,n)	10.6 - 14.0	N_n, E_γ, N_γ	[108]
	HIγS	(γ,n)	15.6, 15.8, 16.0	n-ToF, PSD, $W_n(\theta,\phi)$, E_γ, N_γ	[122]
^{86}Kr	HIγS	(γ,n)	9.86 - 13.0	N_n, E_γ, N_γ	[120]
^{89}Y	NS	(γ,n), (γ,νn)	11.0 - 40.0	N_n, E_γ, N_γ	[90]
^{90}Zr	HIγS	(γ,n)	9.0 - 13.0	N_n, E_γ, N_γ	[123]
^{96}Zr	AIST	(γ,n)	8.1 - 14.0	N_n, E_γ, N_γ	[106]
^{94}Mo	AIST	(γ,n)	10.0 - 12.0	N_n, E_γ, N_γ	[111]
	HIγS	(γ,n)	9.5 - 13.0	N_n, E_γ, N_γ	[123]
^{95}Mo	AIST	(γ,n)	7.55 - 13.0	N_n, E_γ, N_γ	[111]
^{96}Mo	AIST	(γ,n)	9.4 - 12.0	N_n, E_γ, N_γ	[111]
^{97}Mo	AIST	(γ,n)	7.55 - 13.0	N_n, E_γ, N_γ	[111]
^{98}Mo	AIST	(γ,n)	9.0 - 12.0	N_n, E_γ, N_γ	[111]
^{100}Mo	AIST	(γ,n)	8.5 - 11.5	N_n, E_γ, N_γ	[111]
^{103}Rh	NS	(γ,n), (γ,νn)	9.0 - 42.0	N_n, E_γ, N_γ	[90]
^{105}Pd	AIST	(γ,n)	7.25 - 10.4	N_n, E_γ, N_γ	[107]
^{106}Pd	AIST	(γ,n)	9.6 - 13.7	N_n, E_γ, N_γ	[107]
^{108}Pd	AIST	(γ,n)	9.4 - 13.7	N_n, E_γ, N_γ	[107]
^{116}Sn	AIST	(γ,n)	9.6 - 12.5	N_n, E_γ, N_γ	[105]
^{117}Sn	AIST	(γ,n)	6.8 - 12.0	N_n, E_γ, N_γ	[105]
^{118}Sn	AIST	(γ,n)	9.4 - 12.0	N_n, E_γ, N_γ	[109]
^{119}Sn	AIST	(γ,n)	6.78 - 12.9	N_n, E_γ, N_γ	[109]
^{120}Sn	AIST	(γ,n)	9.2 - 12.0	N_n, E_γ, N_γ	[109]
^{122}Sn	AIST	(γ,n)	8.8 - 12.0	N_n, E_γ, N_γ	[109]
^{124}Sn	AIST	(γ,n)	9.5 - 11.75	N_n, E_γ, N_γ	[109]
^{127}I	NS	(γ,n)	14.0 - 16.7	n-ToF, $W_n(\theta,\phi)$, E_γ, N_γ	[154]
^{139}La	AIST	(γ,n)	9.1 - 12.2	N_n, E_γ, N_γ	[575]
^{142}Ce	HIγS	(γ,n)	7.6 - 9.7	N_μ, E_γ, N_γ	[121]
^{141}Pr	AIST	(γ,n)	9.5 - 12.4	N_n, E_γ, N_γ	[575]
^{143}Nd	NS	(γ,n)	6.1 - 12.5	N_n, E_γ, N_γ	[115]
^{144}Nd	NS	(γ,n)	8.0 - 12.5	N_n, E_γ, N_γ	[115]
^{145}Nd	NS	(γ,n)	6.1 - 12.5	N_n, E_γ, N_γ	[115]
^{146}Nd	NS	(γ,n)	7.2 - 12.3	N_n, E_γ, N_γ	[115]
^{148}Nd	NS	(γ,n)	7.0 - 12.0	N_n, E_γ, N_γ	[115]
^{144}Sm	NS	(γ,n)	10.6 - 12.6	N_n, E_γ, N_γ	[114]
^{147}Sm	NS	(γ,n)	6.5 - 12.6	N_n, E_γ, N_γ	[114]
^{148}Sm	NS	(γ,n)	8.25 - 12.6	N_n, E_γ, N_γ	[114]
^{149}Sm	NS	(γ,n)	6.5 - 12.6	N_n, E_γ, N_γ	[114]
^{150}Sm	NS	(γ,n)	8.1 - 12.5	N_n, E_γ, N_γ	[114]
^{152}Sm	AIST	(γ,n)	8.30 - 11.89	N_n, E_γ, N_γ	[103]
	NS	(γ,n)	8.4 - 12.8	N_n, E_γ, N_γ	[114]
^{154}Sm	NS	(γ,n)	8.2 - 12.5	N_n, E_γ, N_γ	[114]
^{159}Tb	NS	(γ,n), (γ,νn)	8.0 - 42.0	N_n, E_γ, N_γ	[90]
^{162}Dy	NS	(γ,n)	8.3 - 13.6	N_n, E_γ, N_γ	[118]
^{163}Dy	NS	(γ,n)	6.5 - 13.4	N_n, E_γ, N_γ	[118]

Continued on next page

Table 6 – *Continued from previous page*

Isotope	Facility	Reaction	Energy range (MeV)	Deduced quantity	Ref.
^{165}Ho	NS	(γ,n)	3.3 - 16.7	$T_{1/2}(^{164}Ho)$ E_γ, N_γ	[164]
	NS	(γ,n), (γ,νn)	8.0 - 43.0	N_n, E_γ, N_γ	[90]
^{169}Tm	NS	(γ,n), (γ,νn)	8.0 - 40.0	N_n, E_γ, N_γ	[90]
^{181}Ta	AIST	(γ,n)	7.8 - 12.0	N_n, E_γ, N_γ	[98]
	AIST	(γ,n)	9.2 - 12.3	N_μ, N_n, E_γ, N_γ	[101]
	NS	(γ,n), (γ,νn)	8.0 - 43.0	N_n, E_γ, N_γ	[90]
^{186}W	AIST	(γ,n)	4.0 - 11.0	N_n, E_γ, N_γ	[99]
	AIST	(γ,n)	7.3 - 10.9	N_n, E_γ, N_γ	[100]
^{185}Re	NS	(γ,n)	2.0 - 20.0	$T_{1/2}(^{184}Re)$, E_γ, N_γ	[163]
^{187}Re	AIST	(γ,n)	7.3 - 10.9	N_n, E_γ, N_γ	[100]
^{188}Os	AIST	(γ,n)	7.3 - 10.9	N_n, E_γ, N_γ	[100]
^{197}Au	AIST	(γ,n)	8.23 - 12.27	N_n, E_γ, N_γ	[103]
	AIST	(γ,n)	9.3 - 13.4	N_n, E_γ, N_γ	[110]
	NS	(γ,n)	14.0 - 16.7	n-ToF, $W_n(\theta,\phi)$, E_γ, N_γ	[154]
^{203}Tl	NS	(γ,n)	9.0 - 13.0	N_n, E_γ, N_γ	[119]
^{205}Tl	NS	(γ,n)	9.0 - 13.0	N_n, E_γ, N_γ	[119]
^{206}Pb	AIST	(γ,n)	7.0 - 13.5	N_n, E_γ, N_γ	[112]
^{207}Pb	AIST	(γ,n)	7.0 - 13.5	N_n, $W_n(\theta,\phi)$, E_γ, N_γ	[112]
		(γ,n)	6.5 - 12.5	$W_n(\theta,\phi)$, E_γ, N_γ	[113]
^{208}Pb	AIST	(γ,n)	7.0 - 13.5	N_n, $W_n(\theta,\phi)$, E_γ, N_γ	[112]
		(γ,n)	6.5 - 12.5	$W_n(\theta,\phi)$, E_γ, N_γ	[113]
^{209}Bi	NS	(γ,n), (γ,νn)	7.0 - 40.0	N_n, E_γ, N_γ	[116]
^{232}Th	HIγS	(γ,f)	5.30 - 7.60	$\epsilon_n(\theta)$, E_γ, N_γ	[158]
			5.30 - 7.60	$\epsilon_n(\theta)$, E_γ, N_γ	[159]
			4.30 - 6.00	N_n, $W_n(\theta,\phi)$, PSD, E_γ, N_γ	[274]
^{233}U	HIγS	(γ,f)	5.30 - 7.60	$\epsilon_n(\theta)$, E_γ, N_γ	[159]
^{235}U	HIγS	(γ,f)	5.30 - 7.60	$\epsilon_n(\theta)$, E_γ, N_γ	[158]
			5.30 - 7.60	$\epsilon_n(\theta)$, E_γ, N_γ	[159]
			8.95 - 16.95	N_μ, E_γ, N_γ	[204]
			9.0 - 17.0	N_μ, E_γ, N_γ	[205]
^{238}U	HIγS	(γ,f)	5.30 - 7.60	$\epsilon_n(\theta)$, E_γ, N_γ	[158]
			4.70 - 6.0	N_μ, E_γ, N_γ	[465]
			5.30 - 7.60	$\epsilon_n(\theta)$, E_γ, N_γ	[159]
			8.98 - 16.95	N_μ, E_γ, N_γ	[204]
			9.0 - 17.0	N_μ, E_γ, N_γ	[205]
			4.30 - 6.0	N_n, $W_n(\theta,\phi)$, PSD, E_γ, N_γ	[274]
			9.0 - 17.0	FPY, E_γ, N_γ	[203]
^{237}Np	HIγS	(γ,f)	5.30 - 7.60	$\epsilon_n(\theta)$, E_γ, N_γ	[159]
^{239}Pu	HIγS	(γ,f)	5.30 - 7.60	$\epsilon_n(\theta)$, E_γ, N_γ	[158]
			5.30 - 7.60	$\epsilon_n(\theta)$, E_γ, N_γ	[159]
			11.0	N_μ, E_γ, N_γ	[202]
			9.0 - 17.0	N_μ, E_γ, N_γ	[205]
			9.0 - 17.0	FPY, E_γ, N_γ	[203]
^{240}Pu	HIγS	(γ,f)	5.30 - 7.60	$\epsilon_n(\theta)$, E_γ, N_γ	[159]
^{241}Am	HIγS	(γ,f)	9.0 - 15.60	N_μ, E_γ, N_γ	[561]

References

[1] R. Dicke, P. Peebles, P. Roll, and D. Wilkinson, Astrophys. J. 142 (1965) 414.

[2] H. Tsuchiya, T. Enoto, S. Yamada, T. Yuasa, M. Kawaharada, T. Kitaguchi, M. Kokubun, H. Kato, M. Okano, S. Nakamura, and K. Makishima, Phys. Rev. Lett. 99 (2007) 165002.

[3] T. Enoto, Y. Wada, Y. Furuta, K. Nakazawa, T. Yuasa, K. Okuda, K. Makishima, M. Sato, Y. Sato, T. Nakano, D. Umemoto, and H. Tsuchiya, Nature 551 (2017) 481.

[4] D. Strickland and G. Mourou, Opt. Comm. 56 (1985) 219.

[5] R. Beck, Prog. Part. Nucl. Phys. 55 (2005) 91.

[6] K. Strauch, Annu. Rev. Nucl. Sci. 2 (1953) 105.

[7] J. S. Levinger, Annu. Rev. Nucl. Sci. 4 (1954) 13.

[8] F. R. Metzger, Prog. in Nucl. Phys. 7 (1959) 53.

[9] M. Danos and E. G. Fuller, Annu. Rev. Nucl. Sci. 15 (1965) 29.

[10] U. E. P. Berg and U. Kneissl, Annu. Rev. Nucl. Part. Sci. 37 (1987) 33.

[11] U. Kneissl, H. H. Pitz, and A. Zilges, Prog. Part. Nucl. Phys. 37 (1996) 349.

[12] H. R. Weller, M. W. Ahmed, H. Gao, W. Tornow, Y. K. Wu, M. Gai, and R. Miskimen, Prog. Part. Nucl. Phys. 62 (2009) 257 .

[13] J. Chadwick and M. Goldhaber, Nature 134 (1934) 237.

[14] L. Szilard and T. A. Chalmers, Nature 134 (1934) 494.

[15] W. Bothe and W. Gentner, Z. Phys. 71 (1937) 236.

[16] L. R. Hafstad, N. P. Heydenburg, and M. A. Tuve, Phys. Rev. 50 (1936) 504.

[17] G. C. Baldwin and G. S. Klaiber, Phys. Rev. 71 (1947) 3.

[18] L. I. Schiff, Phys. Rev. 70 (1946) 761.

[19] E. Hayward and E. G. Fuller, Phys. Rev. 106 (1957) 991.

[20] *Gordon research conference on photonuclear physics 1959*, www.grc.org/photonuclear-reactions-conference/1959/, accessed: 2021-03-09.

[21] F. R. Metzger, Phys. Rev. 187 (1969) 1680.

[22] K. Wienhard, C. Bläsing, K. Ackermann, K. Bangert, U. E. P. Berg, K. Kobras, W. Naatz, D. Rück, R. K. M.Schneider, and R. Stock, Z. Phys. A 302 (1981) 185.

[23] R. Moreh, W. M. Sandefur, W. C. Sellyey, D. C. Sutton, and R. Vodhanel, Phys. Rev. C 25 (1982) 1824.

[24] K. Govaert, W. Mondelaers, E. Jacobs, D. De Frenne, K. Persyn, S. Pomme, M.-L. Yoneama, S. Lindenstruth, K. Huber, A. Jung, B. Starck, R. Stock, C. Wesselborg, R.-D. Heil, U. Kneissl, and H. H. Pitz, Nucl. Instr. Meth. Phys. Res. A 337 (1994) 265.

[25] U. Kneissl, Prog. Part. Nucl. Phys. 24 (1990) 41.

[26] A. Richter, Prog. Part. Nucl. Phys. 34 (1995) 261.

[27] S. S. Colgate and F. C. Gilbert, Phys. Rev. 89 (1953) 790.

[28] A. Veyssière, H. Beil, R. Bergère, P. Carlos, J. Fagot, A. Leprêtre, and J. Ahrens, Nucl. Instr. and Meth. 165 (1979) 417.

[29] S. C. Fultz, R. L. Bramblett, J. T. Caldwell, N. E. Hansen, and C. P. Jupiter, Phys. Rev. 128 (1962) 2345.

[30] U. Kneissl, E. A. Koop, G. Kuhl, K. H. Leister, and A. Weller, Nucl. Instr. and Meth. 127 (1975) 1.

[31] J. S. O'Connell, Rev. Sci. Instr. 32 (1961) 1314.

[32] J. S. O'Connell, P. A. Tipler, and P. Axel, Phys. Rev. 126 (1962) 228.

[33] J. W. Knowles, W. F. Mills, R. N. King, G. E. Lee-Whiting, S. Yen, B. O. Pich, J. C. Kim, T. E. Drake, L. S. Cardman, and R. L. Gulbranson, Nucl. Instr. and Meth. 193 (1982) 463.

[34] P. Axel, K. Min, N. Stein, and D. C. Sutton, Phys. Rev. Lett. 10 (1963) 299.

[35] R. M. Laszewski, Phys. Rev. C 34 (1986) 1114.

[36] R. M. Laszewski, R. Alarcon, and S. D. Hoblit, Phys. Rev. Lett. 59 (1987) 431.

[37] R. M. Laszewski, R. Alarcon, D. S. Dale, and S. D. Hoblit, Phys. Rev. Lett. 61 (1988) 1710.

[38] R. H. Milburn, Phys. Rev. Lett. 10 (1963) 75.

[39] F. R. Arutyunian and V. A. Tumanian, Phys. Lett. 4 (1963) 176.

[40] R. Hajima, Phys. Procedia 84 (2016) 35.

[41] P. Moon, Proc. Phys. Soc. A 63 (1950) 1189.

[42] P. Moon, Proc. Phys. Soc. A 64 (1951) 76.

[43] P. Moon and A. Storruste, Proc. Phys. Soc. A 66 (1953) 585.

[44] A. Bohr and B. R. Mottelson, *Nuclear Structure Vol. I*, World Scientific, Singapore (1998).

[45] U. Friman-Gayer, C. Romig, T. Hüther, K. Albe, S. Bacca, T. Beck, M. Berger, J. Birkhan, K. Hebeler, O. J. Hernandez, J. Isaak, S. König, N. Pietralla, P. C. Ries, J. Rohrer, R. Roth, D. Savran, M. Scheck, A. Schwenk, R. Seutin, and V. Werner, Phys. Rev. Lett. 126 (2021) 102501.

[46] R. Moreh, O. Beck, D. Jäger, Y. Finkelstein, U. Kneissl, J. Margraf, H. Maser, and H. Pitz, Phys. Rev. B 56 (1997) 187.

[47] N. Pietralla, P. von Brentano, R.-D. Herzberg, U. Kneissl, J. Margraf, H. Maser, H. H. Pitz, and A. Zilges, Phys. Rev. C 52 (1995) R2317.

[48] W. E. Lamb, Phys. Rev. 55 (1939) 190.

[49] N. Pietralla, V. N. Litvinenko, S. Hartman, F. F. Mikhailov, I. V. Pinayev, G. Swift, M. W. Ahmed, J. H. Kelley, S. O. Nelson, R. Prior, K. Sabourov, A. P. Tonchev, and H. R. Weller, Phys. Rev. C 65 (2002) 047305.

[50] K. Krane, R. Steffen, and R. Wheeler, Atomic Data and Nuclear Data Tables 11 (1973) 351.

[51] N. Pietralla, M. W. Ahmed, C. Fransen, V. N. Litvinenko, A. P. Tonchev, and H. R. Weller, AIP Conf. Proc. 656 (2003) 365.

[52] L. Fagg and S. Hanna, Rev. Mod. Phys. 31 (1959) 711.

[53] A. I. Titov, M. Fujiwara, and K. Kawase, J. Phys. G 32 (2006) 1097.

[54] J. Beller, C. Stumpf, M. Scheck, N. Pietralla, D. Deleanu, D. M. Filipescu, T. Glodariu, W. Haxton, A. Idini, J. H. Kelley, E. Kwan, G. Martinez-Pinedo, R. Raut, C. Romig, R. Roth, G. Rusev, D. Savran, A. P. Tonchev, W. Tornow, J. Wagner, H. R. Weller, N. V. Zamfir, and M. Zweidinger, Phys. Lett. B 741 (2015) 128.

[55] U. Kneissl, N. Pietralla, and A. Zilges, J. Phys. G 32 (2006) R217.

[56] T. Beck, J. Beller, N. Pietralla, M. Bhike, J. Birkhan, V. Derya, U. Gayer, A. Hennig, J. Isaak, B. Löher, V. Y. Ponomarev, A. Richter, C. Romig, D. Savran, M. Scheck, W. Tornow, V. Werner, A. Zilges, and M. Zweidinger, Phys. Rev. Lett. 118 (2017) 212502.

[57] J. Isaak, D. Savran, B. Löher, T. Beck, U. Friman-Gayer, Krishichayan, N. Pietralla, V. Y. Ponomarev, M. Scheck, W. Tornow, V. Werner, A. Zilges, and M. Zweidinger, Phys. Rev. C (2021), in press.

[58] A. P. Tonchev, S. L. Hammond, J. H. Kelley, E. Kwan, H. Lenske, G. Rusev, W. Tornow, and N. Tsoneva, Phys. Rev. Lett. 104 (2010) 072501.

[59] C. Romig, D. Savran, J. Beller, J. Birkhan, A. Endres, M. Fritzsche, J. Glorius, J. Isaak, N. Pietralla, M. Scheck, L. Schnorrenberger, K. Sonnabend, and M. Zweidinger, Phys. Lett. B 744 (2015) 369.

[60] T. Beck, V. Werner, N. Pietralla, M. Bhike, N. Cooper, U. Friman-Gayer, J. Isaak, R. V. Jolos, J. Kleemann, Krishichayan, O. Papst, W. Tornow, C. Bernards, B. P. Crider, R. S. Ilieva, B. Löher, C. Mihai, F. Naqvi, S. Pascu, E. E. Peters, F. M. Prados-Estevez, T. J. Ross, D. Savran, J. R. Vanhoy, and A. Zilges, Phys. Rev. Lett. 125 (2020) 092501.

[61] N. Pietralla, Z. Berant, V. N. Litvinenko, S. Hartman, F. F. Mikhailov, I. V. Pinayev, G. Swift, M. W. Ahmed, J. H. Kelley, S. O. Nelson, R. Prior, K. Sabourov, A. P. Tonchev, and H. R. Weller, Phys. Rev. Lett. 88 (2002) 012502.

[62] N. Pietralla, T. Li, M. Fritzsche, M. Ahmed, T. Ahn, A. Costin, J. Enders, J. Li, S. Müller, P. von Neumann-Cosel, I. Pinayev, V. Ponomarev, D. Savran, A. Tonchev, W. Tornow, H. Weller, V. Werner, Y. Wu, and A. Zilges, Phys. Lett. B 681 (2009) 134.

[63] K. E. Ide, T. Beck, V. Werner, M. Berger, S. W. Finch, U. Friman-Gayer, J. Kleemann, Krishichayan, B. Löher, O. Papst, N. Pietralla, D. Savran, W. Tornow, M. Weinert, J. Wiederhold, and A. Zilges, Phys. Rev. C 103 (2021) 054302.

[64] G. Alaga, K. Alder, A. Bohr, and B. R. Mottelson, K. Dan. Vidensk. Selesk. Mat. Fys. Medd. 29 (1955) 1.

[65] N. Pietralla, Phys. Rev. C 59 (1999) 2941.

[66] J. Beller, N. Pietralla, J. Barea, M. Elvers, J. Endres, C. Fransen, J. Kotila, O. Möller, A. Richter, T. R. Rodríguez, C. Romig, D. Savran, M. Scheck, L. Schnorrenberger, K. Sonnabend, V. Werner, A. Zilges, and M. Zweidinger, Phys. Rev. Lett. 111 (2013) 172501.

[67] D. Savran, S. Müller, A. Zilges, M. Babilon, M. W. Ahmed, J. H. Kelley, A. Tonchev, W. Tornow, H. R. Weller, N. Pietralla, J. Li, I. V. Pinayev, and Y. K. Wu, Phys. Rev. C 71 (2005) 034304.

[68] P. C. Ries, H. Pai, T. Beck, J. Beller, M. Bhike, V. Derya, U. Gayer, J. Isaak, B. Löher, Krishichayan, L. Mertes, N. Pietralla, C. Romig, D. Savran, M. Schilling, W. Tornow, S. Typel, V. Werner, J. Wilhelmy, A. Zilges, and M. Zweidinger, Phys. Rev. C 100 (2019) 021301.

[69] L. I. Schiff, Phys. Rev. 83 (1951) 252.

[70] B. Löher, D. Savran, T. Aumann, J. Beller, M. Bhike, N. Cooper, V. Derya, M. Duchene, J. Endres, A. Hennig, P. Humby, J. Isaak, J. Kelley, M. Knörzer, N. Pietralla, V. Ponomarev, C. Romig, M. Scheck, H. Scheit, J. Silva, A. Tonchev, W. Tornow, F. Wamers, H. Weller, V. Werner, and A. Zilges, Phys. Lett. B 756 (2016) 72.

[71] B. Löher, V. Derya, T. Aumann, J. Beller, N. Cooper, M. Duchene, J. Endres, E. Fiori, J. Isaak, J. Kelley, M. Knörzer, N. Pietralla, C. Romig, D. Savran, M. Scheck, H. Scheit, J. Silva, A. P. Tonchev, W. Tornow, H. Weller, V. Werner, and A. Zilges, Nucl. Instr. Meth. Phys. Res. A 723 (2013) 136.

[72] J. Isaak, D. Savran, B. Löher, T. Beck, M. Bhike, U. Gayer, Krishichayan, N. Pietralla, M. Scheck, W. Tornow, V. Werner, A. Zilges, and M. Zweidinger, Phys. Lett. B 788 (2019) 225 .

[73] C. A. Ur, A. Zilges, N. Pietralla, J. Beller, B. Boisdeffre, M. O. Cernaianu, V. Derya, B. Löher, M. Matei, G. Pascovici, C. Petcu, C. Romig, D. Savran, G. Suliman, E. Udup, and V. Werner, Rom. Rep. Phys. 68 (2016) S483.

[74] P. Söderström, G. Suliman, C. Ur, D. Balabanski, T. Beck, L. Capponi, A. Dhal, V. Iancu, S. Ilie, M. Iovea, A. Kusoglu, C. Petcu, N. Pietralla, G. Turturica, E. Udup, J. Wilhelmy, and A. Zilges, Acta Phys. Pol. B 50 (2019) 329.

[75] K. A. Tanaka, K. M. Spohr, D. L. Balabanski, S. Balascuta, L. Capponi, M. O. Cernaianu, M. Cuciuc, A. Cucoanes, I. Dancus, A. Dhal, B. Diaconescu, D. Doria, P. Ghenuche, D. G. Ghita, S. Kisyov, V. Nastasa, J. F. Ong, F. Rotaru, D. Sangwan, P.-A. Söderström, D. Stutman, G. Suliman, O. Tesileanu, L. Tudor, N. Tsoneva, C. A. Ur, D. Ursescu, and N. V. Zamfir, Matter Radiat. Extremes 5 (2020) 024402.

[76] J. Chadwick and M. Goldhaber, Proc. R. Soc. A 151 (1941) 479.

[77] G. S. Levinger and H. A. Bethe, Phys. Rev. 78 (1950) 115.

[78] W. Thomas, Naturwissenschaften 13 (1925) 627.

[79] W. Kuhn, Z. Phys. 33 (1925) 408.

[80] F. Reiche and W. Thomas, Z. Phys. 34 (1925) 331.

[81] N. Bohr, Nature 137 (1936) 344.

[82] M. B. Chadwick, P. Obloinský, P. Hodgson, and G. Reffo, Phys. Rev. C 44 (1991) 814.

[83] W. Hauser and H. Feshbach, Phys. Rev. 87 (1952) 366.

[84] V. F. Weisskopf and D. H. Ewing, Phys. Rev. 57 (1940) 472.

[85] H. Feshbach, *Theoretical Nuclear Physics: Nuclear Reactions*, John Wiley & Sons (1992).

[86] A. Koning and D. Rochman, Nucl. Data Sheets 113 (2012) 2841.

[87] M. Herman, R. Capote, B. Carlson, P. Obložinský, M. Sin, A. Trkov, H. Wienke, and V. Zerkin, Nucl. Data Sheets 108 (2007) 2655.

[88] R. Capote, M. Herman, P. Obložinský, P. Young, S. Goriely, T. Belgya, A. Ignatyuk, A. Koning, S. Hilaire, V. Plujko, M. Avrigeanu, O. Bersillon, M. Chadwick, T. Fukahori, Z. Ge, Y. Han, S. Kailas, J. Kopecky, V. Maslov, G. Reffo, M. Sin, E. Soukhovitskii, and P. Talou, Nucl. Data Sheets 110 (2009) 3107.

[89] Handbook of photonuclear data for applications. Cross sections and measurements, Tech. Report IAEA-TECDOC-1178, IAEA (2000).

[90] T. Kawano, Y. Cho, P. Dimitriou, D. Filipescu, N. Iwamoto, V. Plujko, X. Tao, H. Utsunomiya, V. Varlamov, R. Xu, R. Capote, I. Gheorghe, O. Gorbachenko, Y. Jin, T. Renstrøm, M. Sin, K. Stopani, Y. Tian, G. Tveten, J. Wang, T. Belgya, R. Firestone, S. Goriely, J. Kopecky, M. Krtička, R. Schwengner, S. Siem, and M. Wiedeking, Nucl. Data Sheets 163 (2020) 109.

[91] H. A. Bethe, Rev. Mod. Phys. 9 (1937) 69.

[92] S. Goriely, S. Péru, G. Colò, X. Roca-Maza, I. Gheorghe, D. Filipescu, and H. Utsunomiya, Phys. Rev. C 102 (2020) 064309.

[93] H. Utsunomiya, Y. Yonezawa, H. Akimune, T. Yamagata, M. Ohta, M. Fujishiro, H. Toyokawa, and H. Ohgaki, Phys. Rev. C 63 (2000) 018801.

[94] C. W. Arnold, T. B. Clegg, C. Iliadis, H. J. Karwowski, G. C. Rich, J. R. Tompkins, and C. R. Howell, Phys. Rev. C 85 (2012) 044605.

[95] H. Utsunomiya, T. Renstrøm, G. M. Tveten, S. Goriely, S. Katayama, T. Ari-izumi, D. Takenaka, D. Symochko, B. V. Kheswa, V. W. Ingeberg, T. Glodariu, Y.-W. Lui, S. Miyamoto, A. C. Larsen, J. E. Midtbø, A. Görgen, S. Siem, L. C. Campo, M. Guttormsen, S. Hilaire, S. Péru, and A. J. Koning, Phys. Rev. C 98 (2018) 054619.

[96] S. Gales, K. A. Tanaka, D. L. Balabanski, F. Negoita, D. Stutman, O. Tesileanu, C. A. Ur, D. Ursescu, I. Andrei, S. Ataman, M. O. Cernaianu, L. D'Alessi, I. Dancus, B. Diaconescu, N. Djourelov, D. Filipescu, P. Ghenuche, D. G. Ghita, C. Matei, K. Seto, M. Zeng, and N. V. Zamfir, Rep. Prog. Phys. 81 (2018) 094301.

[97] N. V. Zamfir, Nucl. Phys. News 25 (2015) 34.

[98] H. Utsunomiya, H. Akimune, S. Goko, M. Ohta, H. Ueda, T. Yamagata, K. Yamasaki, H. Ohgaki, H. Toyokawa, Y.-W. Lui, T. Hayakawa, T. Shizuma, and S. Goriely, Phys. Rev. C 67 (2003) 015807.

[99] P. Mohr, T. Shizuma, H. Ueda, S. Goko, A. Makinaga, K. Hara, T. Hayakawa, Y.-W. Lui, H. Ohgaki, and H. Utsunomiya, Phys. Rev. C 69 (2004) 032801.

[100] T. Shizuma, H. Utsunomiya, P. Mohr, T. Hayakawa, S. Goko, A. Makinaga, H. Akimune, T. Yamagata, M. Ohta, H. Ohgaki, Y.-W. Lui, H. Toyokawa, A. Uritani, and S. Goriely, Phys. Rev. C 72 (2005) 025808.

[101] S. Goko, H. Utsunomiya, S. Goriely, A. Makinaga, T. Kaihori, S. Hohara, H. Akimune, T. Yamagata, Y.-W. Lui, H. Toyokawa, A. J. Koning, and S. Hilaire, Phys. Rev. Lett. 96 (2006) 192501.

[102] H. Utsunomiya, S. Goko, H. Toyokawa, H. Ohgaki, K. Soutome, H. Yonehara, S. Goriely, P. Mohr, and Zs. Fülöp, Eur. Phys. J. A 27 (2006) 153.

[103] K. Hara, H. Harada, F. Kitatani, S. Goko, S. Hohara, T. Kaihori, A. Makinaga, H. Utsunomiya, H. Toyokawa, and K. Yamada, J. Nucl. Sci. Technol. 44 (2007) 938.

[104] H. Utsunomiya, S. Goriely, T. Kondo, T. Kaihori, A. Makinaga, S. Goko, H. Akimune, T. Yamagata, H. Toyokawa, T. Matsumoto, H. Harano, S. Hohara, Y.-W. Lui, S. Hilaire, S. Péru, and A. J. Koning, Phys. Rev. Lett. 100 (2008) 162502.

[105] H. Utsunomiya, S. Goriely, M. Kamata, T. Kondo, O. Itoh, H. Akimune, T. Yamagata, H. Toyokawa, Y. W. Lui, S. Hilaire, and A. J. Koning, Phys. Rev. C 80 (2009) 055806.

[106] H. Utsunomiya, S. Goriely, H. Akimune, H. Harada, F. Kitatani, S. Goko, H. Toyokawa, K. Yamada, T. Kondo, O. Itoh, M. Kamata, T. Yamagata, Y.-W. Lui, S. Hilaire, and A. J. Koning, Phys. Rev. C 81 (2010) 035801.

[107] H. Utsunomiya, S. Goriely, H. Akimune, H. Harada, F. Kitatani, S. Goko, H. Toyokawa, K. Yamada, T. Kondo, O. Itoh, M. Kamata, T. Yamagata, Y.-W. Lui, I. Daoutidis, D. P. Arteaga, S. Hilaire, and A. J. Koning, Phys. Rev. C 82 (2010) 064610.

[108] F. Kitatani, H. Harada, S. Goko, H. Utsunomiya, H. Akimune, T. Kaihori, H. Toyokawa, and K. Yamada, J. Nucl. Sci. Technol. 47 (2010) 367.

[109] H. Utsunomiya, S. Goriely, M. Kamata, H. Akimune, T. Kondo, O. Itoh, C. Iwamoto, T. Yamagata, H. Toyokawa, Y.-W. Lui, H. Harada, F. Kitatani, S. Goko, S. Hilaire, and A. J. Koning, Phys. Rev. C 84 (2011) 055805.

[110] F. Kitatani, H. Harada, S. Goko, H. Utsunomiya, H. Akimune, H. Toyokawa, and K. Yamada, J. Nucl. Sci. Technol. 48 (2011) 1017.

[111] H. Utsunomiya, S. Goriely, T. Kondo, C. Iwamoto, H. Akimune, T. Yamagata, H. Toyokawa, H. Harada, F. Kitatani, Y.-W. Lui, A. C. Larsen, M. Guttormsen, P. E. Koehler, S. Hilaire, S. Péru, M. Martini, and A. J. Koning, Phys. Rev. C 88 (2013) 015805.

[112] T. Kondo, H. Utsunomiya, S. Goriely, I. Daoutidis, C. Iwamoto, H. Akimune, A. Okamoto, T. Yamagata, M. Kamata, O. Itoh, H. Toyokawa, Y.-W. Lui, H. Harada, F. Kitatani, S. Hilaire, and A. J. Koning, Phys. Rev. C 86 (2012) 014316.

[113] T. Kondo, H. Utsunomiya, S. Goriely, C. Iwamoto, H. Akimune, T. Yamagata, H. Toyokawa, H. Harada, F. Kitatani, Y.-W. Lui, S. Hilaire, and A. Koning, Nucl. Data Sheets 119 (2014) 310.

[114] D. M. Filipescu, I. Gheorghe, H. Utsunomiya, S. Goriely, T. Renstrøm, H.-T. Nyhus, O. Tesileanu, T. Glodariu, T. Shima, K. Takahisa, S. Miyamoto, Y.-W. Lui, S. Hilaire, S. Péru, M. Martini, and A. J. Koning, Phys. Rev. C 90 (2014) 064616.

[115] H.-T. Nyhus, T. Renstrøm, H. Utsunomiya, S. Goriely, D. M. Filipescu, I. Gheorghe, O. Tesileanu, T. Glodariu, T. Shima, K. Takahisa, S. Miyamoto, Y.-W. Lui, S. Hilaire, S. Péru, M. Martini, L. Siess, and A. J. Koning, Phys. Rev. C 91 (2015) 015808.

[116] I. Gheorghe, H. Utsunomiya, S. Katayama, D. Filipescu, S. Belyshev, K. Stopani, V. Orlin, V. Varlamov, T. Shima, S. Amano, S. Miyamoto, Y.-W. Lui, T. Kawano, and S. Goriely, Phys. Rev. C 96 (2017) 044604.

[117] I. Gheorghe, H. Utsunomiya, S. Katayama, D. Filipescu, S. Belyshev, K. Stopani, V. Orlin, V. Varlamov, T. Shima, S. Amano, S. Miyamoto, Y.-W. Lui, T. Kawano, and S. Goriely, Phys. Rev. C 99 (2019) 059901.

[118] T. Renstrøm, H. Utsunomiya, H. T. Nyhus, A. C. Larsen, M. Guttormsen, G. M. Tveten, D. M. Filipescu, I. Gheorghe, S. Goriely, S. Hilaire, Y.-W. Lui, J. E. Midtbø, S. Péru, T. Shima, S. Siem, and O. Tesileanu, Phys. Rev. C 98 (2018) 054310.

[119] H. Utsunomiya, T. Renstrøm, G. M. Tveten, S. Goriely, T. Ari-izumi, D. Filipescu, J. Kaur, Y.-W. Lui, W. Luo, S. Miyamoto, A. C. Larsen, S. Hilaire, S. Péru, and A. J. Koning, Phys. Rev. C 99 (2019) 024609.

[120] R. Raut, A. P. Tonchev, G. Rusev, W. Tornow, C. Iliadis, M. Lugaro, J. Buntain, S. Goriely, J. H. Kelley, R. Schwengner, A. Banu, and N. Tsoneva, Phys. Rev. Lett. 111 (2013) 112501.

[121] A. Sauerwein, K. Sonnabend, M. Fritzsche, J. Glorius, E. Kwan, N. Pietralla, C. Romig, G. Rusev, D. Savran, L. Schnorrenberger, A. P. Tonchev, W. Tornow, and H. R. Weller, Phys. Rev. C 89 (2014) 035803.

[122] S. A. Yates, B. Fallin, C. R. Howell, Krishichayan, W. Tornow, and S. M. Grimes, Phys. Rev. C 98 (2018) 054621.

[123] A. Banu, E. G. Meekins, J. A. Silano, H. J. Karwowski, and S. Goriely, Phys. Rev. C 99 (2019) 025802.

[124] H. Beil, R. Bergère, P. Carlos, A. Leprêtre, A. D. Miniac, and A. Veyssière, Nucl. Phys. A227 (1974) 427.

[125] D. Filipescu, A. Anzalone, D. Balabanski, S. S. Belyshev, F. Camera, M. La Cognata, P. Constantin, L. Csige, P. V. Cuong, M. Cwiok, V. Derya, W. Dominik, M. Gai, S. Gales, I. Gheorghe, B. Ishkhanov, A. Krasznahorkay, A. A. Kuznetsov, C. Mazzocchi, V. Orlin, N. Pietralla, M. Sin, C. Spitaleri, K. Stopani, O. Tesileanu, C. Ur, I. Ursu, H. Utsunomiya, V. Varlamov, H. Weller, N. Zamfir, and A. Zilges, Eur. Phys. J. A 51 (2015) 185.

[126] R. J. deBoer, A. Best, J. Görres, K. Smith, W. Tan, M. Wiescher, R. Raut, G. Rusev, A. P. Tonchev, and W. Tornow, Phys. Rev. C 89 (2014) 055802.

[127] J. R. Tompkins, C. W. Arnold, H. J. Karwowski, G. C. Rich, L. G. Sobotka, and C. R. Howell, Phys. Rev. C 84 (2011) 044331.

[128] E. C. Schreiber, R. S. Canon, B. T. Crowley, C. R. Howell, J. H. Kelley, V. N. Litvinenko, S. O. Nelson, S. H. Park, I. V. Pinayev, R. M. Prior, K. Sabourov, M. Spraker, W. Tornow, Y. Wu, E. A. Wulf, and H. R. Weller, Phys. Rev. C 61 (2000) 061604.

[129] W. Tornow, V. N. Litvinenko, A. Hutcheson, N. G. Czakon, C. R. Howell, G. J. Weisel, S. Mikhailov, I. V. Pinayev, J. H. Kelley, and H. Witala, Phys. Lett. B 574 (2003) 8.

[130] K. Y. Hara, H. Utsunomiya, S. Goko, H. Akimune, T. Yamagata, M. Ohta, H. Toyokawa, K. Kudo, A. Uritani, Y. Shibata, Y.-W. Lui, and H. Ohgaki, Phys. Rev. D 68 (2003) 072001.

[131] M. W. Ahmed, M. A. Blackston, B. A. Perdue, W. Tornow, H. R. Weller, B. Norum, B. Sawatzky, R. M. Prior, and M. C. Spraker, Phys. Rev. C 77 (2008) 044005.

[132] M. A. Blackston, M. W. Ahmed, B. A. Perdue, H. R. Weller, B. Bewer, R. E. Pywell, W. A. Wurtz, R. Igarashi, S. Kucuker, B. Norum, K. Wang, J. Li, S. F. Mikhailov, V. G. Popov, Y. K. Wu, and B. D. Sawatzky, Phys. Rev. C 78 (2008) 034003.

[133] W. Tornow, H. Karwowski, J. Kelley, R. Raut, G. Rusev, S. Stave, A. Tonchev, A. Deltuva, A. Fonseca, L. Marcucci, M. Viviani, A. Kievsky, J. Golak, R. Skibiński, H. Witała, and R. Schiavilla, Phys. Lett. B 702 (2011) 121.

[134] G. Laskaris, Q. Ye, B. Lalremruata, Q. J. Ye, M. W. Ahmed, T. Averett, A. Deltuva, D. Dutta, A. C. Fonseca, H. Gao, J. Golak, M. Huang, H. J. Karwowski, J. M. Mueller, L. S. Myers, C. Peng, B. A. Perdue, X. Qian, P. U. Sauer, R. Skibiński, S. Stave, J. R. Tompkins, H. R. Weller, H. Witała, Y. K. Wu, Y. Zhang, and W. Zheng, Phys. Rev. Lett. 110 (2013) 202501.

[135] G. Laskaris, Q. Ye, B. Lalremruata, Q. J. Ye, M. W. Ahmed, T. Averett, A. Deltuva, D. Dutta, A. C. Fonseca, H. Gao, J. Golak, M. Huang, H. J. Karwowski, J. M. Mueller, L. S. Myers, C. Peng, B. A. Perdue, X. Qian, P. U. Sauer, R. Skibiński, S. Stave, J. R. Tompkins, H. R. Weller, H. Witała, Y. K. Wu, Y. Zhang, and W. Zheng, Phys. Rev. C 89 (2014) 024002.

[136] G. Laskaris, X. Yan, J. Mueller, W. Zimmerman, W. Xiong, M. Ahmed, T. Averett, P.-H. Chu, A. Deltuva, C. Flower, A. Fonseca, H. Gao, J. Golak, J. Heideman, H. Karwowski, M. Meziane, P. Sauer, R. Skibiński, I. Strakovsky, H. Weller, H. Witała, and Y. Wu, Phys. Lett. B 750 (2015) 547.

[137] T. Shima, S. Naito, Y. Nagai, T. Baba, K. Tamura, T. Takahashi, T. Kii, H. Ohgaki, and H. Toyokawa, Phys. Rev. C 72 (2005) 044004.

[138] W. Tornow, J. H. Kelley, R. Raut, G. Rusev, A. P. Tonchev, M. W. Ahmed, A. S. Crowell, and S. C. Stave, Phys. Rev. C 85 (2012) 061001.

[139] R. Raut, W. Tornow, M. W. Ahmed, A. S. Crowell, J. H. Kelley, G. Rusev, S. C. Stave, and A. P. Tonchev, Phys. Rev. Lett. 108 (2012) 042502.

[140] W. A. Wurtz, R. E. Pywell, B. E. Norum, S. Kucuker, B. D. Sawatzky, H. R. Weller, S. Stave, and M. W. Ahmed, Phys. Rev. C 90 (2014) 014613.

[141] T. Yamagata, S. Nakayama, H. Akimune, and S. Miyamoto, Phys. Rev. C 95 (2017) 044307.

[142] W. A. Wurtz, R. E. Pywell, B. E. Norum, S. Kucuker, B. D. Sawatzky, H. R. Weller, M. W. Ahmed, and S. Stave, Phys. Rev. C 84 (2011) 044601.

[143] W. A. Wurtz, R. E. Pywell, B. E. Norum, S. Kucuker, B. D. Sawatzky, H. R. Weller, S. Stave, and M. W. Ahmed, Phys. Rev. C 92 (2015) 044603.

[144] S. B. Gerasimov, Sov. J. Nucl. Phys. 2 (1966) 430.

[145] S. D. Drell and A. C. Hearn, Phys. Rev. Lett. 16 (1966) 908.

[146] S. Naito, Y. Nagai, T. Shima, H. Makii, K. Mishima, K. Tamura, H. Toyokawa, H. Ohgaki, J. Golak, R. Skibiński, H. Witała, W. Glöckle, A. Nogga, and H. Kamada, Phys. Rev. C 73 (2006) 034003.

[147] W. R. Zimmerman, M. W. Ahmed, B. Bromberger, S. C. Stave, A. Breskin, V. Dangendorf, T. Delbar, M. Gai, S. S. Henshaw, J. M. Mueller, C. Sun, K. Tittelmeier, H. R. Weller, and Y. K. Wu, Phys. Rev. Lett. 110 (2013) 152502.

[148] C. Ugalde, B. DiGiovine, D. Henderson, R. Holt, K. Rehm, A. Sonnenschein, A. Robinson, R. Raut, G. Rusev, and A. Tonchev, Phys. Lett. B 719 (2013) 74.

[149] M. Munch, C. Matei, S. D. Pain, M. T. Febbraro, K. A. Chipps, H. J. Karwowski, C. A. Diget, A. Pappalardo, S. Chesnevskaya, G. L. Guardo, D. Walter, D. L. Balabanski, F. D. Becchetti, C. R. Brune, K. Y. Chae, J. Frost-Schenk, M. J. Kim, M. S. Kwag, M. La Cognata, D. Lattuada, R. G. Pizzone, G. G. Rapisarda, G. V. Turturica, C. A. Ur, and Y. Xu, Phys. Rev. C 101 (2020) 055801.

[150] H. Utsunomiya, I. Gheorghe, D. M. Filipescu, T. Glodariu, S. Belyshev, K. Stopani, V. Varlamov, B. Ishkhanov, S. Katayama, D. Takenaka, T. Ari-izumi, S. Amano, and S. Miyamoto, Nucl. Instr. Meth. Phys. Res. A 871 (2017) 135.

[151] S. Agostinelli, J. Allison, K. Amako, J. Apostolakis, H. Araujo, P. Arce, M. Asai, D. Axen, S. Banerjee, G. Barrand, F. Behner, L. Bellagamba, J. Boudreau, and *et al.*, Nucl. Instr. Meth. Phys. Res. A 506 (2003) 250.

[152] R. Pywell, B. Sawatzky, J. Ives, N. Kolb, R. Igarashi, and W. Wurtz, Nucl. Instr. Meth. Phys. Res. A 565 (2006) 725.

[153] H. R. Weller, J. Langenbrunner, R. M. Chasteler, E. L. Tomusiak, J. Asai, R. G. Seyler, and D. R. Lehman, At. Data Nucl. Data Tables 50 (1992)(1) 29.

[154] K. Horikawa, S. Miyamoto, T. Mochizuki, S. Amano, D. Li, K. Imasaki, Y. Izawa, K. Ogata, S. Chiba, and T. Hayakawa, Phys. Lett. B 737 (2014) 109.

[155] A. Agodi, Nuovo Cim. 5 (1957) 21.

[156] J. M. Mueller, M. W. Ahmed, B. J. Davis, H. J. Karwowski, D. M. Markoff, L. S. Myers, M. C. Spraker, S. Stave, J. R. Tompkins, H. R. Weller, and W. R. Zimmerman, Phys. Rev. C 92 (2015) 034604.

[157] T. Hayakawa, T. Shizuma, S. Miyamoto, S. Amano, A. Takemoto, M. Yamaguchi, K. Horikawa, H. Akimune, S. Chiba, K. Ogata, and M. Fujiwara, Phys. Rev. C 93 (2016) 044313.

[158] J. M. Mueller, M. W. Ahmed, B. Davis, J. M. Hall, S. S. Henshaw, M. S. Johnson, H. J. Karwowski, D. Markoff, L. S. Myers, B. A. Perdue, S. Stave, J. R. Tompkins, M. J. Tuffley, and H. R. Weller, Phys. Rev. C 85 (2012) 014605.

[159] J. M. Mueller, M. W. Ahmed, R. H. France, M. S. Johnson, H. J. Karwowski, L. S. Myers, J. Randrup, M. H. Sikora, M. C. Spraker, S. Stave, J. R. Tompkins, R. Vogt, H. R. Weller, C. S. Whisnant, and W. R. Zimmerman, Phys. Rev. C 89 (2014) 034615.

[160] J. Mueller, M. Ahmed, and H. Weller, Nucl. Instr. Meth. Phys. Res. A 754 (2014) 57.

[161] E. Segrè and A. C. Helmholz, Rev. Mod. Phys. 21 (1949) 271.

[162] P. Cole, J. Farley, E. Reedy, R. Spaulding, J. Harmon, and D. Wells, Nucl. Instr. Meth. Phys. Res. B 261 (2007) 822.

[163] T. Hayakawa, S. Miyamoto, Y. Hayashi, K. Kawase, K. Horikawa, S. Chiba, K. Nakanishi, H. Hashimoto, T. Ohta, M. Kando, T. Mochizuki, T. Kajino, and M. Fujiwara, Phys. Rev. C 74 (2006) 065802.

[164] T. Hayakawa, T. Shizuma, S. Miyamoto, S. Amano, K. Horikawa, K. Ishihara, M. Mori, K. Kawase, M. Kando, N. Kikuzawa, S. Chiba, T. Mochizuki, T. Kajino, and M. Fujiwara, Phys. Rev. C 77 (2008) 068801.

[165] A. Tonchev and J. Harmon, Appl. Radiat. Isot. 52 (2000) 873.

[166] V. A. Zheltonozhsky and V. M. Mazur, Phys. At. Nucl. 63 (2000) 323.

[167] A. G. Belov, Y. P. Gangrsky, L. M. Melnikov, V. Y. Ponomarev, N. Tsoneva, C. Stoyanov, A.Tonchev, and N. Balabanov, Phys. At. Nucl. 64 (2001) 1901.

[168] V. A. Zheltonozhsky, V.M.Mazur, and Z. M. Bigan, Phys. At. Nucl. 67 (2004) 875.

[169] Y. P. Gangrsky, N. N. Kolesnikov, V. G. Lukashik, and L. M. Melnikova, Phys. At. Nucl. 67 (2004) 1227.

[170] T. D. Thiep, T. T. An, N. T. Vinh, P. V. Cuong, A. G. Belov, O. D. Maslov, and T. T. T. My, Phys. Part. Nucl. Lett. 3 (2006) 223.

[171] T. D. Thiep, T. T. An, N. T. Vinh, P. V. Cuong, A. G. Belov, O. D. Maslov, and T. T. T. My, Phys. Part. Nucl. Lett. 4 (2007) 397.

[172] T. D. Thiep, T. T. An, N. T. Khai, N. T. Vinh, P. V. Cuong, A. G. Belov, and O. D. Maslov, Phys. Part. Nucl. Lett. 6 (2009) 126.

[173] I. N. Vishnevsky, V. A. Zheltonozhsky, A. N. Savrasov, and N. V. Strilchuk, Phys. Rev. C 79 (2009) 014615.

[174] Y. P. Gangrsky, V. I.Zhemenik, N. N. Kolesnikov, V. G. Lukashik, B. N. Markov, G.V.Myshinskiy, O. D. Maslov, , and G. A. Bozhikov, Phys. At. Nucl. 73 (2010) 1477.

[175] V. M. Mazur, Z. M. Bigan, and D. M. Symochko, jpg 37 (2010) 035101.

[176] V. M. Mazur, D. M. Symochko, Z. M. Bigan, and T. V. Poltorzhytska, Phys. Rev. C 87 (2013) 044604.

[177] T. D. Thiep, T. T. An, P. V. Cuong, N. T. Vinh, B. M. Hue, A. G. Belov, and O. D. Maslov, J. Radioanal. Nucl. Chem. 299 (2014) 477.

[178] S. R. Palvanov, Phys. At. Nucl. 77 (2014) 35.

[179] I. N. Vishnevsky, V. A. Zheltonozhsky, A. N. Savrasov, and V. M. Mazur, Phys. At. Nucl. 79 (2016) 1381.

[180] T. D. Thiep, T. T. An, P. V. Cuong, N. T. Vinh, B. M. Hue, A. G. Belov, O. D. Maslov, G. V. Mishinsky, and V. I. Zhemenik, Phys. Part. Nucl. Lett. 14 (2017) 102.

[181] T. D. Thiep, T. T. An, P. V. Cuong, B. M. Hue, N. T. Vinh, A. G. Belov, and O. D. Maslov, J. Radioanal. Nucl. Chem. 314 (2017) 1777.

[182] T. D. Thiep, T. T. An, P. V. Cuong, N. T. Vinh, B. M. Hue, L. T. Anh, and A. G. Belov, J. Radioanal. Nucl. Chem. 317 (2018) 1263.

[183] V. Zheltonozhsky and A. M. Savrasov, Nucl. Instr. Meth. Phys. Res. B 438 (2019) 20.

[184] J. R. Huizenga and R. Vandenbosch, Phys. Rev. 120 (1960) 1305.

[185] R. Vandenbosch and J. R. Huizenga, Phys. Rev. 120 (1960) 1313.

[186] D. M. Brink, Ph.D thesis, Oxford University (1955).

[187] *NEA Evaluated Nuclear Data Library*, https://www.oecd-nea.org/jcms/pl_20505/evaluated-nuclear-data-library-descriptions, accessed: 2021-04-07.

[188] Z. Bao, H. Beer, F. Käppeler, F. Voss, K. Wisshak, and T. Rauscher, At. Data Nucl. Data Tables 76 (2000) 70.

[189] R. O. Haxby, W. E. Shoupp, W. E. Stephens, and W. H. Wells, Phys. Rev. 58 (1940) 92.

[190] R. O. Haxby, W. E. Shoupp, W. E. Stephens, and W. H. Wells, Phys. Rev. 59 (1941) 57.

[191] A. N. Andreyev, K. Nishio, and K.-H. Schmidt, Rep. Prog. Phys. 81 (2017) 016301.

[192] K.-H. Schmidt and B. Jurado, Rep. Prog. Phys. 81 (2018) 106301.

[193] P. Möller, D. Madland, A. Sierk, and A. Iwamoto, Nature 409 (2001) 785.

[194] K.-H. Schmidt, B. Jurado, C. Amouroux, and C. Schmitt, Nucl. Data Sheets 131 (2016) 107.

[195] S. A. Karamian, J. Adam, A. G. Belov, Y. V. Norseev, V. I. Stegailov, and P. Chaloun, Phys. At. Nucl. 63 (2000) 787.

[196] S. A. Karamian, J. Adam, A. G. Belov, J. J. Carroll, Y. V. Norseev, V. I. Stegailov, and P. Chaloun, Phys. Rev. C 62 (2000) 024601.

[197] Y. P. Gangrsky, V. I. Zhemenik, N. Y. Maslova, G. V. Mishinsky, Y. E. Penionzhkevich, and O. Szöllös, Phys. At. Nucl. 66 (2003) 1211.

[198] Y. P. Gangrsky, V. I. Zhemenik, G. V. Mishinsky, and Y. E. Penionzhkevich, Phys. At. Nucl. 68 (2005) 1417.

[199] H. Naik, F. Carrel, G. N. Kim, F. Laine, A. Sari, S. Normand, and A. Goswami, Eur. Phys. J. A 49 (2013) 94.

[200] H. Naik, G. N. Kim, R. Schwengner, K. Kim, R. John, R. Massarczyk, A. Junghans, A. Wagner, and A. Goswami, Eur. Phys. J. A 51 (2015) 150.

[201] S. S. Belyshev, B. S. Ishkhanov, A. A. Kuznetsov, and K. A. Stopani, Phys. Rev. C 91 (2015) 034603.

[202] M. Bhike, W. Tornow, Krishichayan, and A. P. Tonchev, Phys. Rev. C 95 (2017) 024608.

[203] Krishichayan, M. Bhike, C. R. Howell, A. P. Tonchev, and W. Tornow, Phys. Rev. C 100 (2019) 014608.

[204] Krishichayan, M. Bhike, S. Finch, C. Howell, A. Tonchev, and W. Tornow, Nucl. Instr. Meth. Phys. Res. A 854 (2017) 40.

[205] Krishichayan, S. W. Finch, C. R. Howell, A. P. Tonchev, and W. Tornow, Phys. Rev. C 98 (2018) 014608.

[206] A. Göök, M. Chernykh, C. Eckardt, J. Enders, P. von Neumann-Cosel, A. Oberstedt, S. Oberstedt, and A. Richter, Nucl. Phys. 851 (2011) 1.

[207] A. Göök, C. Eckardt, J. Enders, M. Freudenberger, A. Oberstedt, and S. Oberstedt, Phys. Rev. C 96 (2017) 044301.

[208] H. W. Schmitt, J. H. Neiler, and F. J. Walter, Phys. Rev. 141 (1966) 1146.

[209] A. Göök, M. Chernykh, J. Enders, A. Oberstedt, and S. Oberstedt, Nucl. Instr. Meth. Phys. Res. A 621 (2010) 401.

[210] V. Denyak, V. Khvastunov, S. Paschuk, and H. Schelin, Eur. Phys. J. A 49 (2013) 51.

[211] G. Roche, C. Ducos, and J. Proriol, Phys. Rev. A 5 (1972) 2403.

[212] G. Desobry and A. Boyer, Med. Phys. 18 (1991) 497.

[213] E. Haug, Radiat. Phys. Chem. 77 (2008) 207.

[214] S. Lindenstruth, A. Degener, R. Heil, A. Jung, U. Kneissl, J. Margraf, H. Pitz, H. Schacht, U. Seemann, R. Stock, and C. Wesselborg, Nucl. Instr. Meth. Phys. Res. A 300 (1991) 293.

[215] R. Schwengner, R. Beyer, F. Dönau, E. Grosse, A. Hartmann, A. Junghans, S. Mallion, G. Rusev, K. Schilling, W. Schulze, and A. Wagner, Nucl. Instr. and Meth. A 555 (2005) 211.

[216] K. Kosaka, K. Oishi, T. Nakamura, M. Takada, K. Sato, T. Kamiyama, and Y. Kiyanagi, J. Nucl. Sci. Tech. 47 (2010) 286.

[217] M. May and G. C. Wick, Phys. Rev. 81 (1951) 628.

[218] R. Schwengner, G. Rusev, N. Benouaret, R. Beyer, M. Erhard, E. Grosse, A. R. Junghans, J. Klug, K. Kosev, L. Kostov, C. Nair, N. Nankov, K. D. Schilling, and A. Wagner, Phys. Rev. C 76 (2007) 034321.

[219] M. Huber, P. von Neumann-Cosel, A. Richter, C. Schlegel, R. Schulz, J. J. Carroll, K. N. Taylor, D. G. Richmond, T. W. Sinor, C. B. Collins, and V. Ponomarev, Nucl. Phys. A 559 (1993) 253.

[220] P. Mohr, J. Enders, T. Hartmann, H. Kaiser, D. Schiesser, S. Schmitt, S. Volz, F. Wissel, and A. Zilges, Nucl. Instr. Meth. Phys. Res. A 423 (1999) 480.

[221] K. Sonnabend, D. Savran, J. Beller, M. A. Büssing, A. Constantinescu, M. Elvers, J. Endres, M. Fritzsche, J. Glorius, J. Hasper, J. Isaak, B. Löher, S. Müller, N. Pietralla, C. Romig, A. Sauerwein, L. Schnorrenberger, C. Wälzlein, A. Zilges, and M. Zweidinger, Nucl. Instr. Meth. Phys. Res. A 640 (2011) 6.

[222] *Flerov laboratory of nuclear reactions*, http://flerovlab.jinr.ru/, accessed: 2021-01-22.

[223] T. D. Thiep, T. T. An, N. T. Khai, N. T. Vinh, P. V. Cuong, I. P. Gangrski, A. G. Belov, and O. D. Maslov, Phys. Part. Nucl. Lett. 9 (2012) 648.

[224] V. I. Zagrebaev, Y. Teterev, G. V. Mishinsky, V. I. Zhemenik, S. L. Bogomolov, A. G. Belov, S. V. Mitrofanov, and S. N. Dmitriev, Nucl. Instr. Meth. Phys. Res. B 336 (2014) 74.

[225] D. Testov, *Mt-25 dubna* (2021), private communication.

[226] M. Králík, J. Šolc, D. Chvátil, P. Krist, K. Turek, and C. Granja, Rev. Sci. Instr. 83 (2012) 083502.

[227] *Accelerating new discoveries in nuclear physics*, https://www.llnl.gov/news/accelerating-new-discoveries-nuclear-physics, accessed: 2021-01-22.

[228] A. Tonchev, *Photonuclear capabilities at LLNL using PRISM accelerator* (2021), private communication.

[229] B. Quiter (2021), private communication.

[230] W. Bertozzi, J. A. Caggiano, W. K. Hensley, M. S. Johnson, S. E. Korbly, R. J. Ledoux, D. P. McNabb, E. B. Norman, W. H. Park, and G. A. Warren, Phys. Rev. C 78 (2008) 041601.

[231] B. J. Quiter, T. Laplace, B. A. Ludewigt, S. D. Ambers, B. L. Goldblum, S. Korbly, C. Hicks, and C. Wilson, Phys. Rev. C 86 (2012) 034307.

[232] *National Science Center Kharkov Institute of Physics and Technology*, https://www.kipt.kharkov.ua/en/, accessed: 2021-01-22.

[233] A. Vodin (2021), private communication and to be published.

[234] *The Idaho Accelerator Center*, https://www.isu.edu/physics/facilities–research/idaho-accelerator-center-iac/, accessed: 2021-01-22.

[235] J. Stoner (2021), private communication.

[236] D. P. Wells, C. R. Segebade, and P. L. Cole, AIP Conf. Proc. 1265 (2010) 379.

[237] A. Aksoy, Ö. F. Elçim, Ö. Karslı, Ç. Kaya, and İ. B. Koç, Proc. of FEL2019, Hamburg, Germany 39 (2019) 102.

[238] *Turkish Accelerator and Radiation Facility (TARLA)*, https://tarla.org.tr/facility/, accessed: 2021-01-22.

[239] H. Dapo, *The NRF setup at TARLA* (2021), private communication.

[240] E. Hayward, *Photonuclear Reactions*, Monograph, U.S. National Bureau of Standards (1970).

[241] D. Savran, K. Lindenberg, J. Glorius, B. Löher, S. Müller, N. Pietralla, L. Schnorrenberger, V. Simon, K. Sonnabend, C. Wälzlein, M. Elvers, J. Endres, J. Hasper, and A. Zilges, Nucl. Instr. Meth. Phys. Res. A 613 (2010) 232.

[242] N. Pietralla, Nucl. Phys. News 28 (2018) 4.

[243] L. Schnorrenberger, D. Savran, J. Glorius, K. Lindenberg, B. Löher, N. Pietralla, and K. Sonnabend, Nucl. Instr. Meth. Phys. Res. A 735 (2014) 19 .

[244] M. Gascón, L. Schnorrenberger, B. Pietras, H. Álvarez-Pol, D. Cortina-Gil, P. D. Fernández, I. Duran, J. Glorius, D. González, D. Perez-Loureiro, N. Pietralla, D. Savran, and K. Sonnabend, J. Instr. 8 (2013) P10004.

[245] J. Arends, J. Eyink, A. Hegerath, B. Mecking, and H. Rost, Nucl. Instr. and Meth. 201 (1982) 361.

[246] J. D. Kellie, I. Anthony, S. J. Hall, I. J. D. MacGregor, A. McPherson, P. J. Thorley, S. L. Wan, and F. Zettl, Nucl. Instr. Meth. Phys. Res. A 241 (1985) 153.

[247] T. Terasawa, K. Mori, Y. Fujii, T. Suda, I. Nomura, O. Konno, T. Ichinohe, Y. Torizuka, K. Maeda, P. D. Harty, G. J. O'Keefe, and M. N. Thompson, Nucl. Instr. Meth. Phys. Res. A 248 (1986) 429.

[248] S. N. Dancer, I. J. D. MacGregor, J. R. M. Annand, I. Anthony, G. I. Crawford, S. J. Hall, J. D. Kellie, J. C. McGeorge, R. O. Owens, P. A. Wallace, D. Branford, S. V. Springham, A. C. Shotter, B. Schoch, J. M. Vogt, R. Beck, and G. Liesenfeld, Phys. Rev. Lett. 61 (1988) 1170.

[249] R. Gothe, W. Lang, S. Klein, B. Schoch, V. Metag, H. Ströher, S. Hall, and R. Owens, Phys. Lett. B 355 (1995) 59.

[250] C. J. Y. Powrie, J. C. McGeorge, I. J. D. MacGregor, J. Ahrens, J. R. M. Annand, J. F. Arneil, R. Beck, D. Branford, S. Franczuk, D. I. Glazier, P. Grabmayr, S. J. Hall, T. Hehl, P. D. Harty, D. G. Ireland, J. D. Kellie, K. Livingston, F. A. Natter, S. Oberkirsch, R. O. Owens, J. Ryckebusch, M. Sauer, A. Settele, and D. P. Watts, Phys. Rev. C 64 (2001) 034602.

[251] J. C. McGeorge, J. D. Kellie, J. R. M. Annand, J. Ahrens, I. Anthony, A. Clarkson, D. J. Hamilton, P. S. Lumsden, E. F. McNicoll, R. O. Owens, G. Rosner, and A. Thomas, Eur. Phys. J. A 37 (2008) 129.

[252] J. Robinson, I. J. D. MacGregor, J. R. M. Annand, P. Aguar-Bartolomé, L. K. Akasoy, H. J. Arends, Y. I. Azimov, K. Bantawa, R. Beck, V. S. Bekrenev, H. Berghäuser, A. Braghieri, D. Branford, W. J. Briscoe, J. Brudvik, S. Cherepnya, R. F. B. Codling, B. T. Demissie, M. Dieterle, E. J. Downie, P. Drexler, L. V. Fil'kov, D. I. Glazier, R. Gregor, D. Hamilton, E. Heid, D. Hornidge, D. Howdle, O. Jahn, T. C. Jude, V. L. Kashevarov, I. Keshelashvili, R. Kondratiev, M. Korolija, M. Kotulla, A. A. Koulbardis, S. P. Kruglov, B. Krusche, V. Lisin, K. Livingston, D. M. Manley, J. C. McGeorge, E. F. McNicoll, V. Metag, D. G. Middleton, A. Mushkarenkov, B. M. K. Nefkens, A. Nikolaev, R. Novotny, M. Oberle, M. Ostrick, R. O. Owens, P. B. Otte, B. Oussena, P. Pedroni, A. Polonski, S. Prakhov, G. Rosner, T. Rostomyan, S. Schumann, M. H. Sikora, D. I. Sober, A. Starostin, I. I. Strakovsky, I. M. Suarez, I. Supek, C. M. Tarbert, M. Thiel, A. Thomas, M. Unverzagt, D. P. Watts, D. Werthmueller, and L. Witthauer, Eur. Phys. J. A 49 (2013) 65.

[253] I. D. MacGregor, SciPost Phys. Proc. 3 (2020) 010.

[254] C. Sun and Y. K. Wu, Phys. Rev. ST Accel. Beams 14 (2011) 044701.

[255] C. Sun, J. Li, G. Rusev, A. P. Tonchev, and Y. K. Wu, Phys. Rev. ST Accel. Beams 12 (2009) 062801.

[256] V. N. Litvinenko and J. M. J. Madey, in P. M. Rentzepis, editor, *Time-Resolved Electron and X-Ray Diffraction*, volume 2521, pages 55 – 77, International Society for Optics and Photonics, SPIE (1995).

[257] H. R. Weller, M. W. Ahmed, and Y. K. Wu, Nucl. Phys. News 25 (2015) 19.

[258] H. Zen, Y. Taira, T. Konomi, T. Hayakawa, T. Shizuma, J. Yamazaki, T. Kii, H. Toyokawa, M. Katoh, and H. Ohgaki, Energy Procedia 89 (2016) 335.

[259] H. Wang and F. Gongtao (2021), Shanghai Advanced Research Institute (SARI), private communication.

[260] C. R. Howell, M. W. Ahmed, A. Afanasev, D. Alesini, J. R. M. Annand, A. Aprahamian, D. L. Balabanski, S. V. Benson, A. Bernstein, C. R. Brune, J. Byrd, B. E. Carlsten, A. E. Champagne, S. Chattopadhyay, D. Davis, E. J. Downie, M. J. Durham, G. Feldman, H. Gao, C. G. R. Geddes, H. W. Griesshammer, R. Hajima, H. Hao, D. Hornidge, J. Isaak, R. V. F. Janssens, D. P. Kendellen, M. A. Kovash, P. P. Martel, U.-G. Meissner, R. Miskimen, B. Pasquini, D. R. Phillips, N. Pietralla, D. Savran, M. R. Schindler, M. H. Sikora, W. M. Snow, R. P. Springer, C. Sun, C. Tang, B. Tiburzi, A. P. Tonchev, W. Tornow, C. A. Ur, D. Wang, H. R. Weller, V. Werner, Y. K. Wu, J. Yan, Z. Zhao, A. Zilges, and F. Zomer, *International workshop on next generation gamma-ray source* (2020).

[261] Lyncean Technologies (2021), Fremont, USA, private communication.

[262] G. Turturica, C. Matei, A. Pappalardo, D. Balabanski, S. Chesnevskaya, V. Iancu, C. Ur, H. Karwowski, K. Chipps, M. Febbraro, S. Pain, D. Walter, C. Diget, J. Frost-Schenk, M. Munch, G. Guardo, M. La Cognata, R. Pizzone, G. Rapisarda, K. Chae, M. Kim, and M. Kwag, Nucl. Instr. Meth. Phys. Res. A 921 (2019) 27.

[263] R. Pywell, O. Mavrichi, W. Wurtz, and R. Wilson, Nucl. Instr. Meth. Phys. Res. A 606 (2009) 517.

[264] O. Klein and Y. Nishina, Z. Phys. 52 (1929) 853.

[265] H. Utsunomiya, T. Shima, K. Takahisa, D. M. Filipescu, O. Tesileanu, I. Gheorghe, H. Nyhus, T. Renstrøm, Y. Lui, Y. Kitagawa, S. Amano, and S. Miyamoto, IEEE Trans. Nucl. Sc. 61 (2014) 1252.

[266] K. Horikawa, S. Miyamoto, S. Amano, and T. Mochizuki, Nucl. Instr. Meth. Phys. Res. A 618 (2010) 209.

[267] H. Toyokawa, T. Kii, H. Ohgaki, T. Shima, T. Baba, and Y. Nagai, IEEE Trans. Nucl. Sc. 47 (2000) 1954.

[268] T. Kondo, H. Utsunomiya, H. Akimune, T. Yamagata, A. Okamoto, H. Harada, F. Kitatani, T. Shima, K. Horikawa, and S. Miyamoto, Nucl. Instr. Meth. Phys. Res. A 659 (2011) 462.

[269] B. Löher, PhD thesis, University Mainz, http://ubm.opus.hbz-nrw.de/volltexte/2014/3819/ (2014).

[270] B. L. Berman, J. T. Caldwell, R. R. Harvey, M. A. Kelly, R. L. Bramblett, and S. C. Fultz, Phys. Rev. 162 (1967) 1098.

[271] L. East and R. Walton, Nucl. Instr. and Meth. 72 (1969) 161.

[272] H. Schmitt, Nucl. Phys. 20 (1960) 220.

[273] C. Arnold, T. Clegg, H. Karwowski, G. Rich, J. Tompkins, and C. Howell, Nucl. Instr. Meth. Phys. Res. A 647 (2011) 55.

[274] J. A. Silano and H. J. Karwowski, Phys. Rev. C 98 (2018) 054609.

[275] O. Itoh, H. Utsunomiya, H. Akimune, T. Kondo, M. Kamata, T. Yamagata, H. Toyokawa, H. Harada, F. Kitatani, S. Goko, C. Nair, and Y. Lui, J. Nucl. Sc. Tech. 48 (2011) 834.

[276] A. Tarifeño-Saldivia, J. Tain, C. Domingo-Pardo, F. Calviño, G. Cortés, V. Phong, A. Riego, J. Agramunt, A. Algora, N. Brewer, R. Caballero-Folch, P. Coleman-Smith, T. Davinson, I. Dillmann, A. Estradé, C. Griffin, R. Grzywacz, L. Harkness-Brennan, G. Kiss, M. Kogimtzis, M. Labiche, I. Lazarus, G. Lorusso, K. Matsui, K. Miernik, F. Montes, A. Morales, S. Nishimura, R. Page, Z. Podolyák, V. Pucknell, B. Rasco, P. Regan, B. Rubio, K. Rykaczewski, Y. Saito, H. Sakurai, J. Simpson, E. Sokol, R. Surman, A. Svirkhin, S. Thomas, A. Tolosa, and P. Woods, J. Instr. 12 (2017) P04006.

[277] F. Camera, H. Utsunomiya, V. Varlamov, D. Filipescu, V. Baran, A. Bracco, G. Colo, I. Gheorghe, T. Glodariu, C. Matei, and O. Wieland, Rom. Rep. Phys. 68 (2016) S539.

[278] M. Krzysiek, F. Camera, D. Filipescu, H. Utsunomiya, G. Colò, I. Gheorghe, and Y. Niu, Nucl. Instr. Meth. Phys. Res. A 916 (2019) 257.

[279] P.-A. Söderström, L. Capponi, V. Iancu, D. Lattuada, A. Pappalardo, G. Turturică, E. Açıksöz, D. Balabanski, P. Constantin, G. Guardo, M. Ilie, S. Ilie, C. Matei, D. Nichita, T. Petruse, and A. Spataru, J. Instr. 14 (2019) T11007.

[280] H. Laurent, H. Lefort, D. Beaumel, Y. Blumenfeld, S. Fortier, S. Gales, J. Guillot, J. Roynette, P. Volkov, and S. Brandenburg, Nucl. Instr. Meth. Phys. Res. A 326 (1993) 517.

[281] M. Cavallaro, S. Tropea, C. Agodi, M. Assie, F. Azaiez, C. Boiano, M. Bondì, F. Cappuzzello, D. Carbone, M. De Napoli, N. de Séréville, A. Foti, R. Linares, D. Nicolosi, and J. Scarpaci, Nucl. Instr. Meth. Phys. Res. A 700 (2013) 65.

[282] D. W. Bardayan, J. C. Blackmon, W. Bradfield-Smith, C. R. Brune, A. E. Champagne, T. Davinson, B. A. Johnson, R. L. Kozub, C. S. Lee, R. Lewis, P. D. Parker, A. C. Shotter, M. S. Smith, D. W. Visser, and P. J. Woods, Phys. Rev. C 63 (2001) 065802.

[283] *Silicon Detector Catalogue, Micron Semiconductor Ltd.*, http://www.micronsemiconductor.co.uk, accessed: 2021-04-07.

[284] O. Tesileanu, M. Gai, A. Anzalone, C. Balan, J. Bihalowicz, M. Cwiok, W. Dominik, S. Gales, D. Ghita, Z. Janas, D. Kendellen, M. La Cognata, C. Matei, K. Mikszuta, C. Petcu, M. Pfützner, T. Matulewicz, C. Mazzocchi, and C. Spitaleri, Rom. Rep. Phys. 68 (2016) S699–S734.

[285] S. Chesnevskaya, D. Balabanski, D. Choudhury, P. Constantin, D. Filipescu, D. Ghita, G. Guardo, D. Lattuada, C. Matei, A. Rotaru, and A. State, J. Instr. 13 (2018) T05006.

[286] D. Bazin, T. Ahn, Y. Ayyad, S. Beceiro-Novo, A. Macchiavelli, W. Mittig, and J. Randhawa, Prog. Part. Nucl. Phys. 114 (2020) 103790.

[287] M. Gai, M. W. Ahmed, S. C. Stave, W. R. Zimmerman, A. Breskin, B. Bromberger, R. Chechik, V. Dangendorf, T. Delbar, R. H. France, S. S. Henshaw, T. J. Kading, P. P. Martel, J. E. R. McDonald, P. N. Seo, K. Tittelmeier, H. R. Weller, and A. H. Young, J. Instr. 5 (2010) P12004.

[288] M. Gai, D. Schweitzer, S. Stern, A. Young, R. Smith, M. Cwiok, J. Bihalowicz, H. Czyrkowski, R. Dabrowski, W. Dominik, A. Fijalkowska, Z. Janas, L. Janiak, A. Korgul, T. Matulewicz, C. Mazzocchi, M. Pfützner, M. Zaremba, D. Balabanski, I. Gheorghe, C. Matei, O. Tesileanu, N. Zamfir, M. Ahmed, S. Henshaw, C. Howell, J. Mueller, L. Myers, S. Stave, C. Sun, H. Weller, Y. Wu, A. Breskin, V. Dangendorf, K. Tittelmeier, and M. Freer, Nucl. Instr. Meth. Phys. Res. A 954 (2020) 161779.

[289] U. Titt, A. Breskin, R. Chechik, V. Dangendorf, H. Schmidt-Böcking, and H. Schuhmacher, Nucl. Instr. Meth. Phys. Res. A 416 (1998) 85.

[290] K. Miernik, W. Dominik, H. Czyrkowski, R. Dabrowski, A. Fomitchev, M. Golovkov, Z. Janas, W. Kusmierz, M. Pfützner, A. Rodin, S. Stepantsov, R. Slepniev, G. Ter-Akopian, and R. Wolski, Nucl. Instr. Meth. Phys. Res. A 581 (2007) 194.

[291] R. Smith, M. Gai, M. W. Ahmed, M. Freer, H. O. U. Fynbo, D. Schweitzer, and S. R. Stern, Phys. Rev. C 101 (2020) 021302.

[292] F. Sauli, Nucl. Instr. Meth. Phys. Res. A 386 (1997) 531.

[293] F. Sauli, Nucl. Instr. Meth. Phys. Res. A 805 (2016) 2.

[294] M. Cwiok, M. Bieda, J. Bihalowicz, W. Dominik, Z. Janas, L. Janiak, J. Manczak, T. Matulewicz, C. Mazzocchi, M. Pfützner, P. Podlaski, S. Sharma, M. Zaremba, D. Balabanski, A. Bey, D. Ghita, O. Tesileanu, and M. Gai, Acta Phys. Pol. B 49 (2018) 509.

[295] E. Pollacco, S. Anvar, H. Baba, P. Baron, D. Bazin, C. Belkhiria, B. Blank, J. Chavas, P. Chomaz, E. Delagnes, F. Druillole, P. Hellmuth, C. Huss, E. Galyaev, B. Lynch, W. Mittig, T. Murakami, L. Nalpas, J.-L. Pedroza, R. Raabe, J. Pibernat, B. Raine, A. Rebii, A. Taketani, F. Saillant, D. Suzuki, N. Usher, and G. Wittwer, Phys. Procedia 37 (2012) 1799.

[296] T. Kii, T. Shima, T. Baba, and Y. Nagai, Nucl. Instr. Meth. Phys. Res. A 552 (2005) 329.

[297] B. DiGiovine, D. Henderson, R. Holt, R. Raut, K. Rehm, A. Robinson, A. Sonnenschein, G. Rusev, A. Tonchev, and C. Ugalde, Nucl. Instr. Meth. Phys. Res. A 781 (2015) 96.

[298] C. Budtz-Jorgensen, H.-H. Knitter, C. Straede, F.-J. Hambsch, and R. Vogt, Nucl. Instr. Meth. Phys. Res. A 258 (1987) 209.

[299] L. Gaudefroy, T. Roger, J. Pancin, C. Spitaels, J. Aupiais, and J. Mottier, Nucl. Instr. Meth. Phys. Res. A 855 (2017) 133.

[300] A. Göök, W. Geerts, F.-J. Hambsch, S. Oberstedt, M. Vidali, and S. Zeynalov, Nucl. Instr. Meth. Phys. Res. A 830 (2016) 366.

[301] R. J. W. Frost and A. G. Smith, Int. J. Mod. Phys. Conf. Series 44 (2016) 1660231.

[302] A. B. Migdal, J. Phys. (USSR) 8 (1944) 331.

[303] M. N. Harakeh and A. van der Woude, *Giant Resonances: Fundamental High-Frequency Modes of Nuclear Excitation*, Oxford University Press (2001).

[304] P. Bortignon, A. Bracco, and R. Broglia, *Giant Resonances: Nuclear Structure at Finite Temperature*, CRC Press (1998).

[305] B. L. Berman and S. C. Fultz, Rev. Mod. Phys. 47 (1975) 713.

[306] B. S. Ishkhanov, V. N. Orlin, N. N. Peskov, and V. V. Varlamov, Phys. Part. Nucl. 48 (2017) 76.

[307] H. Harada, Y. Shigetome, H. Ohgaki, T. Noguchi, and T. Yamazaki, Phys. Rev. Lett. 80 (1998) 33.

[308] S. S. Henshaw, M. W. Ahmed, G. Feldman, A. M. Nathan, and H. R. Weller, Phys. Rev. Lett. 107 (2011) 222501.

[309] V. A. Plujko, O. M. Gorbachenko, R. Capote, and P. Dimitriou, At. Data Nucl. Data Tables 123–124 (2018) 1.

[310] R. Pitthan, F. R. Buskirk, E. B. Dally, J. N. Dyer, and X. K. Maruyama, Phys. Rev. Lett. 33 (1974) 849.

[311] D. S. Dale, R. M. Laszewski, and R. Alarcon, Phys. Rev. Lett. 68 (1992) 3507.

[312] H. R. Weller, M. W. Ahmed, J. M. Mueller, L. S. Myers, W. R. Zimmerman, G. Feldman, and M. H. Sikora, Acta Phys. Pol. B 44 (2013) 587.

[313] F. Iachello, Phys. Lett. B 160 (1985) 1.

[314] M. Spieker, S. Pascu, A. Zilges, and F. Iachello, Phys. Rev. Lett. 114 (2015) 192504.

[315] I. Tanihata, J. Phys. G 22 (1996) 157.

[316] G. A. Bartholomew, Annu. Rev. Nucl. Sci. 11 (1961) 259.

[317] J. S. Brzosko, E. Gierlik, A. Soltan, and Z. Wilhelmi, Can. J. Phys. 47 (1969) 2849.

[318] R. M. Laszewski and P. Axel, Phys. Rev. C 19 (1979) 342.

[319] A. Bracco, E. G. Lanza, and A. Tamii, Prog. Part. Nucl. Phys. 106 (2019) 360.

[320] D. Savran, T. Aumann, and A. Zilges, Prog. Part. Nucl. Phys. 70 (2013) 210.

[321] R. Mohan, M. Danos, and L. C. Biedenharn, Phys. Rev. C 3 (1971) 1740.

[322] N. Alamanos, R. A. Broglia, and E. Vigezzi, Eur. Phys. J. A 55 (2019) 221.

[323] R.-D. Herzberg, P. von Brentano, J. Eberth, J. Enders, R. Fischer, N. Huxel, T. Klemme, P. von Neumann-Cosel, N. Nicolay, N. Pietralla, V. Y. Ponomarev, J. Reif, A. Richter, C. Schlegel, R. Schwengner, S. Skoda, H. G. Thomas, I. Wiedenhöver, G. Winter, and A. Zilges, Phys. Lett. B 390 (1997) 49.

[324] A. Zilges, S. Volz, M. Babilon, T. Hartmann, P. Mohr, and K. Vogt, Phys. Lett. B 542 (2002) 43.

[325] T. Shizuma, F. Minato, M. Omer, T. Hayakawa, H. Ohgaki, and S. Miyamoto, Phys. Rev. C 103 (2021) 024309.

[326] J. Wilhelmy, M. Müscher, G. Rusev, R. Schwengner, R. Beyer, M. Bhike, P. Erbacher, F. Fiedler, U. Friman-Gayer, J. Glorius, R. Greifenhagen, S. Hammer, T. Hensel, J. Isaak, A. R. Junghans, Krishichayan, B. Löher, S. E. Müller, N. Pietralla, S. Reinicke, D. Savran, P. Scholz, K. Sonnabend, T. Szücs, M. Tamkas, W. Tornow, S. Turkat, A. Wagner, and A. Zilges, Phys. Rev. C 102 (2020) 044327.

[327] H. K. Toft, A. C. Larsen, A. Bürger, M. Guttormsen, A. Görgen, H. T. Nyhus, T. Renstrøm, S. Siem, G. M. Tveten, and A. Voinov, Phys. Rev. C 83 (2011) 044320.

[328] D. Savran and J. Isaak, Nucl. Instr. Meth. Phys. Res. A 899 (2018) 28.

[329] D. Savran, M. Babilon, A. M. van den Berg, M. N. Harakeh, J. Hasper, A. Matic, H. J. Wörtche, and A. Zilges, Phys. Rev. Lett. 97 (2006) 172502.

[330] M. Spieker, A. Heusler, B. A. Brown, T. Faestermann, R. Hertenberger, G. Potel, M. Scheck, N. Tsoneva, M. Weinert, H.-F. Wirth, and A. Zilges, Phys. Rev. Lett. 125 (2020) 102503.

[331] P. Adrich, A. Klimkiewicz, M. Fallot, K. Boretzky, T. Aumann, D. Cortina-Gil, U. Datta Pramanik, Th. W. Elze, H. Emling, H. Geissel, M. Hellström, K. L. Jones, J. V. Kratz, R. Kulessa, Y. Leifels, C. Nociforo, R. Palit, H. Simon, G. Surowka, K. Sümmerer, and W. Walus, Phys. Rev. Lett. 95 (2005) 132501.

[332] O. Wieland, A. Bracco, F. Camera, G. Benzoni, N. Blasi, S. Brambilla, F. C. L. Crespi, S. Leoni, B. Million, R. Nicolini, A. Maj, P. Bednarczyk, J. Grebosz, M. Kmiecik, W. Meczynski, J. Styczen, T. Aumann, A. Banu, T. Beck, F. Becker, L. Caceres, P. Doornenbal, H. Emling, J. Gerl, H. Geissel, M. Gorska, O. Kavatsyuk, M. Kavatsyuk, I. Kojouharov, N. Kurz, R. Lozeva, N. Saito, T. Saito, H. Schaffner, H. J. Wollersheim, J. Jolie, P. Reiter, N. Warr, G. deAngelis, A. Gadea, D. Napoli, S. Lenzi, S. Lunardi, D. Balabanski, G. LoBianco, C. Petrache, A. Saltarelli, M. Castoldi, A. Zucchiatti, J. Walker, and A. Bürger, Phys. Rev. Lett. 102 (2009) 092502.

[333] T. Aumann, Eur. Phys. J. A 55 (2019) 234.

[334] F. R. Metzger, Phys. Rev. C 11 (1975) 2085.

[335] M. Babilon, W. Bayer, D. Galaviz, T. Hartmann, C. Hutter, P. Mohr, W. Rochow, K. Sonnabend, K. Vogt, S. Volz, and A. Zilges, Phys. Rev. C 66 (2002) 028801.

[336] W. Andrejtscheff, C. Kohstall, P. von Brentano, C. Fransen, U. Kneissl, N. Pietralla, and H. H. Pitz, Phys. Lett. B 506 (2001) 239.

[337] V. Derya, N. Tsoneva, T. Aumann, M. Bhike, J. Endres, M. Gooden, A. Hennig, J. Isaak, H. Lenske, B. Löher, N. Pietralla, D. Savran, W. Tornow, V. Werner, and A. Zilges, Phys. Rev. C 93 (2016) 034311.

[338] D. Bandyopadhyay, C. C. Reynolds, S. R. Lesher, C. Fransen, N. Boukharouba, M. T. McEllistrem, and S. W. Yates, Phys. Rev. C 68 (2003) 014324.

[339] M. Wilhelm, E. Radermacher, A. Zilges, and P. von Brentano, Phys. Rev. C 54 (1996) 449(R).

[340] A. Zilges, R.-D. Herzberg, P. von Brentano, F. Dönau, R. D. Heil, R. V. Jolos, U. Kneissl, J. Margraf, H. H. Pitz, and C. Wesselborg, Phys. Rev. Lett. 70 (1993) 2880.

[341] J. Bryssinck, L. Govor, F. Bauwens, D. Belic, P. von Brentano, D. De Frenne, C. Fransen, A. Gade, E. Jacobs, U. Kneissl, C. Kohstall, A. Linnemann, A. Nord, N. Pietralla, H. H. Pitz, M. Scheck, F. Stedile, and V. Werner, Phys. Rev. C 65 (2002) 024313.

[342] M. Scheck, H. von Garrel, N. Tsoneva, D. Belic, P. von Brentano, C. Fransen, A. Gade, J. Jolie, U. Kneissl, C. Kohstall, A. Linnemann, A. Nord, N. Pietralla, H. H. Pitz, F. Stedile, C. Stoyanov, and V. Werner, Phys. Rev. C 70 (2004) 044319.

[343] M. Scheck, P. v. Brentano, C. Fransen, U. Kneissl, C. Kohstall, A. Linnemann, D. Mücher, N. Pietralla, H. H. Pitz, C. Scholl, F. Stedile, S. Walter, V. Werner, and S. W. Yates, Phys. Rev. C 75 (2007) 044313.

[344] U. Kneissl, A. Zilges, J. Margraf, I. Bauske, P. von Brentano, H. Friedrichs, R. D. Heil, R.-D. Herzberg, H. H. Pitz, B. Schlitt, and C. Wesselborg, Phys. Rev. Lett. 71 (1993) 2180.

[345] C. Fransen, N. Pietralla, P. von Brentano, A. Dewald, J. Gableske, A. Gade, A. Lisetskiy, and V. Werner, Phys. Lett. B 508 (2001) 219.

[346] K. Heyde, P. von Neumann-Cosel, and A. Richter, Rev. Mod. Phys. 82 (2010) 2365.

[347] D. Bohle, A. Richter, W. Steffen, A. E. L. Dieperink, N. L. Iudice, F. Palumbo, and O. Scholten, Phys. Lett. B 137 (1984) 27.

[348] D. Bohle, A. Richter, U. Berg, J. Drexler, R. Heil, U. Kneissl, H. Metzger, R. Stock, B. Fischer, H. Hollick, and D. Kollewe, Nucl. Phys. A 458 (1986) 205.

[349] D. Zawischa, J. Phys. G 24 (1998) 683.

[350] W. Ziegler, C. Rangacharyulu, A. Richter, and C. Spieler, Phys. Rev. Lett. 65 (1990) 2515.

[351] W. Ziegler, N. Huxel, P. von Neumann-Cosel, C. Rangacharyulu, A. Richter, C. Spieler, C. De Coster, and K. Heyde, Nucl. Phys. A 564 (1993) 366.

[352] H. Pai, T. Beck, J. Beller, R. Beyer, M. Bhike, V. Derya, U. Gayer, J. Isaak, Krishichayan, J. Kvasil, B. Löher, V. O. Nesterenko, N. Pietralla, G. Martínez-Pinedo, L. Mertes, V. Y. Ponomarev, P.-G. Reinhard, A. Repko, P. C. Ries, C. Romig, D. Savran, R. Schwengner, W. Tornow, V. Werner, J. Wilhelmy, A. Zilges, and M. Zweidinger, Phys. Rev. C 93 (2016) 014318.

[353] C. Fransen, N. Pietralla, Z. Ammar, D. Bandyopadhyay, N. Boukharouba, P. von Brentano, A. Dewald, J. Gableske, A. Gade, J. Jolie, U. Kneissl, S. R. Lesher, A. F. Lisetskiy, M. T. McEllistrem, M. Merrick, H. H. Pitz, N. Warr, V. Werner, and S. W. Yates, Phys. Rev. C 67 (2003) 024307.

[354] G. Rusev, R. Schwengner, F. Donau, M. Erhard, S. Frauendorf, E. Grosse, A. R. Junghans, L. Kaubler, K. Kosev, L. K. Kostov, S. Mallion, K. D. Schilling, A. Wagner, H. von Garrel, U. Kneissl, C. Kohstall, M. Kreutz, H. H. Pitz, M. Scheck, F. Stedile, P. von Brentano, C. Fransen, J. Jolie, A. Linnemann, N. Pietralla, and V. Werner, Phys. Rev. C 73 (2006) 044308.

[355] A. Linnemann, C. Fransen, M. Gorska, J. Jolie, U. Kneissl, P. Knoch, D. Mücher, H. H. Pitz, M. Scheck, C. Scholl, and P. v. Brentano, Phys. Rev. C 72 (2005) 064323.

[356] C. Kohstall, D. Belic, P. von Brentano, C. Fransen, A. Gade, R.-D. Herzberg, J. Jolie, U. Kneissl, A. Linnemann, A. Nord, N. Pietralla, H. H. Pitz, M. Scheck, F. Stedile, V. Werner, and S. W. Yates, Phys. Rev. C 72 (2005) 034302.

[357] A. Linnemann, C. Fransen, J. Jolie, U. Kneissl, P. Knoch, C. Kohstall, D. Mücher, H. H. Pitz, M. Scheck, C. Scholl, F. Stedile, P. v. Brentano, N. Warr, and V. Werner, Phys. Rev. C 75 (2007) 024310.

[358] H. von Garrel, P. von Brentano, C. Fransen, G. Friessner, N. Hollmann, J. Jolie, F. Käppeler, L. Käubler, U. Kneissl, C. Kohstall, L. Kostov, A. Linnemann, D. Mücher, N. Pietralla, H. H. Pitz, G. Rusev, M. Scheck, K. D. Schilling, C. Scholl, R. Schwengner, F. Stedile, S. Walter, V. Werner, and K. Wisshak, Phys. Rev. C 73 (2006) 054315.

[359] M. Scheck, D. Belic, P. von Brentano, J. J. Carroll, C. Fransen, A. Gade, H. von Garrel, U. Kneissl, C. Kohlstall, A. Linnemann, N. Pietralla, H. H. Pitz, F. Stedile, R. Toman, and V. Werner, PRC 67 (2003) 064313.

[360] A. Linnemann, P. von Brentano, J. Eberth, J. Enders, A. Fitzler, C. Fransen, E. Guliyev, R. D. Herzberg, L. Käubler, A. A. Kuliev, P. von Neumann-Cosel, N. Pietralla, H. Prade, A. Richter, R. Schwengner, H. G. Thomas, D. Weisshaar, and I. Wiedenhöver, Phys. Lett. B 554 (2003) 15.

[361] B. Quiter, B. Ludewigt, V. Mozin, C. Wilson, and S. Korbly, Nucl. Instr. Meth. Phys. Res. B 269 (2011) 1130.

[362] F. Stedile, E. Fill, D. Belic, P. von Brentano, C. Fransen, A. Gade, U. Kneissl, C. Kohstall, A. Linnemann, P. Matschinsky, A. Nord, N. Pietralla, H. H. Pitz, M. Scheck, and V. Werner, Phys. Rev. C 63 (2001) 024320.

[363] A. Nord, J. Enders, A. E. de Almeida Pinto, D. Belic, P. von Brentano, C. Fransen, U. Kneissl, C. Kohstall, A. Linnemann, P. von Neumann-Cosel, N. Pietralla, H. H. Pitz, A. Richter, F. Stedile, and V. Werner, Phys. Rev. C 67 (2003) 034307.

[364] A. Makinaga, R. Massarczyk, R. Schwengner, M. Beard, F. Dönau, M. Anders, D. Bemmerer, R. Beyer, R. Hannaske, A. R. Junghans, M. Kempe, T. Kögler, M. Röder, K. Schmidt, and A. Wagner, Phys. Rev. C 90 (2014) 044301.

[365] C. T. Angell, R. Hajima, T. Shizuma, B. Ludewigt, and B. J. Quiter, Phys. Rev. Lett. 117 (2016) 142501.

[366] E. Kwan, G. Rusev, A. S. Adekola, F. Dönau, S. L. Hammond, C. R. Howell, H. J. Karwowski, J. H. Kelley, R. S. Pedroni, R. Raut, A. P. Tonchev, and W. Tornow, Phys. Rev. C 83 (2011) 041601.

[367] C. T. Angell, R. Yee, T. H. Joshi, E. Swanberg, E. B. Norman, C. L. Hicks, A. Klimenko, S. Korbly, C. Wilson, W. D. Kulp, G. A. Warren, T. H. Bray, R. Copping, P. A. Glans, T. Tyliszczak, and D. K. Shuh, Phys. Rev. C 82 (2010) 054310.

[368] S. Walter, F. Stedile, J. J. Carroll, C. Fransen, G. Friessner, N. Hollmann, H. v. Garrel, J. Jolie, O. Karg, F. Käppeler, U. Kneissl, C. Kohstall, P. v. Neumann-Cosel, A. Linnemann, D. Mücher, N. Pietralla, H. H. Pitz, G. Rusev, M. Scheck, C. Scholl, R. Schwengner, V. Werner, and K. Wisshak, Phys. Rev. C 75 (2007) 034301.

[369] G. Rusev, R. Schwengner, F. Dönau, S. Frauendorf, L. Käubler, L. K. Kostov, S. Mallion, K. D. Schilling, A. Wagner, E. Grosse, H. von Garrel, U. Kneißl, C. Kohstall, M. Kreutz, H. H. Pitz, M. Scheck, F. Stedile, P. von Brentano, J. Jolie, A. Linnemann, N. Pietralla, and V. Werner, Phys. Rev. Lett. 95 (2005) 062501.

[370] N. Pietralla, C. Fransen, D. Belic, P. von Brentano, C. Frießner, U. Kneissl, A. Linnemann, A. Nord, H. H. Pitz, T. Otsuka, I. Schneider, V. Werner, and I. Wiedenhöver, Phys. Rev. Lett. 83 (1999) 1303.

[371] N. Pietralla, D. Belic, P. von Brentano, C. Fransen, R.-D. Herzberg, U. Kneissl, H. Maser, P. Matschinsky, A. Nord, T. Otsuka, H. H. Pitz, V. Werner, and I. Wiedenhöver, Phys. Rev. C 58 (1998) 796.

[372] N. Pietralla, P. von Brentano, and A. Lisetskiy, Prog. Part. Nucl. Phys. 60 (2008) 225.

[373] V. Werner, D. Belic, P. von Brentano, C. Fransen, A. Gade, H. von Garrel, J. Jolie, U. Kneissl, C. Kohstall, A. Linnemann, A. Lisetskiy, N. Pietralla, H. Pitz, M. Scheck, K.-H. Speidel, F. Stedile, and S. Yates, Phys. Lett. B 550 (2002) 140.

[374] T. C. Li, N. Pietralla, C. Fransen, H. v. Garrel, U. Kneissl, C. Kohstall, A. Linnemann, H. H. Pitz, G. Rainovski, A. Richter, M. Scheck, F. Stedile, P. v. Brentano, P. v. Neumann-Cosel, and V. Werner, Phys. Rev. C 71 (2005) 044318.

[375] G. A. Bartholomew, E. D. Earle, A. J. Ferguson, J. W. Knowles, and M. A. Lone, Adv. Nucl. Phys. 7 (1973) 229.

[376] M. Arnold, J. Birkhan, J. Pforr, N. Pietralla, F. Schließmann, M. Steinhorst, and F. Hug, Phys. Rev. Accel. Beams 23 (2020) 020101.

[377] M. Salvatores and G. Palmiotti, Prog. Part. Nucl. Phys. 66 (2011) 144.

[378] M. Chadwick, M. Herman, P. Obložinský, M. Dunn, Y. Danon, A. Kahler, D. Smith, B. Pritychenko, G. Arbanas, R. Arcilla, R. Brewer, D. Brown, R. Capote, A. Carlson, Y. Cho, H. Derrien, K. Guber, G. Hale, S. Hoblit, S. Holloway, T. Johnson, T. Kawano, B. Kiedrowski, H. Kim, S. Kunieda, N. Larson, L. Leal, J. Lestone, R. Little, E. McCutchan, R. MacFarlane, M. MacInnes, C. Mattoon, R. McKnight, S. Mughabghab, G. Nobre, G. Palmiotti, A. Palumbo, M. Pigni, V. Pronyaev, R. Sayer, A. Sonzogni, N. Summers, P. Talou, I. Thompson, A. Trkov, R. Vogt, S. van der Marck, A. Wallner, M. White, D. Wiarda, and P. Young, Nucl. Data Sheets 112 (2011) 2887 .

[379] P. Axel, Phys. Rev. 126 (1962) 671.

[380] M. Wiescher, F. Käppeler, and K. Langanke, Annu. Rev. Astron. Astroph. 50 (2012) 165.

[381] M. Mumpower, R. Surman, G. McLaughlin, and A. Aprahamian, Prog. Part. Nucl. Phys. 86 (2016) 86 .

[382] A. C. Larsen, A. Spyrou, S. N. Liddick, and M. Guttormsen, Prog. Part. Nucl. Phys. 107 (2019) 69.

[383] S. Goriely, P. Dimitriou, M. Wiedeking, T. Belgya, R. Firestone, J. Kopecky, M. Krtička, V. Plujko, R. Schwengner, S. Siem, H. Utsunomiya, S. Hilaire, S. Péru, Y. S. Cho, D. M. Filipescu, N. Iwamoto, T. Kawano, V. Varlamov, and R. Xu, Eur. Phys. J. A 55 (2019) 172.

[384] R. Schwengner, R. Massarczyk, R. Beyer, M. Bhike, B. A. Brown, Krishichayan, K. Sieja, W. Tornow, D. Bemmerer, M. Butterling, V. Derya, M. Dietz, F. Fiedler, U. Friman-Gayer, A. Frotscher, M. Grieger, A. Hartmann, A. R. Junghans, T. Kögler, F. Ludwig, B. Lutz, H. Pai, T. Szücs, M. P. Takács, and A. Wagner, Phys. Rev. C 101 (2020) 064303.

[385] R. Schwengner, G. Rusev, N. Tsoneva, N. Benouaret, R. Beyer, M. Erhard, E. Grosse, A. R. Junghans, J. Klug, K. Kosev, H. Lenske, C. Nair, K. D. Schilling, and A. Wagner, Phys. Rev. C 78 (2008) 064314.

[386] G. Rusev, R. Schwengner, F. Dönau, M. Erhard, E. Grosse, A. R. Junghans, K. Kosev, K. D. Schilling, A. Wagner, F. Bečvář, and M. Krtička, Phys. Rev. C 77 (2008) 064321.

[387] G. Rusev, R. Schwengner, R. Beyer, M. Erhard, E. Grosse, A. R. Junghans, K. Kosev, C. Nair, K. D. Schilling, A. Wagner, F. Dönau, and S. Frauendorf, Phys. Rev. C 79 (2009) 061302.

[388] M. Erhard, A. R. Junghans, C. Nair, R. Schwengner, R. Beyer, J. Klug, K. Kosev, A. Wagner, and E. Grosse, Phys. Rev. C 81 (2010) 034319.

[389] A. Makinaga, R. Schwengner, G. Rusev, F. Dönau, S. Frauendorf, D. Bemmerer, R. Beyer, P. Crespo, M. Erhard, A. R. Junghans, J. Klug, K. Kosev, C. Nair, K. D. Schilling, and A. Wagner, Phys. Rev. C 82 (2010) 024314.

[390] R. Massarczyk, R. Schwengner, F. Dönau, E. Litvinova, G. Rusev, R. Beyer, R. Hannaske, A. R. Junghans, M. Kempe, J. H. Kelley, T. Kögler, K. Kosev, E. Kwan, M. Marta, A. Matic, C. Nair, R. Raut, K. D. Schilling, G. Schramm, D. Stach, A. P. Tonchev, W. Tornow, E. Trompler, A. Wagner, and D. Yakorev, Phys. Rev. C 86 (2012) 014319.

[391] G. Schramm, R. Massarczyk, A. R. Junghans, T. Belgya, R. Beyer, E. Birgersson, E. Grosse, M. Kempe, Z. Kis, K. Kosev, M. Krtička, A. Matic, K. D. Schilling, R. Schwengner, L. Szentmiklósi, A. Wagner, and J. L. Weil, Phys. Rev. C 85 (2012) 014311.

[392] R. Massarczyk, G. Schramm, A. R. Junghans, R. Schwengner, M. Anders, T. Belgya, R. Beyer, E. Birgersson, A. Ferrari, E. Grosse, R. Hannaske, Z. Kis, T. Kögler, K. Kosev, M. Marta, L. Szentmiklósi, A. Wagner, and J. L. Weil, Phys. Rev. C 87 (2013) 044306.

[393] R. Massarczyk, R. Schwengner, F. Dönau, S. Frauendorf, M. Anders, D. Bemmerer, R. Beyer, C. Bhatia, E. Birgersson, M. Butterling, Z. Elekes, A. Ferrari, M. E. Gooden, R. Hannaske, A. R. Junghans, M. Kempe, J. H. Kelley, T. Kögler, A. Matic, M. L. Menzel, S. Müller, T. P. Reinhardt, M. Röder, G. Rusev, K. D. Schilling, K. Schmidt, G. Schramm, A. P. Tonchev, W. Tornow, and A. Wagner, Phys. Rev. Lett. 112 (2014) 072501.

[394] R. Massarczyk, R. Schwengner, L. A. Bernstein, M. Anders, D. Bemmerer, R. Beyer, Z. Elekes, R. Hannaske, A. R. Junghans, T. Koegler, M. Roeder, K. Schmidt, A. Wagner, and L. Wagner, Phys. Rev. C 92 (2015) 044309.

[395] R. Massarczyk, G. Schramm, T. Belgya, R. Schwengner, R. Beyer, D. Bemmerer, Z. Elekes, E. Grosse, R. Hannaske, A. R. Junghans, Z. Kis, T. Kögler, C. Lorenz, K. Schmidt, L. Szentmiklósi, A. Wagner, and J. L. Weil, Phys. Rev. C 93 (2016) 014301.

[396] T. Shizuma, N. Iwamoto, A. Makinaga, R. Massarczyk, R. Schwengner, R. Beyer, D. Bemmerer, M. Dietz, A. Junghans, T. Kögler, F. Ludwig, S. Reinicke, S. Schulz, S. Urlaß, and A. Wagner, Phys. Rev. C 98 (2018) 064317.

[397] M. Müscher, J. Wilhelmy, R. Massarczyk, R. Schwengner, M. Grieger, J. Isaak, A. R. Junghans, T. Kögler, F. Ludwig, D. Savran, D. Symochko, M. P. Takács, M. Tamkas, A. Wagner, and A. Zilges, Phys. Rev. C 102 (2020) 014317.

[398] R. Schwengner, R. Massarczyk, M. Scheck, W. Tornow, G. Battaglia, T. Beck, D. Bemmerer, N. Benouaret, R. Beyer, M. Butterling, F. Fiedler, S. W. Finch, C. Fransen, U. Friman-Gayer, A. Frotscher, R. Gonzalez, M. Grieger, A. Hartmann, T. Hensel, E. Hoemann, H. Hoffmann, R. V. F. Janssens, S. Johnson, M. D. Jones, A. R. Junghans, N. Kelly, J. Kleemann, Krishichayan, D. R. Little, F. Ludwig, S. E. Müller, D. O'Donnell, O. Papst, E. Pirovano, J. Sinclair, M. P. Takács, S. Turkat, S. Urlaß, A. Wagner, V. Werner, O. Wieland, and J. Wilhelmy, Phys. Rev. C 103 (2021) 024312.

[399] J. W. Norbury, M. N. Thompson, K. Shoda, and H. Tsubota, Austral. J. Phys. 31 (1978) 471.

[400] A. Junghans, G. Rusev, R. Schwengner, A. Wagner, and E. Grosse, Phys. Lett. B 670 (2008) 200.

[401] E. Grosse, A. R. Junghans, and R. Massarczyk, Eur. Phys. J. A 53 (2017) 225.

[402] A. Koning, D. Rochman, J.-C. Sublet, N. Dzysiuk, M. Fleming, and S. van der Marck, Nucl. Data Sheets 155 (2019) 1.

[403] J. Isaak, D. Savran, M. Krticka, M. W. Ahmed, J. Beller, E. Fiori, J. Glorius, J. H. Kelley, B. Löher, N. Pietralla, C. Romig, G. Rusev, M. Scheck, L. Schnorrenberger, J. Silva, K. Sonnabend, A. P. Tonchev, W. Tornow, H. R. Weller, and M. Zweidinger, Phys. Lett. B 727 (2013) 361.

[404] C. Romig, J. Beller, J. Glorius, J. Isaak, J. H. Kelley, E. Kwan, N. Pietralla, V. Y. Ponomarev, A. Sauerwein, D. Savran, M. Scheck, L. Schnorrenberger, K. Sonnabend, A. P. Tonchev, W. Tornow, H. R. Weller, A. Zilges, and M. Zweidinger, Phys. Rev. C 88 (2013) 044331.

[405] M. Scheck, V. Y. Ponomarev, T. Aumann, J. Beller, M. Fritzsche, J. Isaak, J. H. Kelley, E. Kwan, N. Pietralla, R. Raut, C. Romig, G. Rusev, D. Savran, K. Sonnabend, A. P. Tonchev, W. Tornow, H. R. Weller, and M. Zweidinger, Phys. Rev. C 87 (2013) 051304.

[406] P. M. Goddard, N. Cooper, V. Werner, G. Rusev, P. D. Stevenson, A. Rios, C. Bernards, A. Chakraborty, B. P. Crider, J. Glorius, R. S. Ilieva, J. H. Kelley, E. Kwan, E. E. Peters, N. Pietralla, R. Raut, C. Romig, D. Savran, L. Schnorrenberger, M. K. Smith, K. Sonnabend, A. P. Tonchev, W. Tornow, and S. W. Yates, Phys. Rev. C 88 (2013) 064308.

[407] N. Pietralla, J. Isaak, and V. Werner, Eur. Phys. J. A 55 (2019) 237.

[408] H. Utsunomiya, T. Renstrøm, G. M. Tveten, S. Goriely, T. Ari-izumi, V. W. Ingeberg, B. V. Kheswa, Y.-W. Lui, S. Miyamoto, S. Hilaire, S. Péru, and A. J. Koning, Phys. Rev. C 100 (2019) 034605.

[409] J. Ahrens, H. Borchert, K. Czock, H. Eppler, H. Gimm, H. Gundrum, M. Kröning, P. Riehn, G. Sita Ram, A. Zieger, and B. Ziegler, Nucl. Phys. 251 (1975) 479.

[410] J. Ahrens, Nucl. Phys. 446 (1985) 229.

[411] S. S. Dietrich and B. L. Berman, At. Data Nucl. Data Tables 38 (1988) 199.

[412] H. Ohgaki, S. Sugiyama, T. Yamazaki, T. Mikado, M. Chiwaki, K. Yamada, R. Suzuki, T. Noguchi, and T. Tomimasu, IEEE Trans. Nucl. Sci. 38 (1991) 386.

[413] H. Utsunomiya, Y. Yonezawa, H. Akimune, T. Yamagata, M. Ohta, M. Fujishiro, H. Toyokawa, and H. Ohgaki, Phys. Rev. C 63 (2000) 018801.

[414] S. Amano, K. Horikawa, K. Ishihara, S. Miyamoto, T. Hayakawa, T. Shizuma, and T. Mochizuki, Nucl. Instr. Meth. Phys. Res. A 602 (2009) 337.

[415] T. Renstrøm, H.-T. Nyhus, H. Utsunomiya, R. Schwengner, S. Goriely, A. C. Larsen, D. M. Filipescu, I. Gheorghe, L. A. Bernstein, D. L. Bleuel, T. Glodariu, A. Görgen, M. Guttormsen, T. W. Hagen, B. V. Kheswa, Y.-W. Lui, D. Negi, I. E. Ruud, T. Shima, S. Siem, K. Takahisa, O. Tesileanu, T. G. Tornyi, G. M. Tveten, and M. Wiedeking, Phys. Rev. C 93 (2016) 064302.

[416] S. Goriely and V. Plujko, Phys. Rev. C 99 (2019) 014303.

[417] M. Martini, S. Péru, S. Hilaire, S. Goriely, and F. Lechaftois, Phys. Rev. C 94 (2016) 014304.

[418] S. Goriely, S. Hilaire, S. Péru, M. Martini, I. Deloncle, and F. Lechaftois, Phys. Rev. C 94 (2016) 044306.

[419] S. Goriely, S. Hilaire, S. Péru, and K. Sieja, Phys. Rev. C 98 (2018) 014327.

[420] H. Utsunomiya, I. Gheorghe, D. Filipescu, K. Stopani, S. Belyshev, H. Wang, G. Fan, T. Ariizumi, Y. Lui, D. Symochko, M. Krzysiek, S. Miyamoto, S. Goriely, and T. Kawano, EPJ Web Conf. 239 (2020) 01002.

[421] T. Rauscher, Nucl. Phys. News 28 (2018) 12.

[422] J. J. Cowan, C. Sneden, J. E. Lawler, A. Aprahamian, M. Wiescher, K. Langanke, G. Martínez-Pinedo, and F.-K. Thielemann, Rev. Mod. Phys. 93 (2021) 015002.

[423] M. Arnould and S. Goriely, Phys. Rep. 384 (2003) 1.

[424] R. J. deBoer, M. Wiescher, J. Görres, R. Longland, C. Iliadis, G. Rusev, and A. P. Tonchev, Phys. Rev. C 82 (2010) 025802.

[425] H. Utsunomiya, P. Mohr, A. Zilges, and M. Rayet, Nucl. Phys. A777 (2006) 459.

[426] P. Mohr, Phys. Rev. C 61 (2000) 045802.

[427] K. Vogt, P. Mohr, M. Babilon, J. Enders, T. Hartmann, C. Hutter, T. Rauscher, S. Volz, and A. Zilges, Phys. Rev. C 63 (2001) 055802.

[428] K. Sonnabend, K. Vogt, D. Galaviz, S. Müller, and A. Zilges, Phys. Rev. C 70 (2004) 035802.

[429] K. Sonnabend, P. Mohr, K. Vogt, A. Zilges, A. Mengoni, T. Rauscher, H. Beer, F. Kappeler, and R. Gallino, Astrophys. J. 583 (2003) 506.

[430] A. Makinaga, H. Utsunomiya, S. Goriely, T. Kaihori, S. Goko, H. Akimune, T. Yamagata, H. Toyokawa, T. Matsumoto, H. Harano, H. Harada, F. Kitatani, Y. K. Hara, S. Hohara, and Y.-W. Lui, Phys. Rev. C 79 (2009) 025801.

[431] D. Belic, C. Arlandini, J. Besserer, J. de Boer, J. J. Carroll, J. Enders, T. Hartmann, F. Käppeler, H. Kaiser, U. Kneissl, M. Loewe, H. J. Maier, H. Maser, P. Mohr, P. von Neumann-Cosel, A. Nord, H. H. Pitz, A. Richter, M. Schumann, S. Volz, and A. Zilges, Phys. Rev. Lett. 83 (1999) 5242.

[432] D. Belic, C. Arlandini, J. Besserer, J. de Boer, J. J. Carroll, J. Enders, T. Hartmann, F. Käppeler, H. Kaiser, U. Kneissl, E. Kolbe, K. Langanke, M. Loewe, H. Maier, H. Maser, P. Mohr, P. von Neumann-Cosel, A. Nord, H. H. Pitz, A. Richter, M. Schumann, F.-K. Thielemann, S. Volz, and A. Zilges, Phys. Rev. C 65 (2002) 035801.

[433] W. Tornow, M. Bhike, S. W. Finch, and Krishichayan, Nucl. Instr. Meth. Phys. Res. A 928 (2019) 79.

[434] K. L. Malatji, M. Wiedeking, S. Goriely, C. P. Brits, B. V. Kheswa, F. L. Bello Garrote, D. L. Bleuel, F. Giacoppo, A. Görgen, M. Guttormsen, K. Hadynska-Klek, T. W. Hagen, V. W. Ingeberg, M. Klintefjord, A. C. Larsen, P. Papka, T. Renstrøm, E. Sahin, S. Siem, L. Siess, G. M. Tveten, and F. Zeiser, Phys. Lett. B 791 (2019) 403.

[435] U. Kneissl, Prog. Part. Nucl. Phys. 46 (2001) 79.

[436] C. Matei, D. Balabanski, D. M. Filipescu, and O. Tesileanu, J. of Phys.: Conf. Ser. 940 (2018) 012025.

[437] Q. Ye, G. Laskaris, W. Chen, H. Gao, W. Zheng, X. Zong, T. Averett, G. D. Cates, and W. A. Tobias, Eur. Phys. J. A 44 (2010) 55.

[438] K. Kramer, X. Zong, R. Lu, D. Dutta, H. Gao, X. Qian, Q. Ye, X. Zhu, T. Averett, and S. Fuchs, Nucl. Instr. Meth. Phys. Res. A 582 (2007) 318.

[439] G. Laskaris, W. Ji, X. Yan, J. Zhou, W. R. Zimmerman, M. W. Ahmed, T. Averett, A. Deltuva, A. C. Fonseca, H. Gao, J. Golak, A. Kafkarkou, H. J. Karwowski, B. Lalremruata, J. Manfredi, J. M. Mueller, P. U. Sauer, R. Skibiński, A. P. Smith, M. B. Tsang, H. R. Weller, H. Witała, Y. K. Wu, and Z. W. Zhao, Phys. Rev. C 103 (2021) 034311.

[440] F. Hoyle, Astrophys. J. Suppl. Ser. 1 (1954) 121.

[441] D. N. F. Dunbar, R. E. Pixley, W. A. Wenzel, and W. Whaling, Phys. Rev. 92 (1953) 649.

[442] C. W. Cook, W. A. Fowler, C. C. Lauritsen, and T. Lauritsen, Phys. Rev. 107 (1957) 508.

[443] M. Freer and H. Fynbo, Prog. Part. Nucl. Phys. 78 (2014) 1.

[444] H. Morinaga, Phys. Rev. 101 (1956) 254.

[445] D. M. Brink, *Proceedings of International School of Physics "Enrico Fermi", Course XXXVI*, Academic Press (1966).

[446] M. Freer, M. Itoh, T. Kawabata, H. Fujita, H. Akimune, Z. Buthelezi, J. Carter, R. W. Fearick, S. V. Förtsch, M. Fujiwara, U. Garg, N. Hashimoto, K. Kawase, S. Kishi, T. Murakami, K. Nakanishi, Y. Nakatsugawa, B. K. Nayak, R. Neveling, S. Okumura, S. M. Perez, P. Papka, H. Sakaguchi, Y. Sasamoto, F. D. Smit, J. A. Swartz, H. Takeda, S. Terashima, M. Uchida, I. Usman, Y. Yasuda, M. Yosoi, and J. Zenihiro, Phys. Rev. C 86 (2012) 034320.

[447] S. Ishikawa, Phys. Rev. C 90 (2014) 061604.

[448] R. Smith, T. Kokalova, C. Wheldon, J. E. Bishop, M. Freer, N. Curtis, and D. J. Parker, Phys. Rev. Lett. 119 (2017) 132502.

[449] D. Dell'Aquila, I. Lombardo, G. Verde, M. Vigilante, L. Acosta, C. Agodi, F. Cappuzzello, D. Carbone, M. Cavallaro, S. Cherubini, A. Cvetinovic, G. D'Agata, L. Francalanza, G. L. Guardo, M. Gulino, I. Indelicato, M. La Cognata, L. Lamia, A. Ordine, R. G. Pizzone, S. M. R. Puglia, G. G. Rapisarda, S. Romano, G. Santagati, R. Spartà, G. Spadaccini, C. Spitaleri, and A. Tumino, Phys. Rev. Lett. 119 (2017) 132501.

[450] T. Rana, S. Bhattacharya, C. Bhattacharya, S. Manna, S. Kundu, K. Banerjee, R. Pandey, P. Roy, A. Dhal, G. Mukherjee, V. Srivastava, A. Dey, A. Chaudhuri, T. Ghosh, A. Sen, M. Asgar, T. Roy, J. Sahoo, J. Meena, A. Saha, R. Saha, M. Sinha, and A. Roy, Phys. Lett. B 793 (2019) 130.

[451] S. Polikanov, V. A. Druin, V. A. Karnaukhov, V. L. Mikheev, A. A. Pleve, N. K. Skobelev, V. G. Subbotin, G. M. Ter-Akopyan, and V. A. Fomichev, J. Exp. Theor. Phys. 42 (1962) 1464.

[452] V. Strutinsky, Nucl. Phys. 95 (1967) 420.

[453] P. Möller, S. Nilsson, and R. Sheline, Phys. Lett. B 40 (1972) 329.

[454] B. B. Back, H. C. Britt, J. D. Garrett, and O. Hansen, Phys. Rev. Lett. 28 (1972) 1707.

[455] S. Ćwiok, W. Nazarewicz, J. Saladin, W. Płóciennik, and A. Johnson, Phys. Lett. B 322 (1994) 304.

[456] M. Kowal and J. Skalski, Phys. Rev. C 85 (2012) 061302.

[457] P. Jachimowicz, M. Kowal, and J. Skalski, Phys. Rev. C 87 (2013) 044308.

[458] P. Thirolf and D. Habs, Prog. Part. Nucl. Phys. 49 (2002) 325.

[459] J. Blons, B. Fabbro, C. Mazur, D. Paya, M. Ribrag, and Y. Patin, Nucl. Phys. 477 (1988) 231.

[460] J. Blons, Nucl. Phys. 502 (1989) 121.

[461] A. Krasznahorkay, M. Hunyadi, M. N. Harakeh, M. Csatlós, T. Faestermann, A. Gollwitzer, G. Graw, J. Gulyás, D. Habs, R. Hertenberger, H. J. Maier, Z. Máté, D. Rudolph, P. Thirolf, J. Timár, and B. D. Valnion, Phys. Rev. Lett. 80 (1998) 2073.

[462] J. Blons, C. Mazur, and D. Paya, Phys. Rev. Lett. 35 (1975) 1749.

[463] C. D. Bowman, I. G. Schröder, K. C. Duvall, and C. E. Dick, Phys. Rev. C 17 (1978) 1086.

[464] P. A. Dickey and P. Axel, Phys. Rev. Lett. 35 (1975) 501.

[465] L. Csige, D. M. Filipescu, T. Glodariu, J. Gulyás, M. M. Günther, D. Habs, H. J. Karwowski, A. Krasznahorkay, G. C. Rich, M. Sin, L. Stroe, O. Tesileanu, and P. G. Thirolf, Phys. Rev. C 87 (2013) 044321.

[466] D. Brown, M. Chadwick, R. Capote, A. Kahler, A. Trkov, M. Herman, A. Sonzogni, Y. Danon, A. Carlson, M. Dunn, D. Smith, G. Hale, G. Arbanas, R. Arcilla, C. Bates, B. Beck, B. Becker, F. Brown, R. Casperson, J. Conlin, D. Cullen, M.-A. Descalle, R. Firestone, T. Gaines, K. Guber, A. Hawari, J. Holmes, T. Johnson, T. Kawano, B. Kiedrowski, A. Koning, S. Kopecky, L. Leal, J. Lestone, C. Lubitz, J. Márquez Damián, C. Mattoon, E. McCutchan, S. Mughabghab, P. Navratil, D. Neudecker, G. Nobre, G. Noguere, M. Paris, M. Pigni, A. Plompen, B. Pritychenko, V. Pronyaev, D. Roubtsov, D. Rochman, P. Romano, P. Schillebeeckx, S. Simakov, M. Sin, I. Sirakov, B. Sleaford, V. Sobes, E. Soukhovitskii, I. Stetcu, P. Talou, I. Thompson, S. van der Marck, L. Welser-Sherrill, D. Wiarda, M. White, J. Wormald, R. Wright, M. Zerkle, G. Y̌erovnik, and Y. Zhu, Nucl. Data Sheets 148 (2018) 1.

[467] T. Scott Carman, V. Litveninko, J. Madey, C. Neuman, B. Norum, P. G. O'Shea, N. Russell Roberson, C. Y. Scarlett, E. Schreiber, and H. R. Weller, Nucl. Instr. Meth. Phys. Res. A 378 (1996) 1.

[468] P. G. Thirolf and D. Habs, Eur. Phys. J. Spec. Top. 223 (2014) 1213.

[469] V. Varlamov and B. Ishkhanov, INDC(CCP)-433 (2002).

[470] D. Ridikas, M.-L. Giacri, M. B. Chadwick, J.-C. David, D. Doré, X. Ledoux, A. Van Lauwe, and W. B. Wilson, Nucl. Instr. Meth. Phys. Res. A 562 (2006) 710.

[471] G. Suliman, V. Iancu, C. Ur, M. Iovea, I. Daito, and H. Ohgaki, Rom. Rep. Phys. 68 (2016) S799.

[472] W. Bertozzi and R. J. Ledoux, Nucl. Instr. Meth. Phys. Res. B 241 (2005) 820.

[473] J. Pruet, D. P. McNabb, C. A. Hagmann, F. V. Hartemann, and C. P. J. Barty, J. Appl. Phys. 99 (2006) 123102.

[474] B. Ludewigt, B. Quiter, and S. Ambers, DOE report FTLB11MP0212 (2011).

[475] N. Kikuzawa, R. Hajima, N. Nishimori, E. Minehara, T. Hayakawa, T. Shizuma, H. Toyokawa, and H. Ohgaki, Appl. Phys. Express 2 (2009) 036502.

[476] C. A. Hagmann, J. M. Hall, M. S. Johnson, D. P. McNabb, J. H. Kelley, C. Huibregtse, E. Kwan, G. Rusev, and A. P. Tonchev, J. Appl. Phys. 106 (2009).

[477] C. Angell, R. Hajima, T. Hayakawa, T. Shizuma, H. Karwowski, and J. Silano, Nucl. Instr. Meth. Phys. Res. B 347 (2015) 11.

[478] G. A. Warren, R. S. Detwiler, and P. N. Peplowski, in *IEEE Nuclear Science Symposium Medical Imaging Conference* (2010).

[479] R. S. Kemp, A. Danagoulian, R. R. Macdonald, and J. R. Vavrek, Proc. Natl. Acad. Sci. U.S.A. 113 (2016) 8618.

[480] A. S. Adekola, C. T. Angell, S. L. Hammond, A. Hill, C. R. Howell, H. J. Karwowski, J. H. Kelley, and E. Kwan, Phys. Rev. C 83 (2011) 034615.

[481] S. L. Hammond, A. S. Adekola, C. T. Angell, H. J. Karwowski, E. Kwan, G. Rusev, A. P. Tonchev, W. Tornow, C. R. Howell, and J. H. Kelley, Phys. Rev. C 85 (2012) 044302.

[482] M. Johnson, C. Hagmann, J. Hall, D. McNabb, J. Kelley, C. Huibregtse, E. Kwan, G. Rusev, and A. Tonchev, Nucl. Instr. Meth. Phys. Res. B 285 (2012) 72.

[483] R. T. Kouzes, E. R. Siciliano, J. E. Tanner, and G. A. Warren, Nucl. Instr. Meth. Phys. Res. A 922 (2019) 222.

[484] T. Hayakawa, N. Kikuzawa, R. Hajima, T. Shizuma, N. Nishimori, M. Fujiwara, and M. Seya, Nucl. Instr. Meth. Phys. Res. A 621 (2010) 695.

[485] R. Hajima, T. Hayakawa, N. Kikuzawa, and E. Minehara, J. Nucl. Sci. Technol. 45 (2008) 441.

[486] H. Lan, T. Song, X. Huang, S. Zhao, J. Zhou, Z. Zhu, Y. Xu, D. L. Balabanski, and W. Luo, Sci. Rep. 11 (2021) 1306.

[487] W. Bertozzi, S. E. Korbly, R. J. Ledoux, and W. Park, Nucl. Instr. Meth. Phys. Res. B 261 (2007) 331.

[488] *J.A. Caggiano, G.A. Warren, S.E. Korbly, R.A. Hasty, A. Klimenko, and W.H. Park*, in 2007 IEEE Nuclear Science Symposium Conference Record, Honolulu, HI, USA, 2007, pp. 2045-2046.

[489] T. Hayakawa, H. Ohgaki, T. Shizuma, R. Hajima, N. Kikuzawa, E. Minehara, T. Kii, and H. Toyokawa, Rev. Sci. Instr. 80 (2009) 045110.

[490] *D.L. Balabanski, B. Blümich, N. Gelli, V. Iancu, M. Iovea, A. Kriznar, M. Massi, A. Mazzinghi, I. Ortega-Feliu. M.A. Respaldiza, C. Ruberto, S. Scricano, G. Suliman, Z. Szőkefalvi-Nagy, C.A. Ur, and W. Zia,*, in Nuclear Physics for Cultural Heritage, eds. A. Mackova et al., (EDP Sciences, Molhouse, 2016) p. 37.

[491] H. Toyokawa, H. Ohgaki, T. Hayakawa, T. Kii, T. Shizuma, R. Hajima, N. Kikuzawa, K. Masuda, F. Kitatani, and H. Harada, Jap. J. Appl. Phys. 50 (2011) 100209.

[492] G. Mariani, L. Bruselli, T. Kuwert, E. E. Kim, A. Flotats, O. Israel, M. Dondi, and N. Watanabe, Eur. J. Nucl. Med. Mol. Imaging 37 (2010) 1959.

[493] N. Estre, D. Eck, J. Pettier, E. Payan, C. Roure, and E. Simon, IEEE Trans. Nucl. Sci. 62 (2015) 3104.

[494] H. Zen, H. Ohgaki, Y. Taira, T. Hayakawa, T. Shizuma, I. Daito, J. Yamazaki, T. Kii, H. Toyokawa, and M. Katoh, AIP Adv. 9 (2019) 035101.

[495] K. Ali, H. Ohgaki, H. Zen, T. Kii, T. Hayakawa, T. Shizuma, H. Toyokawa, Y. Taira, V. Iancu, G. Turturica, C. A. Ur, M. Fujimoto, and M. Katoh, IEEE Trans. Nucl. Sci. 67 (2020) 1976.

[496] K. Siegbahn, *Alpha-, Beta- and Gamma-Ray Spectroscopy*, North Holland (1979).

[497] M. Omer and R. Hajima, Nucl. Instr. Meth. Phys. Res. B 405 (2017) 43.

[498] G. Turturica, V. Iancu, G. Suliman, and C. Ur, Nucl. Instr. Meth. Phys. Res. B 436 (2018) 68.

[499] G. V. Turturica, V. Iancu, A. Pappalardo, P.-A. Söderström, E. Açıksöz, D. L. Balabanski, L. Capponi, P. Constantin, V. Fugaru, G. L. Guardo, M. Ilie, S. Ilie, M. Iovea, D. Lattuada, D. Nichita, T. Petruse, A. Spataru, and C. A. Ur, Eur. Phys. J. Plus 135 (2020) 140.

[500] I. Daito, H. Ohgaki, G. Suliman, V. Iancu, C. Ur, and M. Iovea, Energy Procedia 89 (2016) 389.

[501] N. Dikiy, A. Dovbnya, V. Nikiforov, and V. Uvarov, Probl. At. Sci. Technol. 46 (2006) 181.

[502] A. Dovbnya, G. Kovtun, A. Torgovkin, V. Uvarov, and B. Shramenko, Probl. At. Sci. Technol. 47 (2006) 168.

[503] N. Aizatsky, N. Dikiy, A. Dovbnya, D.Ehst, Y. Lyashko, V. Nikiforov, A. Tenishev, A. Torgovkin, V. Uvarov, V. Shevchenko, and B. Shramenko, Probl. At. Sci. Technol. 66 (2010) 140.

[504] N. Dikiy, A. Dovbnya, Y. Lyashko, E. Medvedeva, D. Medvedev, and V. Uvarov, Probl. At. Sci. Technol. 48 (2007) 118.

[505] N. Dikiy, A. Dovbnya, N. Krasnoselsky, Y. Lyashko, E. Medvedeva, D. Medvedev, V. Uvarov, and I. Fedorets, Probl. At. Sci. Technol. 115 (2018) 146.

[506] N. Dikiy, Y. Lyashko, E. Medvedeva, D. Medvedev, V. Uvarov, and I. Fedorets, Probl. At. Sci. Technol. 124 (2019) 149.

[507] N. Dikiy, Y. Lyashko, V. Shevchenko, A. Tenishev, V. Uvarov, and A. Zakharchenko, Probl. At. Sci. Technol. 126 (2020) 158.

[508] N. Aizatskyi, N. Dikiy, A. Dovbnya, M. Dolzhek, Y. Lyashko, E. Medvedeva, and D. Medvedev, Probl. At. Sci. Technol. 91 (2014) 182.

[509] J. Bagger, R. Laxdal, Y. Bylinsky, O. Kester, A. Gottberg, P. Schaffer, K. Hayashi, S. Koscielniak, M. Marchetto, and F. Ames, Proc. 9th Int. Part. Acc. Conf. (2018) 6.

[510] D. Habs and U. Köster, Appl. Phys. B 103 (2011) 501–519.

[511] H. Ejiri, T. Shima, S. Miyamoto, K. Horikawa, Y. Kitagawa, Y. Asano, S. Daté, and Y. Ohashi, J. Phys. Soc. Jap. 80 (2011) 094202.

[512] W. Luo, M. Bobeica, I. Gheorghe, D. M. Filipescu, D. Niculae, and D. L. Balabanski, Appl. Phys. B 122 (2016) 8.

[513] Y. Oganessian, S. Dmitriev, J. Kliman, O. Maslov, G. Starodub, A. Belov, and S. Tretiakova, Nucl. Phys. 701 (2002) 87.

[514] F. Ibrahim, J. Obert, O. Bajeat, J. Buhour, D. Carminati, F. Clapier, C. Donzaud, M. Ducourtieux, J. Dufour, S. Essabaa, S. Gal'es, D. Guillemaud-Mueller, F. Hosni, O. Hubert, A. Joinet, U. Köster, C. Lau, H. Lefort, G. L. Scornet, J. Lettry, A. Mueller, M. Mirea, N. Pauwels, O. Perru, J. Potier, J. Proust, F. Pougheon, H. Ravn, L. Rinolfi, G. Rossat, H. Safa, M. Saint Laurent, M. Santana-Leitner, O. Sorlin, and D. Verney, Eur. Phys. J. A 15 (2002) 357.

[515] F. Azaiez, S. Essabaa, F. Ibrahim, and D. Verney, Nucl. Phys. News 23 (2013) 5.

[516] *TRIUMF Five-Year Plan 2020–2025*, https://fiveyearplan.triumf.ca, accessed: 2021-01-22.

[517] C. P. J. Barty, *Modulated method for efficient, narrow-bandwidth, laser Compton x-ray and gamma-ray sources*, US Patent 9,706,631 B2 (Jul. 2017) and private communication.

[518] T. Akagi, A. Kosuge, S. Araki, R. Hajima, Y. Honda, T. Miyajima, M. Mori, R. Nagai, N. Nakamura, M. Shimada, T. Shizuma, N. Terunuma, and J. Urakawa, Phys. Rev. Accel. Beams 19 (2016) 114701.

[519] S. H. Park and E.-S. Kim, J. Korean Phys. Soc. 75 (2019) 887.

[520] K. Deitrick, G. Hoffstaetter, C. Franck, B. Muratori, P. Williams, G. Krafft, B. Terzić, J. Crone, and H. Owen, Phys. Rev. Accel. Beams 24 (2021) 050701.

[521] D. Angal-Kalinin, G. Arduini, B. Auchmann, J. Bernauer, A. Bogacz, F. Bordry, S. Bousson, C. Bracco, O. Brüning, R. Calaga, K. Cassou, V. Chetvertkova, E. Cormier, E. Daly, D. Douglas, K. Dupraz, B. Goddard, J. Henry, A. Hutton, E. Jensen, W. Kaabi, M. Klein, P. Kostka, N. Lasheras, E. Levichev, F. Marhauser, A. Martens, A. Milanese, B. Militsyn, Y. Peinaud, D. Pellegrini, N. Pietralla, Y. Pupkov, R. Rimmer, K. Schirm, D. Schulte, S. Smith, A. Stocchi, A. Valloni, C. Welsch, G. Willering, D. Wollmann, F. Zimmermann, and F. Zomer, J. Phys. G 45 (2018) 065003.

[522] M. W. Krasny, *The Gamma Factory proposal for CERN* (2015).

[523] C. Curatolo, W. Placzek, M. Krasny, L. Serafini, and M. Zanetti, PoS LHCP2018 (2018) 089.

[524] M. W. Krasny, A. Petrenko, and W. Płaczek, Prog. Part. Nucl. Phys. 114 (2020) 103792.

[525] D. Budker, J. R. Crespo López-Urrutia, A. Derevianko, V. V. Flambaum, M. W. Krasny, A. Petrenko, S. Pustelny, A. Surzhykov, V. A. Yerokhin, and M. Zolotorev, Ann. Phys. 532 (2020) 2000204.

[526] C. Doll, H. G. Börner, T. von Egidy, H. Fujimoto, M. Jentschel, and H. Lehmann, J. Res. Natl. Inst. Stand. Technol. 105 (2000) 167.

[527] M. Jentschel, M. M. Günther, D. Habs, and P. G. Thirolf, AIP Conf. Proc. 1462 (2012) 185.

[528] E. Esarey, C. B. Schroeder, and W. P. Leemans, Rev. Mod. Phys. 81 (2009) 1229.

[529] H. E. Tsai, C. G. R. Geddes, T. Ostermavr, G. O. Muñoz, J. van Tilborg, S. K. Barber, F. Isono, H. . Mao, K. K. Swanson, R. Lehe, A. J. Gonsalves, K. Nakamura, C. Toth, C. B. Schroeder, E. Esarey, and W. P. Leemans, in *2018 IEEE Advanced Accelerator Concepts Workshop (AAC)*, pages 1–5 (2018).

[530] A. J. Gonsalves, K. Nakamura, J. Daniels, C. Benedetti, C. Pieronek, T. C. H. de Raadt, S. Steinke, J. H. Bin, S. S. Bulanov, J. van Tilborg, C. G. R. Geddes, C. B. Schroeder, C. Tóth, E. Esarey, K. Swanson, L. Fan-Chiang, G. Bagdasarov, N. Bobrova, V. Gasilov, G. Korn, P. Sasorov, and W. P. Leemans, Phys. Rev. Lett. 122 (2019) 084801.

[531] T. Szücs, D. Bemmerer, A. Caciolli, Z. Fülöp, R. Massarczyk, C. Michelagnoli, T. P. Reinhardt, R. Schwengner, M. P. Takács, C. A. Ur, A. Wagner, and L. Wagner, Phys. Rev. C 92 (2015) 014315.

[532] R. Longland, C. Iliadis, G. Rusev, A. P. Tonchev, R. J. deBoer, J. Görres, and M. Wiescher, Phys. Rev. C 80 (2009) 055803.

[533] R. Schwengner, A. Wagner, Y. Fujita, G. Rusev, M. Erhard, D. De Frenne, E. Grosse, A. R. Junghans, K. Kosev, and K. D. Schilling, Phys. Rev. C 79 (2009) 037303.

[534] C. T. Angell, R. Hajima, T. Hayakawa, T. Shizuma, H. J. Karwowski, and J. Silano, Phys. Rev. C 90 (2014) 054315.

[535] J. Sinclair, M. Scheck, S. W. Finch, Krishichayan, U. Friman-Gayer, W. Tornow, G. Battaglia, T. Beck, R. Chapman, M. M. R. Chishti, C. Fransen, R. Gonzales, E. Hoemann, J. Isaak, R. V. F. Janssens, D. A. Jaroszynski, S. Johnson, M. D. Jones, J. M. Keatings, N. Kelly, J. Kleemann, D. Little, B. Löher, K. R. Mashtakov, M. Müscher, D. O'Donnell, O. Papst, E. E. Peters, D. Savran, M. Schilling, R. Schwengner, P. Spagnoletti, M. Spieker, V. Werner, J. Wilhelmy, O. Wieland, S. W. Yates, and A. Zilges, Eur. Phys. J. A 56 (2020) 105.

[536] N. Pietralla, H. R. Weller, V. N. Litvinenko, M. W. Ahmed, and A. P. Tonchev, Nucl. Instr. Meth. Phys. Res. A 483 (2002) 556.

[537] T. C. Li, N. Pietralla, A. P. Tonchev, M. W. Ahmed, T. Ahn, C. Angell, M. A. Blackston, A. Costin, K. J. Keeter, J. Li, A. Lisetskiy, S. Mikhailov, Y. Parpottas, B. A. Perdue, G. Rainovski, W. Tornow, H. R. Weller, and Y. K. Wu, Phys. Rev. C 73 (2006) 054306.

[538] U. Gayer, T. Beck, M. Bhike, J. Isaak, N. Pietralla, P. C. Ries, D. Savran, M. Schilling, W. Tornow, and V. Werner, Phys. Rev. C 100 (2019) 034305.

[539] T. Hartmann, J. Enders, P. Mohr, K. Vogt, S. Volz, and A. Zilges, Phys. Rev. C 65 (2002) 034301.

[540] J. Isaak, D. Savran, M. Fritzsche, D. Galaviz, T. Hartmann, S. Kamerdzhiev, J. H. Kelley, E. Kwan, N. Pietralla, C. Romig, G. Rusev, K. Sonnabend, A. P. Tonchev, W. Tornow, and A. Zilges, Phys. Rev. C 83 (2011) 034304.

[541] V. Derya, D. Savran, J. Endres, M. N. Harakeh, H. Hergert, J. H. Kelley, P. Papakonstantinou, N. Pietralla, V. Y. Ponomarev, R. Roth, G. Rusev, A. P. Tonchev, W. Tornow, H. J. Wortche, and A. Zilges, Phys. Lett. B 730 (2014) 288.

[542] H. Pai, J. Beller, N. Benouaret, J. Enders, T. Hartmann, O. Karg, P. von Neumann-Cosel, N. Pietralla, V. Y. Ponomarev, C. Romig, M. Scheck, L. Schnorrenberger, S. Volz, and M. Zweidinger, Phys. Rev. C 88 (2013) 054316.

[543] Krishichayan, M. Bhike, W. Tornow, G. Rusev, A. P. Tonchev, N. Tsoneva, and H. Lenske, Phys. Rev. C 91 (2015) 044328.

[544] J. Wilhelmy, B. A. Brown, P. Erbacher, U. Gayer, J. Isaak, Krishichayan, B. Löher, M. Müscher, H. Pai, N. Pietralla, P. Ries, D. Savran, P. Scholz, M. Spieker, W. Tornow, V. Werner, and A. Zilges, Phys. Rev. C 98 (2018) 034315.

[545] T. Shizuma, T. Hayakawa, H. Ohgaki, H. Toyokawa, T. Komatsubara, N. Kikuzawa, T. Inakura, M. Honma, and H. Nakada, Phys. Rev. C 87 (2013) 024301.

[546] M. Scheck, V. Y. Ponomarev, M. Fritzsche, J. Joubert, T. Aumann, J. Beller, J. Isaak, J. H. Kelley, E. Kwan, N. Pietralla, R. Raut, C. Romig, G. Rusev, D. Savran, L. Schorrenberger, K. Sonnabend, A. P. Tonchev, W. Tornow, H. R. Weller, A. Zilges, and M. Zweidinger, Phys. Rev. C 88 (2013) 044304.

[547] V. Werner, N. Cooper, P. M. Goddard, P. Humby, R. S. Ilieva, G. Rusev, J. Beller, C. Bernards, B. P. Crider, J. Isaak, J. H. Kelley, E. Kwan, B. Löher, E. E. Peters, N. Pietralla, C. Romig, D. Savran, M. Scheck, A. P. Tonchev, W. Tornow, S. W. Yates, and M. Zweidinger, EPJ Web Conf. 93 (2015) 01031.

[548] N. Cooper, F. Reichel, V. Werner, L. Bettermann, B. Alikhani, S. Aslanidou, C. Bauer, L. Coquard, M. Fritzsche, Y. Fritzsche, J. Glorius, P. M. Goddard, T. Möller, N. Pietralla, M. Reese, C. Romig, D. Savran, L. Schnorrenberger, F. Siebenhühner, V. V. Simon, K. Sonnabend, M. K. Smith, C. Walz, S. W. Yates, O. Yevetska, and M. Zweidinger, Phys. Rev. C 86 (2012) 034313.

[549] A. Makinaga, R. Massarczyk, M. Beard, R. Schwengner, H. Otsu, T. Al-Abdullah, M. Anders, D. Bemmerer, R. Hannaske, R. John, A. R. Junghans, S. E. Müller, M. Röder, K. Schmidt, and A. Wagner, Phys. Rev. C 94 (2016) 044304.

[550] R. Schwengner, R. Massarczyk, G. Rusev, N. Tsoneva, D. Bemmerer, R. Beyer, R. Hannaske, A. R. Junghans, J. H. Kelley, E. Kwan, H. Lenske, M. Marta, R. Raut, K. D. Schilling, A. Tonchev, W. Tornow, and A. Wagner, Phys. Rev. C 87 (2013) 024306.

[551] L. Käubler, K. D. Schilling, R. Schwengner, F. Dönau, E. Grosse, D. Belic, P. von Brentano, M. Bubner, C. Fransen, M. Grinberg, U. Kneissl, C. Kohstall, A. Linnemann, P. Matschinsky, A. Nord, N. Pietralla, H. H. Pitz, M. Scheck, F. Stedile, and V. Werner, Phys. Rev. C 65 (2002) 054315.

[552] L. Käubler, H. Schnare, R. Schwengner, H. Prade, F. Dönau, P. von Brentano, J. Eberth, J. Enders, A. Fitzler, C. Fransen, M. Grinberg, R.-D. Herzberg, H. Kaiser, P. von Neumann-Cosel, N. Pietralla, A. Richter, G. Rusev, C. Stoyanov, and I. Wiedenhöver, Phys. Rev. C 70 (2004) 064307.

[553] N. Benouaret, R. Schwengner, G. Rusev, F. Dönau, R. Beyer, M. Erhard, E. Grosse, A. R. Junghans, K. Kosev, C. Nair, K. D. Schilling, A. Wagner, and N. Bendjaballah, Phys. Rev. C 79 (2009) 014303.

[554] C. Fransen, N. Pietralla, A. P. Tonchev, M. W. Ahmed, J. Chen, G. Feldman, U. Kneissl, J. Li, V. N. Litvinenko, B. Perdue, I. V. Pinayev, H. H. Pitz, R. Prior, K. Sabourov, M. Spraker, W. Tornow, H. R. Weller, V. Werner, Y. K. Wu, and S. W. Yates, Phys. Rev. C 70 (2004) 044317.

[555] G. Rusev, N. Tsoneva, F. Dönau, S. Frauendorf, R. Schwengner, A. P. Tonchev, A. S. Adekola, S. L. Hammond, J. H. Kelley, E. Kwan, H. Lenske, W. Tornow, and A. Wagner, Phys. Rev. Lett. 110 (2013) 022503.

[556] J. N. Orce, C. Fransen, A. Linnemann, C. J. McKay, S. R. Lesher, N. Pietralla, V. Werner, G. Friessner, C. Kohstall, D. Mücher, H. H. Pitz, M. Scheck, C. Scholl, F. Stedile, N. Warr, S. Walter, P. v. Brentano, U. Kneissl, M. T. McEllistrem, and S. W. Yates, Phys. Rev. C 75 (2007) 014303.

[557] A. Gade, D. Belic, P. von Brentano, C. Fransen, H. von Garrel, J. Jolie, U. Kneissl, C. Kohstall, A. Linnemann, H. H. Pity, M. Scheck, F. Stedile, and V. Werner, Phys. Rev. C 67 (2003) 034304.

[558] I. Pysmenetska, S. Walter, J. Enders, H. von Garrel, O. Karg, U. Kneissl, C. Kohstall, P. von Neumann-Cosel, H. H. Pitz, V. Y. Ponomarev, M. S. check, F. Stedile, and S. Volz, Phys. Rev. C 73 (2006) 017302.

[559] B. Özel-Tashenov, J. Enders, H. Lenske, A. M. Krumbholz, E. Litvinova, P. von Neumann-Cosel, I. Poltoratska, A. Richter, G. Rusev, D. Savran, and N. Tsoneva, Phys. Rev. C 90 (2014) 024304.

[560] R. Massarczyk, G. Rusev, R. Schwengner, F. Dönau, C. Bhatia, M. E. Gooden, J. H. Kelley, A. P. Tonchev, and W. Tornow, Phys. Rev. C 90 (2014) 054310.

[561] A. P. Tonchev, S. L. Hammond, C. R. Howell, C. Huibregtse, A. Hutcheson, J. H. Kelley, E. Kwan, R. Raut, G. Rusev, W. Tornow, T. Kawano, D. J. Vieira, and J. B. Wilhelmy, Phys. Rev. C 82 (2010) 054620.

[562] A. Gade, N. Pietralla, P. von Brentano, D. Belic, C. Fransen, U. Kneissl, C. Kohstall, A. Linnemann, H. H. Pitz, M. Scheck, N. A. Smirnova, F. Stedile, and V. Werner, Phys. Rev. C 69 (2004) 054321.

[563] C. T. Angell, S. L. Hammond, H. J. Karwowski, J. H. Kelley, M. Krtička, E. Kwan, A. Makinaga, and G. Rusev, Phys. Rev. C 86 (2012) 051302(R).

[564] M. Tamkas, E. Açıksöz, J. Isaak, T. Beck, N. Benouaret, M. Bhike, I. Boztosun, A. Durusoy, U. Gayer, Krishichayan, B. Löher, N. Pietralla, D. Savran, W. Tornow, V. Werner, A. Zilges, and M. Zweidinger, Nucl. Phys. A 987 (2019) 79.

[565] O. Papst, V. Werner, J. Isaak, N. Pietralla, T. Beck, C. Bernards, M. Bhike, N. Cooper, B. P. Crider, U. Friman-Gayer, J. Kleemann, Krishichayan, B. Löher, F. Naqvi, E. E. Peters, F. M. Prados-Estévez, R. S. Ilieva, T. J. Ross, D. Savran, W. Tornow, and J. R. Vanhoy, Phys. Rev. C 102 (2020) 034323.

[566] N. Benouaret, J. Beller, H. Pai, N. Pietralla, V. Y. Ponomarev, C. Romig, L. Schnorrenberger, M. Zweidinger, M. Scheck, J. Isaak, D. Savran, K. Sonnabend, R. Raut, G. Rusev, A. P. Tonchev, W. Tornow, H. R. Weller, and J. H. Kelley, J. Phys. G 43 (2016) 115101.

[567] J. Enders, P. von Brentano, J. Eberth, A. Fitzler, C. Fransen, R.-D. Herzberg, H. Kaiser, L. Käubler, P. von Neumann-Cosel, N. Pietralla, V. Y. Ponomarev, H. Prade, A. Richter, H. Schnare, R. Schwengner, S. Skoda, H. G. Thomas, H. Tiesler, D. Weisshaar, and I. Wiedenhöver, Phys. Lett. B 486 (2000) 279.

[568] N. Ryezayeva, T. Hartmann, Y. Kalmykov, H. Lenske, P. von Neumann-Cosel, V. Y. Ponomarev, A. Richter, A. Shevchenko, S. Volz, and J. Wambach, Phys. Rev. Lett. 89 (2002) 272502.

[569] J. Enders, P. von Brentano, J. Eberth, A. Fitzler, C. Fransen, R.-D. Herzberg, H. Kaiser, L. Käubler, P. von Neumann-Cosel, N. Pietralla, V. Y. Ponomarev, A. Richter, and R. S. I. Wiedenhöver, Nucl. Phys. A724 (2003) 243.

[570] T. Shizuma, T. Hayakawa, H. Ohgaki, H. Toyokawa, T. Komatsubara, N. Kikuzawa, A. Tamii, and H. Nakada, Phys. Rev. C 78 (2008) 061303.

[571] R. Schwengner, R. Massarczyk, B. A. Brown, R. Beyer, F. Dönau, M. Erhard, E. Grosse, A. R. Junghans, K. Kosev, C. Nair, G. Rusev, K. D. Schilling, and A. Wagner, Phys. Rev. C 81 (2010) 054315.

[572] T. Shizuma, T. Hayakawa, H. Ohgaki, H. Toyokawa, T. Komatsubara, A. Tamii, and H. Nakada, J. Phys. Conf. Ser. 312 (2011) 092056.

[573] K. Sumiyoshi, H. Utsunomiya, S. Goko, and T. Kajino, Nucl. Phys. 709 (2002) 467.

[574] H. Utsunomiya, S. Katayama, I. Gheorghe, S. Imai, H. Yamaguchi, D. Kahl, Y. Sakaguchi, T. Shima, K. Takahisa, and S. Miyamoto, Phys. Rev. C 92 (2015) 064323.

[575] H. Utsunomiya, A. Makinaga, S. Goko, T. Kaihori, H. Akimune, T. Yamagata, M. Ohta, H. Toyokawa, S. Müller, Y.-W. Lui, and S. Goriely, Phys. Rev. C 74 (2006) 025806.